

Advanced sparse optimization algorithms for interferometric imaging inverse problems in astronomy

JASLEEN BIRDI

A thesis submitted for the degree of

Doctor of Philosophy (PhD)

in

Heriot-Watt University

Institute of Sensors, Signals and Systems

School of Engineering and Physical Sciences

under the supervision of

Professor Yves Wiaux

March 2019



The copyright in this thesis is owned by the author. Any quotation from the thesis or use of any of the information contained in it must acknowledge this thesis as the source of the quotation or information.

Abstract

In the quest to produce images of the sky at unprecedented resolution with high sensitivity, new generation of astronomical interferometers have been designed. To meet the sensing capabilities of these instruments, techniques aiming to recover the sought images from the incompletely sampled Fourier domain measurements need to be reinvented. This goes hand-in-hand with the necessity to calibrate the measurement modulating unknown effects, which adversely affect the image quality, limiting its dynamic range. The contribution of this thesis consists in the development of advanced optimization techniques tailored to address these issues, ranging from radio interferometry (RI) to optical interferometry (OI).

In the context of RI, we propose a novel convex optimization approach for full polarization imaging relying on sparsity-promoting regularizations. Unlike standard RI imaging algorithms, our method jointly solves for the Stokes images by enforcing the polarization constraint, which imposes a physical dependency between the images. These priors are shown to enhance the imaging quality via various performed numerical studies. The proposed imaging approach also benefits from its scalability to handle the huge amounts of data expected from the new instruments. When it comes to deal with the critical and challenging issues of the direction-dependent effects calibration, we further propose a non-convex optimization technique that unifies calibration and imaging steps in a global framework, in which we adapt the earlier developed imaging method for the imaging step. In contrast to existing RI calibration modalities, our method benefits from well-established convergence guarantees even in the non-convex setting considered in this work and its efficiency is demonstrated through several numerical experiments.

Last but not least, inspired by the performance of these methodologies and drawing ideas from them, we aim to solve image recovery problem in OI that poses its own set of challenges primarily due to the partial loss of phase information. To this end, we propose a sparsity regularized non-convex optimization algorithm that is equipped with convergence guarantees and is adaptable to both monochromatic and hyperspectral OI imaging. We validate it by presenting the simulation results.

Acknowledgements

Pursuing a PhD is a journey in itself. While I finish this journey, I would like to extend thanks to many people who have contributed towards it.

First and foremost, I would like to express my gratitude to my PhD advisor, Professor Yves Wiaux, for giving me the opportunity to work on this research project, for his supervision and for engaging in many stimulating scientific discussions. I am also grateful to a special mentor, Dr. Audrey Repetti, for her guidance throughout my PhD. Audrey, your (in)numerous comments while reviewing the articles, your patience to answer even the stupid questions I might have asked, have been truly invaluable.

I would also like to thank my thesis examiners, Professor Oleg Smirnov and Dr. Alexander Belyaev, for critically examining my thesis and providing constructive feedback. I want to thank Dr. Arwa Dabbech and Dr. Pierre-Antoine Thouvenin for taking out time to read my thesis and giving very useful comments. Thanks a lot, all those corrections and feedback have clearly shaped the thesis in a better way.

Thanks to my lab mates (the current as well as the old ones) and friends from the BASP group: Abdullah, Arwa, Audrey, Marica, P.-A., Roberto, Matthieu, Elie, Alex, Silvia and Zhouye. Thank you for providing a great working environment and being always available for scientific discussions. Having lunches together and discussing lives outside the lab was a temporary getaway from the usual long working hours. Marica and Roberto, I owe you a big thank you. Specially for your support in those last days and yes, for helping me bind the thesis on such a short notice!

This thesis would not have been possible if it wasn't for my family. Mummy, Daddy, Didi and Jiju, thank you for always believing in me even when I didn't and supporting my decision of moving abroad for PhD. I can't thank you enough for your continued understanding. Finally, a big thanks to my partner for his constant support. Bashdeep, your role in the completion of this journey has been integral. Thank you for instilling confidence in me when I doubted myself, keeping up my mood in the difficult of the times and pushing me always.

Edinburgh, 2019

ACADEMIC REGISTRY
Research Thesis Submission

Please note this form should be bound into the submitted thesis.

Name:	JASLEEN BIRDI		
School:	School of Engineering and Physical Sciences		
Version: <i>(i.e. First, Resubmission, Final)</i>	Final	Degree Sought:	Doctor of Philosophy

Declaration

In accordance with the appropriate regulations I hereby submit my thesis and I declare that:

1. The thesis embodies the results of my own work and has been composed by myself
2. Where appropriate, I have made acknowledgement of the work of others
3. Where the thesis contains published outputs under Regulation 6 (9.1.2) these are accompanied by a critical review which accurately describes my contribution to the research and, for multi-author outputs, a signed declaration indicating the contribution of each author (complete Inclusion of Published Works Form – see below)
4. The thesis is the correct version for submission and is the same version as any electronic versions submitted*.
5. My thesis for the award referred to, deposited in the Heriot-Watt University Library, should be made available for loan or photocopying and be available via the Institutional Repository, subject to such conditions as the Librarian may require
6. I understand that as a student of the University I am required to abide by the Regulations of the University and to conform to its discipline.
7. Inclusion of published outputs under Regulation 6 (9.1.2) shall not constitute plagiarism.
8. I confirm that the thesis has been verified against plagiarism via an approved plagiarism detection application e.g. Turnitin.

* Please note that it is the responsibility of the candidate to ensure that the correct version of the thesis is submitted.

Signature of Candidate:		Date:	
-------------------------	--	-------	--

Submission

Submitted By <i>(name in capitals)</i> :	
Signature of Individual Submitting:	
Date Submitted:	

For Completion in the Student Service Centre (SSC)

Received in the SSC by <i>(name in capitals)</i> :			
Method of Submission <i>(Handed in to SSC; posted through internal/external mail)</i> :			
E-thesis Submitted <i>(mandatory for final theses)</i>			
Signature:		Date:	

Contents

Abstract	i
Acknowledgements	ii
Contents	iv
List of Tables	vii
List of Figures	viii
Abbreviations	xi
List of Notations	xii
List of Publications	xv
1 Introduction	1
1.1 The rise of interferometers	4
1.2 Challenges faced in radio interferometry	6
1.3 Problems with imaging in optical regimes	9
1.4 Thesis organization and contribution	11
2 Problem setup in radio interferometry	14
2.1 Introduction	14
2.2 Basic principle of radio interferometry	14
2.3 Observation model	15
2.3.1 Emergence of RIME	15
2.3.2 Calibration effects	23
2.4 RIME matrix formalism	24
2.5 Conclusion	27
3 Sparse representations and optimization framework	28
3.1 Introduction	28
3.2 Inverse problems	30
3.3 The world of sparsity	31
3.3.1 Exploiting sparsity for signal recovery	33

3.3.2	Sparse recovery methods	37
3.4	A tour of convex optimization framework	40
3.4.1	Proximal splitting methods	41
3.4.2	Primal-dual methods	44
3.5	Non-convex optimization	45
3.5.1	Overview	45
3.5.2	Non-convex regularizations for sparse recovery	48
3.6	Conclusion	48
4	Standard radio interferometric approaches	50
4.1	Introduction	50
4.2	Imaging techniques	51
4.2.1	CLEAN and its family	51
4.2.2	Maximum Entropy Method	54
4.2.3	Non-negative least squares	55
4.2.4	Sparse optimization methods	55
4.3	Calibration modalities	58
4.3.1	External Calibration	59
4.3.2	Self-Calibration	59
4.3.3	DDE calibration	61
4.4	Conclusion	65
5	Stokes parameters imaging in radio interferometry	67
5.1	Motivation	68
5.2	Adopted measurement model	69
5.3	Polarized SARA - Proposed imaging approach	72
5.3.1	Epigraphical projection	74
5.3.2	Algorithm formulation	77
5.3.3	Polarization constraint for TV based problems	84
5.4	Simulations and Results	87
5.4.1	Computational complexity	89
5.4.2	Effect of polarization constraint	90
5.4.3	Comparisons performed	91
5.4.4	Simulation settings	93
5.4.5	Results and discussion	94
5.5	Generalization to real data	104
5.6	Results on real data	106
5.7	Conclusion	107
6	Self DDE calibration and imaging for radio interferometry	111
6.1	Motivation	112
6.2	Stokes I imaging and DDE calibration	113
6.2.1	Description of the proposed method	113
6.2.2	Simulations and results	117

6.2.3	Sparse images with point sources	119
6.2.4	Image with an extended source	123
6.3	Concluding remarks	125
6.4	Full polarization DDE calibration and imaging	126
6.4.1	Calibration problem	128
6.4.2	Polca SARA - Proposed calibration & imaging approach	131
6.4.3	Algorithm formulation	133
6.4.4	Convergence properties	138
6.4.5	Computational complexity	139
6.5	Simulations and results	140
6.5.1	Comparisons performed	141
6.5.2	Simulation settings	143
6.5.3	Results and analysis	144
6.6	Conclusion	157
7	From radio to optical interferometric imaging	159
7.1	Motivation	160
7.2	Background	160
7.2.1	Basics of Optical Interferometry	160
7.2.2	Phase retrieval algorithms	163
7.2.3	Standard approaches for OI imaging	165
7.3	Monochromatic OI imaging	168
7.3.1	Observation model	168
7.3.2	Proposed regularized minimization problem	169
7.3.3	Proposed algorithm	173
7.4	Simulations and results	178
7.4.1	Simulation settings	178
7.4.2	Synthetic uv coverage	180
7.4.3	Realistic uv coverage	186
7.5	Hyperspectral OI imaging	188
7.5.1	Problem statement	188
7.5.2	Algorithmic details	191
7.6	Simulations and results	191
7.7	Conclusion	195
8	Conclusions and Perspectives	196
	Bibliography	200

List of Tables

5.1	SNR and NRMSE values for the reconstructed images corresponding to the forward-jet and counter-jet models, obtained by different sparsifying regularizations.	94
5.2	Percentage of pixels not satisfying the polarization constraint in the reconstructed images obtained by without imposing the polarization constraint in the reconstruction process.	95
6.1	Cygnus A (top two tables) and Hydra A (bottom two tables) results: SNR and Dynamic range values for different considered cases.	146

List of Figures

1.1	Electromagnetic spectrum depicting different radiations spanning over a range of frequencies and wavelengths.	2
1.2	Image of sky at optical and radio wavelengths.	3
1.3	The Very Large Array (VLA) consisting of 27 radio antennas, operated by NRAO in Socorro, New Mexico.	5
2.1	Block diagram depicting an antenna pair within a typical interferometer.	17
2.2	Illustration of radio interferometric coordinate system.	19
2.3	Illustration of a radio interferometric baseline.	20
2.4	Illustration of uv coverage of the VLA telescope with 27 antennas.	22
2.5	Schematic representation of a $2 \times 2N$ matrix, represented as a 2×2 block matrix.	25
3.1	Illustration of sparsity of (a) an original intensity image of the W28 supernova remnant in the: (b) Haar wavelet basis and (c) gradient (TV) domain. Credits for (a): Image courtesy of NRAO.	32
3.2	Illustration of the ℓ_1 norm inducing sparsity.	34
3.3	Illustration of weighted- ℓ_1 norm for better recovery of a sparse signal in comparison with ℓ_1 norm.	37
3.4	Graphs depicting convex and non-convex functions.	38
3.5	Illustration of the soft-thresholding operation.	42
3.6	Projection of a point $\tilde{\mathbf{S}}$ onto a convex set \mathcal{C}	43
3.7	Graphs depicting non-convex functions.	47
5.1	Illustration of the adopted block-data splitting technique for the measurement model.	71
5.2	Diagram depicting epigraph of a function \tilde{f}	76
5.3	The EHT uv coverage used for simulations for Stokes imaging.	88
5.4	The two sets of ground truth images used for performing simulations for Stokes imaging.	89
5.5	The NRMSE plots for the Stokes I image and the linear polarization image.	96
5.6	Results for the Stokes I image corresponding to the forward-jet model.	98
5.7	Results for the linear polarization image corresponding to the forward-jet model.	99
5.8	Results for the Stokes I image corresponding to the counter-jet model.	100

5.9	Results for the linear polarization image corresponding to the counter-jet model.	101
5.10	The polarization error images for the forward-jet and the counter-jet showing the pixels where the polarization constraint is not satisfied. . .	103
5.11	Results obtained for Stokes I and linear polarization intensity ($ P $) images from VLA data, displayed in log scale.	108
5.12	Zoomed west jet hotspot in Stokes I and linear polarization intensity images from our method's reconstructions and MS-CLEAN restored images.	108
5.13	Polarization error images corresponding to MS-CLEAN restored and model images.	109
6.1	Example of considered DDEs, with $K = 7 \times 7$ non-zero Fourier coefficients.	115
6.2	The diagrams of the proposed method (left) and the traditional selfcal method using StEFCal and CLEAN (right).	116
6.3	Results obtained for simulations using the proposed method and estimating only the DIEs with StEFCal-FB, varying the number of sources and total flux of $\bar{\epsilon}_1$, while fixing $E(\mathbf{x}_o) = 10$	120
6.4	Results corresponding to the simulations performed considering point sources image with 50 sources in $\bar{\epsilon}_1$, and comparing different considered cases.	121
6.5	Results corresponding to the simulations performed with M31 image using $\kappa = 0.1$ (first two columns) and $\kappa = 1$ (last two columns), and comparing different considered cases.	124
6.6	Cygnus A (first row) and Hydra A (second row) ground truth images used for performing simulations.	140
6.7	Cygnus A Stokes I true image in first row and reconstructed images (best ones over 5 performed simulations for each case) in other rows for the different considered cases.	149
6.8	Cygnus A Stokes Q true image in first row and reconstructed images (best ones over 5 performed simulations for each case) in other rows for the different considered cases.	150
6.9	Cygnus A Stokes U true image in first row and reconstructed images (best ones over 5 performed simulations for each case) in other rows for the different considered cases.	151
6.10	Hydra A Stokes I true image in first row and reconstructed images (best ones over 5 performed simulations for each case) in other rows for the different considered cases.	152
6.11	Hydra A Stokes Q true image in first row and reconstructed images (best ones over 5 performed simulations for each case) in other rows for the different considered cases.	153
6.12	Hydra A Stokes U true image in first row and reconstructed images (best ones over 5 performed simulations for each case) in other rows for the different considered cases.	154

6.13	Plots comparing the pixel values of (a) Cygnus A and (b) Hydra A true and recovered linear polarization images P , for its real $\text{Re}(\cdot)$ component (Stokes Q) on left and imaginary $\text{Im}(\cdot)$ component (Stokes U) on right.	156
7.1	Illustration of the principle behind phase closure analysis.	162
7.2	Original image $\text{LkH}\alpha$, of size 64×64 , used for simulations for OI imaging.	178
7.3	Discretized spatial frequencies coverage plans for the image of size 64×64 , used for simulations.	179
7.4	SNR graph obtained for positivity and reality constrained case with $\text{LkH}\alpha$ image and synthetic uv coverage for $u_{\mathcal{P}} = 0.2$, considering $\text{iSNR} = 30$ dB and varying $u_{\mathcal{B}}$. Different curves correspond to different number of initializations.	180
7.5	SNR graphs obtained with $\text{LkH}\alpha$ image and synthetic uv coverage, considering $\text{iSNR} = 30$ dB, varying $u_{\mathcal{B}}$ for two different power spectrum under-sampling ratios: (a) $u_{\mathcal{P}} = 0.05$ and (b) $u_{\mathcal{P}} = 0.2$.	183
7.6	Reconstructed (first row) and error (second row) images corresponding to median SNR (over 10 simulations), obtained by considering the true image $\text{LkH}\alpha$ with synthetic uv coverage for $(u_{\mathcal{P}}, u_{\mathcal{B}}) = (0.05, 0.1)$.	183
7.7	Reconstructed (first row) and error (second row) images corresponding to median SNR (over 10 simulations), obtained by considering the true image $\text{LkH}\alpha$ with synthetic uv coverage for $(u_{\mathcal{P}}, u_{\mathcal{B}}) = (0.05, 0.1)$.	185
7.8	The figure illustrating the orientation uncertainty in the recovered image when no phase information is taken into account.	186
7.9	SNR graph obtained with $\text{LkH}\alpha$ image and realistic uv coverage, considering $\text{iSNR} = 30$ dB, varying $u_{\mathcal{B}}$. Comparison between different regularization terms is depicted.	187
7.10	Reconstructed (first row) and error (second row) images corresponding to median SNR (over 10 simulations), obtained by considering the true image $\text{LkH}\alpha$ with realistic uv coverage for $u_{\mathcal{B}} = 0.2$.	187
7.11	SNR graphs obtained for the reconstruction of two different hyperspectral image cubes with the realistic uv coverage, considering $\text{iSNR} = 30$ dB for each spectral channel, varying $u_{\mathcal{B}}$. Each graph compares the SNR values for single-channel reconstruction with ℓ_1 regularization and reconstruction by considering joint sparsity with $\ell_{2,1}$ regularization.	192
7.12	Results for hyperspectral imaging with realistic uv coverage for $L = 8$, $u_{\mathcal{B}} = 0.1$ and $\text{LkH}\alpha$ as the original image. Reconstructed images obtained by considering ℓ_1 and $\ell_{2,1}$ regularizations are displayed followed by their respective error images.	193
7.13	Results for hyperspectral imaging with realistic uv coverage for $L = 8$, $u_{\mathcal{B}} = 0.1$ and synthetic image as the original image. Reconstructed images obtained by considering ℓ_1 and $\ell_{2,1}$ regularizations are displayed followed by their respective error images.	194

Abbreviations

2D	Two-dimensional
3D	Three-dimensional
CS-CLEAN	Cotton-Schwab CLEAN
CS	Compressive Sensing
DDEs	Direction-dependent effects
DIEs	Direction-independent effects
FFT	Fast Fourier transform
FB	Forward-backward
MAP	Maximum a Posteriori
MS-CLEAN	Multi-Scale CLEAN
OI	Optical Interferometry
RI	Radio Interferometry
RIME	Radio Interferometric Measurement Equation
SARA	Sparsity Averaging Reweighted Analysis
SNR	Signal-to-noise ratio
TV	Total variation

List of Notations

Standard notations

x	Scalar
\mathbf{x}	Vector
\mathbf{X}	Matrix
$\mathbf{X}_{i,j}$	Component in i^{th} row and j^{th} column of matrix \mathbf{X}
$\mathbf{X}_{i,:}$	i^{th} row of matrix \mathbf{X}
$\mathbf{X}_{:,j}$	j^{th} column of matrix \mathbf{X}
$(\cdot)^*$	Conjugate of its argument
$(\cdot)^\dagger$	Hermitian conjugate of its argument
$\mathbf{1}_N$	Ones row vector of size N
\mathbf{I}_N	Identity matrix of size $N \times N$
$\ \mathbf{x}\ _p$	ℓ_p norm of vector \mathbf{x}
$\ \mathbf{X}\ _F$	Frobenius norm of matrix \mathbf{X}
$ x $	Absolute value of its argument x
$ \mathbf{x} $	Element-wise absolute value of its argument \mathbf{x}

Common notations

N	Image dimension
M	Number of measurements
n_a	Number of antennas
T	Number of time instants
λ	Observation wavelength
λ_l	Observation wavelength for l^{th} frequency channel

ν	Observation frequency
$\bar{\mathbf{S}}$	Original unknown Stokes matrix of size $2 \times 2N$
\bar{x}	Original unknown total intensity image of size N
\mathbf{F}	2D Fourier matrix
Ψ	Sparsity basis for the image/s estimation

Modelling notations & configurable algorithmic parameters

Stokes imaging

\mathbf{Y}'	Visibility matrix of size $4 \times M$
$\tilde{\mathbf{S}}$	Reshaped Stokes matrix of size $N \times 4$ containing the Stokes images in its columns
γ	Parameter affecting the algorithm's convergence speed
ϑ	Tolerance parameter for ℓ_2 bound constraint
ε	Stopping criterion parameter for Stokes imaging
ϱ	Stopping criterion parameter linked to the polarization constraint
$\varepsilon_1, \varepsilon_2, \varepsilon_3, K'$	Parameters related to adaptive ℓ_2 bound scheme

Imaging & calibration

\mathbf{x}_0	Image containing the known brightest sources of \bar{x}
ϵ	Image containing the unknown sources of \bar{x} and correction for the amplitude of the known sources
$\bar{\mathbf{d}}_{t,\alpha}$	Original unknown DDE related to antenna α at time instant t
$\check{\mathbf{U}}_\alpha$	Compact-support Fourier kernels matrix corresponding to $\bar{\mathbf{d}}_{t,\alpha}$
$\mathbf{Y}_{t,\alpha,\beta}$	2×2 visibility matrix for antenna pair (α, β) at time instant t
\mathbf{S}_0	Stokes matrix containing the high amplitude, thresholded part of $\bar{\mathbf{S}}$ obtained with 1GC
\mathbf{E}	Stokes matrix containing the unknown part of $\bar{\mathbf{S}}$

$\bar{\mathbf{D}}_{t,\alpha}$	Original unknown DDE for antenna α and time instant t of size $2 \times 2N$
$\bar{\mathbf{U}}_{\alpha,1} = \bar{\mathbf{U}}_{\alpha,2} = \bar{\mathbf{U}}_{\alpha}$	Compact-support Fourier kernels corresponding to $\bar{\mathbf{D}}_{t,\alpha}$
$\bar{\mathbf{U}}_1$ (and $\bar{\mathbf{U}}_2$)	Concatenation of matrices $(\bar{\mathbf{U}}_{\alpha,1})_{1 \leq \alpha \leq n_a}$ (and $(\bar{\mathbf{U}}_{\alpha,2})_{1 \leq \alpha \leq n_a}$)
K and P	Support sizes in spatial and temporal Fourier domains of DDEs, respectively
$L^{(i)}$ and $J^{(i)}$	Number of inner-loop FB iterations for the DDEs and the images updates, respectively
μ	Regularization parameters for the images
$\bar{\gamma}$	Regularization parameter for the DDEs
ε_U and ε_E	Stopping criterion parameters for the DDEs and the images update, respectively
ε_0	Global stopping criterion parameter for the joint calibration and imaging algorithm
<u>OI imaging</u>	
$\bar{\mathbf{u}}_1 = \bar{\mathbf{u}}_2 = \bar{\mathbf{u}}_3 = \bar{\mathbf{x}}$	Original unknown total intensity image for monochromatic imaging
$\bar{\mathbf{u}}_{1,l} = \bar{\mathbf{u}}_{2,l} = \bar{\mathbf{u}}_{3,l} = \bar{\mathbf{x}}_l$	Original unknown image for l^{th} spectral channel for hyperspectral imaging
$\bar{\mathbf{X}}_1$ ($\bar{\mathbf{X}}_2$, and $\bar{\mathbf{X}}_3$)	Concatenation of the images $(\bar{\mathbf{u}}_{1,l})_{1 \leq l \leq L}$ ($(\bar{\mathbf{u}}_{2,l})_{1 \leq l \leq L}$, and $(\bar{\mathbf{u}}_{3,l})_{1 \leq l \leq L}$) for L spectral channels
μ	Regularization parameter for the images
t_{\max}	Number of FB iterations for each image update

List of Publications

International Journal articles

- **Birdi, J.**, Repetti, A. and Wiaux, Y., “Polca SARA - Full polarization, direction-dependent calibration and sparse imaging for radio interferometry”, arXiv: 1904.00663 [astro-ph.IM], 2019.
- **Birdi, J.**, Repetti, A. and Wiaux, Y., “Sparse interferometric Stokes imaging under the polarization constraint (Polarized SARA)”, *Monthly Notices of the Royal Astronomical Society*, vol. 478, pp. 4442-4463, 2018.
- Repetti, A., **Birdi, J.**, Dabbech, A. and Wiaux, Y., “Non-convex optimization for self-calibration of direction-dependent effects in radio interferometric imaging”, *Monthly Notices of the Royal Astronomical Society*, vol. 470, pp. 3981-4006, 2017.
- **Birdi, J.**, Repetti, A. and Wiaux, Y., “A regularized tri-linear approach for optical interferometric imaging”, *Monthly Notices of the Royal Astronomical Society*, vol. 468, pp. 1142-1155, 2017.

International Conference papers

- **Birdi, J.**, Repetti, A. and Wiaux, Y., “Scalable algorithm for polarization constrained sparse interferometric Stokes imaging”, *2018 IEEE 10th Sensor Array and Multichannel Signal Processing Workshop (SAM)*, Sheffield, UK, pp. 465-469, July 2018. Invited paper.

- Repetti, A., **Birdi, J.** and Wiaux, Y., “Joint imaging and DDEs calibration for radio interferometry”, *Biomedical and Astronomical Signal Processing (BASP) Frontiers workshop*, Villars-sur-Ollon, Switzerland, vol. 29, pp. 25, 2017. Invited paper.
- **Birdi, J.**, Repetti, A. and Wiaux, Y., “Sparsity regularized optical interferometric imaging”, *Signal Processing with Adaptive Sparse Structured Representations (SPARS) workshop*, Lisbon, Portugal, p. 130, June 2017.
- Repetti, A., **Birdi, J.** and Wiaux, Y., “Non-convex blind deconvolution approach for sparse radio interferometric imaging”, *Signal Processing with Adaptive Sparse Structured Representations (SPARS) workshop*, Lisbon, Portugal, p. 44, June 2017.

Chapter 1

Introduction

Contents

1.1	The rise of interferometers	4
1.2	Challenges faced in radio interferometry	6
1.3	Problems with imaging in optical regimes	9
1.4	Thesis organization and contribution	11

The quest to understand the depths of the universe has fascinated mankind for a long time. Whether it is the beholding sight of the stars and galaxies in the sky or the curiosity to know the deepest secrets behind the origin and evolution of the universe, astronomy has always been of great interest to the human kind, making it one of the oldest sciences of all time. Over the past centuries, there has been a radical change in our understanding of the universe. This has been achieved by studying the celestial emission, spanning the whole electromagnetic spectrum (Figure 1.1). Out of this, optical and radio astronomy are of particular interest. Optical astronomy is the most known branch of astronomy which deals with the observations of the astronomical objects in the visible light range, i.e. wavelengths from 400 nm to 700 nm, and is known to the star gazers since time immemorial. It is the branch of astronomy that has been instrumental in providing us with the fundamental information about the structure of our galaxy and its evolution. While playing a key role in the detection of exoplanets, the other interesting targets well studied by optical astronomy include protostellar systems and nearby galaxies. It also gives insights into the composition of the interstellar medium.

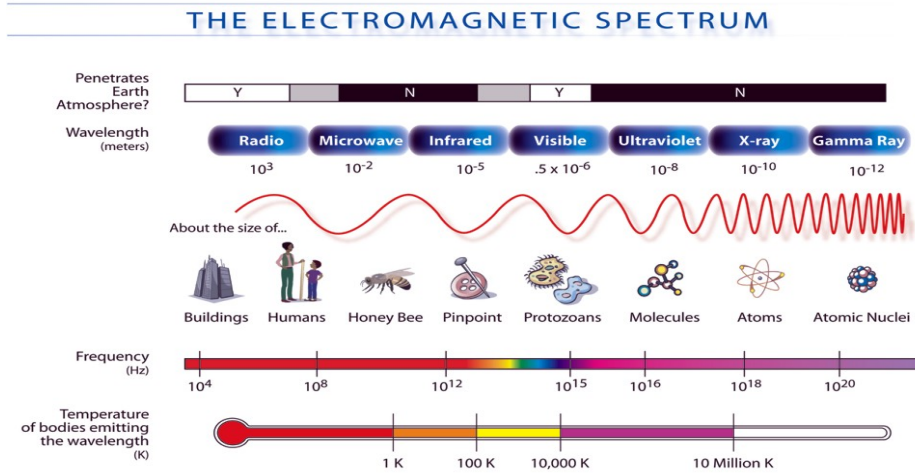


FIGURE 1.1: Electromagnetic spectrum depicting different radiations spanning over a range of frequencies and wavelengths. Source: NASA public domain image (CC BY-SA 3.0).

While optical astronomy remains pivotal in providing astronomical information, there are many interesting phenomena happening in other wavelength ranges which cannot be probed by optical astronomy. For instance, observing in radio frequencies provides unique information for astronomy. Radio astronomy encompasses the study of a wide variety of highly energetic celestial objects emitting radiations at radio frequencies, i.e. frequencies ranging from 3 kHz to 300 GHz (which in terms of wavelengths correspond to 100 km - 1 mm). It serves as a means to explore the parts of the universe which are undetectable in the visible domain of the electromagnetic spectrum. It therefore complements optical astronomy, enlightening the astronomical community with a whole new set of celestial objects and astrophysical phenomena. This is illustrated in Figure 1.2 which provides a comparative view of the sky at optical and radio wavelengths, with the Milky way galaxy's plane lying horizontally passing through the centre of each of the image. As can be seen, the radio sky, depicting the neutral hydrogen emission at 21 cm, is in contrast with the optical sky.

Since the first detection of the radio signals from space in 1930s, radio astronomy has come a long way making revolutionary contribution to our current knowledge of the universe. The long wavelength characteristic of radio waves renders various benefits to radio astronomy in comparison with the other fields. For instance, their

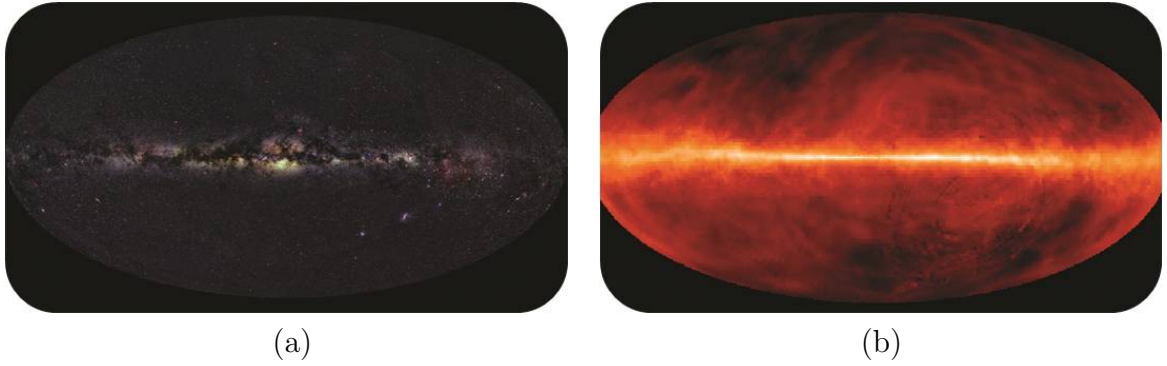


FIGURE 1.2: The sky seen at (a) optical and (b) radio wavelengths. Credits: (a) Axel Mellinger, SkyView; (b) J. Dickey (UMn), F. Lockman (NRAO), SkyView.

long wavelengths diminish their scattering and absorptivity, thus these radiations are permeable even through cloudy skies, interstellar gas and dust. This makes it possible to detect star formation obscured by gas and dust, as well as to discover other galaxies. Another perk of radio astronomy is the discovery of a whole new class of celestial objects and phenomena, such as pulsars, quasars, active galactic nuclei (AGNs), etc. To add to the list, the detection of the characteristic emission of hydrogen, the most abundant element in the universe, at 21 cm is a peculiar feature of radio astronomy, providing the key to map the structure of galaxies.

Yet another interest of radio astronomy comes from the perspective of studying polarization state of the astronomical sources, which are difficult to measure with optical astronomy. In general, measuring polarization is an integral part of the process of understanding the universe, offering a way to probe details in addition to the astrophysical information gleaned by the intensity alone. It acts as an indispensable tool to explore the intervening interstellar medium of propagation of the radio waves. Particularly, study of the polarized radiations aids in determining the magnetic field distributions around the source of interest as well as along the propagation path. Without the incorporation of the effects of magnetic fields, only a fragmentary understanding of the stars and galaxies is observed. Interestingly, analysing the polarization of the cosmic microwave background (CMB) sheds lights on the physics of the early universe.

In summary, radio astronomy opens the door to the detection and study of numerous

astrophysical sources and phenomena, making itself an invaluable tool for understanding the universe.

1.1 The rise of interferometers

In order to exploit the wealth of information provided by radio astronomy, radio emission from various celestial objects are collected by the radio antennas on Earth. Unlike optical waves, the radio waves having vastly longer wavelengths, carry very low energies. Coupled with the far reaches of the source, this results into faint radiations collected by the receiver antennas. Thus, large sized dishes need to be employed to increase the amount of radiation collected and achieve a higher sensitivity. Such large sized dishes are also favourable from the resolution perspective. More precisely, the angular resolution θ (in radians) of a telescope is limited by the classical diffraction theory to

$$\theta = 1.22 \frac{\lambda}{D}, \quad (1.1)$$

where λ is the observation wavelength and D is the diameter of the telescope, both in units of length. The factor 1.22 comes from the position of the first minimum of the intensity pattern produced by diffraction through a circular aperture [1]. As such, with the long wavelength characteristic of the radio waves, single-dish telescopes with large diameters need to be designed for high angular resolutions. For instance, a 6 m optical telescope dish reaches a resolution of ~ 0.025 arcsec. On the contrary, even a 500 m radio telescope dish, the largest filled-aperture radio telescope in the world, can only provide ~ 3 arcmin resolution in the L Band (having wavelength range of 30-15 cm) [2]. In fact, in terms of the radio astronomy science goals, it is also crucial to probe radio sources, especially their positions, with high precision to cross-match these with the measurements made in other parts of the electromagnetic spectrum. Nevertheless, in spite of the existence of large single-dish telescopes for radio astronomy, these are not enough to achieve an angular resolution comparable to optical telescopes.

To resolve this conundrum, scientists leveraged interferometry to probe radio emission, a technique which led to a Nobel Prize in Physics in 1974. A radio interferometer



FIGURE 1.3: The Very Large Array (VLA) consisting of 27 radio antennas, operated by NRAO in Socorro, New Mexico. Credit: Alex Savello, NRAO public domain image (CC BY 3.0).

consists of an array of antennas which collectively behave as a single very large aperture telescope, one such example shown in Figure 1.3. In this setting, the resolution of an interferometer is not determined by the diameter of individual antennas, but by the largest separation between the constituting antennas. Since the development of first radio interferometer, there has been an upsurge in the number of interferometers being constructed. This includes the Very Large Array (VLA) in New Mexico, USA, the Atacama Large Millimeter/submillimeter Array (ALMA) in Chile, LOw Frequency ARray (LOFAR) primarily in Netherlands, MeerKAT in South Africa, the Murchison Widefield Array (MWA) in Australia, to name a few. Furthermore, a widespread collection of radio telescopes and thus enhanced resolution is achieved by the Very Long Baseline Interferometry (VLBI), which consists of antennas spread all across the Earth. More recently, the Event Horizon Telescope (EHT), a ground-based VLBI array, has been designed to observe the immediate environment around a black hole at angular resolutions comparable to the event horizon. Its first results from the observations of the center of the galaxy M87 shows the first image of a black hole, providing strong evidence for the presence of supermassive black holes [3]. A remarkable addition to the family of radio interferometers will be the Square Kilometre Array (SKA), the world's largest radio telescope. One of the largest endeavours in scientific history, in its functional stage SKA will cover almost a square kilometre of the collecting area and hence its name. Consisting of thousands of dishes and a collection of aperture arrays spreading over two continents (Africa and Australia), it will provide

access to unprecedented resolution of the radio sky images at unparalleled sensitivity. Scientific goals of SKA include probing the Epoch of reionization by seeing back to the universe *First Light*, testing Einstein's general theory of relativity, to name a few. It is also expected to broaden our understanding of the ubiquitous magnetism in the universe. These fields invisible to the optical telescopes, can be detected via polarized radiations. Processes like synchrotron emission generate polarized radiations, and by studying these, we can determine the magnetic field distributions. It will give insights into the magnetic fields distribution in our galaxy and a comparison with that of other galaxies. It will give answers to some of the crucial questions pertinent to the origin and evolution of magnetism as well as questions related to the role played by magnetism in the stars and galaxies formations.

1.2 Challenges faced in radio interferometry

Study of the Stokes parameters' images by astronomers renders a way to achieve the aforementioned scientific goals. These parameters characterize the brightness distribution of the sought radio sky, providing a representation of the total intensity as well as the polarization state of the radio emission [4]. However, these images containing the required information about the underlying astrophysical process are not a direct output of the interferometers. Instead, the measurements acquired by interferometers, termed as complex visibilities, are related to the Fourier transform of the sought images [4]. And from these Fourier domain measurements, the images of interest need to be recovered. Moreover, each visibility measurement is acquired by a pair of antennas in the interferometer. Given the limited number of antennas, only an incomplete sampling of the Fourier plane is achieved. This leads to a highly under-determined image reconstruction problem in radio interferometry [5] and demands the development of sophisticated imaging techniques adapted to solve it.

To add to it, while producing high fidelity images using the imaging techniques, calibration poses an issue of concern [6]. In essence, calibration consists in solving for the unknown effects that corrupt the signal of interest from its origin till its reception by the antenna to produce the final output. These unknown effects, often represented

by 2×2 Jones matrix, involve instrumental terms such as antenna gains, as well as the terms corresponding to atmospheric/ionospheric perturbations, which in turn are often source direction-dependent [6]. As such, their direction dependency need to be taken into account in the calibration process. In the wake of new generation radio interferometers that aim to produce images of the sky with unprecedented resolution, high dynamic range and sensitivity, calibration of these direction-dependent effects has become pivotal. Without the incorporation of these effects, the produced target sky image suffers particularly from limited dynamic range. The importance of calibration can be further highlighted from the context of polarization. For many astrophysical sources, the polarized intensity is lower in magnitude in comparison with the total intensity. Moreover, it is comparable to the magnitude of the antenna gain terms and leakage terms appearing in the calibration matrix. Thus, the polarization of the source can be mapped accurately only if these calibration terms are estimated well. Overall, it can be said that the estimation of these calibration terms is a requisite to produce highly resolved, accurate maps of the radio emission.

In view of the discussion above, some of the major challenges brought by the new radio interferometers can be listed as follows:

- *Imaging quality*: These interferometers are envisaged to provide highly resolved images, associated with increased dynamic ranges. In order to use such capabilities of these interferometers to their fullest potential, new imaging techniques must be designed. Such techniques must incorporate sophisticated priors to enhance the image reconstruction quality both in terms of resolution and dynamic range.
- *Polarization imaging*: In light of the importance of study of polarization state of the radiations from astronomical sources, the designed technique must be able to perform polarization imaging in addition to total intensity imaging. In particular, owing to the small magnitude of the polarized intensity in comparison with the total intensity, producing high quality polarization images is a difficult task.

- *Scalability*: With the advent of new generation interferometers, the amount of acquired data will be enormous. For instance, in the case of SKA, the expected data rate is around five terabytes per second stemming from the data collected across thousands of frequency bands ($\sim 65,000$) over wide fields of view [7]. From such volume of datasets, the aim is to produce high quality sky images of gigapixel sizes. Thus, the techniques to solve the associated image recovery problems need to be fast and scalable to the high dimensionality of the problem.
- *Calibration*: Calibration modalities must be devised to estimate the unknown measurement modulations that otherwise have detrimental effect on the reconstructed images. In particular, accounting and solving for the direction-dependency of these effects has become crucial to reach the precision level offered by the new generation interferometers.
- *Convergence guarantees*: While handling the aforementioned points, it is desirable to have the developed algorithm benefiting from guarantees to converge to the solution of the underlying problem. This feature renders stability to the designed algorithm and ensures recovery of a meaningful solution.

While radio interferometry benefits from well-established imaging and calibration algorithms, in general, these are not suffice to overcome the above mentioned challenges presented by the new generation radio interferometers. In particular, CLEAN is the standard imaging algorithm in radio interferometry relying on a greedy iterative deconvolution approach [8]. However, the quality of images reconstructed by the celebrated CLEAN algorithm (and its variants) is expected to be inadequate to fully justify the imaging capabilities of these interferometers. In this respect, its performance has been shown to be surpassed by the recently proposed compressive sensing based imaging approaches [9–11]. These approaches exploit the sparsity of the images of interest in some sparsifying domain by leveraging convex optimization framework [5, 12]. Moreover, in contrast with the CLEAN based approaches that are not designed to scale with the flurry of the data produced by these interferometers, the compressive sensing based techniques exploit the versatility of the underlying optimization framework to achieve scalability [9, 13, 14]. Nevertheless, these techniques have been

proposed mainly for total intensity imaging, and do not account for specialised priors for full polarization imaging. On the calibration front, while earlier techniques were developed only for calibrating direction-independent effects, algorithms aiming to calibrate for direction-dependent effects have been proposed in the past years, mainly relying on a reference sky model of interest [15, 16]. Since the latter might not always be available, the calibration modalities need to be integrated with imaging techniques to design a global approach that aims to estimate both the calibration effects and the sought images. However, when any of the existing calibration and imaging approaches are combined, the convergence to the solution is not ascertained.

The objective of this thesis is to address these issues. Working in this direction, we first propose a polarimetric specific imaging method for radio interferometry using the versatile convex optimization framework. Furthermore, to deal with the problem of calibration, we propose a full polarization joint calibration and imaging technique that not only accounts for direction-dependent effects, but is also shipped with global convergence guarantees.

1.3 Problems with imaging in optical regimes

The optical interferometers are relatively recent when compared to the radio interferometers. Particularly, in the last two decades or so, the emergence of new generation optical interferometers including the CHARA array operated by Georgia State University, USA, Navy Precision Optical Interferometer (NPOI) in USA, the Very Large Telescope (VLT) in Chile, operated by European Southern Observatory, have opened the doors to unprecedented insights into the vastness of the universe [17]. Reaching the angular resolutions of the order of sub-milliarcseconds, the domain of optical interferometry is proving to be a powerful tool to probe the astrophysical sources ranging from the ones in our solar system to the central supermassive black holes of active galactic nuclei. Moreover, the optical interferometers are paving the way for hyperspectral imaging aiming to provide high resolution images even in the spectral dimension [18, 19].

Despite being a means of invaluable astrophysical information, the short wavelength property of the optical waves renders difficulty for optical interferometry. While it requires dealing with mechanical stabilities and controlling the long delay lines with high precision, it also causes the signal from the source to suffer from the atmospheric turbulence induced phase distortions [17]. Because of former instrumental factors, the optical interferometers in general consist of only a few number of optical telescopes (typically 4-6) leading to the acquisition of very few measurements in the Fourier domain of the sought image. On the other hand, the optical waves being affected by the random phase fluctuations while traversing through the atmosphere leads to cancellation of complex visibilities values [20]. In fact, optical interferometric measurements consist of phase insensitive observables: power spectrum (squared modulus of visibilities) and bispectrum (triple product of the complex visibilities acquired by three telescopes), that results into partial loss of phase information [21]. In other words, in comparison with radio interferometry, additional difficulties arise in optical interferometry primarily because of the loss of phase information coupled with a highly under-sampled Fourier domain, thereby resulting in a highly under-determined inverse problem for image recovery [20]. Moreover, given the non-linearity of the underlying observation model, the associated problem to be solved becomes non-convex.

Owing to the above difficulties, the radio interferometric techniques cannot be directly applied here and new approaches tailored to the optical interferometric problem need to be designed. Although some optical interferometric imaging techniques have been developed in the past years, they mainly suffer from convergence guarantees while solving the underlying non-convex optimization problem [22, 23].

Our goal here is to counteract these issues and solve this challenging problem of image recovery. To this end, we seek to bridge the gap between radio and optical interferometry. More precisely, drawing upon the ideas from radio interferometric imaging and calibration methodologies, we propose an optical interferometric imaging approach with convergence guarantees.

1.4 Thesis organization and contribution

The thesis organization along with the main contributions of the research work carried out is summarized as follows:

Chapter 2: Problem setup in radio interferometry

This chapter details the radio interferometric measurement framework, providing background knowledge to the reader about this subject. Using this framework, I present the radio interferometric imaging and calibration inverse problems to be solved.

Chapter 3: Sparse representations and optimization framework

This chapter is dedicated to provide an optimization background to the reader to facilitate his/her understanding of the techniques developed in this thesis to solve the underlying problems. Particularly, I introduce the notion of sparsity coupled with the compressive sensing framework and discuss the existing sparse recovery algorithms in literature. At this point, I put special emphasis on convex and non-convex optimization frameworks, describing different optimization tools that will be used later for algorithmic developments.

Chapter 4: Standard radio interferometric approaches

This chapter presents the standard imaging and calibration approaches in radio interferometry. The description of these state-of-the-art methods is essential to gain insights into the current state of affairs in radio interferometry and to fully understand their possible shortcomings, overcoming which is the aim of the research work carried out here.

The rest of the chapters are devoted to the presentation of the original research work undertaken in this thesis, with the last chapter providing the conclusion.

Chapter 5: Stokes parameters imaging in radio interferometry

This chapter provides a detailed description of a novel algorithm we have developed for full polarization imaging in radio interferometry using sophisticated priors. First, the proposed method enforces the physical polarization constraint, that is the polarized intensity being a lower bound on the total intensity. Second, each Stokes parameter map is regularized through an average sparsity prior in the context of a reweighted analysis approach (SARA) [24]. Finally, a distributed data-block model combined with an acceleration scheme and an adaptive noise bound estimation strategy are adopted to offer scalability to the real data sets [11, 14]. The resulting approach, dubbed Polarized SARA, solves the corresponding joint Stokes imaging inverse problem by leveraging convex optimization techniques, offering a highly flexible and parallelizable structure. We conduct several numerical experiments for the proposed approach, presenting a proof of concept [25]. We further showcase its performance on a real dataset [26].

This work has been published in [25] and [26].

Chapter 6: Self DDE calibration and imaging for radio interferometry

This chapter addresses the critical issue of calibration and presents a global algorithm we have developed to estimate jointly the sought images and the direction-dependent calibration terms. In particular, it employs a non-convex optimization technique to solve the underlying problem. We begin by designing the algorithm for total intensity imaging and calibration only [27–29]. Inspired by the achieved promising results, we further extend it to incorporate the full polarization model [30]. The key features of the proposed method include its global convergence guarantees and its flexibility to incorporate sophisticated priors to regularize the imaging as well as the calibration problem. Exploiting it, we adapt Polarized SARA method for the full polarization imaging step in the proposed global approach. We perform extensive simulation studies to investigate the performance of the proposed algorithm.

Part of this work has been published in [27–29] and the other part is submitted for publication [30].

Chapter 7: From radio to optical interferometric imaging

This chapter focuses on describing the image reconstruction algorithm we have developed for optical interferometry. In this context, image recovery amounts to solving an ill-posed, non-linear inverse problem. To tackle this challenging problem, we work with its tri-linear formulation with the aim of exploiting the introduced linearity [31]. Using this model, we define the estimated image as a solution of a regularized non-convex minimization problem, promoting sparsity of the sought image in a suitable sparsifying domain. In order to solve the resultant problem, we develop an algorithm that is able to deal with both smooth and non-smooth functions, and benefits from convergence guarantees even in a non-convex context. Finally, we generalize our model and algorithm to the hyperspectral case, promoting a joint sparsity prior. We present simulation results, both for monochromatic and hyperspectral cases, to validate the proposed approach.

This work has been published in [32] and [33].

Chapter 8: Conclusions and Perspectives

This chapter provides the concluding remarks for the thesis. It further indicates the future perspectives, outlining the possible directions for the extension and applicability of the work proposed in this thesis.

Chapter 2

Problem setup in radio interferometry

Contents

2.1	Introduction	14
2.2	Basic principle of radio interferometry	14
2.3	Observation model	15
2.3.1	Emergence of RIME	15
2.3.2	Calibration effects	23
2.4	RIME matrix formalism	24
2.5	Conclusion	27

2.1 Introduction

The aim of this chapter is to provide a detailed description of the measurement framework in radio interferometry (RI). Starting with an explanation of the underlying technique for interferometry, the RI measurement model is derived. This goes hand in hand with a discussion on the encountered calibration issues, thereby formulating the imaging-cum-calibration problem solving which is the focus of this thesis.

2.2 Basic principle of radio interferometry

The principle of interferometry can be deduced from the wave nature of the electromagnetic radiations emanated from the astronomical sources. In particular, it follows

the observations made by the commonly known Young's double slit experiment [34]. In this experiment, passage of light waves from a monochromatic source through two slits produced a fringe pattern, thereby providing the first demonstration of the wave character of light. A radio interferometer replicates this phenomena to provide the RI measurements. In this context, the information about the source in the sky can be retrieved by studying its electric field distribution in the emitted electromagnetic radiations. For this purpose, the antennas within an interferometer receive these radiations from the source while pointing towards it on the celestial sphere¹. Typically, the antennas point towards a phase reference position, which is usually the centre of the source of interest and is identified by a unit vector \mathbf{s}_0 . This is also referred to as the phase centre. Furthermore, the source being located sufficiently distant from the antennas, these radiations can be assumed to be received in the form of plane waves. For simplification, let us consider an antenna pair within the interferometer. Each antenna measures different parts of the incoming electromagnetic radiations' wavefronts. The signals from the two antennas are correlated and similarly to the previously mentioned experiment, it produces an interference fringe pattern, whose amplitude and phase vary depending on the antennas separation. These complex measurements, referred to as the complex visibilities, acquired by each antenna pair are the outputs provided by an interferometer from which the unknown sought images are recovered.

2.3 Observation model

In this section, a derivation of the radio interferometric measurement equation (RIME) is provided based on [35, 36].

2.3.1 Emergence of RIME

Consider an element of the target radio source at a position $\mathbf{s} = \mathbf{s}_0 + \boldsymbol{\sigma}$ subtending a solid angle $d\theta$. Let the electromagnetic radiations emitted at a frequency ν from the source of interest be characterized by its electric field \mathbf{e} , described within an

¹The notion of celestial sphere is in fact abstract, representing an Earth concentric, large radius sphere on whose inner surface the celestial objects are perceived to be projected.

orthonormal coordinate system, $(\mathbf{x}, \mathbf{y}, \mathbf{z})$. Considering \mathbf{z} lying along the direction of the phase centre \mathbf{s}_0 , for each observation direction $\boldsymbol{\sigma}$, \mathbf{e} can be decomposed into a vector

$$\mathbf{e}(\boldsymbol{\sigma}) = \begin{pmatrix} \mathbf{e}_x \\ \mathbf{e}_y \end{pmatrix} (\boldsymbol{\sigma}). \quad (2.1)$$

The polarization state of the incoming electromagnetic radiations, i.e. the signal of interest, is described in terms of the Stokes parameters - I, Q, U and V which, using the above notation, are defined as follows [1]:

$$I = \langle \mathbf{e}_x \mathbf{e}_x^* \rangle + \langle \mathbf{e}_y \mathbf{e}_y^* \rangle \quad (2.2)$$

$$Q = \langle \mathbf{e}_x \mathbf{e}_x^* \rangle - \langle \mathbf{e}_y \mathbf{e}_y^* \rangle \quad (2.3)$$

$$U = \langle \mathbf{e}_x \mathbf{e}_y^* \rangle + \langle \mathbf{e}_y \mathbf{e}_x^* \rangle \quad (2.4)$$

$$V = -i (\langle \mathbf{e}_x \mathbf{e}_y^* \rangle - \langle \mathbf{e}_y \mathbf{e}_x^* \rangle), \quad (2.5)$$

where $\langle \cdot \rangle$ stands for time averaging of its argument over a small interval. While I represents the total intensity, Q and U refer to the linear polarization, and V corresponds to the circular polarization. The net linear polarization can be deduced as $P = Q + iU$. The magnitude of this complex valued quantity provides the linear polarization intensity, while the electric vector polarization angle (EVPA) can be obtained from its phase.

The signal is received by each antenna, which in turn consists of two feeds such that each feed probes a specific polarization component. Figure 2.1 gives an example where the horizontal and vertical components of the signal's electric field vector are depicted. Depending on the considered polarization state, the feeds can consist of either two linear dipoles (X and Y) or circularly polarized receptors (R and L). To keep it general, we denote the two feeds by a and b . The incident field \mathbf{e} induces voltage in the receiver antennas. The voltage \mathbf{v}_α generated at each antenna α , is linked to the field coming from direction $\boldsymbol{\sigma}$ by the relation

$$\mathbf{v}_\alpha(\boldsymbol{\sigma}) = \begin{pmatrix} \mathbf{v}_{\alpha_a} \\ \mathbf{v}_{\alpha_b} \end{pmatrix} (\boldsymbol{\sigma}) = \mathbf{J}_\alpha(\boldsymbol{\sigma}) \mathbf{e}(\boldsymbol{\sigma}), \quad (2.6)$$

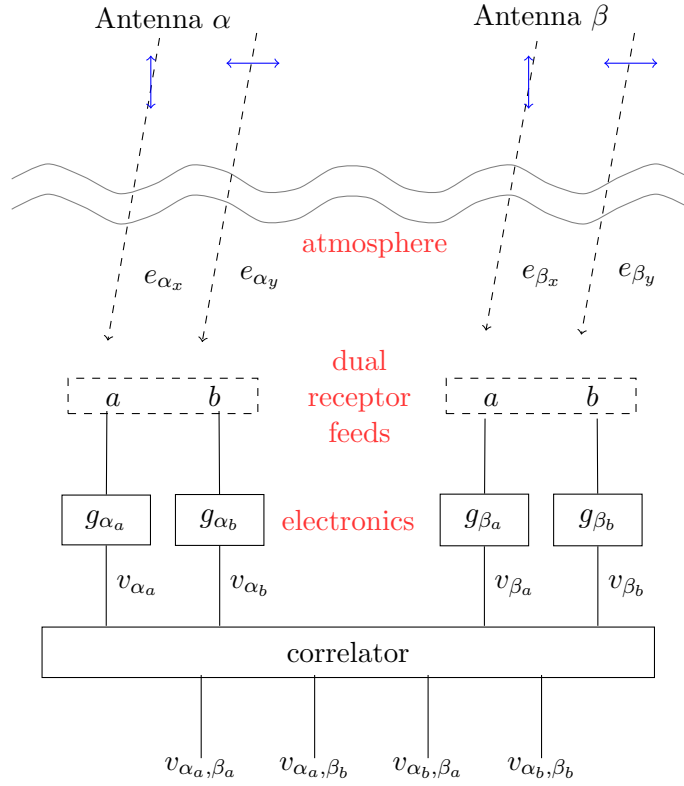


FIGURE 2.1: Block diagram depicting an antenna pair within a typical interferometer [36].

where v_{α_a} and v_{α_b} are the voltages at the feeds a and b of antenna α , respectively, and $\mathbf{J}_\alpha(\boldsymbol{\sigma})$ is the 2×2 Jones matrix that encompasses all the effects and interactions of the signal, coming from direction $\boldsymbol{\sigma}$ to α^{th} antenna, with its propagation medium. It presents itself as a multiplication due to the assumption that the wave propagation and all the transformations along its path are linear. Recalling from earlier discussion, the output of an interferometer is obtained by correlating the voltages from each antenna pair. Using equation (2.6) and considering an antenna pair (α, β) , this produces a 2×2 visibility matrix given by

$$\mathbf{Y}_{\alpha, \beta}(\boldsymbol{\sigma}) = \langle v_\alpha(\boldsymbol{\sigma}) v_\beta^\dagger(\boldsymbol{\sigma}) \rangle \quad (2.7)$$

$$= \mathbf{J}_\alpha(\boldsymbol{\sigma}) \mathbf{B}(\boldsymbol{\sigma}) \mathbf{J}_\beta^\dagger(\boldsymbol{\sigma}), \quad (2.8)$$

where $(\cdot)^\dagger$ denotes the Hermitian conjugate of its argument. $\mathbf{B}(\boldsymbol{\sigma}) = \langle \mathbf{e}(\boldsymbol{\sigma}) \mathbf{e}^\dagger(\boldsymbol{\sigma}) \rangle$ is the brightness matrix which consists of a linear combination of the Stokes parameters. Using the definition of the Stokes parameters in equations (2.2)-(2.5), it is given by

[36]

$$\mathbf{B}(\boldsymbol{\sigma}) = \begin{bmatrix} I + Q & U + iV \\ U - iV & I - Q \end{bmatrix} (\boldsymbol{\sigma}). \quad (2.9)$$

Furthermore, equation (2.8) assumes that $\mathbf{J}_\alpha(\boldsymbol{\sigma})$ and $\mathbf{J}_\beta(\boldsymbol{\sigma})$ do not vary during the averaging time interval. As explained earlier, another thing to consider is that in practice, a signal encounters multiple effects while propagating from the source to the receiver antenna and finally resulting into the interferometric output. For P number of different effects, these effects manifest themselves as P matrix multiplications, hence forming a Jones chain as follows

$$\mathbf{J}_\alpha(\boldsymbol{\sigma}) = \mathbf{J}_{\alpha,1}(\boldsymbol{\sigma}) \mathbf{J}_{\alpha,2}(\boldsymbol{\sigma}) \dots \mathbf{J}_{\alpha,P}(\boldsymbol{\sigma}). \quad (2.10)$$

The ordering of the terms in Jones chain is dictated by the physical order of the occurrence of effects along the propagation path. In this context, the rightmost matrices represent the perturbations introduced ‘near the source’, while the left matrices describe the effects ‘at the receiver end’. A description of these physical and instrumental effects is provided in the next section. Among which, the most fundamental effect is the phase delay. Linked with the signal propagation, it arises because of the differences in the geometric path length of the radiations from the source to antennas α and β constituting a pair.

To describe this phase difference and its implications, let us introduce the conventional RI coordinate systems. On the one hand, the antenna position is specified in the system with axes $(\mathbf{u}, \mathbf{v}, \mathbf{w})$, depicted in Figure 2.2. In this system, \mathbf{u} and \mathbf{v} are the coordinate axes in the plane normal to the source direction with \mathbf{u} pointing towards east and \mathbf{v} towards north, whereas \mathbf{w} is the axis in the direction of the phase centre [4]. On the other hand, a location $\boldsymbol{\sigma}$ on the celestial sphere is represented in a parallel coordinate system $(\mathbf{l}, \mathbf{m}, \mathbf{n})$ such that (l, m, n) refer to the direction cosines with respect to these axes, with $n = \sqrt{1 - l^2 - m^2}$. In particular, the image plane lm is taken tangential to the celestial sphere at the phase centre \mathbf{s}_0 , which is the centre of the radio sky image.

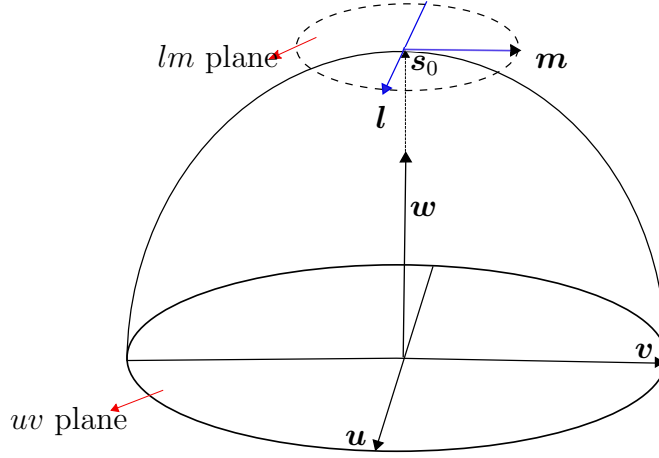


FIGURE 2.2: Illustration of radio interferometric coordinate system, $(\mathbf{u}, \mathbf{v}, \mathbf{w})$. The uv plane is normal to the direction of the source, \mathbf{s}_0 with the \mathbf{w} axis pointing towards \mathbf{s}_0 . The associated lm plane is taken tangential to the celestial sphere at the point of intersection of \mathbf{s}_0 with the sphere.

Given these coordinate systems, the phase difference in the signal coming from a direction $\boldsymbol{\sigma}$ and observed at antenna α with respect to the phase centre is formally given by

$$\kappa_\alpha = 2\pi(u_\alpha l + v_\alpha m + w_\alpha(n-1)), \quad (2.11)$$

where $(u_\alpha, v_\alpha, w_\alpha)$ are the coordinates of the antenna α in units of observation wavelength, λ . This phase difference, affecting each component of the signal equally, can be represented by a scalar matrix. The corresponding phase delay matrix is thus given by

$$\mathbf{K}_\alpha(\boldsymbol{\sigma}) = e^{-i\kappa_\alpha} \mathbf{I}_2 = e^{-i2\pi(u_\alpha l + v_\alpha m + w_\alpha(n-1))} \mathbf{I}_2, \quad (2.12)$$

with \mathbf{I}_2 denoting a 2×2 identity matrix. The representation of a scalar matrix is independent of the chosen coordinate system and thus, it can be put anywhere within the Jones chain. In turn, the effective Jones matrix \mathbf{J}_α in equation (2.10) boils down to $\mathbf{J}_\alpha(\boldsymbol{\sigma}) = \mathbf{D}_\alpha(\boldsymbol{\sigma}) \mathbf{K}_\alpha(\boldsymbol{\sigma})$ where $\mathbf{D}_\alpha(\boldsymbol{\sigma})$ encompasses the rest of the corrupting, calibration effects. Plugging it in equation (2.8) that describes the measurements for a single direction in sky, and integrating it over all the possible directions results into the total visibility $\mathbf{Y}_{\alpha,\beta}$ as follows

$$\mathbf{Y}_{\alpha,\beta} = \int_{4\pi} \mathbf{D}_\alpha(\boldsymbol{\sigma}) \mathbf{B}(\boldsymbol{\sigma}) \mathbf{D}_\beta^\dagger(\boldsymbol{\sigma}) \mathbf{K}_\alpha(\boldsymbol{\sigma}) \mathbf{K}_\beta^\dagger(\boldsymbol{\sigma}) d\theta. \quad (2.13)$$

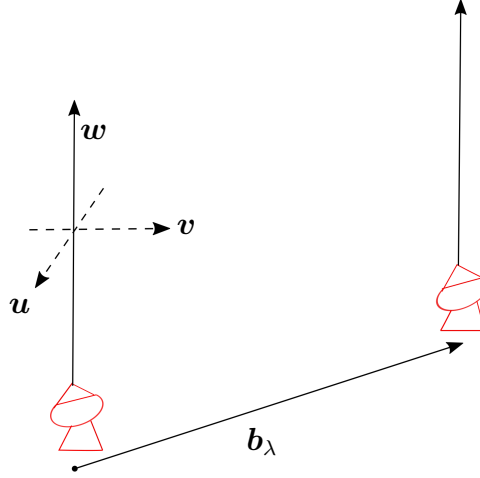


FIGURE 2.3: Illustration of a radio interferometric baseline. The baseline \mathbf{b}_λ is given by the separation vector between the two antennas, with its components projected onto the $(\mathbf{u}, \mathbf{v}, \mathbf{w})$ axes.

This equation can be reformulated by expressing it in terms of the components (l, m, n) , thereby giving

$$\mathbf{Y}_{\alpha,\beta} = \int_{\mathbf{l}} \frac{1}{n} \mathbf{D}_\alpha(\mathbf{l}) \mathbf{B}(\mathbf{l}) \mathbf{D}_\beta^\dagger(\mathbf{l}) e^{-i2\pi(u_{\alpha,\beta}l + v_{\alpha,\beta}m + w_{\alpha,\beta}(n-1))} d^2\mathbf{l}, \quad (2.14)$$

where $\mathbf{l} = (l, m)$, $d\theta = \frac{dl dm}{n}$. $u_{\alpha,\beta} = u_\alpha - u_\beta$, $v_{\alpha,\beta} = v_\alpha - v_\beta$, and $w_{\alpha,\beta} = w_\alpha - w_\beta$ denote the *baseline* coordinates [4]. A baseline is a RI terminology for the separation vector between two antennas, illustrated in Figure 2.3. From equation (2.14), it can be observed that each acquired complex visibility measurement is identified by the baseline associated with the antenna pair involved. In fact, the visibility plane consists of the baselines components (u, v) , forming the so called *uv* plane.

Furthermore, in equation (2.14), the term $\mathbf{W}_{\alpha,\beta} = \frac{1}{n} e^{-i2\pi w_{\alpha,\beta}(n-1)}$ arising from non-coplanarity of the antennas can be considered as a Jones matrix for each antenna, incorporated within the associated net Jones matrix. Consequently, the radio interferometric measurement equation (RIME) is given by

$$\mathbf{Y}_{\alpha,\beta} = \int_{\mathbf{l}} \mathbf{D}_\alpha(\mathbf{l}) \mathbf{B}(\mathbf{l}) \mathbf{D}_\beta^\dagger(\mathbf{l}) e^{-i2\pi(u_{\alpha,\beta}l + v_{\alpha,\beta}m)} d^2\mathbf{l}, \quad (2.15)$$

$$= \mathcal{F}(\mathbf{D}_\alpha \mathbf{B} \mathbf{D}_\beta^\dagger) \quad (2.16)$$

where \mathcal{F} computes the two-dimensional (2D) Fourier transform of its argument. Thus,

RIME provides 2D Fourier transform relationship between the measurements and the target sky images modified by the Jones matrices, evaluated at the sampled spatial frequency point $(u_{\alpha,\beta}, v_{\alpha,\beta})$. This is indeed a specific expression of the van Cittert Zernike theorem that links the interference fringe pattern and the source brightness distribution [4, 37].

Several remarks can be made regarding equation (2.15). First, in practice, the measurements are degraded by an additive noise. The noise arising primarily from the receivers is independent for each of the constituting receivers. Keeping this in mind, it is a usual assumption to approximate the measurement noise by independent and identically distributed (i.i.d.) Gaussian noise [4]. Second, in general, the visibilities exhibit time as well as frequency dependency. This is due to the fact that the Jones matrices and the brightness distribution can show variation with respect to the observation time instant t and the observation frequency ν . Moreover, the baselines and hence the sampled (u, v) points depend on these parameters. This time and frequency dependency can be signified by adding the subscripts t, ν in the corresponding variables, and the most general form of measurement equation (2.15) can then be expressed as

$$\mathbf{Y}_{t,\alpha,\beta,\nu} = \int_{\mathbf{l}} \mathbf{D}_{t,\alpha,\nu}(\mathbf{l}) \mathcal{L}(\mathbf{S}_{t,\nu}(\mathbf{l})) \mathbf{D}_{t,\beta,\nu}^\dagger(\mathbf{l}) e^{-i2\pi(u_{t,\alpha,\beta}l + v_{t,\alpha,\beta}m)} d^2\mathbf{l} + \mathbf{\Omega}_{t,\alpha,\beta}, \quad (2.17)$$

where $\mathbf{\Omega}_{t,\alpha,\beta} \in \mathbb{C}^{2 \times 2}$ is the additive Gaussian noise and the operator \mathcal{L} acts on the Stokes matrix $\mathbf{S}_{t,\nu}(\mathbf{l}) = \begin{bmatrix} I & Q \\ U & V \end{bmatrix}_{t,\nu}(\mathbf{l})$ to give the brightness matrix $\mathbf{B}_{t,\nu}(\mathbf{l})$ (as in equation (2.9)). The latter formulation is introduced in equation (2.17) to highlight directly the relation between the visibilities and the Stokes parameters, that are the unknown quantities to be recovered from the measured visibilities.

Concerning the sampling, as previously explained, each baseline corresponds to a point in the uv plane and thus, the number of (u, v) points probed is dictated by the number of antennas in the interferometer. While an extensive sampling of the uv plane is desirable to access maximum possible information about the brightness distribution of the sought source, only a limited number of (u, v) points can actually be sampled given the finite number of antennas. One way to enhance the uv coverage is to move

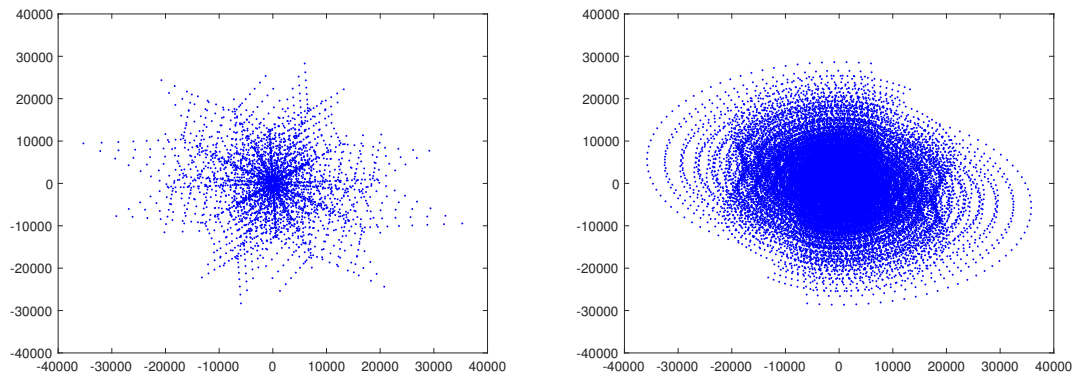


FIGURE 2.4: Illustration of uv coverage of the VLA telescope with 27 antennas. From left to right, the coverages obtained with short and longer observation durations, respectively are shown.

the antennas such that new baselines are created, which however is accompanied by a lot of inconvenience and may not be feasible always. Instead, a dense (u, v) sampling is achievable by what's called Earth rotation aperture synthesis [38]. To be precise, as the Earth rotates, the baseline position varies with respect to the target source and hence, distinct (u, v) points are probed. Consequently, the (u, v) sampling grows with the observation time as illustrated in Figure 2.4, without needing to change the antenna configuration. In turn, it gives access to more Fourier modes of the uv plane. It is worth highlighting that the resultant uv coverage is still under-sampled, providing only partial information about the sought images. The image recovery problem then amounts to estimating the unknown Stokes images from these under-sampled noisy Fourier measurements.

Finally, while performing image recovery, the Fourier transform of the true sky brightness distribution at the sampled (u, v) points in the Fourier domain needs to be evaluated (equation (2.17)). For computational purposes, it is advantageous to bin these continuous sampled points on a regular grid instead. This process, called *gridding*, enables the usage of a fast Fourier transform (FFT) to compute the required Fourier transforms over the underlying grid [39]. To this end, each point in the discrete grid is obtained by performing interpolation over the sampled visibilities lying within a certain region around the underlying grid point. Very often, a weighting scheme is adopted before gridding the data to improve the reconstruction quality. While several

such schemes exist in the literature, the bottom-line is to assign a weight to each visibility, chosen as per the scientific goal of interest [40, 41]. In this context, ‘natural’ weights are given by the inverse of the noise variances of the visibilities, thereby increasing the sensitivity, whereas ‘uniform’ weights are computed by the inverse of the uv sampling density function for the visibilities, and hence offering a higher resolution. Another scheme called ‘robust’ weighting provides a compromise between the two approaches, that is between the sensitivity and the resolution.

2.3.2 Calibration effects

As previously mentioned, the Jones matrices encompass all the calibration effects corrupting the signal from its point of origin till its processing by the interferometric hardware to produce the observed visibilities. These effects can be attributed to both instrumental and atmospheric origins. To give an intuitive idea, the signal coming from the source of interest in sky undergoes Faraday rotation while traversing through the ionosphere, which then encounters phase delays because of atmospheric perturbations. In turn, it is modulated by the antenna primary beam and when it is finally received by the antenna, it faces polarization leakage followed by application of antenna gain. As such, the sequence of various terms in Jones chain needs to be preserved in the order in which these perturbation occur as the signal makes its way from the source to the final output of the antenna. Mathematically speaking, it refers to non-commutative property of the involved Jones matrices, and the corresponding Jones chain can be represented by the following structure [42]:

$$\mathbf{J}_\alpha = \mathbf{B}_\alpha \mathbf{G}_\alpha \mathbf{L}_\alpha \mathbf{E}_\alpha \mathbf{P}_\alpha \mathbf{T}_\alpha \mathbf{F}_\alpha, \quad (2.18)$$

where the various constituting terms can be described as follows:

- \mathbf{F}_α : Faraday rotation entailing the rotation of the plane of polarization of the incoming wave while propagating through ionosphere,
- \mathbf{T}_α : Phase delays introduced by the propagation of the signal through troposphere and ionosphere,

- \mathbf{P}_α : Parallactic angle accounting for the antenna mount axis rotation with respect to the sky,
- \mathbf{E}_α : Primary beam gain varying with observation direction in the field of view,
- \mathbf{L}_α : Polarization leakage arising from the cross-talk between the two polarizer feeds,
- \mathbf{G}_α : Complex gain term comprising of the gain of the receiver elements,
- \mathbf{B}_α : Bandpass response incorporating the frequency-dependent component of the receiver gain.

An important thing to be noticed is that the Jones matrices vary in their own specific manner with respect to observation time, direction and frequency. For instance, the complex gain matrix \mathbf{G}_α exhibits a temporal variation, whereas the bandpass matrix \mathbf{B}_α primarily has a frequency dependence. The other frequency dependent components include the atmospheric phase delay as well as the angle of Faraday rotation. On the other hand, concerning about the direction dependency, while the terms pertaining to instrumentation effects (complex gain terms) appearing towards left hand side of the Jones chain do not show a dependence on (l, m) coordinates, the other perturbation terms on the right including primary beam pattern, parallactic angle, atmospheric phase delays and Faraday rotation vary within the field-of-view. The former class of terms are categorised as direction-independent effects (DIEs), whereas the latter as direction-dependent effects (DDEs).

2.4 RIME matrix formalism

In order to recover the Stokes parameters from the given measurements, we formulate the inverse problem (2.17) in the discrete domain. It amounts to sampling the continuous variables such that the field of view is discretized into a grid, with the vectorized form of this grid being represented by the index $n \in \{-N/2, \dots, N/2 - 1\}$. Furthermore, in the current work, we consider the Stokes images without having time or frequency dependence. In addition, for the Jones matrices, we deal with their

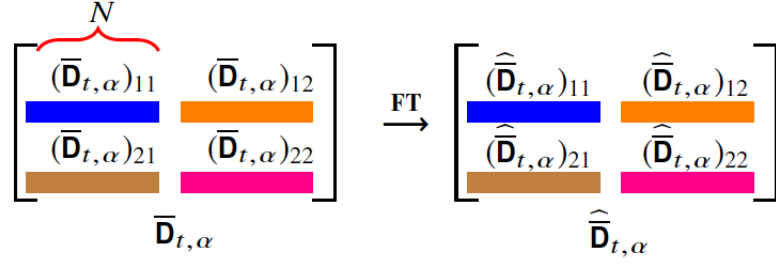


FIGURE 2.5: Schematic representation of a $2 \times 2N$ matrix, $\bar{\mathbf{D}}_{t,\alpha}$ (left) that can be seen as a 2×2 block matrix, with each block $(\bar{\mathbf{D}}_{t,\alpha})_{ii'}, \{i, i'\} \in \{1, 2\}^2$ containing a vectorized image of dimension N . The Fourier transformation (FT) of this matrix computes 2D Fourier transform of each of the block images. For each block in matrix $\bar{\mathbf{D}}_{t,\alpha}$ on left, its corresponding FT is shown by the same colored vectors in matrix $\hat{\bar{\mathbf{D}}}_{t,\alpha}$ on right.

temporal dependency considered at a single observation frequency. Hence, for ease of notation, hereafter we drop the frequency and time index from the Stokes parameters, and frequency index from the other variables.

Within the considered representation, we thus have the Stokes matrix $\bar{\mathbf{S}} \in \mathbb{R}^{2 \times 2N}$, and for each antenna α and time instant t , the DDEs (representing the calibration effects) $\bar{\mathbf{D}}_{t,\alpha} \in \mathbb{C}^{2 \times 2N}$. As illustrated in Figure 2.5, these matrices can also be seen as 2×2 block matrices², whose each block is a row vector of dimension N . In particular, for the Stokes matrix $\bar{\mathbf{S}} = \begin{bmatrix} \bar{\mathbf{s}}_1 & \bar{\mathbf{s}}_2 \\ \bar{\mathbf{s}}_3 & \bar{\mathbf{s}}_4 \end{bmatrix}$, the elements $\bar{\mathbf{s}}_1, \bar{\mathbf{s}}_2, \bar{\mathbf{s}}_3$ and $\bar{\mathbf{s}}_4$, each of size N , are respectively the discretizations of the Stokes parameters I, Q, U and V . On the other hand, for the DDEs, for each index n , we have the effective 2×2 Jones matrix $\bar{\mathbf{D}}_{t,\alpha}(n) \in \mathbb{C}^{2 \times 2}$. Moreover, if for every $(i, i') \in \{1, 2\}^2$, $[\bar{\mathbf{D}}_{t,\alpha}]_{ii'} = \delta_{t,\alpha} \mathbf{1}_N$ with $\delta_{t,\alpha} \in \mathbb{C}$ and $\mathbf{1}_N$ being N dimensional unitary row vector, then $\bar{\mathbf{D}}_{t,\alpha}$ reduces to a DIE.

Following the introduced notations, each component of the visibility matrix $\mathbf{Y}_{t,\alpha,\beta}$,

²In this regard, for any such matrix $\bar{\mathbf{S}}$, $\bar{\mathbf{S}}(n)$ denotes the 2×2 matrix consisting of the n^{th} elements of each of the blocks in the parent block matrix $\bar{\mathbf{S}}$. In particular, for $(i, i') \in \{1, 2\}^2$, the notation $[\bar{\mathbf{S}}(n)]_{ii'}$ refers to the n^{th} element of the row vector block contained in the i^{th} row and i'^{th} column of the argument block matrix.

indexed by $[\cdot]_{ii'}$ with $(i, i') \in \{1, 2\}^2$, at discrete spatial frequency $k_{t,\alpha,\beta}$ can be represented as

$$[\mathbf{Y}_{t,\alpha,\beta}]_{ii'} = \sum_{j,j'=1}^2 \sum_{n=-N/2}^{N/2-1} [\overline{\mathbf{D}}_{t,\alpha}(n)]_{ij} [\mathcal{L}(\overline{\mathbf{S}}(n))]_{jj'} [\overline{\mathbf{D}}_{t,\beta}^*(n)]_{j'i'} e^{-i2\pi(k_{t,\alpha,\beta})\frac{n}{N}} + [\Omega_{t,\alpha,\beta}]_{ii'}, \quad (2.19)$$

where for $n \in \{-N/2, \dots, N/2 - 1\}$, analogous to the continuous version (2.17), $\mathcal{L}(\overline{\mathbf{S}}(n)) = \overline{\mathbf{B}}(n) \in \mathbb{C}^{2 \times 2}$ is the brightness matrix.

Given the observation model (2.19), the task at hand is to recover the Stokes images from the acquired visibilities. In the case of having either pre-calibrated data or knowledge of DDEs/DDEs beforehand, the problem needs to be solved only for image recovery. On the other hand, within a more realistic setting, the DDEs are often unknown. These need to be calibrated jointly with the imaging to obtain a good estimation of the target sky. In this thesis, we consider both the cases, i.e. imaging only and imaging with calibration. To estimate these variables of interest, for the sake of brevity, the resultant inverse problem associated with (2.19) can be written as

$$\mathbf{Y} = \tilde{\Phi}(\overline{\mathbf{S}}, \overline{\mathbf{D}}) + \Omega, \quad (2.20)$$

where $\tilde{\Phi}$ is the measurement operator mapping the images of interest coupled with the DDEs to the acquired visibilities \mathbf{Y} . This gives the standard inverse problem for imaging and calibration in RI. In the particular case of known DDEs, the problem needs to be solved only for the Stokes images and the operator $\tilde{\Phi}$ becomes linear with respect to the sought images. This linear operator taking into account the known DDEs can be denoted by Φ and problem (2.20) can then be rewritten as

$$\mathbf{Y} = \Phi(\overline{\mathbf{S}}) + \Omega, \quad (2.21)$$

providing the underlying RI imaging inverse problem.

2.5 Conclusion

In this chapter, I have discussed at length the RI measurement framework starting from the source to the final interferometric output. The various effects encountered during this whole process manifest themselves as calibration effects affecting the sought sky brightness distribution. The associated imaging and calibration inverse problem has been set up which, in the particular case of known calibration terms, reduces to an imaging inverse problem. The ways to solve these inverse problems is the topic of discussion for the next chapters. Particularly, these methods rely on exploiting some suitable prior information about the images of interest. In this context, recent years have seen the emergence of *sparsity* based techniques lying within the paradigm of compressive sensing (CS) and exploiting the optimization framework, that have demonstrated themselves as promising candidates for RI imaging. As a matter of fact, the analogies of the standard RI imaging algorithm - CLEAN with sparsity promoting methods have also been shown lately. Therefore, at this stage, the reader will benefit from going through a tour of sparsity and optimization framework, gaining background knowledge for better understanding of the existing RI algorithms as well as of the ones proposed in this thesis.

Chapter 3

Sparse representations and optimization framework

Contents

3.1	Introduction	28
3.2	Inverse problems	30
3.3	The world of sparsity	31
3.3.1	Exploiting sparsity for signal recovery	33
3.3.2	Sparse recovery methods	37
3.4	A tour of convex optimization framework	40
3.4.1	Proximal splitting methods	41
3.4.2	Primal-dual methods	44
3.5	Non-convex optimization	45
3.5.1	Overview	45
3.5.2	Non-convex regularizations for sparse recovery	48
3.6	Conclusion	48

3.1 Introduction

This chapter is devoted to provide a mathematical background to the reader. It will aid in understanding the approaches discussed and developed later in this thesis to solve the underlying inverse problems. In particular, I focus on the notion of sparsity and review the associated standard recovery algorithms. Inspired by the versatility offered by the convex optimization framework among the classes of these

sparse recovery approaches, I provide a detailed description of this framework and the associated optimization toolbox. Furthermore, I shed light on a general class of non-convex continuous optimization problems within which the RI calibration problem falls. *Parts of this chapter have been taken from the optimization background provided in [26] and [32].*

Before going into the details, I provide here some basic notations that will be used throughout the thesis. In particular, the scalars are denoted by lower case, italic letters (x), vectors by lower case, bold italic letters (\mathbf{x}) and matrices by upper case, bold straight letters (\mathbf{X}).

For any vector $\boldsymbol{\alpha}$, its ℓ_0 pseudo-norm represents a cardinality function counting its non-zero entries, and is given by $\|\boldsymbol{\alpha}\|_0 = \#(i | \alpha_i \neq 0)$, where $\#(\cdot)$ denotes the cardinality of its argument.

In general, the ℓ_p norm of $\boldsymbol{\alpha}$ is defined as

$$\|\boldsymbol{\alpha}\|_p = \left(\sum_i |\alpha_i|^p \right)^{1/p}, \quad \text{with } p \in \mathbb{R}_+^*. \quad (3.1)$$

The commonly used ℓ_1 and ℓ_2 norms can be deduced from it by considering $p = 1$ and 2, respectively. It is straightforward to see then that, on the one hand, the ℓ_1 norm computes the sum of the absolute value of all the elements of its argument. On the other hand, the widely popular ℓ_2 norm represents the usual Euclidean distance of the underlying vector from the origin. In terms of matrices, the Frobenius norm is often used. For any matrix $\bar{\mathbf{A}} \in \mathbb{C}^{J \times I}$, it is defined as

$$\|\bar{\mathbf{A}}\|_F = \left(\sum_{j=1}^J \sum_{i=1}^I |\bar{A}_{ji}|^2 \right)^{1/2}. \quad (3.2)$$

It can be observed that the ℓ_2 and the Frobenius norms are the Euclidean norms for vector and matrix space, respectively.

I further introduce the notation: $\tilde{\mathbf{S}} = \mathcal{R}(\mathbf{S})$ where $\mathcal{R}: \mathbb{R}^{2 \times 2N} \rightarrow \mathbb{R}^{N \times 4}$ is the operator consisting in placing the four images contained in the matrix \mathbf{S} in four columns to

give $\tilde{\mathbf{S}}$. Its adjoint $\mathcal{R}^\dagger : \mathbb{R}^{N \times 4} \rightarrow \mathbb{R}^{2 \times 2N}$ does the contrary, i.e. stores the four images in the rows of a 2×2 block matrix. Employing this notation, the underlying inverse problem (2.21) can be rewritten as $\mathbf{Y} = \Phi'(\tilde{\mathbf{S}}) + \Omega$, with the operator $\Phi'(\cdot) = \Phi(\mathcal{R}^\dagger(\cdot))$. It will be useful later as it provides a compact notation.

3.2 Inverse problems

Inverse problems are widely encountered in many fields with the core idea of estimating the causal factors responsible for the given set of measurements. A typical inverse problem is of the form $\mathbf{Y} = \Phi(\bar{\mathbf{S}}) + \Omega$, where, from the known observations \mathbf{Y} that are degraded by some noise Ω , the unknown true images $\bar{\mathbf{S}}$ need to be recovered. A common approach to solve such a problem is by using a least squares criterion [43]. It estimates the sought images by minimizing a data fitting term, i.e.

$$\underset{\mathbf{S}}{\text{minimize}} \quad \|\Phi(\mathbf{S}) - \mathbf{Y}\|_F^2, \quad (3.3)$$

which ensures the data consistency of the estimated solution. However, in many practical applications, the underlying inverse problem is ill-posed in that it does not have a unique solution. To give an intuitive idea, in the context of RI imaging, the noisy measurements contain a partial information about the images of interest as only a sub-set of the Fourier space is sampled. There thus lies the possibility of existence of many solutions satisfying the data constraints. Solving such an ill-posed inverse problem is then a challenging task and ensuring only data consistency is not sufficient, leading to data over-fitting. To overcome these difficulties, regularization strategy is often employed [44]. It consists in reformulating the original minimization problem to be solved as

$$\underset{\mathbf{S}}{\text{minimize}} \quad \|\Phi(\mathbf{S}) - \mathbf{Y}\|_F^2 + \mu r(\mathbf{S}), \quad (3.4)$$

where r is the regularization function whose role is to incorporate additional information about the target images, and the regularization parameter $\mu > 0$ determines the trade-off between the two terms.

In general, an equivalent formulation of problem (3.4) also exists, giving its constrained version as

$$\underset{\mathbf{S}}{\text{minimize}} \ r(\mathbf{S}) \text{ subject to } \|\Phi(\mathbf{S}) - \mathbf{Y}\|_F \leq \epsilon, \quad (3.5)$$

where $\epsilon > 0$ is determined from the noise level. While in problem (3.4) the parameter μ needs to be tuned, problem (3.5) requires the value of ϵ to be specified. In the cases with prior knowledge of the noise statistics governing the problem, it may be possible to theoretically determine ϵ . To give an example, in the context of RI imaging, [45] uses the assumption of i.i.d. complex Gaussian noise relating the constraint term in (3.5) to a χ^2 distribution, thereby obtaining the value of ϵ . Nonetheless, depending upon the problem under consideration, one of the two formulations may be preferred.

Finally, concerning the regularization function r , it is chosen as per the desirable features in the sought images. The choice of such a regularization function then plays a key role in the reconstruction quality of the images. In this context, the concept of *sparsity* has drawn huge interest especially in the last two decades [46, 47]. The next sections are focused on the notion of sparsity priors, providing a background knowledge.

3.3 The world of sparsity

By definition, a vector $\boldsymbol{\alpha} \in \mathbb{C}^J$ is k -sparse if it contains at most k non-zero coefficients. In practice, the signal may not be strictly sparse, but *compressible*, in the sense that only a few coefficients have a non-negligible amplitude [48]. Sparsity of the signal can also be achieved in a data representation space, that is not necessarily its domain [49]. In other words, the unknown signal depends on a smaller number of unknown parameters. Mathematically, for a vector $\mathbf{s} \in \mathbb{R}^N$, it is written as

$$\mathbf{s} = \Psi \boldsymbol{\alpha} \quad (3.6)$$

such that \mathbf{s} is represented by a sparse vector $\boldsymbol{\alpha}$ in the sparsifying dictionary $\Psi \in \mathbb{C}^{N \times J}$. Within the same context, for a matrix $\tilde{\mathbf{S}} \in \mathbb{R}^{N \times 4}$ containing an image in each of its columns, the matrix formulation of equation (3.6) can be written as $\tilde{\mathbf{S}} = \Psi \mathbf{A}$. Here the

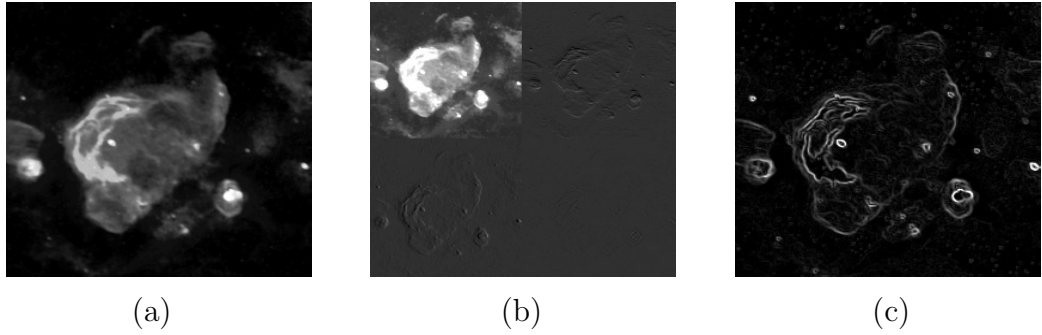


FIGURE 3.1: Illustration of sparsity of (a) an original intensity image of the W28 supernova remnant in the: (b) Haar wavelet basis and (c) gradient (TV) domain. Credits for (a): Image courtesy of NRAO.

matrix $\mathbf{A} \in \mathbb{C}^{J \times 4}$ denotes the sparse representation for the considered images. More precisely, each column of \mathbf{A} contains a sparse vector associated with the corresponding column image in $\tilde{\mathbf{S}}$ via the dictionary Ψ .

The choice of an appropriate dictionary depends on the nature of the images under consideration. Many studies conducted over the past few years have investigated the suitability of sparsifying dictionaries for different types of images [49, 50]. For example, considering the simplest case of a sparse image (i.e. an image consisting of point sources), Ψ can be set to the Dirac basis, i.e. identity matrix with $J = N$, promoting sparsity in the image domain itself. In the case of piece-wise constant images, sparsity can be promoted in the gradient domain, using total variation (TV) based regularizations [51]. When the underlying images are smooth and have more complex structures, the wavelet domain [52], a collection of wavelet bases [45], stand as potential candidates for the sparsifying dictionary Ψ . Apart from these dictionaries, other possibilities include the isotropic undecimated wavelet transform (IUWT) [53] and the curvelets [54], to name a few. While the former is appropriate for images consisting of isotropic sources/structures, the latter is suited for elongated, well-curved patterns. To give an example, Figure 3.1 depicts the sparse representation of an original image in two different sparsifying bases. Figure 3.1(b) and (c) show that the information in the original image is concentrated in a small number of non-zero coefficients when represented in appropriate transformed domains.

While we have introduced the notion of sparsity, the next step is to describe how

to actually use them for image recovery in general. The next section focuses on addressing it, providing image recovery problem formulations exploiting sparsity.

3.3.1 Exploiting sparsity for signal recovery

Sparsity has presented itself as a powerful prior for signal recovery from the given measurements. One of the earliest instances of sparse signal recovery can be dated back to 1980's showing the recovery of geophysical signals comprising of spike trains from an under-sampled set of Fourier measurements [55, 56]. A more recent exploitation of the notion of sparsity that gained tremendous attention in the signal processing community is the Compressive Sensing (CS) [48], a data acquisition and reconstruction theory. From the data acquisition point of view, under certain assumptions, the theory asserts that acquisition of much less measurements than required by the conventional Nyquist-Shannon sampling theorem is sufficient to recover exactly the sought signal with high probability [57–59]. From the reconstruction perspective, considering the sparsity of signal in some dictionary and fulfilment of some technical conditions, the CS theory claims that finding the sparsest estimate satisfying the measurements corresponds to a unique solution of the underlying problem [58]. In general, in the context of sparse recovery problems, a natural way to impose sparsity is to use the ℓ_0 pseudo-norm of the sought variable and the associated ℓ_0 -minimization problem is of the form

$$\underset{\mathbf{A}}{\text{minimize}} \quad \|\mathbf{A}\|_0 \quad \text{subject to} \quad \|\mathbf{Y} - \Phi'(\Psi\mathbf{A})\|_F \leq \epsilon, \quad (3.7)$$

where $\epsilon > 0$ denotes an upper bound on the Frobenius norm of the additive noise. By definition, minimizing the ℓ_0 norm eventually leads to a reduction in the number of non-zero elements, thereby promoting sparse estimates. However, this problem is non-convex and is not guaranteed to converge to a global minimum. In addition, it usually involves combinatorial search that can become intractable especially for large dimensional problems [60]. A common practice is then to consider its convex relaxation, the ℓ_1 norm [61].

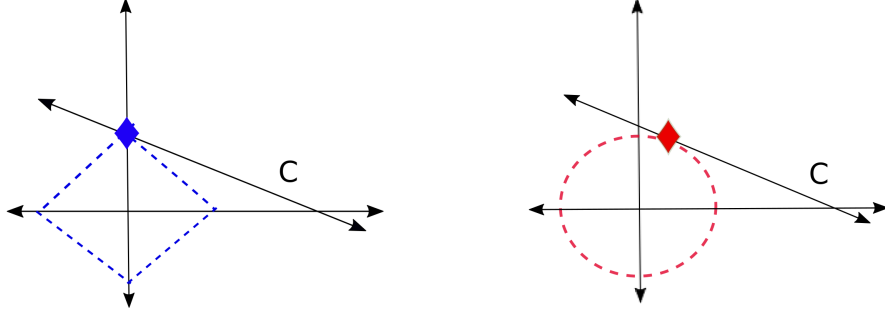


FIGURE 3.2: Illustration of the ℓ_1 norm favouring a sparse vector in \mathbb{R}^2 approximated by a one-dimensional affine space C [62]. The dashed lines denote the smallest ℓ_1 (blue) and ℓ_2 (red) balls meeting C at the respective diamond-shaped points.

ℓ_1 minimization strategy

The ℓ_1 norm is commonly used as a proxy of ℓ_0 norm. The enforcement of sparsity by the ℓ_1 norm can be better understood from Figure 3.2. In this figure, the dashed lines show an ℓ_1 ball (blue) and an ℓ_2 ball (red) in \mathbb{R}^2 , respectively obtained by a set of vectors having the same ℓ_1 and ℓ_2 norms. For each of these ℓ_p balls, the point of intersection (blue diamond for $p = 1$ and red for $p = 2$) of the smallest possible ball with line C denoting an affine space can be interpreted as the vector with smallest ℓ_p norm belonging to C . In this manner, it is straightforward to observe that ℓ_1 norm favours a sparse solution [62, 63].

Using the ℓ_1 norm as the sparsity inducing term gives rise to the well known basis pursuit denoising (BPDN) problem, having the following form

$$\underset{\mathbf{A}}{\text{minimize}} \quad \|\mathbf{A}\|_1 \quad \text{subject to} \quad \|\mathbf{Y} - \Phi'(\Psi\mathbf{A})\|_F \leq \epsilon. \quad (3.8)$$

This ℓ_1 minimization strategy lies at the heart of the CS framework to recover the sparse signals. More precisely, under specific conditions on the measurement operator Φ' , CS theory provides reconstruction guarantees for equation (3.8) [57, 64].

Variants of ℓ_1 minimization problem

In particular, problem (3.8) represents a synthesis-based approach as its solution \mathbf{A}^* can be used to synthesize the signal of interest \mathbf{S}^* using the relation $\mathbf{S}^* = \mathcal{R}^\dagger(\Psi\mathbf{A}^*)$.

An alternative formulation is rendered by what is called analysis-based approach that solves directly for the sought signal instead of its sparse representation. The associated minimization problem is defined as

$$\underset{\tilde{\mathbf{S}}}{\text{minimize}} \quad \|\Psi^\dagger \tilde{\mathbf{S}}\|_1 \quad \text{subject to} \quad \|\mathbf{Y} - \Phi'(\tilde{\mathbf{S}})\|_F \leq \epsilon. \quad (3.9)$$

When the considered dictionary is orthonormal, both synthesis- and analysis-based approaches are equivalent. On the other hand, in the case of using overcomplete dictionary, the two approaches exhibit unequivalence [65]. In general, both of these formulations have their own sets of merits and demerits. For instance, while using the overcomplete dictionaries, the synthesis-based approach takes advantage of the redundancy in the employed dictionary for a better modelling of the complex signals [66], whereas the analysis-based approach benefits from the lower problem dimensionality as it does not depend on the dictionary size. Nevertheless, comparing between the two formulations is still an active area of investigation.

Finally, for the sake of completeness and recalling from Section 3.2, another possible variation of problem (3.9) (or of (3.8)) can be provided. It comes from its associated Lagrangian function and gives its unconstrained formulation as

$$\underset{\tilde{\mathbf{S}}}{\text{minimize}} \quad \mu \|\Psi^\dagger \tilde{\mathbf{S}}\|_1 + \frac{1}{2} \|\mathbf{Y} - \Phi'(\tilde{\mathbf{S}})\|_F^2, \quad (3.10)$$

where $\mu > 0$.

Reweighted ℓ_1

Although ℓ_1 minimization, popularized by CS as a proxy for ℓ_0 minimization, has been extensively used in scientific applications, one thing to be pointed out is that unlike ℓ_0 pseudo norm, it is dependent on the magnitude of the underlying signal's coefficients. To address this imbalance, several approximations of the ℓ_0 pseudo norm have been proposed in the literature [67–69]. In particular, as proposed in [67], ℓ_0 minimization behaviour can be nicely approximated by reweighted- ℓ_1 minimization that is explained as follows.

Given any signal $\tilde{\mathbf{S}}$, its weighted ℓ_1 norm is defined as

$$\|\Psi^\dagger \tilde{\mathbf{S}}\|_{\mathbf{W},1} = \|\mathbf{W}\Psi^\dagger \tilde{\mathbf{S}}\|_1 = \sum_{i=1}^4 \sum_{j=1}^J W_{j,i} |[\Psi^\dagger \tilde{\mathbf{S}}]_{j,i}|, \quad (3.11)$$

where the subscripts j and i in the notation $[\cdot]_{j,i}$ respectively stand for the row and column indices of the argument matrix, and $\mathbf{W} \in \mathbb{R}_+^{J \times 4}$ is the weighting matrix. In the case when this matrix is chosen to be identity, the ℓ_1 regularization term is obtained. With the definition (3.11), the weighted- ℓ_1 regularized version of problem (3.9) is given by

$$\underset{\tilde{\mathbf{S}}}{\text{minimize}} \quad \|\Psi^\dagger \tilde{\mathbf{S}}\|_{\mathbf{W},1} \quad \text{subject to} \quad \|\mathbf{Y} - \Phi'(\tilde{\mathbf{S}})\|_F \leq \epsilon. \quad (3.12)$$

Regarding the weights that need to be determined, [67] proposed to solve iteratively a sequence of the weighted ℓ_1 minimization problems (e.g. problem (7.22)) - referred to as the reweighting scheme. The weights for each reweighting iteration, indexed by $r^* \in \mathbb{N}$, are computed from the previous solution $(\tilde{\mathbf{S}}^*)^{(r^*)}$ as follows:

$$(\forall j \in \{1, \dots, J\}) \quad W_{j,i}^{(r^*+1)} = \frac{\delta^{(r^*+1)}}{\delta^{(r^*+1)} + |[\Psi^\dagger(\tilde{\mathbf{S}}^*)^{(r^*)}]_{j,i}|}, \quad (3.13)$$

where $i \in \{1, \dots, 4\}$ and $\delta^{(r^*+1)} > 0$ acts as a stabilization parameter whose role is to ensure that zero valued coefficients result in well defined weights. In essence, with definition (3.13), large weights are associated with small-valued coefficients to penalize them, whereas small weights are linked with large-valued coefficients to promote them. Moreover, $\delta^{(r^*+1)}$ is decreased iteration-by-iteration such that $\delta^{(r^*+1)} \rightarrow 0$ when $r^* \rightarrow +\infty$, and hence the weighted ℓ_1 norm approaches to the ℓ_0 norm. Thus, reweighting procedure tends to alleviate the magnitude dependency of the usual ℓ_1 norm.

To give an example, Figure 3.3 depicts the recovery of correct sparse signal by using weighted- ℓ_1 minimization. More precisely, for the ℓ_1 ball centred at origin with radius $\|\mathbf{S}_0\|_1$, the feasible data constraint set intersects in its interior. As such, ℓ_1 minimization fails in recovering the correct solution $\|\mathbf{S}_0\|_1$ (case (b) in Figure 3.3). On the other hand, by using suitable weights, the weighted- ℓ_1 ball's shape changes in a manner that the constraint set no longer intersect with the ball's interior, thereby

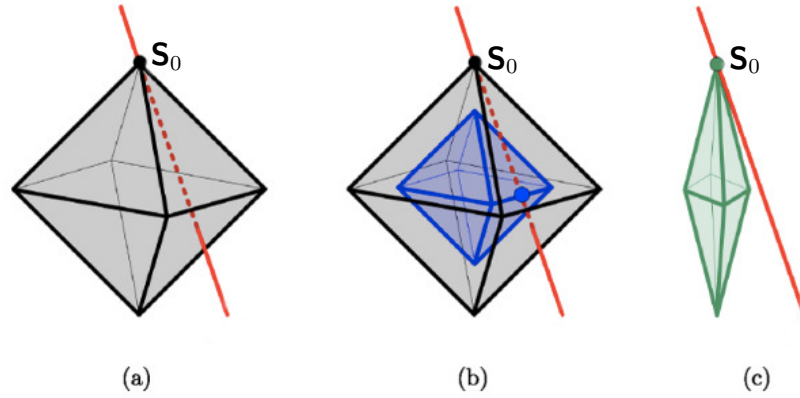


FIGURE 3.3: Illustration of weighted- ℓ_1 norm providing better recovery of a sparse signal in comparison with ℓ_1 norm. (a) shows the unknown sparse signal \mathbf{S}_0 with its associated ℓ_1 ball, and the constraint set (red line) $\mathbf{Y} = \Phi'(\tilde{\mathbf{S}})$. (b) depicts existence of a signal $\mathbf{S} \neq \mathbf{S}_0$ such that $\|\mathbf{S}\|_1 < \|\mathbf{S}_0\|_1$. (c) shows a weighted ℓ_1 ball in which case there is no $\mathbf{S} \neq \mathbf{S}_0$ with $\|\mathbf{W}\mathbf{S}\|_1 < \|\mathbf{W}\mathbf{S}_0\|_1$. Illustration extracted from [67].

finding the correct solution (case (c) in Figure 3.3).

3.3.2 Sparse recovery methods

The previous section has provided a variety of minimization problems, whether using the ℓ_0 or (weighted) ℓ_1 prior, that need to be solved for the recovery of sparse signal from the given measurements. The literature is brimming with methods performing the sparse signal recovery in an efficient manner while benefiting from the stable reconstruction guarantees. In general, these methods can be broadly categorised into greedy, convex-optimization and Bayesian techniques, that are briefly described in the following.

Greedy methods

These methods offer a way to solve the ℓ_0 minimization problem for sparse recovery by relying on representation of the signal of interest as a linear combination of the basic elements (atoms) of a suitably chosen dictionary. The idea is to iteratively refine the sparse representation of the sought signal by *greedily* searching for the columns in the dictionary having the maximum correlation with the noise residual. Working on this principle, the most commonly used method is Matching Pursuit (MP) [60, 70]. Although gaining immense success, MP suffers from large number

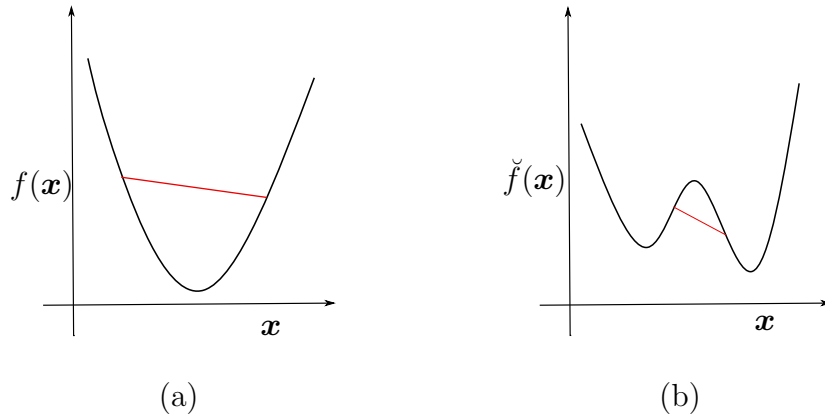


FIGURE 3.4: Graphs of one-dimensional functions where for convex function $f(\mathbf{x})$ in (a), the line segment (in red) joining two points on the graph lies above its graph, whereas for non-convex function $\tilde{f}(\mathbf{x})$ in (b), such a line segment lies below the graph.

of iterations that might be required to reach a solution. To counteract this issue, another MP based method, namely Orthogonal Matching Pursuit (OMP) has been proposed upper-bounding the number of maximum MP iterations [71, 72]. In the context of a signal that is not strictly sparse, Stagewise OMP (StOMP) offers a computationally more efficient alternative to OMP [73]. The MP family is further extended by the development of techniques including Compressive Sampling Matching Pursuit (CoSaMP) [74], Regularized OMP methods [75, 76], to name a few, providing uniform signal recovery guarantees that depend only on the sparsity of the signal and the sampling operator.

As mentioned in [77], another popular algorithm within the class of greedy methods is the iterative hard-thresholding algorithm (IHT) [78]. At each iteration, it consists in computing a gradient descent step on the usual least squares criterion using the current estimate of the sought k -sparse signal. This is followed by a hard-thresholding step, i.e. keeping only the largest k coefficients while setting all the other signal coefficients to zero. Its uniform performance guarantees have been demonstrated in [79].

In essence, greedy algorithms provide a straightforward way to conduct sparse signal recovery. However, the obtained solution by these algorithms may not be guaranteed to be the global optimum of the underlying non-convex problem.

Convex optimization-based approaches

By definition, a function $f: \mathbb{R}^N \rightarrow \mathbb{R}$ is convex if it satisfies

$$f(\lambda \mathbf{x}_1 + (1 - \lambda) \mathbf{x}_2) \leq \lambda f(\mathbf{x}_1) + (1 - \lambda) f(\mathbf{x}_2), \quad (3.14)$$

for all $\mathbf{x}_1, \mathbf{x}_2 \in (\mathbb{R}^N)^2$ and any $\lambda \in [0, 1]$. In simple terms, for a convex function, the line segment joining any two points on the function's graph lies either above or on the graph, as illustrated in Figure 3.4. Optimization problems composed of convex functions and subject to convex constraints are referred to as the convex optimization problems. Such problems have many desirable features, particularly the fact that any local minimum is a global minimum.

Within the considered settings, the previously introduced ℓ_1 minimization problems for sparse recovery (problems (3.8) - (3.10)) incorporating convex functions (ℓ_1 and ℓ_2 norms) fall under the realm of convex problems, that can be efficiently solved leveraging the convex optimization framework. Recently in the wake of CS, many improved algorithms have been developed to take into account the non-smooth terms (such as ℓ_1 term) in the minimization problem and to handle large dimensional problems. One possibility is to cast the BPDN problem as a second order cone programming problem that can be solved by interior-point methods [80]. A computationally faster alternative is offered by the method of Gradient Projection for Sparse Reconstruction (GPSR) [47] or by the use of soft-thresholding/shrinkage, leading to algorithms such as the iterative shrinkage-thresholding algorithm (ISTA) [46, 81–83], fast ISTA (FISTA) [84], to name a few. The key idea behind these methods is to perform a gradient descent step on the least-squares criterion followed by the soft-thresholding operation. Intuitively, this operation consists in setting all the coefficients of its argument that are less than some threshold to zero while shrinking the others by the threshold value. This operation thus induces sparsity. Within the optimization literature, ISTA can also be interpreted as a proximal splitting method, in particular forward-backward algorithm [85].

To summarize, efficient convex optimization algorithms exist for sparse recovery. The associated convergence guarantees to the global optimum plays a key role in drawing

attention towards these approaches. Moreover, leveraging the versatility of the convex optimization framework, new techniques tailoring the needs of the chosen application area can be designed.

Bayesian methods

These methods rely on making appropriate assumptions on the statistics of the signal of interest. Particularly, they deal with the posterior distributions, incorporating a prior distribution on the sought signal. Maximum a Posteriori (MAP) estimation provides one such popular technique, aiming to find an estimate of the signal that maximizes the posterior distribution. Within the sparse recovery settings, sparsity can be promoted by choosing a suitable prior distribution. For instance, in the case of Laplacian prior, the standard ℓ_1 regularized minimization problem can be achieved. Therefore, in simple terms, MAP estimation can also be seen as a form of regularized regression. Sparse Bayesian learning (SBL) approaches present another family of probabilistic approaches consisting in learning the sparsity prior by methods such as Relevance Vector Machines (RVMs) [86, 87]. Particularly for inverse problems encountered in CS, Bayesian compressive sensing (BCS) algorithm has also been designed that employs techniques like Fast Marginal Likelihood Maximization [88].

Although the Bayesian based methods benefit from several advantages, such as their robustness and providing error bars with the estimated solutions, they might not be very adapted to large dimensional problems [89].

3.4 A tour of convex optimization framework

Among the different classes of sparse recovery techniques introduced before, convex optimization methods are more attractive especially within the CS context and form a well-known component of the commonly used optimization toolboxes. This can be attributed to a range of desirable features they offer, such as convergence guarantees to the global minimum of the optimization problem, adaptability and scalability for complex, large dimensional problems. Driven by these features, the research work undertaken in this thesis exploits various tools lying within this framework. Therefore,

it is beneficial to provide a more thorough understanding of the class of approaches within this framework, especially proximal splitting and primal-dual methods that will be used later for algorithmic developments in the manuscript.

3.4.1 Proximal splitting methods

Within the broad class of convex optimization approaches, we focus on iterative algorithms based on proximal splitting methods. The main advantages of these methods are their flexibility to deal with sophisticated minimization problems, and their scalability offering the possibility to handle large dimensional variables. An overview of these methods can be found in [90, 91]. They can be employed to solve a wide class of problems expressed in the following generic form

$$\underset{\tilde{\mathbf{S}}}{\text{minimize}} \sum_{k=1}^K f_k(\tilde{\mathbf{S}}), \quad (3.15)$$

where for $k \in \{1, \dots, K\}$, f_k is a proper, lower-semicontinuous convex function from $\mathbb{R}^{N \times 4}$ to $] -\infty, +\infty]$. It is important to emphasize that many problems encountered in practice can be cast in the form (3.15). Indeed, any constrained problem can be reformulated as (3.15). This can be achieved by casting one of the functions f_k as an indicator function of the constraint set of interest, and defined as follows. The indicator function of a non-empty closed convex set $\mathcal{C} \subset \mathbb{R}^{N \times 4}$, at a given point $\tilde{\mathbf{S}} \in \mathbb{R}^{N \times 4}$, is defined as

$$\iota_{\mathcal{C}}(\tilde{\mathbf{S}}) = \begin{cases} 0, & \text{if } \tilde{\mathbf{S}} \in \mathcal{C}, \\ +\infty, & \text{otherwise.} \end{cases} \quad (3.16)$$

Another interesting point of problem (3.15) is that it can take into account both smooth and non-smooth functions. In practice, to handle these functions, proximal splitting methods will use the gradient for each of the smooth functions and the proximity operator for each non-smooth function. Formally, the proximity operator of a function $f: \mathbb{R}^{N \times 4} \rightarrow] -\infty, +\infty]$ at the point $\tilde{\mathbf{S}}$ is defined as

$$\text{prox}_f(\tilde{\mathbf{S}}) = \underset{\mathbf{U} \in \mathbb{R}^{N \times 4}}{\text{argmin}} f(\mathbf{U}) + \frac{1}{2} \|\mathbf{U} - \tilde{\mathbf{S}}\|_F^2. \quad (3.17)$$

This operator has been introduced by [92] and extensively used in signal and image processing to deal with non-smooth functions [90]. In particular, for the sparsity inducing ℓ_1 norm, the proximity operator is given by the *soft-thresholding operator* [93]. Considering $f(\cdot) = \mu \|\cdot\|_1$ in the definition of proximity operator (3.17), the resultant operation is performed by the soft-thresholding operator \mathcal{T} as follows:

$$\mathcal{T}_\mu(\tilde{\mathbf{S}}) = \mathbf{U}^* = \max\{|\tilde{\mathbf{S}}| - \mu, \mathbf{0}\} \cdot \text{sign}(\tilde{\mathbf{S}}), \quad (3.18)$$

that is performed component-wise such that each component of \mathbf{U}^* is given by

$$U_{j,i}^* = \begin{cases} -\tilde{S}_{j,i} + \mu & \text{if } \tilde{S}_{j,i} < -\mu, \\ 0 & \text{if } -\mu \leq \tilde{S}_{j,i} \leq \mu, \\ \tilde{S}_{j,i} - \mu & \text{otherwise,} \end{cases} \quad (3.19)$$

where $i \in \{1, 2, 3, 4\}$ and $j \in \{1, \dots, N\}$. Intuitively, this operation consists in forcing the elements smaller than some threshold μ to zero, while reducing the rest of the elements by this threshold value. Therefore, using any iterative algorithm for ℓ_1 minimization, iteration-by-iteration, the smaller values are removed and finally, only the elements having significant values are left, hence promoting sparsity. This is further illustrated in Figure 3.5 for an element $\tilde{S}_{j,i}$ of $\tilde{\mathbf{S}}$ for a better understanding.

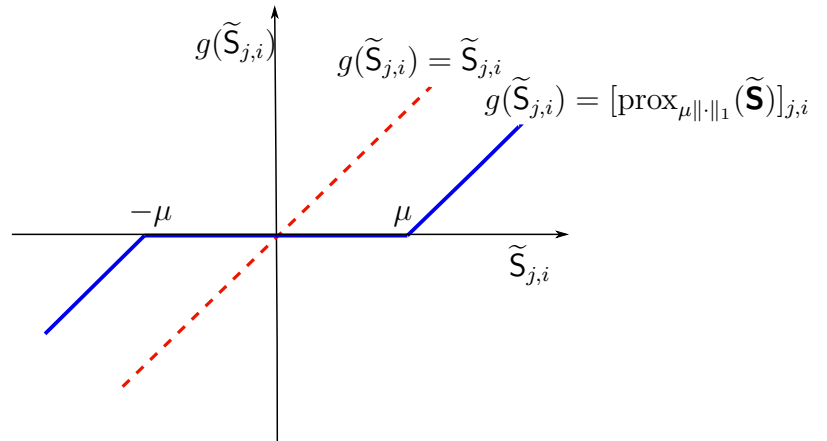


FIGURE 3.5: Illustration of the soft-thresholding operation.

Finally, the proximity operator can be seen as a generalization of the projection operator $\mathcal{P}_{\mathcal{C}}$ onto a closed convex set \mathcal{C} when f is chosen to be the indicator function of \mathcal{C} . In this context, equation (3.17) reduces to

$$\mathcal{P}_{\mathcal{C}}(\tilde{\mathbf{S}}) = \underset{\mathbf{U} \in \mathbb{R}^{N \times 4}}{\operatorname{argmin}} \iota_{\mathcal{C}}(\mathbf{U}) + \frac{1}{2} \|\mathbf{U} - \tilde{\mathbf{S}}\|_F^2 = \underset{\mathbf{U} \in \mathcal{C}}{\operatorname{argmin}} \|\mathbf{U} - \tilde{\mathbf{S}}\|_F^2, \quad (3.20)$$

thus finding the closest point from $\tilde{\mathbf{S}}$ in \mathcal{C} with respect to the Euclidean distance, as depicted in Figure 3.6.

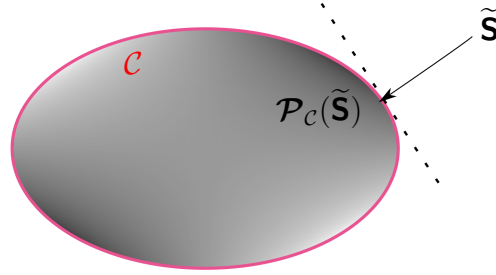


FIGURE 3.6: Projection of a point $\tilde{\mathbf{S}}$ onto a convex set \mathcal{C} .

Popular proximal-splitting methods include the forward-backward (FB) algorithm [94, 95], Douglas-Rachford algorithm [96]. In fact, many well-known algorithms from the literature can be seen as special instances of proximal splitting methods. To give an example, let us recall problem (3.10) consisting of a sum of ℓ_1 and ℓ_2 terms:

$$\underset{\tilde{\mathbf{S}}}{\operatorname{minimize}} \underbrace{\mu \|\Psi^\dagger \tilde{\mathbf{S}}\|_1}_{f_1(\tilde{\mathbf{S}})} + \underbrace{\frac{1}{2} \|\mathbf{Y} - \Phi'(\tilde{\mathbf{S}})\|_F^2}_{f_2(\tilde{\mathbf{S}})}.$$

Within the framework of proximal splitting methods, an efficient means to solve this problem consists in resorting to a FB algorithm. To be precise, the FB algorithm finds the solution to the underlying problem in an iterative manner where at each iteration $l \in \mathbb{N}^*$, the sought variable is updated as

$$\tilde{\mathbf{S}}^{(l+1)} = \underbrace{\operatorname{prox}_{\delta^{(l)} f_1}}_{\text{backward step}} \left(\underbrace{\tilde{\mathbf{S}}^{(l)} - \delta^{(l)} \nabla f_2(\tilde{\mathbf{S}}^{(l)})}_{\text{forward step}} \right), \quad (3.21)$$

where a forward gradient step is performed on the Lipschitz-differentiable function f_2 . The resultant variable is acted upon by a backward proximity step for the non-smooth function f_1 . For the case when functions f_1 and f_2 are convex, the sequence generated by the FB algorithm is proven to converge to a solution of the underlying problem [97, 98], provided the stepsize $\delta^{(l)}$ satisfies $0 < \inf_{l \in \mathbb{N}} \delta^{(l)} \leq \sup_{l \in \mathbb{N}} \delta^{(l)} < 2\kappa^{-1}$, where κ is the Lipschitz constant of ∇f_2 . Furthermore, it can be noticed that when f_1 is defined as the ℓ_1 norm, the proximity step reduces to a soft-thresholding operation, leading to the ISTA algorithm introduced earlier in the chapter.

3.4.2 Primal-dual methods

In the particular yet common case of composite problems where the non-smooth functions are composed with a linear operator, adapted methods need to be designed. For instance, consider the following problem

$$\underset{\tilde{\mathbf{S}} \in \mathbb{R}^{N \times 4}}{\text{minimize}} \ f_1(\tilde{\mathbf{S}}) + f_2(\mathbf{T}\tilde{\mathbf{S}}), \quad (3.22)$$

where $f_1: \mathbb{R}^{N \times 4} \rightarrow]-\infty, +\infty]$ and $f_2: \mathbb{R}^{Q \times 4} \rightarrow]-\infty, +\infty]$ are proper, lower-semi-continuous convex functions, and $\mathbf{T} \in \mathbb{R}^{Q \times N}$ is a linear operator. Considering f_1 to be a differentiable function and f_2 to be a non-smooth function, one possibility to solve this problem is by using the FB algorithm, alternating between a gradient step on f_1 and a proximity step on $f_2 \circ \mathbf{T}$. However, using this approach may require the inversion of the operator \mathbf{T} or performing sub-iterations to compute the proximity step. This can be problematic especially when the dimension of the underlying problem increases. To overcome this issue, recently several primal-dual methods have been proposed [90, 91, 99–102]. Basically, they provide *full splitting* and solve simultaneously for the primal and the dual problems. More formally, the dual problem associated with the primal problem (3.22) is given by

$$\underset{\mathbf{V} \in \mathbb{R}^{Q \times 4}}{\text{minimize}} \ f_1^*(-\mathbf{T}^\dagger \mathbf{V}) + f_2^*(\mathbf{V}), \quad (3.23)$$

where \mathbf{T}^\dagger is the adjoint operator of \mathbf{T} and f_1^* (resp. f_2^*) is the Legendre-Fenchel conjugate function of f_1 (resp. f_2) [103], that is defined as

$$f_1^*(\mathbf{U}) = \sup_{\tilde{\mathbf{S}}} (\langle \tilde{\mathbf{S}}, \mathbf{U} \rangle_F - f(\tilde{\mathbf{S}})), \quad (3.24)$$

for any $\mathbf{U} \in \mathbb{R}^{N \times 4}$ and $\langle \cdot, \cdot \rangle_F$ denoting the Frobenius inner product of the argument matrices. The key idea behind employing the dual problem stems from the Fenchel-Rockafellar duality theorem stating that the dual problem provides a lower bound on the minimum value obtained by the primal one. The difference between these two optimal primal and dual values is known as the “duality gap”. For the considered settings for the functions f_1 and f_2 , this duality gap vanishes and the minimum values of the primal and dual problems are equal. Exploiting this feature, efficient algorithms aimed at concurrently solving primal and dual problems can be designed [100, 101]. Such algorithms seek to find a Kuhn-Tucker point $(\tilde{\mathbf{S}}', \mathbf{V}')$ that satisfies

$$-\mathbf{T}^\dagger \mathbf{V}' = \nabla f_1(\tilde{\mathbf{S}}'), \quad \mathbf{T} \tilde{\mathbf{S}}' \in \partial f_2^*(\mathbf{V}'), \quad (3.25)$$

and thus provides the solutions $\tilde{\mathbf{S}}'$ and \mathbf{V}' to the primal and the dual problems, respectively.

A notable advantage of the primal-dual methods is the splitting achieved over all the functions involved in the minimization problem. This includes the gradient and the proximity operators as well as the involved linear operator. The latter prevents the need to invert the linear operator [104]. These methods, thus, offer computational advantages over other splitting methods.

3.5 Non-convex optimization

3.5.1 Overview

Non-convex optimization problems present another class of problems that arise naturally in many practical cases. Contrary to convex problems, these problems consist of a function or a constraint set, or both that are non-convex. In particular, a function is said to be non-convex if it violates condition (3.14). To give further intuition, let us

consider a function $f(\mathbf{x}, \mathbf{z}) = \mathbf{x}\mathbf{z}$ consisting in taking the product of its argument vectors. As can be observed from Figure 3.7(a), the line segment joining the two points (highlighted in red) on the function's graph lies below the graph, thereby concluding its non-convexity. As a matter of fact, such a function can be extended to more than two variables and is widely encountered in many application areas. In its most general form, the corresponding data model can then be represented as

$$\bar{\mathbf{Y}} = f(\bar{\mathbf{X}}_1, \bar{\mathbf{X}}_2, \dots, \bar{\mathbf{X}}_K) + \bar{\boldsymbol{\Omega}}, \quad (3.26)$$

where $f: (\mathbb{R}^{N \times 4})^K \rightarrow \mathbb{C}^{4 \times M}$ is a multivariate function consisting in taking the products (possibly composed with some linear operators) of its arguments $\bar{\mathbf{X}}_k$'s where for every $k \in \{1, \dots, K\}$, $\bar{\mathbf{X}}_k \in \mathbb{R}^{N \times 4}$. This data model is then non-linear thereby inducing non-convexity in the associated minimization problem:

$$\underset{\mathbf{X}_1, \dots, \mathbf{X}_K}{\text{minimize}} \check{F}(\mathbf{X}_1, \dots, \mathbf{X}_K), \quad (3.27)$$

where \check{F} is the net objective function consisting of sum of usual data fidelity term corresponding to the model (3.26) and the regularization terms for the optimization variables. The RI observation model presented in equation (2.19) (and (2.20)) is one such instance of a non-linear data model leading to a non-convex optimization problem to be solved.

Solving for non-convex problems is a highly challenging task. Particularly, they are difficult to minimize to obtain a global minimum that stems from the fact that for these problems, the local minimum may not necessarily coincide with the global minimum. Moreover, there might exist many local minima of the problem that makes it highly likely for the adopted solver to get stuck in a local minima. As such, the initialization provided to the solver plays a crucial role in the quality of the estimated solution. The importance of initialization and the possibility to converge to a local minimum rather than a global minimum is further depicted in Figure 3.7(b) for an intuitive understanding. Adding onto these issues, obtaining theoretical convergence guarantees for this class of problems is a difficulty in itself.

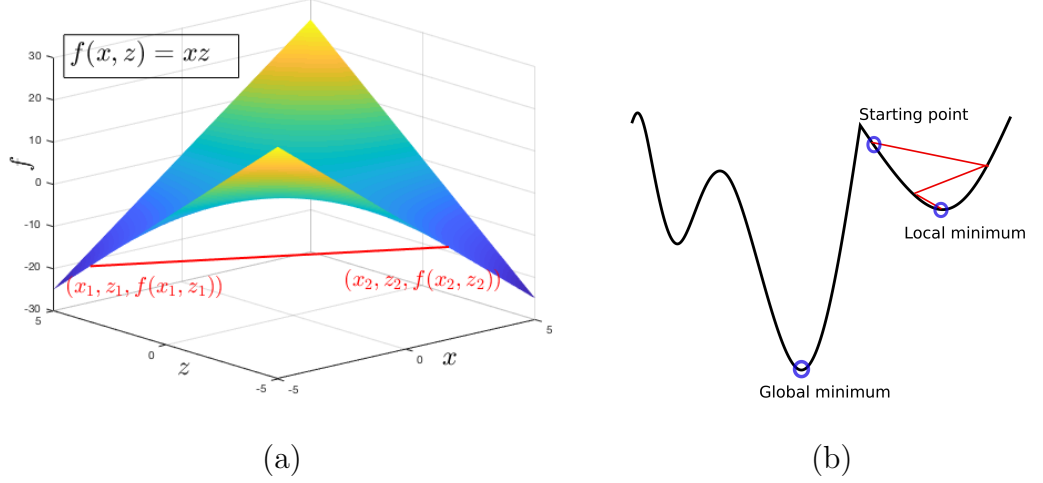


FIGURE 3.7: Graphs depicting non-convex functions. (a) A line segment (in red) joining two points on the graph of two-dimensional function f lies below its graph, thereby illustrating its non-convexity. (b) A one-dimensional non-convex function graph highlighting the critical role played by initialization while solving non-convex problems.

Within the scope of this thesis, we focus on non-convex minimization problems of the form (3.27). A primitive way to solve such problems is by the principle of alternating minimization (AM). As the name suggests, the key idea behind it is to solve for each of the variables while keeping the others fixed, in an alternating and iterative manner. That is, starting with an initial point $(\mathbf{x}_1^{(0)}, \dots, \mathbf{x}_K^{(0)})$, at each iteration $l \in \mathbb{N}^*$, the basic AM algorithm consists in the following

$$\begin{aligned}
 \mathbf{x}_1^{(l+1)} &\leftarrow \underset{\mathbf{x}_1}{\operatorname{argmin}} \check{F}(\mathbf{x}_1, \mathbf{x}_2^{(l)}, \dots, \mathbf{x}_K^{(l)}) \\
 &\vdots \\
 \mathbf{x}_K^{(l+1)} &\leftarrow \underset{\mathbf{x}_K}{\operatorname{argmin}} \check{F}(\mathbf{x}_1^{(l+1)}, \mathbf{x}_2^{(l+1)}, \dots, \mathbf{x}_K).
 \end{aligned} \tag{3.28}$$

Many popular algorithms rely on the AM principle such as the coordinate descent method [105], block coordinate method [106], block coordinate variable metric forward-backward algorithms [107], to name a few. In particular, the convergence of the latter has been established under mild technical assumptions [107, 108]. Furthermore, it makes use of the fact that for each sub-problem solving for a (block)variable while keeping the other fixed, the objective function is linear with respect to it. As a result,

convex sub-problems need to be solved that is done using FB iterations. It is worth emphasizing then it might be possible to exploit various convex optimization tools to solve the challenging class of non-convex problems.

3.5.2 Non-convex regularizations for sparse recovery

In the context of sparse recovery, while Sections 3.3.1 and 3.3.2 have described typical ℓ_0 minimization or ℓ_1 minimization problems, there also exists approaches solving the general ℓ_p minimization problems ($p \in (0, 1)$) [109] that can be done using reweighting schemes [110, 111]. Keeping aside the non-convexity of these problems, they require fewer measurements than the ℓ_1 minimization to ensure a satisfactory recovery of a sparse signal [109]. Similarly, particularly for the case of $p = 1$, the previously introduced reweighted ℓ_1 minimization problem while reconciling the magnitude dependency of ℓ_1 norm, provide an exact recovery of the sought signal using fewer measurements than usual ℓ_1 minimization [67]. In particular, this problem can be seen as a heuristic to a log-prior based non-convex problem and as such the whole reweighting procedure is not accompanied by strong provable guarantees. Nevertheless, each sub-problem (ℓ_1 minimization) is a convex problem that can be solved efficiently using any of the sparse recovery methods described in section 3.3.2 and is shipped with convergence guarantees. Moreover in practice, several works have demonstrated that reweighted ℓ_1 minimization outperforms the standard ℓ_1 minimization [67, 112]. More specifically, the effectiveness of this scheme has been demonstrated for radio-interferometric imaging in [14, 45].

3.6 Conclusion

In this chapter, I have provided an overview of the concept of sparsity and the algorithms exploiting it to recover an unknown signal. More specifically, the role played by CS techniques for sparse recovery is highlighted. The underlying convex optimization toolbox is detailed, primarily focusing on the proximal splitting and primal-dual methods on which the algorithmic developments in this thesis are based. The discussion is further extended to the non-convex optimization setting that will be beneficial while dealing with non-convex problems (eg. RI imaging and calibration problem) in this

manuscript. Overall, the mathematical treatment provided in this chapter sets the stage for the description of the existing standard RI approaches in the next chapter and the development of the proposed techniques in the later chapters.

Chapter 4

Standard radio interferometric approaches

Contents

4.1	Introduction	50
4.2	Imaging techniques	51
4.2.1	CLEAN and its family	51
4.2.2	Maximum Entropy Method	54
4.2.3	Non-negative least squares	55
4.2.4	Sparse optimization methods	55
4.3	Calibration modalities	58
4.3.1	External Calibration	59
4.3.2	Self-Calibration	59
4.3.3	DDE calibration	61
4.4	Conclusion	65

4.1 Introduction

This chapter presents an overview of the standard approaches employed in RI to solve imaging and calibration problems. For imaging purposes, the well-established methods and the newly developed approaches exploiting the previously discussed CS based sparse recovery methodology are described. In the context of calibration, various techniques aiming for the estimation of DIES or/and DDEs are presented.

4.2 Imaging techniques

With the given background knowledge gained for image recovery techniques using sparsity as a prior, we now move on to describe the methods developed for RI imaging. In a nutshell, the measured visibilities in RI are related to the true sky brightness distribution via Fourier transformation, sampled at discrete uv points by the interferometer. From the image domain perspective, the inverse Fourier transformed visibilities - referred to as ‘dirty image’, can be seen as a convolution of the interferometer’s point spread function (PSF) with the true image of interest, contaminated by an additive noise. In RI terminology, the PSF, obtained by inverse Fourier transform of the uv sampling function, is called the ‘dirty beam’. The corresponding task of recovering the sought images from the visibilities then amounts to a deconvolution process, i.e. removing the effect of the PSF from the dirty image. Moreover, the acquired incomplete and noisy information is not sufficient for accurate image recovery. From an optimization point of view, the associated imaging inverse problem can be seen as naturally falling under the CS framework [5] and thus, it can also be efficiently solved drawing on the ideas from a suitable sparse recovery technique and adapting it for RI imaging.

In light of the discussion above, the standard imaging approaches in RI are detailed below.

4.2.1 CLEAN and its family

Initially proposed in early 1970’s by [8], the CLEAN algorithm has emerged as the standard RI imaging technique. Its widespread use in the radio astronomical community can be attributed to its effectiveness in restoring high quality images from the acquired data as well as its simplicity making it easily understandable by the radio astronomers. The underlying assumption for Högbom CLEAN [8] is that the sought image consists of only point or compact sources. As such, the sky model can be effectively represented by various delta functions centred at these sources. Using this model, it consists in a greedy, non-linear iterative deconvolution approach. More precisely, it involves the computation of the dirty image wherein the maximum

absolute valued intensity pixel is searched for. This is followed by a beam removal step (i.e. to remove the effect of the dirty beam) where a fraction, defined by the so called loop gain factor, of this pixel's value convolved with the dirty beam is removed. The position and the amplitude of the removed peak is added as a delta function to the recovered 'model' image. The process of beam removal is continued until the maximum intensity value in the dirty image becomes lower than some threshold value dependent on the noise level. At this stage, the dirty image mainly contains noise and is often termed as 'residual' image. The resultant model image consists of multiple delta functions at different locations, which is often non-physical, in particular for extended emission. In order to have a more realistic representation of the radio sky, the model image is convolved with the CLEAN beam, typically a Gaussian fitted to the primary lobe of the dirty beam. The final 'restored' image of this algorithm is generated by adding the residual image to the smoothed model image.

A point to be noted is that in the beam removal step, the full dirty beam is employed by Högbom CLEAN. While it renders accuracy, it can also become computationally intensive. [113] proposed a comparatively fast version of the basic CLEAN algorithm by introducing what are called major and minor cycles. Minor cycles are performed to identify the peak in the dirty image coupled with the beam removal step, the noteworthy difference being the usage of only a small patch of the dirty beam. This leads to a speed-up in the overall approach, however at the cost of potentially creating an inaccurate residual image. In order to compensate this, as soon as the peak intensity in the dirty image falls below a threshold level, a major cycle is performed to recompute the residual image, by subtracting the contribution of the model image in the Fourier domain from the gridded visibilities. The Cotton-Schwab CLEAN (CS-CLEAN) [114] presents a variant of Clark algorithm in [113] where the subtraction of the Fourier transformed model image in the major cycle takes place in the degridded visibility data domain, thereby removing gridding errors. This improved variant also benefits from CLEANing multiple sources simultaneously and independently in the minor cycles, whereas the contribution of all these CLEANed components is removed together in the major cycle.

Although the initial CLEAN-based algorithms dealt with the delta function sky model, lately many variants of CLEAN have been developed to account for the sky models consisting of extended emission. One such variant is presented by Steer-Dewdney-Ito (SDI) CLEAN [115]. It relies on removing a group of CLEAN components having values higher than some fraction of the peak value in the residual image. It thus helps in suppressing CLEAN stripes that appear in the recovered image if only a single CLEAN component is removed while deconvolving smooth, extended emission. Another popular variant is the Multi-Scale CLEAN (MS-CLEAN) [116], which treats the components of the sky model image at different scale sizes. Its performance is often dependent on the scales that can either be chosen by the user or set automatically when implemented in WSCLEAN package [117]. In practice, CS-CLEAN is the standard variant now together with MS-CLEAN.

In terms of implementation of CLEAN (or its variants), many parameters are involved to ensure its stability due to its greedy nature. For instance, to stop cleaning, user can specify the desired threshold below which if the peak in the residual images falls, cleaning stops. On the other hand, for an automated processing, a auto-threshold function can be adopted. In this context, in the WSCLEAN package, the threshold value is set automatically depending on the residual noise level. Another feature is the selection of the CLEAN components in a restricted region, defined by a clean binary mask. The idea is to limit the region where radio emission is expected and is advantageous in reducing the computational cost by searching for the peaks only in masked regions. Such a mask can either be specified by the user or generated automatically (referred to as auto-masking) during the cleaning process using the auto-multithresh algorithm [118]. The latter is incorporated in `tclean` task in Common Astronomy Software Applications (CASA) package¹. In particular, at the beginning of a minor cycle, it updates the mask by using multiple thresholds relying on noise and sidelobe levels in the current residual image. It can also ‘prune’ the regions from the mask that represent false astronomical emission, typically the regions that are smaller than some fraction of the beam.

¹https://casa.nrao.edu/casadocs/latest/global-task-list/task_tclean/about

The celebrated CLEAN algorithm for RI imaging can also be seen from the lens of sparse recovery methods. Working pixel by pixel, CLEAN implicitly considers the sought image to be sparse in its domain, and shares many attributes with the MP algorithm described earlier [60]. Analogies of CLEAN with a sparsity regularized gradient descent method have also been shown in [9, 24, 119]. In simple terms, it aims to minimize the residual norm $\|\mathbf{Y} - \Phi'(\tilde{\mathbf{S}})\|_F^2$ subject to a sparsity constraint on the sought image. The update step is reminiscent of a typical forward-backward step. More precisely, the computation of the dirty residual image $\Phi'^{\dagger}(\mathbf{Y} - \Phi'(\tilde{\mathbf{S}}))$ corresponds to a gradient step on the differentiable ℓ_2 norm term, whereas the beam removal step resembles the proximity step for the considered sparsity prior, i.e. the soft-thresholding operation. At each iteration, it selects a fraction of the peak value to be removed from the residual image, which is then added to the model image. This fraction determined by the loop gain factor is analogous to the soft-thresholding parameter in ℓ_1 -optimization terminology.

With regards to polarimetric imaging, the aforementioned CLEAN-based approaches apply the same technique as developed for Stokes I imaging, to recover each of the Stokes parameters. In particular, these algorithms operate by either searching for the CLEAN components separately in each of the Stokes images or in the net image given by: $I^2 + Q^2 + U^2 + V^2$. Another technique called Generalized Complex CLEAN has been proposed in [120] for polarimetric imaging. This technique is basically a modification of the CLEAN algorithm. Unlike CLEANing independently for the real valued Stokes Q and U images, as done in the traditional CLEAN methods, the authors in [120] propose to CLEAN the complex valued linear polarization image P . It offers the advantage of rotational invariance and detection of more true components in sources near the noise level.

4.2.2 Maximum Entropy Method

Although CLEAN is the most popular technique in RI imaging, another standard approach consists in the Maximum Entropy Method (MEM) [121]. Solving an optimization problem, this method aims to find an image that maximizes an entropy function while being consistent with the acquired data. The entropy function includes

a prior image and the estimated image is biased towards the choice of the prior image. For instance, a prior flat image promotes smoothness of the estimated image. Using the suitable penalty functions, MEM can also take into account the positivity of the sought image. An extension of this approach for Stokes parameters imaging has been developed as well [122–125]. In particular, the polarimetric MEM can be used to incorporate the physical polarization constraint via a special entropy function, thereby solving jointly for the underlying Stokes parameters.

4.2.3 Non-negative least squares

Another approach to tackle the RI imaging problem stems from the estimation of the original image by solving a constrained least-squares minimization problem. More precisely, it consists of minimizing the ℓ_2 squared norm of the difference between the observed and the predicted model, subject to the constraint that the sought image is non-negative. To solve the resultant non-negative least-squares (NNLS) problem, [126] developed the first algorithm that is based on an active set method [127]. In the context of RI imaging, it has been studied in detail in [128]. In particular, NNLS has been shown to perform well to recover sources that are too compact for MEM and too extended for CLEAN to be dealt with properly. Moreover, NNLS produces high-fidelity recovered sources and thus, is very suitable to be implemented with a calibration technique in a self-calibration loop. In addition to the non-negativity constraint, recently there have been some works suggesting the sought image's pixel values to be upper-bounded within the NNLS framework [129].

4.2.4 Sparse optimization methods

The above mentioned techniques, particularly CLEAN, have been used extensively to produce sought images from the acquired data. They are, however, not expected to meet the imaging requirements of the upcoming interferometers. In particular for the celebrated CLEAN algorithm, its imaging reconstruction quality is often limited by the nominal resolution of the interferometer. In addition, it may suffer from convergence issues and might not always be stable. Its stability is highly dependent on the choice of various parameters that need to be tuned during its implementation, whether

automatically or manually. As an alternative to the standard RI techniques, in the wake of CS, several sparsity regularized RI imaging techniques have been proposed in the last decade. For instance, the SARA approach in [45] enforces average sparsity of the sought image in a concatenation of multiple representations, the synthesis-based approach in [12] uses the Dirac basis and the isotropic undecimated wavelet transform (IUWT) as the sparsifying dictionary, and the approach in [130] developed to solve specifically for the LOFAR data employs a synthesis approach exploiting curvelets and IUWT dictionaries [49]. A hybrid synthesis-by-analysis greedy sparse recovery technique has also been proposed in [131]. These methods, however, have been developed to image Stokes I only. I now describe in detail the methods relevant to the work proposed in this thesis.

SARA

In the spirit of promoting average sparsity of the underlying signal over multiple representations, [45] proposed the Sparsity Averaging Reweighted Analysis (SARA) algorithm for RI imaging. It stems from the fact that an astronomical image in general can consist of multiple features, such as point sources, with a diffuse emission background and complex extended structures. In this respect, the image can be seen as having average sparsity in multiple domains rather than a single domain. Exploiting this feature, the authors proposed to enforce sparsity in a dictionary consisting of a concatenation of multiple orthonormal bases: $\Psi = \frac{1}{\sqrt{q}}[\Psi_1, \Psi_2, \dots, \Psi_q] \in \mathbb{R}^{N \times J}$, with $J = qN$. These orthonormal bases Ψ_i 's are chosen to be the Dirac basis and the first eight Daubechies wavelet bases. While the Dirac basis encapsulate the point and compact sources, the continuous extended structures are well represented by the wavelet bases. Furthermore, the Haar wavelet basis in the chosen collection of wavelet bases provides an alternative to sparsity in the gradient domain.

In order to enforce the considered priors, this algorithm relies on solving a reweighted ℓ_1 analysis problem, mimicking the ℓ_0 minimization behaviour. It consists in iteratively solving a sequence of weighted ℓ_1 minimization problems of the form (7.22), subject to positivity of the sought intensity image and considering $\tilde{\mathbf{S}}$ to be containing only Stokes I image.

In its original formulation, the authors in [45] employed the Douglas-Rachford splitting technique to solve the minimization problem proposed by the SARA approach. On a further note, [9] adapted the SARA minimization problem within other two convex optimization algorithms, tailoring to the demands of the upcoming telescopes. These algorithms, namely alternating direction method of multipliers (ADMM) and primal-dual forward-backward (PDFB), renders a parallelizability and distributed strategy to achieve scalability to big data. In particular, PDFB approach solves jointly for the primal problem and its dual formulation [91]. This comes with the computational advantages as discussed in Section 3.4.2, especially achieving full proximal splitting over the underlying functions that is in contrast with ADMM [132]. Though applied only for Stokes I image reconstruction, the quality of reconstruction, both in terms of resolution and sensitivity, obtained by these techniques have shown to outperform that obtained by CLEAN on simulated as well as on few real data sets [9, 11, 14, 24, 120].

TV regularized sparse recovery

The aforementioned methods have been presented for Stokes I imaging only. Very recently, the first application of the sparsity regularized methods for polarimetric imaging has been developed in [133]. In this case, the authors promote the sparsity of the underlying images using the ℓ_1 norm along with the total variation (TV) regularization [51, 134], and solve the resultant problem using a monotonic version of FISTA [84, 135]. A remark to be made here is that similar to CLEAN, this approach also solves independent imaging inverse problems for each of the underlying Stokes parameters. Regarding the choice of the sparsifying dictionary, the authors show effectiveness of TV and ℓ_1 +TV sparsifying regularizations in producing good quality images. In particular, for these regularizations, the authors have considered the isotropic TV norm. Basically, the TV norm is defined for a 2D image $\mathbf{U} \in \mathbb{R}^{N_1 \times N_2}$ as the $\ell_{2,1}$ norm of the horizontal and the vertical gradients of this image [51]². More

²Here we consider the images are represented in vectorized form of dimension $N = N_1 \times N_2$. However, the 2D images can easily be obtained by reshaping these vectors.

formally, it is given by

$$\|\mathbf{U}\|_{\text{TV}} = \|\nabla \mathbf{U}\|_{2,1} = \sum_{n_1=1}^{N_1} \sum_{n_2=1}^{N_2} \sqrt{|\nabla_x \mathbf{U}|_{n_1, n_2}|^2 + |\nabla_y \mathbf{U}|_{n_1, n_2}|^2}, \quad (4.1)$$

where $\nabla = [\nabla_x, \nabla_y]$ is the concatenation of the horizontal gradient operator $\nabla_x: \mathbb{R}^{N_1 \times N_2} \rightarrow \mathbb{R}^{N_1 \times N_2}$ and the vertical gradient operator $\nabla_y: \mathbb{R}^{N_1 \times N_2} \rightarrow \mathbb{R}^{N_1 \times N_2}$.

The authors validate their technique on simulated EHT data and obtain higher resolved Stokes images than obtained by CLEAN.

4.3 Calibration modalities

The imaging approaches described earlier are applicable to the DIE calibrated data. In fact, by neglecting the presence of DDEs, these methods consider Jones matrices as identity, which leads to mis-modelling errors severely affecting the image reconstruction quality. Furthermore, in practice, the DDEs are unknown. As such, the associated Jones matrices are not only required to be incorporated in the observation model, but more importantly, these must be calibrated for to estimate the unknown effects. In general, the process of calibration can be carried out using either of the two approaches: Jones-specific and global approach, both of which have their own merits and demerits. On the one hand, the Jones-specific formalism involves the usage of parametric model/s to specify different Jones matrices within a Jones chain, using the physics behind respective propagation effects [136–138]. The task is then to estimate the unknowns in this model. With such specific representation of the various effects, the associated models are generated using only a few number of parameters. It thus requires estimation of only a small number of parameters while calibrating using this approach. The downside is that, due to these models being too specific, even a slight deviation from reality can have detrimental effect on the reconstruction quality. Moreover, not all the interferometers are represented by the same models. As such, these models need to be adapted for the interferometer under consideration. On the other hand, in the context of the global approach, instead of dealing with each of the Jones matrices separately, a global matrix incorporating the combined effects from all

the Jones matrices is considered [139]. The calibration problem is then designed to estimate the elements of this global matrix. This approach thus offers the flexibility to account for even those effects which were not modelled in the Jones-specific formalism. In addition, since no specifications need to be made about the underlying physics models, these approaches tend to be more robust. However, this non-modelling leads to estimation of far more number of parameters when compared with Jones-specific approach.

The standard calibration techniques in RI adopting either of the above two approaches are described below.

4.3.1 External Calibration

The technique of RI calibration started with the strategy of estimating the unknown gains using the observations made on external bright calibrator sources. These sources have well known properties, such as their intensity, position. For external calibration to work, the chosen calibrator source must be situated close enough to the science target in the sky to ensure the similarity of the perturbations encountered, failing which interpolation might be required [140]. At the same time, the two sources must not be too close to have inseparable contributions in the acquired data. Additionally, such observations need to be made at frequent intervals to track the time evolution of the calibration errors. A concerning issue with this technique is that it relies on prior knowledge of the calibrator source which is not necessarily always available. Moreover, it only solves for calibration errors in the calibrator source's direction, and hence may not be sufficient for antennas having a wide field-of-view.

4.3.2 Self-Calibration

It was in 1980s that scientists came up with the idea of self-calibration [141, 142], a more evolved calibration technique. This immensely successful scheme, often abbreviated as selfcal, relies on alternating between the calibration and the imaging process, in an iterative manner. To be more precise, this iterative procedure starts with a sky reference model that might contain some errors. Using this model, the DIE calibration is carried out that can be cast as a non-linear least squares minimization problem

(as discussed in Section 3.5.1). A commonly used approach to solve this problem is the Levenberg-Marquardt (LM) solver, which is a gradient-based approach [143]. The obtained solutions are then used to update the image via the adopted imaging technique. Consequently, this approach provides a refined, high dynamic range sky model along with the calibration terms estimates.

Computationally speaking, the conventional LM algorithm for calibration exhibits cubic scaling with the number of receiving antennas. As such, despite its good performance, it is not suitable for new generation interferometers having a large number of antennas, thereby calling for the need of developing fast solvers. StEFCal provides one such fast solver, as described in the following.

StEFCal

With the idea of developing fast solvers, [144] introduced the concept behind alternating direction implicit (ADI) method for RI, indicating that it could be faster to estimate the gains for all antennas in a successive manner. Particularly, for single antenna gain estimation, all the other antennas are assumed to be already calibrated. Exploiting this technique, [145] proposed a statistically efficient and fast calibration (StEFCal) solver. Developed for the estimation of antenna gains representing DIES, it aims to solve the inverse problem of the form:

$$\bar{\mathbf{Y}} = \mathbf{C}\bar{\mathbf{X}}\mathbf{C}^\dagger + \bar{\mathbf{\Omega}}, \quad (4.2)$$

where $\bar{\mathbf{Y}}$ contains the observed visibilities corrupted by the additive noise $\bar{\mathbf{\Omega}}$ and \mathbf{C} is the diagonal matrix containing the antenna gains. In the full polarization case, \mathbf{C} stands for a block-diagonal matrix instead, with each of its 2×2 block representing Jones matrix associated with dual-feed antenna gains [146]. Furthermore, $\bar{\mathbf{X}}$ in equation (4.2) is the matrix representing the model visibilities formed by the Fourier transform of the underlying brightness matrix at the spatial frequencies probed by the antenna pairs. To solve problem (4.2), [145] proposed to reformulate it using a bi-linear approach by introducing $\mathbf{C}_1 = \mathbf{C}_2 = \mathbf{C}$. The resultant problem is solved using an iterative method based on an ADI algorithm. This method alternates at

each iteration between the estimation of \mathbf{C}_1 and \mathbf{C}_2 , assuming they are independent. Its analogy with the alternating minimization strategy discussed in Section 3.5.1 can be noticed. Particularly for ADI, the update of \mathbf{C}_1 is taken to be the exact minimizer of the least-squares objective function, i.e. $\mathbf{C}_1^* = \operatorname{argmin} \|\mathbf{C}_1 \bar{\mathbf{X}} \mathbf{C}_2^\dagger - \bar{\mathbf{Y}}\|_F^2$, while the update of \mathbf{C}_2 is taken to be exactly equal to \mathbf{C}_1 , i.e. $\mathbf{C}_2^* = \mathbf{C}_1$. Moreover, for n_a number of total antennas, this problem can in turn be split into n_a independent linear least-squares problems, each solving for the respective antenna gain.

This algorithm has been shown to provide lower computational complexity, having quadratic scaling with respect to the number of antennas. The authors also provide the convergence conditions for StEFCal. Nevertheless, it works under the assumption of exact knowledge of the original image or at least when the bright sources of the original image are known. The authors then suggest to combine the StEFCal calibration method with an imaging algorithm in order to estimate more accurately the image once we have an estimation of the DDEs, and to iterate this process. However, this combined DDE calibration and imaging approach does not benefit from the StEFCal convergence guarantees.

Another issue of concern is that this approach is not adapted to DDE calibration that is pivotal to produce sky images at unprecedented resolution with high sensitivity new generation radio interferometers. The incorporation of the DDEs in the calibration process is also essential to produce high quality images without limiting their dynamic ranges [138]. To this end, several DDE calibration techniques have been proposed in the last years, as described below.

4.3.3 DDE calibration

Peeling

This scheme aims to calibrate for the DDEs of the bright sources in a sequential manner [147], i.e. solving a series of calibration problems source by source. The order of peeling of sources within a sequence is governed by decreasing order of the sources' brightness. For each source, the peeling comprises of alternating between the corresponding calibration and imaging steps. In particular, for a considered single

direction in sky, the DDE can in fact be seen as a DIE. Thus, it can be calibrated using conventional selfcal and in simple terms, providing the DDE in the direction of the underlying source. Using the obtained antenna-based phase corrections and the source model, the predicted visibility contribution of this source is subtracted (‘peeled’) from the net measured data. This process is then repeated for the next bright sources.

The peeling technique has been further leveraged by a Source Peeling and Atmospheric Modeling (SPAM) calibration method developed in [137, 148]. This method consists in modelling the ionosphere as a phase screen, whose parameters are estimated by fitting the calibrated phases obtained from peeling with the modelled phases, using the LM algorithm. Subsequently, this model can be used for the prediction of correction phases in any arbitrary desired direction within the field of view. To apply these corrections, SPAM relies on a facet-based imaging approach. For each considered facet, it applies the previously calculated phase correction for the facet centre, defined by a bright source or approximate centre of a cluster of closely located bright sources, to the whole facet.

Faceting

This technique relies on partitioning the sky into a number of facets and applying the DDE calibration solution for the facet centre to the whole facet [15, 149, 150]. In particular, this scheme works under the assumption that the DDEs show smooth variation over the field of view, thereby having (approximately) constant value across a given facet. The DDE calibration is then performed for all the small facets into which the whole sky image is divided. Finally, these corrected facets are stitched together to produce a corrected image of the sky. It is to be noted that such facet-based approaches require specification of the facet centres, which may need to be done manually by the user.

SAGE

Space Alternating Generalized Expectation Maximization (SAGE) calibration technique is an alternative to traditional LM calibration techniques solving for the underlying non-linear least squares problem [16, 139, 151]. It leverages the principle of expectation-maximization algorithm [152], using a different assignment of noise to the complete data. Typically, it considers the target sky to be composed of well separated, discrete sources such that the acquired visibilities can be seen as a linear superposition of the signals from each source. With this idea in mind, at each iteration, the data model is represented by a sum of signals from a chosen set of sources (the so called hidden data space [151]) and the contribution from all other sources. The algorithm then performs two steps: Expectation (E) step - evaluating the expectation value of the hidden data space conditionally to the complete observed data and the current estimate of the calibration parameter vector associated with the chosen set of sources, and the Maximization (M) step - estimating the associated parameter vector by solving a least squares criterion between the previously obtained conditional mean and the predicted model of the hidden data space. Moreover, at each iteration, this strategy is followed for all the sources, updating their corresponding parameter vectors.

[139] have demonstrated the superiority of this algorithm in comparison with the conventional LM algorithm, in terms of accuracy and higher rate of convergence coupled with low computational cost. However, in the scenarios with large number of sources in the observed radio sky, manual inspection of sources' characteristics for partitioning purposes will not be viable. As such, the authors highlighted the importance of designing an automatic way of partitioning to enable usage of SAGE calibration for such datasets. On top of it, regularization schemes need to be investigated to enhance the solution accuracy.

A-projection

While the facet-based approaches solve for the DDEs in their image domain, another approach for calibrating the DDEs arises from their convolutional nature, allowing their estimation in the Fourier domain. More precisely, the multiplication of the DDEs in the image domain can be equivalently seen as their convolution in the Fourier

domain. The A-Projection algorithm [138] makes use of the latter characteristic and offers a way to correct for *known* DDEs whose associated Jones matrix (and in turn, the corresponding Mueller matrix) is approximately unitary, such as antenna power patterns induced calibration errors. Furthermore, the proposed approach relies on the assumption of finite support of the associated Jones matrix in the Fourier domain. In other words, this matrix has appreciable values only in a limited neighbourhood of the origin. From image domain perspective, it can be seen as having Jones matrix with smoothly varying values. Following the limited support and unitarity assumption of the Jones matrix, this can be embedded into the forward and backward operators while performing degriding and gridding steps, respectively. On the one hand, the former step consists in using the interpolation kernels to degrid the FFT computed discrete Fourier coefficients of the underlying model image to the continuous sampled points. It is used in the evaluation of the residual visibilities. On the other hand, the latter step (i.e gridding) works inversely, gridding the continuous (residual) visibilities on a discrete grid to obtain the residual image.

Although this FFT based approach benefits from a computational point of view, its application is limited to the correction of *known* DDEs only.

Pointing selfcal

This algorithm has been developed in [153] to account for the DDEs which are not known beforehand and need to be solved for during the calibration process. In particular, the authors consider the case of antenna pointing errors, modelling them using only few parameters. Combining this model with the *a priori* known primary beam effects results into the net Jones matrix. The A-Projection algorithm is then used to compute the forward model, giving residual visibilities. Finally, a gradient descent step is performed on the squared norm of the residual visibilities to update the antenna pointing error parameters.

To summarize, the RI literature has many calibration techniques, both for DDEs and DDEs. These techniques often rely on a pre-determined known model of sky. In practice, such a model may not always be available. In such a scenario, imaging

procedure needs to be taken into account as well. These algorithms then adopt the basic structure of the selfcal loop, i.e. alternating between the calibration and the imaging cycles, where for the former, they use the corresponding proposed technique, while for the latter, typically CLEAN (or its variants) is used. However, by doing so, the global algorithm fails to have any convergence guarantees.

4.4 Conclusion

In this chapter, I have discussed the standard approaches employed in RI for imaging and calibration purposes. In general, only the imaging procedure needs to be implemented when the calibration errors are assumed to be absent or neglected. In this regard, the recently emerged sparse recovery methods have shown promising performance. While providing comparable (or in many instances, superior) imaging quality as obtained by well-established CLEAN based approaches, these techniques also offer more flexibility, particularly scalability to big data and hence, are suitable for new generation radio interferometers. Nevertheless, all these techniques have been designed primarily for Stokes I imaging. For polarimetric imaging, they can be extended to solve independent problems for each of the Stokes parameters using the same approach. Furthermore, to account for (and estimate) the calibration terms, I have presented an overview of the techniques from RI literature for both DIES and DDEs estimation. In the most general settings, when neither the sky model nor the calibration terms are known, the need for joint calibration and imaging has also been highlighted. In this case, any of the calibration methods can be combined with an imaging modality, both chosen from aforementioned techniques, but at the cost of no global convergence guarantees.

Gathering all the information provided in the chapters so far, I now move onto the contribution phase of this thesis. Particularly, to counteract the shortcomings of the existing methods in RI literature, we propose new ones. To begin with, we consider only imaging problem, and unlike existing Stokes I imaging oriented methods, we develop a polarimetric specific technique using sophisticated priors, and explore its

scalability aspect. It is followed by the consideration of calibration terms in the observation model, for which we design a full polarization joint calibration and imaging technique with convergence guarantees. Finally, we extend these ideas to solve the challenging problem of imaging in optical interferometry (OI), bridging the gap between RI and OI. In this case, noticing the similarity of the underlying inverse problem with the RI calibration problem, we exploit the optimization strategy adopted for RI to propose an OI imaging algorithm.

Chapter 5

Stokes parameters imaging in radio interferometry

Contents

5.1	Motivation	68
5.2	Adopted measurement model	69
5.3	Polarized SARA - Proposed imaging approach	72
5.3.1	Epigraphical projection	74
5.3.2	Algorithm formulation	77
5.3.3	Polarization constraint for TV based problems	84
5.4	Simulations and Results	87
5.4.1	Computational complexity	89
5.4.2	Effect of polarization constraint	90
5.4.3	Comparisons performed	91
5.4.4	Simulation settings	93
5.4.5	Results and discussion	94
5.5	Generalization to real data	104
5.6	Results on real data	106
5.7	Conclusion	107

This chapter has been adapted from the published works [25] and [26].

5.1 Motivation

Previously discussed standard RI imaging techniques when applied for polarimetric imaging, solve independently for each of the Stokes parameters. In practice, the Stokes parameters are not completely independent but rather constrained by a physical non-linear relation imposing the polarized intensity to be a lower bound on the total intensity: $\sqrt{Q^2 + U^2 + V^2} \leq I$. This constraint, referred to as the polarization constraint, can also be seen as a generalization of the simpler positivity constraint on the total intensity image in the context of unpolarized imaging. Nevertheless, none of the state-of-the-art sparse recovery methods described in previous chapter (including CLEAN and its variants) take this constraint explicitly into account, thus resulting in possibly non-physical image reconstructions. One way to impose this constraint is by employing the strategy of the change of variables. It consists in expressing the polarimetric images in terms of their fractional polarization and position angle, and solving directly for these variables [125]. However, adopting this approach amounts to solving non-convex optimization problem, which may not benefit from convergence guarantees to global minimum.

The work described in this chapter is motivated by the need for the development of a polarimetric imaging specific method, that can not only incorporate sophisticated priors (such as the polarization constraint) in the minimization problem but also benefits from well-established convergence guarantees. To achieve this, we leverage the flexibility offered by the powerful convex optimization framework and propose a new sparse recovery method for joint estimation of Stokes images in RI. Our contribution is threefold. First, within the proposed sparse modelling framework, the novelty of our method lies in taking into account the polarization constraint explicitly in the image reconstruction process, solving for a convex optimization problem. Second, we generalize to polarimetric imaging the SARA approach introduced for Stokes I imaging in [24, 154]. The resultant approach, referred to as Polarized SARA, promotes average sparsity of each of the Stokes images I , Q , U and V . To solve the corresponding image reconstruction problem, we develop an iterative algorithm based on a primal-dual method [90, 100, 101, 155]. Third, motivated by the huge amounts of data provided

by the new generation radio interferometers, we work on the scalability aspect of the underlying imaging algorithm. This involves introducing the distribution and parallelization scheme within the proposed approach, that further leverages an acceleration strategy [9, 14]. When it comes to dealing with real data, our method also benefits from an adaptive scheme to estimate the unknown noise bound parameters [11].

Starting with the RI imaging model, I present in detail the proposed scalable, full polarization imaging approach in this chapter. This is followed by its performance analysis on simulated and real data. Finally, I give the concluding remarks for the work described in this chapter.

5.2 Adopted measurement model

In the case of performing only image recovery, a reformulation of equation (2.19) is often preferred wherein the visibility matrix containing the measurements made by an antenna pair (α, β) at time instant t is represented by a vector $\mathbf{y}_{t,\alpha,\beta} \in \mathbb{C}^4$. Each element $p \in \{1, \dots, 4\}$ of the visibility vector \mathbf{y} is given by

$$[y_{t,\alpha,\beta}]_p = \sum_{q=1}^4 \sum_{n=-N/2}^{N/2-1} [\overline{\mathbf{M}}_{t,\alpha,\beta}(n)]_{pq} [\tilde{\mathcal{L}}(\overline{\mathbf{S}}(n))]_q e^{-i2\pi(k_{t,\alpha,\beta})\frac{n}{N}} + [\omega_{t,\alpha,\beta}]_p, \quad (5.1)$$

where $\omega_{t,\alpha,\beta} \in \mathbb{C}^4$ is a realization of an additive Gaussian noise, and $\tilde{\mathcal{L}}(\overline{\mathbf{S}}(n))$ operates on the Stokes matrix to produce the brightness matrix $\overline{\mathbf{B}}(n)$, followed by its vectorization. Furthermore, $\overline{\mathbf{M}}_{t,\alpha,\beta} = (\overline{\mathbf{D}}_{t,\alpha} \otimes \overline{\mathbf{D}}_{t,\beta}^\dagger) \in \mathbb{C}^{4 \times 4N}$ is the Mueller matrix formed by the outer product of the Jones matrices for antennas α and β at time instant t , and in turn, this matrix can be seen as a 4×4 block matrix with each block given by an N -dimensional row vector. Let us note that, for the Fourier transformed Mueller matrix, denoted by $\widehat{\overline{\mathbf{M}}}_{t,\alpha,\beta}$, each block can be seen as obtained by the complex convolution of the Fourier transforms of the corresponding Jones matrices [156].

In line with equation (5.1), the overall measurement model can be written as

$$\mathbf{y} = \check{\Phi}(\overline{\mathbf{S}}) + \omega, \quad (5.2)$$

where $\mathbf{y} \in \mathbb{C}^{4M}$ is the resultant visibility vector corrupted by the noise vector $\boldsymbol{\omega} \in \mathbb{C}^{4M}$. The measurement operator $\check{\Phi}$ mapping the images of interest to the acquired visibilities is modelled as

$$\check{\Phi}(\bar{\mathbf{S}}) = \boldsymbol{\Theta} \cdot \mathbf{G} \mathbf{F} \tilde{\mathbf{Z}} \tilde{\mathcal{L}}(\bar{\mathbf{S}}), \quad (5.3)$$

with \cdot denoting the Hadamard product. The operation $\tilde{\mathcal{L}}(\bar{\mathbf{S}})$ generates the brightness vector $\mathbf{b} \in \mathbb{C}^{4N}$ that needs to be Fourier transformed at the sampled spatial frequencies. To evaluate these Fourier transforms in a computationally efficient manner, we make use of the non-uniform fast Fourier Transform that relies on interpolating the Fourier coefficients from discrete to continuous domain [157]. In this context, first, the zero-padding matrix $\tilde{\mathbf{Z}} \in \mathbb{C}^{\kappa 4N \times 4N}$ oversamples the images in \mathbf{b} , by a factor κ in each dimension achieving a finer grid, and accounts for the scale factors to pre-compensate for the interpolation convolution kernels. A fast Fourier transform operator $\mathbf{F} \in \mathbb{C}^{\kappa 4N \times \kappa 4N}$ is then applied to compute the 2D Fourier transform of each of these oversampled images. To interpolate these discrete Fourier coefficients to the continuous frequency points, compact support convolution kernels (the so called de-gridding kernels) are embedded in the matrix $\mathbf{G} \in \mathbb{C}^{4M \times \kappa 4N}$. More precisely, the matrix \mathbf{G} is modelled to take into account the de-gridding kernels as well as the components of the Fourier transformed Mueller matrix. In particular, each of the four rows of \mathbf{G} associated with a frequency $k_{t,\alpha,\beta}$ contains the convolution of the de-gridding kernel with the corresponding elements of $\widehat{\mathbf{M}}_{t,\alpha,\beta}$ centred on $k_{t,\alpha,\beta}$. The application of this matrix on the Fourier transformed over-sampled images produce the measurements. As a matter of fact, the measurement operator in equation (5.3) bears a direct correspondence with the measurement operator used for Stokes I imaging [10, 14], that can be seen as a particular case of the considered full polarization imaging setting. Furthermore, the noise statistics are incorporated via the matrix $\boldsymbol{\Theta} \in \mathbb{R}^{4M}$. Its elements are the inverse of the square root of the noise variances corresponding to the respective measurements in the associated measurement vector. Thus, the measurements \mathbf{y} are considered as the result of the Hadamard product between $\boldsymbol{\Theta}$ and the unweighted measurements from the radio interferometer.

For notational convenience, we define $\Phi' = \mathcal{M} \circ \check{\Phi} \circ \mathcal{R}^\dagger$, i.e. $\Phi'(\cdot) = \mathcal{M}(\check{\Phi}(\mathcal{R}^\dagger(\cdot)))$

$$\mathbf{Y}' = \begin{bmatrix} \mathbf{Y}'_1 \\ \vdots \\ \mathbf{Y}'_{n_d} \end{bmatrix} \quad \mathbf{\Omega}' = \begin{bmatrix} \mathbf{\Omega}'_1 \\ \vdots \\ \mathbf{\Omega}'_{n_d} \end{bmatrix}$$

$$\Phi'(\tilde{\mathbf{S}}) = \begin{bmatrix} \Phi'_1(\tilde{\mathbf{S}}) \\ \vdots \\ \Phi'_{n_d}(\tilde{\mathbf{S}}) \end{bmatrix} = \begin{bmatrix} \mathcal{M}_1 \\ \vdots \\ \mathcal{M}_{n_d} \end{bmatrix} \left(\begin{bmatrix} \mathbf{\Theta}_1 \\ \vdots \\ \mathbf{\Theta}_{n_d} \end{bmatrix} \cdot \begin{bmatrix} \mathbf{G}_1 \\ \vdots \\ \mathbf{G}_{n_d} \end{bmatrix} \mathbf{F} \tilde{\mathbf{Z}} \tilde{\mathcal{L}}(\mathcal{R}^\dagger(\tilde{\mathbf{S}})) \right)$$

FIGURE 5.1: Illustration of the adopted block-data splitting technique for the measurement model.

where the operator $\mathcal{M} : \mathbb{C}^{4M} \rightarrow \mathbb{C}^{4 \times M}$ reshapes a \mathbb{C}^{4M} vector into a $\mathbb{C}^{4 \times M}$ matrix. Regarding \mathcal{R} , let us recall $\tilde{\mathbf{S}} = \mathcal{R}(\mathbf{S})$ with operator \mathcal{R} consisting in placing the four Stokes images within the matrix \mathbf{S} in four columns to give $\tilde{\mathbf{S}} \in \mathbb{R}^{N \times 4}$. Employing this notation, we use $\tilde{\mathbf{S}}$ instead of \mathbf{S} to describe the Stokes matrix in the rest of this chapter, and inverse problem (5.2) can then be rewritten as

$$\mathbf{Y}' = \Phi'(\tilde{\mathbf{S}}) + \mathbf{\Omega}'. \quad (5.4)$$

Here, each column, associated with a sampled spatial frequency $k_{t,\alpha,\beta}$, of the measurement matrix $\mathbf{Y}' \in \mathbb{C}^{4 \times M}$ contains the visibilities acquired at that frequency, and $\mathbf{\Omega}'$ denotes the corresponding additive noise matrix.

Moreover, to achieve the scalability capability for large dimensional problems, we adopt a block-data splitting technique [9]. It corresponds to decomposing the measurements (5.4) into n_d blocks, such that $\mathbf{Y}' = (\mathbf{Y}'_j)_{1 \leq j \leq n_d}$, where, for every $j \in \{1, \dots, n_d\}$, $\mathbf{Y}'_j \in \mathbb{C}^{4 \times M_j}$ is given by

$$\mathbf{Y}'_j = \Phi'_j(\tilde{\mathbf{S}}) + \mathbf{\Omega}'_j. \quad (5.5)$$

Here, $\mathbf{\Omega}'_j$ corresponds to the j^{th} block of the additive noise matrix $\mathbf{\Omega}'$, and the measurement operator Φ'_j is given by $\Phi'_j(\tilde{\mathbf{S}}) = \mathcal{M}_j(\mathbf{\Theta}_j \cdot \mathbf{G}_j \mathbf{F} \tilde{\mathbf{Z}} \tilde{\mathcal{L}}(\mathcal{R}^\dagger(\tilde{\mathbf{S}})))$, $\mathbf{\Theta}_j$ and \mathbf{G}_j being the j^{th} block matrices of $\mathbf{\Theta}$ and \mathbf{G} , respectively. \mathcal{M}_j is the operator reshaping the $4M_j$ vector into a $4 \times M_j$ matrix. For ease of understanding, this strategy is also depicted in Figure 5.1.

5.3 Polarized SARA - Proposed imaging approach

Objective function for polarimetric imaging

The estimation of the Stokes images from the degraded measurements consists in solving inverse problem (5.5). Given its ill-posedness and as explained in Chapter 3, the problem needs to be regularized by injecting *a priori* information in the reconstruction process. We thus aim to solve a minimization problem consisting of a data fidelity and a regularization term, described as follows.

Leveraging the block-data splitting of the observation model, we propose to enforce the data fidelity term in a distributed manner [9]. It consists in constraining the residual blocks $\mathbf{Y}'_j - \Phi'_j(\tilde{\mathbf{S}})$ to belong to the ℓ_2 ball centered on $\mathbf{0}$ with radius $\epsilon_j > 0$, by choosing

$$f(\Phi'(\tilde{\mathbf{S}})) = \sum_{j=1}^{n_d} f_j(\Phi'_j(\tilde{\mathbf{S}})) \quad \text{with} \quad f_j(\Phi'_j(\tilde{\mathbf{S}})) = \iota_{\mathbb{B}_j(\mathbf{Y}'_j, \epsilon_j)}(\Phi'_j(\tilde{\mathbf{S}})), \quad (5.6)$$

where, for every $j \in \{1, \dots, n_d\}$, $\mathbb{B}_j(\mathbf{Y}'_j, \epsilon_j) = \{\mathbf{B} \in \mathbb{C}^{4 \times M_j} : \|\mathbf{B} - \mathbf{Y}'_j\|_F \leq \epsilon_j\}$ is the ℓ_2 ball centred on \mathbf{Y}'_j with radius ϵ_j chosen according to the theoretical noise level.

Concerning the regularization term, we propose to define it as a sum of several functions accounting for the following prior information.

Real-valuedness. The Stokes images should be real-valued. This condition can be enforced by the use of an indicator function of a set $\mathbb{U} = \mathbb{R}^{N \times 4}$.

Sparsity regularization. Leveraging the CS theory, we promote sparsity of the Stokes images in a sparsifying dictionary Ψ . In this context, as discussed in Section 3.3.1, adopting the reweighting scheme that consists in iteratively solving the weighted ℓ_1 minimization problems provides a better estimation of the sought images in ℓ_0 sense as compared to the ℓ_1 norm. Therefore, we propose to use the weighted ℓ_1 norm as the sparsifying regularization term. A remark to be made here is that any linear sparsifying operator could be used in the proposed method. However, inspired

by the sparsity averaging proposed in [24, 154] for Stokes I imaging, we extend it to polarimetric imaging and choose to promote sparsity averaging for each of the Stokes parameter maps I , Q , U and V . It consists in choosing Ψ as the concatenation of the first eight Daubechies wavelets and Dirac basis (see e.g. [9, 70]). Using this dictionary coupled with the reweighting scheme corresponds to the SARA regularization.

Furthermore, to exploit parallelization capabilities, we propose to split the corresponding weighted ℓ_1 term as a sum over the different bases involved as well as over the different Stokes images, i.e.

$$g(\Psi^\dagger \tilde{\mathbf{S}}) = \|\Psi^\dagger \tilde{\mathbf{S}}\|_{\mathbf{w},1} = \sum_{l=1}^{n_b} g_l(\Psi_l^\dagger \tilde{\mathbf{S}}) \quad (5.7)$$

where $g_l(\Psi_l^\dagger \tilde{\mathbf{S}}) = \sum_{i=1}^4 \|[\mathbf{W}_l]_{:,i} \Psi_l^\dagger \tilde{\mathbf{S}}_{:,i}\|_1$. For each $l \in \{1, \dots, n_b\}$, $\Psi_l^\dagger \in \mathbb{R}^{J \times N}$ and $\mathbf{W}_l \in \mathbb{R}_+^{J \times 4}$ is the weighting matrix (as per the weights defined in equation (3.13)). For the chosen SARA regularization, $n_b = 9$.

It is to be emphasized here that unlike the case of ℓ_1 norm, usage of the weighted ℓ_1 norm also offers the advantage of no tuning of regularization parameters. More precisely, since Stokes Q , U and V images are lower in intensity than Stokes I , the latter dominates in the ℓ_1 norm term. To overcome this unequal contribution of the Stokes images, different regularization parameters need to be chosen for each image. On the contrary, thanks to the weights in (5.7), all the Stokes images are normalized, thereby having equal importance in this sparsity term, avoiding the need to use any additional parameters to enhance the contribution of the Stokes Q , U and V images.

Polarization constraint. One of the key contributions of the work carried out here is to exploit the physical relation between the Stokes images by enforcing the polarization constraint in the reconstruction process. Formally, this constraint can be defined by the following set:

$$\mathbb{P} = \left\{ \tilde{\mathbf{S}} \in \mathbb{R}^{N \times 4} \mid (\forall n \in \{1, \dots, N\}) -\tilde{\mathbf{S}}_{n,1} + \|\tilde{\mathbf{S}}_{n,2:4}\|_2 \leq 0 \right\}, \quad (5.8)$$

where, for every $n \in \{1, \dots, N\}$, $\tilde{\mathbf{S}}_{n,1}$ denotes the n^{th} coefficient of the first column of the matrix $\tilde{\mathbf{S}}$, and the notation $\tilde{\mathbf{S}}_{n,2:4}$ signifies the n^{th} coefficients of the columns 2 to 4 of the matrix $\tilde{\mathbf{S}}$. Imposing the polarization constraint then amounts to using an indicator function of the set \mathbb{P} . It can be noticed that this constraint also implicitly enforces the positivity of the total intensity image (Stokes I).

With the above mentioned prior information at hand, the resulting minimization problem to be solved for the Stokes images is given by

$$\underset{\tilde{\mathbf{S}}}{\text{minimize}} \quad f(\Phi'(\tilde{\mathbf{S}})) + \iota_{\mathbb{U}}(\tilde{\mathbf{S}}) + g(\Psi^\dagger \tilde{\mathbf{S}}) + \iota_{\mathbb{P}}(\tilde{\mathbf{S}}). \quad (5.9)$$

It can be observed that enforcing the polarization constraint in problem (5.9) involves projecting the variable $\tilde{\mathbf{S}}$ onto the set \mathbb{P} . However, the associated projection does not have a closed form. To impose this constraint, we propose to employ a splitting technique based on epigraphical projection that is described in detail in the next section.

Remark: In the case when the polarization constraint is not taken into account, the positivity of the total intensity image is no longer ensured and it needs to be imposed explicitly. This can be done by modifying the set \mathbb{U} to a set \mathbb{U}' given by

$$\mathbb{U}' = \left\{ \tilde{\mathbf{S}} \in \mathbb{R}^{N \times 4} \mid \tilde{\mathbf{S}}_{:,1} \in \mathbb{R}_+^N, \tilde{\mathbf{S}}_{:,2:4} \in \mathbb{R}^{N \times 3} \right\}. \quad (5.10)$$

In such a case, problem (5.9) simplifies to

$$\underset{\tilde{\mathbf{S}}}{\text{minimize}} \quad f(\Phi'(\tilde{\mathbf{S}})) + \iota_{\mathbb{U}'}(\tilde{\mathbf{S}}) + g(\Psi^\dagger \tilde{\mathbf{S}}). \quad (5.11)$$

5.3.1 Epigraphical projection

The requirement to satisfy the polarization constraint is that the Stokes matrix belongs to the set \mathbb{P} . In order to enforce this constraint, we utilize the epigraphical projection techniques developed by [158]. The epigraphical projection is a recently

proposed technique used to handle minimization problems involving sophisticated constraints (see e.g. [159–162]). Leveraging these techniques, we propose to introduce an auxiliary variable $\mathbf{Z} \in \mathbb{R}^{N \times 2}$ in the minimization problem (5.9). The polarization constraint set can then be split into simpler constraint sets, such that the projection onto these sets can be efficiently computed. Doing so, problem (5.9) can be equivalently rewritten as

$$\underset{\tilde{\mathbf{S}}, \mathbf{Z}}{\text{minimize}} f(\Phi'(\tilde{\mathbf{S}})) + \iota_{\mathbb{U}}(\tilde{\mathbf{S}}) + g(\Psi^\dagger \tilde{\mathbf{S}}) \quad (5.12)$$

subject to $(\forall n \in \{1, \dots, N\})$

$$\begin{cases} h_1(\tilde{\mathbf{S}}_{n,1}) \leq Z_{n,1}, & (5.12a) \\ h_2(\tilde{\mathbf{S}}_{n,2:4}) \leq Z_{n,2}, & (5.12b) \\ Z_{n,1} + Z_{n,2} \leq 0, & (5.12c) \end{cases}$$

where the functions h_1 and h_2 are defined as

$$(\forall \zeta \in \mathbb{R}) \quad h_1(\zeta) = -\zeta, \quad (5.13)$$

$$(\forall \zeta \in \mathbb{R}^3) \quad h_2(\zeta) = \|\zeta\|_2. \quad (5.14)$$

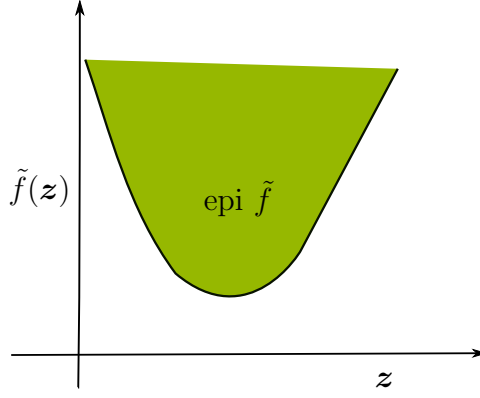
To understand this modified minimization problem, one can observe that the polarization constraint set \mathbb{P} , defined in equation (5.8), can be rewritten as

$$\mathbb{P} = \left\{ \tilde{\mathbf{S}} \in \mathbb{R}^{N \times 4} \mid (\forall n \in \{1, \dots, N\}) \ h_1(\tilde{\mathbf{S}}_{n,1}) + h_2(\tilde{\mathbf{S}}_{n,2:4}) \leq 0 \right\}. \quad (5.15)$$

Therefore, the Stokes matrix $\tilde{\mathbf{S}}$ satisfying the constraint defined by set \mathbb{P} is equivalent to have the variables $(\tilde{\mathbf{S}}, \mathbf{Z})$ satisfying the constraints defined by equations (5.12a) - (5.12c).

In order to simplify the notation of the minimization problem (5.12), we need to introduce the definition of the epigraph of a proper, lower semi-continuous function $\tilde{f}: \mathbb{R}^N \rightarrow]-\infty, +\infty]$. As illustrated in Figure 5.2, it corresponds to the set of points lying on or above the graph of \tilde{f} , and formally, it is given by [163]

$$\text{epi } \tilde{f} = \left\{ (\mathbf{z}, v) \in \mathbb{R}^N \times \mathbb{R} \mid \tilde{f}(\mathbf{z}) \leq v \right\}. \quad (5.16)$$


 FIGURE 5.2: Diagram depicting epigraph of a function \tilde{f} .

Using this definition, conditions (5.12a) and (5.12b) respectively represent the epigraph of the functions h_1 and h_2 . More precisely, condition (5.12a) implies that for every $n \in \{1, \dots, N\}$, $(\tilde{\mathbf{S}}_{n,1}, \mathbf{Z}_{n,1}) \in \text{epi } h_1$. For a compact notation, we define $\mathbb{E}_1 = (\text{epi } h_1)^N$ to be the product space such that

$$(\tilde{\mathbf{S}}_{:,1}, \mathbf{Z}_{:,1}) \in \mathbb{E}_1 \Leftrightarrow (\forall n \in \{1, \dots, N\}) (\tilde{\mathbf{S}}_{n,1}, \mathbf{Z}_{n,1}) \in \text{epi } h_1. \quad (5.17)$$

Similarly, defining $\mathbb{E}_2 = (\text{epi } h_2)^N$, condition (5.12b) is equivalent to

$$(\tilde{\mathbf{S}}_{:,2:4}, \mathbf{Z}_{:,2}) \in \mathbb{E}_2 \Leftrightarrow (\forall n \in \{1, \dots, N\}) (\tilde{\mathbf{S}}_{n,2:4}, \mathbf{Z}_{n,2}) \in \text{epi } h_2. \quad (5.18)$$

Thus, the constraints (5.12a) and (5.12b) can be imposed as $\iota_{\mathbb{E}_1}(\tilde{\mathbf{S}}_{:,1}, \mathbf{Z}_{:,1})$ and $\iota_{\mathbb{E}_2}(\tilde{\mathbf{S}}_{:,2:4}, \mathbf{Z}_{:,2})$, respectively. Furthermore, to impose condition (5.12c), we introduce

$$\mathbb{V} = \{ \mathbf{Z} \in \mathbb{R}^{N \times 2} \mid (\forall n \in \{1, \dots, N\}) Z_{n,1} + Z_{n,2} \leq 0 \}. \quad (5.19)$$

Then, condition (5.12c) can be represented as an indicator function of the set \mathbb{V} . Finally, imposing the constraints (5.12a) - (5.12c) using their respective indicator functions leads to the following minimization problem

$$\underset{\tilde{\mathbf{S}}, \mathbf{Z}}{\text{minimize}} \quad f(\Phi'(\tilde{\mathbf{S}})) + \iota_{\mathbb{U}}(\tilde{\mathbf{S}}) + \gamma g(\Psi^\dagger \tilde{\mathbf{S}}) + \iota_{\mathbb{V}}(\mathbf{Z}) + \iota_{\mathbb{E}_1}(\tilde{\mathbf{S}}_{:,1}, \mathbf{Z}_{:,1}) + \iota_{\mathbb{E}_2}(\tilde{\mathbf{S}}_{:,2:4}, \mathbf{Z}_{:,2}), \quad (5.20)$$

where $\gamma > 0$ is a free parameter only affecting the convergence speed.

It is to be noted that the minimization problem (5.20) considers the SARA regularization and imposes the polarization constraint explicitly. We refer to this proposed method of joint Stokes imaging as Polarized SARA. In the same line of thought, solving the problem of Stokes imaging with SARA regularization but without polarization constraint, i.e. problem (5.11), is termed as Polarized SARA without constraint.

5.3.2 Algorithm formulation

In order to solve the resultant problem (5.20), we develop a method based on a primal-dual forward-backward algorithm, which offers a highly flexible and parallelizable structure [100, 101, 155]. The proposed algorithm is given in Algorithm 1. As per discussion in Chapter 3, primal-dual methods consist in solving jointly the primal and the dual problems. In our case, the primal problem to be solved is given in (5.20). This problem can be written in a compact form as follows

$$\begin{aligned} & \underset{\substack{\tilde{\mathbf{S}} \in \mathbb{R}^{N \times 4}, \\ \mathbf{Z} \in \mathbb{R}^{N \times 2}}}{\text{minimize}} \quad q(\tilde{\mathbf{S}}, \mathbf{Z}) + \gamma g(\Psi^\dagger \tilde{\mathbf{S}}) + f(\Phi'(\tilde{\mathbf{S}})) + p(\tilde{\mathbf{S}}, \mathbf{Z}), \end{aligned} \quad (5.21)$$

where,

$$\begin{aligned} q(\tilde{\mathbf{S}}, \mathbf{Z}) &= \iota_{\mathbb{U}}(\tilde{\mathbf{S}}) + \iota_{\mathbb{V}}(\mathbf{Z}), \\ p(\tilde{\mathbf{S}}, \mathbf{Z}) &= \iota_{\mathbb{E}_1}(\tilde{\mathbf{S}}_{:,1}, \mathbf{Z}_{:,1}) + \iota_{\mathbb{E}_2}(\tilde{\mathbf{S}}_{:,2:4}, \mathbf{Z}_{:,2}). \end{aligned}$$

Then, according to the optimization background provided in section (3.4.2) (see e.g. [91] for further detail), the dual problem associated with (5.21) is given by

$$\begin{aligned} & \underset{\substack{\mathbf{A}_l \in \mathbb{R}^{J \times 4}, \mathbf{B}_j \in \mathbb{C}^{4 \times M_j}, \\ \mathbf{C} \in \mathbb{R}^{N \times 4}, \mathbf{D} \in \mathbb{R}^{N \times 2}}}{\text{minimize}} \quad q^* \left(-\sum_{l=1}^{n_b} \Psi_l \mathbf{A}_l - \sum_{j=1}^{n_d} \Phi_j'^\dagger(\mathbf{B}_j) - \mathbf{C}, -\mathbf{D} \right) + \gamma \sum_{l=1}^{n_b} g_l^*(\mathbf{A}_l / \gamma) \\ & \quad + \sum_{j=1}^{n_d} f_j^*(\mathbf{B}_j) + p^*(\mathbf{C}, \mathbf{D}). \end{aligned} \quad (5.22)$$

In problem (5.22), for every $l \in \{1, \dots, n_b\}$, $\mathbf{A}_l \in \mathbb{R}^{J \times 4}$ is the dual variable corresponding to the l^{th} sparsifying basis in the non-smooth ℓ_1 term (the function g_l in equation (5.7)), and for every $j \in \{1, \dots, n_d\}$, $\mathbf{B}_j \in \mathbb{C}^{4 \times M_j}$ is the dual variable associated with the j^{th} data-block in the data fidelity term (the function f_j in equation (5.6)).

On the other hand, $\mathbf{C} \in \mathbb{R}^{N \times 4}$ and $\mathbf{D} \in \mathbb{R}^{N \times 2}$ are the dual variables associated with the indicator functions of the epigraphs of h_1 and h_2 in problem (5.20).

Using this primal-dual formulation, Algorithm 1 solves alternately for the primal and dual problems. In this regard, the algorithm can be seen as consisting of two major steps, denoted by: Primal updates and Dual updates. At each iteration $k \in \mathbb{N}$, it involves updating the primal variables $\tilde{\mathbf{S}}$ and \mathbf{Z} , followed by the update of the dual variables $\mathbf{A}, \mathbf{B}, \mathbf{C}$ and \mathbf{D} , as detailed in the following.

Primal updates

In Algorithm 1, the primal variables are updated using steps 3 and 5. These updates have a structure reminiscent of the FB steps. Let us recall that FB step consists of alternating between a gradient step and a proximity (or projection) step, whereas in the absence of any smooth term, only the proximity step is performed. This structure can be observed in the update of $\tilde{\mathbf{S}}$ (i.e. step 3), where a projection onto the set \mathbb{U} is carried out. For any matrix \mathbf{X} of size $N \times 4$, this projection onto the set \mathbb{U} is simply given by

$$\mathcal{P}_{\mathbb{U}}(\mathbf{X}) = \text{Re}(\mathbf{X}), \quad (5.23)$$

where the operator $\text{Re}(\cdot)$ provides the real part of its argument. One can notice that an additive term appears in this update step 3, that allows the dual variables to be taken into account. The same analogy can be made for the update step 5 of the variable \mathbf{Z} . This update takes into account the dual variable \mathbf{D} associated with the epigraphical constraints, followed by a projection onto the set \mathbb{V} . Using Proposition 2.1 from [158], the projection onto the set \mathbb{V} is performed as

$$(\forall \mathbf{U} \in \mathbb{R}^{N \times 2}) \quad \mathcal{P}_{\mathbb{V}}(\mathbf{U}) = \tilde{\mathbf{U}}, \quad (5.24)$$

where $\tilde{\mathbf{U}} \in \mathbb{R}^{N \times 2}$ is defined such that, for every $n \in \{1, \dots, N\}$,

$$(\tilde{U}_{n,1}, \tilde{U}_{n,2}) = \begin{cases} (U_{n,1}, U_{n,2}), & \text{if } U_{n,1} + U_{n,2} \leq 0, \\ \frac{1}{2}(U_{n,1} - U_{n,2}, U_{n,2} - U_{n,1}), & \text{otherwise.} \end{cases} \quad (5.25)$$

Algorithm 1 Joint Stokes imaging algorithm - Polarized SARA

1: **given** $\tilde{\mathbf{S}}^{(0)} \in \mathbb{R}^{N \times 4}$, $\mathbf{Z}^{(0)} \in \mathbb{R}^{N \times 2}$, $(\forall l \in \{1, \dots, n_b\}) \mathbf{A}_l^{(0)} \in \mathbb{R}^{J \times 4}$, $\tilde{\mathbf{A}}_l^{(0)} = \Psi_l \mathbf{A}_l^{(0)}$, $\Lambda_l = \gamma \mathbf{W}_l \in \mathbb{R}_+^{J \times 4}$, $(\forall j \in \{1, \dots, n_d\}) \mathbf{B}_j^{(0)} \in \mathbb{C}^{4 \times M_j}$, $\mathbf{Q}_j \in \mathbb{R}_+^{4M_j \times 4M_j}$, $\epsilon_j^{(0)} \in \mathbb{R}_+$, $t_j^{(0)} \in \mathbb{R}_+$, $\tilde{\mathbf{b}}_j^{(0)} = \mathbf{G}_j^\dagger (\Theta_j^\dagger \cdot \mathcal{M}_j^\dagger (\mathbf{B}_j^{(0)}))$, $\mathbf{C}^{(0)} \in \mathbb{R}^{N \times 4}$, $\mathbf{D}^{(0)} \in \mathbb{R}^{N \times 2}$.

2: **For** $k = 0, 1, \dots$

Primal updates

$$3: \quad \tilde{\mathbf{S}}^{(k+1)} = \mathcal{P}_{\mathbb{U}} \left(\tilde{\mathbf{S}}^{(k)} - \tau \left(\rho_1 \sum_{l=1}^{n_b} \tilde{\mathbf{A}}_l^{(k)} + \rho_2 \mathcal{R} \left(\tilde{\mathcal{L}}^\dagger (\tilde{\mathbf{Z}}^\dagger \mathbf{F}^\dagger \sum_{j=1}^{n_d} \tilde{\mathbf{b}}_j^{(k)}) \right) + \rho_3 \mathbf{C}^{(k)} \right) \right)$$

$$4: \quad \check{\mathbf{S}}^{(k+1)} = 2\tilde{\mathbf{S}}^{(k+1)} - \tilde{\mathbf{S}}^{(k)}$$

$$5: \quad \mathbf{Z}^{(k+1)} = \mathcal{P}_{\mathbb{V}} \left(\mathbf{Z}^{(k)} - \tau \rho_3 \mathbf{D}^{(k)} \right)$$

$$6: \quad \check{\mathbf{Z}}^{(k+1)} = 2\mathbf{Z}^{(k+1)} - \mathbf{Z}^{(k)}$$

$$7: \quad \mathbf{R}^{(k+1)} = \mathbf{F} \tilde{\mathbf{Z}} \tilde{\mathcal{L}} (\mathcal{R}^\dagger (\check{\mathbf{S}}^{(k+1)}))$$

Dual updates

Promoting sparsity:

8: **for** $l \in \{1, \dots, n_b\}$ and $\forall i \in \{1, 2, 3, 4\}$ **do in parallel**

$$9: \quad [\mathbf{A}_l^{(k+1)}]_{:,i} = \left(\mathbf{1}_J - \mathcal{T}_{[\Lambda_l]_{:,i}} \right) \left([\mathbf{A}_l^{(k)}]_{:,i} + \Psi_l^\dagger \check{\mathbf{S}}_{:,i}^{(k+1)} \right)$$

$$10: \quad [\tilde{\mathbf{A}}_l^{(k+1)}]_{:,i} = \Psi_l [\mathbf{A}_l^{(k+1)}]_{:,i}$$

11: **end for**

Enforcing data constraint:

12: **for** $j \in \{1, \dots, n_d\}$ **do in parallel**

$$13: \quad \bar{\mathbf{b}}_j^{(k)} = \mathcal{M}_j^\dagger (\mathbf{B}_j^{(k)}) + \mathbf{Q}_j \Theta_j \cdot \mathbf{G}_j (\mathbf{R}^{(k+1)})$$

$$14: \quad \mathbf{B}_j^{(k+1)} = \mathcal{M}_j \left(\bar{\mathbf{b}}_j^{(k)} - \mathbf{Q}_j^{1/2} \mathcal{P}_{\mathbb{L}_j(\mathbf{Y}_j, \epsilon_j^{(k)})} \left(\mathbf{Q}_j^{-1/2} \bar{\mathbf{b}}_j^{(k)} \right) \right)$$

$$15: \quad \tilde{\mathbf{b}}_j^{(k+1)} = \mathbf{G}_j^\dagger \left(\Theta_j^\dagger \cdot \mathcal{M}_j^\dagger (\mathbf{B}_j^{(k+1)}) \right)$$

16: **Update** ℓ_2 bound $\epsilon_j^{(k)}$ \triangleright Skip this step if $\epsilon_j^{(k)}$ is known; take $\epsilon_j^{(k+1)} = \epsilon_j^{(0)}$

17: **end for**

Enforcing polarization constraint:

$$18: \quad \begin{bmatrix} \mathbf{C}_{:,1}^{(k+1)} \\ \mathbf{D}_{:,1}^{(k+1)} \end{bmatrix} = \begin{bmatrix} \mathbf{C}_{:,1}^{(k)} + \check{\mathbf{S}}_{:,1}^{(k+1)} \\ \mathbf{D}_{:,1}^{(k)} + \check{\mathbf{Z}}_{:,1}^{(k+1)} \end{bmatrix} - \mathcal{P}_{\mathbb{E}_1} \left(\begin{bmatrix} \mathbf{C}_{:,1}^{(k)} + \check{\mathbf{S}}_{:,1}^{(k+1)} \\ \mathbf{D}_{:,1}^{(k)} + \check{\mathbf{Z}}_{:,1}^{(k+1)} \end{bmatrix} \right)$$

$$19: \quad \begin{bmatrix} \mathbf{C}_{:,2:4}^{(k+1)} \\ \mathbf{D}_{:,2}^{(k+1)} \end{bmatrix} = \begin{bmatrix} \mathbf{C}_{:,2:4}^{(k)} + \check{\mathbf{S}}_{:,2:4}^{(k+1)} \\ \mathbf{D}_{:,2}^{(k)} + \check{\mathbf{Z}}_{:,2}^{(k+1)} \end{bmatrix} - \mathcal{P}_{\mathbb{E}_2} \left(\begin{bmatrix} \mathbf{C}_{:,2:4}^{(k)} + \check{\mathbf{S}}_{:,2:4}^{(k+1)} \\ \mathbf{D}_{:,2}^{(k)} + \check{\mathbf{Z}}_{:,2}^{(k+1)} \end{bmatrix} \right)$$

20: **end For**

Dual updates

The dual variables are updated in steps 8 - 19 of Algorithm 1. At each iteration k , it requires the evaluation of the proximity operators of the associated functions.

Sparsity prior. Step 9 consists in updating the dual variable \mathbf{A} associated with the sparsity prior defined in equation (5.7). It requires computation of the proximity operator of the ℓ_1 norm corresponding to the soft-thresholding operation [93]. It is performed by the soft-thresholding operator \mathcal{T} using the soft-threshold values given by $\mathbf{\Lambda} = \gamma \mathbf{W}$. This update is performed in parallel for all the Stokes images and in turn for each image, in a parallel fashion over all the bases in the sparsifying dictionary.

Data constraint. The data constraint is enforced in parallel for each data block in steps 12-17. It involves computation of the proximity operator of the associated data fidelity term. In this respect, with the aim of accelerating the convergence of the algorithm without modifying the underlying minimization problem itself, we exploit the notion of the generalized proximity operator [164]. By definition, relative to a strongly positive and self-adjoint operator \mathbf{Q}^1 , the generalized proximity operator is given by

$$\text{prox}_{f}^{\mathbf{Q}}(\mathbf{R}) = \underset{\mathbf{R}}{\text{argmin}} f(\mathbf{R}) + \frac{1}{2}(\mathbf{R} - \mathbf{R})^{\dagger} \mathbf{Q}(\mathbf{R} - \mathbf{R}), \quad (5.26)$$

that reduces to the usual proximity operator when \mathbf{Q} is an identity matrix. Using this definition, for each data block $j \in \{1, \dots, n_d\}$, we incorporate a preconditioning diagonal operator $\mathbf{Q}_j \in \mathbb{R}_+^{4M_j \times 4M_j}$ [155]. The role of this operator is to accelerate the algorithm's convergence by utilizing additional prior information about the data. More precisely, in the considered RI imaging settings, it takes into account the Fourier sampling density, mimicking the uniform weighting scheme in RI [14]. Each diagonal element of this matrix is strictly positive and chosen to be the inverse of the uv sampling density in the neighbourhood of the corresponding data point. With this preconditioning matrix at hand and considering the data fidelity term per block,

¹A strongly positive and self-adjoint linear operator \mathbf{Q} respectively satisfies $\langle \mathbf{z} | \mathbf{Q} \mathbf{z} \rangle \geq \alpha \|\mathbf{z}\|_2^2, \forall \mathbf{z}, \forall \alpha > 0$ and $\mathbf{Q}^{\dagger} = \mathbf{Q}$.

equation (5.26) can then be written as

$$\text{prox}_{f_j}^{\mathbf{Q}_j}(\mathbf{R}) = \underset{\bar{\mathbf{R}}}{\text{argmin}} f_j(\bar{\mathbf{R}}) + \frac{1}{2}(\mathbf{Q}_j^{1/2}\mathbf{R} - \mathbf{Q}_j^{1/2}\bar{\mathbf{R}})^\dagger (\mathbf{Q}_j^{1/2}\mathbf{R} - \mathbf{Q}_j^{1/2}\bar{\mathbf{R}}). \quad (5.27)$$

Using the change of variables $\mathbf{O} = \mathbf{Q}_j^{1/2}\mathbf{R}$ and $\bar{\mathbf{O}} = \mathbf{Q}_j^{1/2}\bar{\mathbf{R}}$, equation (5.27) leads to

$$\text{prox}_{f_j}^{\mathbf{Q}_j}(\mathbf{Q}_j^{-1/2}\mathbf{O}) = \mathbf{Q}_j^{-1/2} \left(\underset{\bar{\mathbf{O}}}{\text{argmin}} f_j(\mathbf{Q}_j^{-1/2}\bar{\mathbf{O}}) + \frac{1}{2}(\mathbf{O} - \bar{\mathbf{O}})^\dagger (\mathbf{O} - \bar{\mathbf{O}}) \right) \quad (5.28)$$

$$= \mathbf{Q}_j^{-1/2} \mathcal{P}_{\mathbb{L}_j}(\mathbf{O}). \quad (5.29)$$

Therefore, algorithmically speaking, to satisfy the ℓ_2 data constraints, the inclusion of the preconditioning operator generalizes the projection onto the ℓ_2 balls to the projection onto the ellipsoids $\mathbb{L}_j(\mathbf{Y}'_j, \epsilon_j) = \{\bar{\mathbf{b}} \in \mathbb{C}^{4M_j} : \|\mathbf{Q}_j^{-1/2}\bar{\mathbf{b}} - \mathcal{M}_j^\dagger(\mathbf{Y}'_j)\|_2 \leq \epsilon_j\}$, performed via the projection operator $\mathcal{P}_{\mathbb{L}_j}$. Intuitively, this can be understood as follows. For uniform uv sampling, \mathbf{Q}_j is essentially identity. In this case, constraining the residual to lie within the ℓ_2 ball \mathbb{B}_j amounts to minimizing the Euclidean distance of the predicted visibilities to \mathbb{B}_j , leading to a projection onto \mathbb{B}_j . For any matrix $\mathbf{B} \in \mathbb{C}^{4 \times M_j}$, the corresponding projection onto the ℓ_2 ball $\mathbb{B}_j(\mathbf{Y}'_j, \epsilon_j)$ of radius ϵ_j and centred on \mathbf{Y}'_j is given by

$$\mathcal{P}_{\mathbb{B}_j(\mathbf{Y}'_j, \epsilon_j)}(\mathbf{B}) = \begin{cases} \epsilon_j \frac{\mathbf{B} - \mathbf{Y}'_j}{\|\mathbf{B} - \mathbf{Y}'_j\|_F} + \mathbf{Y}'_j, & \text{if } \|\mathbf{B} - \mathbf{Y}'_j\|_F > \epsilon_j, \\ \mathbf{B}, & \text{otherwise.} \end{cases} \quad (5.30)$$

However, in the case of RI, low Fourier modes are sampled more than the high Fourier modes. With such sampling scheme at disposal, \mathbf{Q}_j departs from identity. In this case, a skewed ball is instead obtained expressed by an ellipsoid \mathbb{L}_j and thus, the projection onto \mathbb{L}_j needs to be performed. Nevertheless, the residual should still be upper-bounded by the noise level and this is accomplished by the operator $\mathbf{Q}_j^{-1/2}$, moving the resultant ellipsoid projection point to the usual ℓ_2 ball. It is to be emphasized that the incorporation of \mathbf{Q} does not change the underlying minimization problem. It in fact acts only as an algorithmic tool to accelerate the convergence speed of the algorithm by accounting for the uv sampling information and enforcing the data

fidelity term in a different manner. A detailed performance analysis by employing such preconditioning scheme for Stokes I imaging and exploring its connection with CLEAN has been done in [14].

Epigraphical projections and polarization constraint. Steps 18 - 19 consist in updating the dual variables \mathbf{C} and \mathbf{D} , which are associated with the epigraphical projections on the functions h_1 and h_2 . As previously mentioned, these projections are required to enforce the polarization constraint. In particular, in step 18, projection of the underlying variables onto the epigraph of h_1 is needed. For any two variables $(\mathbf{c}, \mathbf{d}) \in (\mathbb{R}^N)^2$, following [158], the projection onto the epigraph of the function h_1 boils down to

$$\mathcal{P}_{\mathbb{E}_1}(\mathbf{c}, \mathbf{d}) = (\tilde{c}_n, \tilde{d}_n)_{1 \leq n \leq N}, \quad (5.31)$$

where

$$(\tilde{c}_n, \tilde{d}_n) = \begin{cases} (c_n, d_n), & \text{if } c_n + d_n \geq 0, \\ \left(\frac{1}{2}(c_n - d_n), \frac{d_n - c_n}{2} \right), & \text{otherwise.} \end{cases} \quad (5.32)$$

On the other hand, step 19 involves projection onto the epigraph of h_2 . For every $(\mathbf{R} \in \mathbb{R}^{N \times 3}, \mathbf{d} \in \mathbb{R}^N)$, this projection is given by

$$\mathcal{P}_{\mathbb{E}_2}(\mathbf{R}, \mathbf{d}) = (\tilde{\mathbf{R}}_{n,:}, \tilde{d}_n)_{1 \leq n \leq N}, \quad (5.33)$$

such that

$$(\tilde{\mathbf{R}}_{n,:}, \tilde{d}_n) = \begin{cases} (\mathbf{0}, 0), & \text{if } \|\mathbf{R}_{n,:}\|_2 < -d_n, \\ (\mathbf{R}_{n,:}, d_n), & \text{if } \|\mathbf{R}_{n,:}\|_2 < d_n, \\ \alpha_n(\mathbf{R}_{n,:}, \|\mathbf{R}_{n,:}\|_2), & \text{otherwise,} \end{cases} \quad (5.34)$$

where $\alpha_n = \frac{1}{2} \left(1 + \frac{d_n}{\|\mathbf{R}_{n,:}\|_2} \right)$ [158].

Convergence properties

The choice of the step sizes $(\rho_1, \rho_2, \rho_3, \tau) \in \mathbb{R}_+^4$ governs the convergence of Algorithm 1 to the solution of the minimization problem (5.20). These parameters should be chosen

in a manner that the following holds [155]

$$\frac{1}{\tau} - \rho_1 \|\Psi\|_2^2 - \rho_2 \|\mathbf{Q}^{1/2} \Phi'\|_2^2 - \rho_3 \geq 0, \quad (5.35)$$

where for any matrix \mathbf{X} , $\|\mathbf{X}\|_2$ denotes its spectral norm and the matrix \mathbf{Q} denotes a concatenation of the preconditioning matrices \mathbf{Q}_j defined earlier for the split data blocks. Then, under this condition, the sequence of iterates $(\tilde{\mathbf{S}}^{(k)})_{k \in \mathbb{N}}$ generated by Algorithm 1 converges to a solution of problem (5.20).

Additional remarks can be made for the proposed approach. The whole procedure of updating primal and dual variables in Algorithm 1 is repeated until the required convergence criterion, defined by the user, is met. Furthermore, it is worth mentioning that Algorithm 1 offers a highly parallelizable implementation where different steps involved can be performed in a parallel manner.

Reweighting scheme

As discussed earlier, we aim to solve the weighted ℓ_1 minimization problem iteratively, and hence approaching towards the solution in the ℓ_0 sense. More precisely, each reweighting iteration, indexed by $r^* \in \mathbb{N}$, consists in solving the weighted ℓ_1 minimization problem (5.20) using Algorithm 1. The weights for each iteration $\mathbf{W}^{(r^*+1)}$ are computed using equation (3.13), which are then used to update the soft-threshold values as $\mathbf{\Lambda}^{(r^*+1)} = \gamma \mathbf{W}^{(r^*+1)}$.

To initialize the weights, let us recall that one of the benefits of using this reweighting scheme is to avoid the tuning of any additional regularization parameters. Keeping this in mind, Algorithm 1 is used to solve the problem consisting of only data fidelity term and the positivity constraint, without imposing sparsity and polarization constraint, i.e. problem (5.11) with function $g = 0$. This corresponds to solving a constrained version of the non-negative least squares problem. Formally, in the algorithm, it consists of updating the primal variable $\tilde{\mathbf{S}}$ and the dual variable \mathbf{B} , with the rest of the primal and dual variables appearing in Algorithm 1 taken to be zero, and the set \mathbb{U} modified to set \mathbb{U}' to take into account positivity of the total intensity image. The solutions obtained are then used to compute the weights (as defined

in (3.13)) for $r^* = 1$ and hence the soft-thresholding values for the first reweighting iteration. Subsequent reweighting iterations solve for the problem (5.20) by passing on the updated values along with the solutions of the primal and dual variables from the previous iteration to Algorithm 1. The resultant reweighting scheme is described in Algorithm 2. This process is repeated until convergence.

Algorithm 2 Reweighting procedure

- 1: **given** $\tilde{\mathbf{S}}^{(0)}, \mathbf{Z}^{(0)}, (\forall l \in \{1, \dots, n_b\}) \mathbf{A}_l^{(0)}, \mathbf{\Lambda}_l^{(0)} = \gamma \mathbf{W}_l^{(0)}, (\forall j \in \{1, \dots, n_d\}) \mathbf{B}_j^{(0)}, \mathbf{C}^{(0)}, \mathbf{D}^{(0)}$
 - 2: **repeat for** $r^* = 0, 1, \dots$
 - 3: $[\tilde{\mathbf{S}}^{(r^*+1)}, \mathbf{Z}^{(r^*+1)}, \mathbf{A}^{(r^*+1)}, \mathbf{B}^{(r^*+1)}, \mathbf{C}^{(r^*+1)}, \mathbf{D}^{(r^*+1)}] = \text{Algorithm 1 } (\dots)$
 - 4: $\forall i \in \{1, 2, 3, 4\}$ and $\forall l \in \{1, \dots, n_b\}$ **compute** $[\mathbf{W}_l]_{:,i}^{(r^*+1)}$ as per equation (3.13)
 - 5: **until convergence**
-

5.3.3 Polarization constraint for TV based problems

For comparison purposes, we consider the full polarization sparse imaging technique solved in [165]. The authors in [165] consider independent problems for each of the Stokes parameters, applied in the context of EHT imaging. The associated model is then given by $\mathbf{Y}'_S = \Phi'_S(\tilde{\mathbf{S}}) + \mathbf{\Omega}'_S$, where the subscript S denotes that the measurements are considered in the Stokes domain by defining the corresponding measurement operator accordingly. In particular, it involves changing from brightness domain in equation (5.4) to Stokes domain that can be done via the operator $\tilde{\mathcal{L}}^\dagger$, and thus, the measurements are directly related to the Fourier transform of the Stokes matrix rather than the brightness matrix.

The authors then propose to solve the following minimization problem

$$\underset{\tilde{\mathbf{S}} \in \mathbb{R}^{N \times 4}}{\text{minimize}} \quad \frac{1}{2} \|\mathbf{Y}'_S - \Phi'_S(\tilde{\mathbf{S}})\|_F^2 + \iota_{\mathbb{U}'}(\tilde{\mathbf{S}}) + \check{g}(\Psi^\dagger \tilde{\mathbf{S}}). \quad (5.36)$$

In this problem, the unconstrained formulation is used and the data fidelity term is given by the squared ℓ_2 term (first term in (5.36)). The polarization constraint is not imposed, justifying the use of the set \mathbb{U}' to impose positivity of the total intensity image. Furthermore, the third term, $\check{g}(\Psi^\dagger \tilde{\mathbf{S}})$ in (5.36) is the sparsity prior imposing the

sparsity of the sought images in some sparsifying dictionary. In this regard, [165] shows that the TV and ℓ_1 +TV sparsifying regularizations are effective in producing super-resolved images and lead to better reconstruction quality than using the standard CLEAN method. For these regularizations, the authors have considered the isotropic TV norm (equation (4.1)).

For the sake of completeness, we hereby propose to generalize the minimization problem (5.36) solved by [165] to incorporate explicitly the polarization constraint. It amounts to

$$\begin{aligned} \underset{\substack{\tilde{\mathbf{S}} \in \mathbb{R}^{N \times 4}, \\ \mathbf{Z} \in \mathbb{R}^{N \times 2}}}{\text{minimize}} \quad & \frac{1}{2} \|\mathbf{Y}'_S - \Phi'_S(\tilde{\mathbf{S}})\|_F^2 + \iota_{\mathbb{U}}(\tilde{\mathbf{S}}) + \check{g}(\Psi^\dagger \tilde{\mathbf{S}}) + \iota_{\mathbb{V}}(\mathbf{Z}) \\ & + \iota_{\mathbb{E}_1}(\tilde{\mathbf{S}}_{:,1}, \mathbf{Z}_{:,1}) + \iota_{\mathbb{E}_2}(\tilde{\mathbf{S}}_{:,2:4}, \mathbf{Z}_{:,2}). \end{aligned} \quad (5.37)$$

This problem can be solved by using a modified version of the primal-dual method proposed in Algorithm 1. In particular, Algorithm 1 can incorporate any convex sparsity regularization function, and can be adapted for the unconstrained problem of interest. The resultant algorithm is provided in Algorithm 3, consisting of the following amendments made in Algorithm 1.

- (i). While Algorithm 1 has been provided for the constrained formulation with the data fidelity term defined in (5.6), problem (5.37), where the data consistency is instead ensured by a differentiable ℓ_2 squared term, can still be solved. The update of variable \mathbf{B} in Algorithm 1 is no longer required, instead the gradient term $\Phi_S'^\dagger(\Phi_S'(\tilde{\mathbf{S}}) - \mathbf{Y}'_S)$ is added in the update of the variable $\tilde{\mathbf{S}}$, as shown in Step 3 of Algorithm 3.
- (ii). For the sparsity prior, depending on the chosen regularization, the corresponding thresholding operator \mathcal{T} and the dictionary Ψ need to be modified in steps 7 - 10 of Algorithm 3. With this in mind, either of the TV and ℓ_1 +TV sparsifying regularizations can be taken into account in Algorithm 3 as follows.

TV regularization: The sparsity prior is given by $\check{g}(\Psi^\dagger \tilde{\mathbf{S}}) = \sum_{i=1}^4 \mu_i \|\nabla \tilde{\mathbf{S}}'_i\|_{2,1}$, where $\tilde{\mathbf{S}}'_i$ is the reshaped matrix form of the vector $\tilde{\mathbf{S}}_{:,i}$ and for every $i \in \{1, 2, 3, 4\}$,

Algorithm 3 Primal-dual algorithm to solve problem (5.37)

1: **given** $\tilde{\mathbf{S}}^{(0)} \in \mathbb{R}^{N \times 4}$, $\mathbf{Z}^{(0)} \in \mathbb{R}^{N \times 2}$, $(\forall l \in \{1, \dots, n_b\}) \mathbf{A}_l^{(0)} \in \mathbb{R}^{J \times 4}$, $\tilde{\mathbf{A}}_l^{(0)} = \Psi_l \mathbf{A}_l^{(0)}$, $\Lambda_l \in \mathbb{R}_+^{J \times 4}$, $\mathbf{C}^{(0)} \in \mathbb{R}^{N \times 4}$, $\mathbf{D}^{(0)} \in \mathbb{R}^{N \times 2}$.

2: **For** $k = 0, 1, \dots$

Primal updates

$$3: \quad \tilde{\mathbf{S}}^{(k+1)} = \mathcal{P}_{\mathbb{U}} \left(\tilde{\mathbf{S}}^{(k)} - \tau \left(\rho_1 \sum_{l=1}^{n_b} \tilde{\mathbf{A}}_l^{(k)} + \Phi_S'^{\dagger} (\Phi_S'(\tilde{\mathbf{S}}^{(k)}) - \mathbf{Y}'_S) + \rho_3 \mathbf{C}^{(k)} \right) \right)$$

$$4: \quad \check{\mathbf{S}}^{(k+1)} = 2\tilde{\mathbf{S}}^{(k+1)} - \tilde{\mathbf{S}}^{(k)}$$

$$5: \quad \mathbf{Z}^{(k+1)} = \mathcal{P}_{\mathbb{V}} \left(\mathbf{Z}^{(k)} - \tau \rho_3 \mathbf{D}^{(k)} \right)$$

$$6: \quad \check{\mathbf{Z}}^{(k+1)} = 2\mathbf{Z}^{(k+1)} - \mathbf{Z}^{(k)}$$

Dual updates

Promoting sparsity:

7: **for** $l \in \{1, \dots, n_b\}$ and $\forall i \in \{1, 2, 3, 4\}$ **do in parallel**

$$8: \quad [\mathbf{A}_l^{(k+1)}]_{:,i} = \left(\mathbf{1}_J - \mathcal{T}_{[\Lambda_l]_{:,i}} \right) \left([\mathbf{A}_l^{(k)}]_{:,i} + \Psi_l^{\dagger} \check{\mathbf{S}}_{:,i}^{(k+1)} \right)$$

$$9: \quad [\tilde{\mathbf{A}}_l^{(k+1)}]_{:,i} = \Psi_l [\mathbf{A}_l^{(k+1)}]_{:,i}$$

10: **end for**

Enforcing polarization constraint:

$$11: \quad \begin{bmatrix} \mathbf{C}_{:,1}^{(k+1)} \\ \mathbf{D}_{:,1}^{(k+1)} \end{bmatrix} = \begin{bmatrix} \mathbf{C}_{:,1}^{(k)} + \check{\mathbf{S}}_{:,1}^{(k+1)} \\ \mathbf{D}_{:,1}^{(k)} + \check{\mathbf{Z}}_{:,1}^{(k+1)} \end{bmatrix} - \mathcal{P}_{\mathbb{E}_1} \left(\begin{bmatrix} \mathbf{C}_{:,1}^{(k)} + \check{\mathbf{S}}_{:,1}^{(k+1)} \\ \mathbf{D}_{:,1}^{(k)} + \check{\mathbf{Z}}_{:,1}^{(k+1)} \end{bmatrix} \right)$$

$$12: \quad \begin{bmatrix} \mathbf{C}_{:,2:4}^{(k+1)} \\ \mathbf{D}_{:,2}^{(k+1)} \end{bmatrix} = \begin{bmatrix} \mathbf{C}_{:,2:4}^{(k)} + \check{\mathbf{S}}_{:,2:4}^{(k+1)} \\ \mathbf{D}_{:,2}^{(k)} + \check{\mathbf{Z}}_{:,2}^{(k+1)} \end{bmatrix} - \mathcal{P}_{\mathbb{E}_2} \left(\begin{bmatrix} \mathbf{C}_{:,2:4}^{(k)} + \check{\mathbf{S}}_{:,2:4}^{(k+1)} \\ \mathbf{D}_{:,2}^{(k)} + \check{\mathbf{Z}}_{:,2}^{(k+1)} \end{bmatrix} \right)$$

13: **end For**

$\mu_i > 0$ is the regularization parameter. Thus, in Algorithm 3, $\Psi = \nabla$ with $n_b = 1$ and the operator $\mathcal{T} = \mathcal{T}_{\text{TV}}$ is the proximity operator for the TV norm [84, 134], using the threshold-size $\Lambda = [\mu_1, \mu_2, \mu_3, \mu_4]$ in step 8.

ℓ_1 +TV regularization: It consists of two terms in the sparsity prior, $\check{g}(\Psi^{\dagger} \tilde{\mathbf{S}}) = \sum_{i=1}^4 v_{1,i} \|\tilde{\mathbf{S}}_{:,i}\|_1 + \sum_{i=1}^4 v_{2,i} \|\nabla \tilde{\mathbf{S}}'_i\|_{2,1}$, with $v_{1,i}$ and $v_{2,i} > 0$. The first term, i.e. ℓ_1 norm, imposes sparsity of the underlying images in the Dirac basis. The second term, i.e. TV term, promotes the sparsity in the gradient domain (4.1). As a result, in this case, the sparsifying dictionary $\Psi = [\mathbf{I}_N, \nabla]$ is the concatenation of the identity

matrix (Dirac basis) and the gradient basis, respectively with $n_b = 2$. Similarly, for $l = 1$ and 2 in step 8, the operator \mathcal{T} is the proximity operator corresponding to the ℓ_1 and the TV norms, respectively. The associated thresholding sizes are given by $\mathbf{\Lambda}_1 = [v_{1,1}, v_{1,2}, v_{1,3}, v_{1,4}]$ and $\mathbf{\Lambda}_2 = [v_{2,1}, v_{2,2}, v_{2,3}, v_{2,4}]$.

One can notice that the same algorithm can be used to solve problem (5.36) as well wherein the polarization constraint is not imposed and only steps 3, 4, 7-10 in Algorithm 3 need to be executed.

Lastly, regarding the terminology, solving problem (5.37) considering TV regularization (resp. $\ell_1 + \text{TV}$) is referred to as TV (resp. $\ell_1 + \text{TV}$) problem with constraint. Similarly, solving problem (5.36) with TV regularization (resp. $\ell_1 + \text{TV}$) is termed as TV (resp. $\ell_1 + \text{TV}$) problem without constraint.

5.4 Simulations and Results

In this section, we discuss the considered simulation settings and describe the different cases for simulations. We then investigate the performance of the proposed Polarized SARA method, implemented in MATLAB, on simulated EHT datasets.

Without any loss of generality for the proposed algorithm, we consider the idealized case and work in the absence of DDEs. In such a scenario, the Mueller matrix is essentially the identity matrix. With these measurement settings, we perform tests on the EHT uv coverage, as shown in Figure 5.3. This realistic coverage, adopted from [133, 165], corresponds to the measurements made at wavelength $\lambda = 1.3$ mm (i.e. observation frequency of 230 GHz), using a VLBI array consisting of six stations. In this case, the maximum observation baseline, $B_{\max} = 7.2 \text{ G}\lambda$.

Furthermore, we consider two sets of images based on physically motivated models of M87 radio emission at 1.3 mm wavelength. The first set of images consists of a forward-jet model, which was initially developed in [166]. We use the version of this model presented in [167], coherent with the EHT observations at the considered wavelength. The second set of images involves a counter-jet model. It is based on general

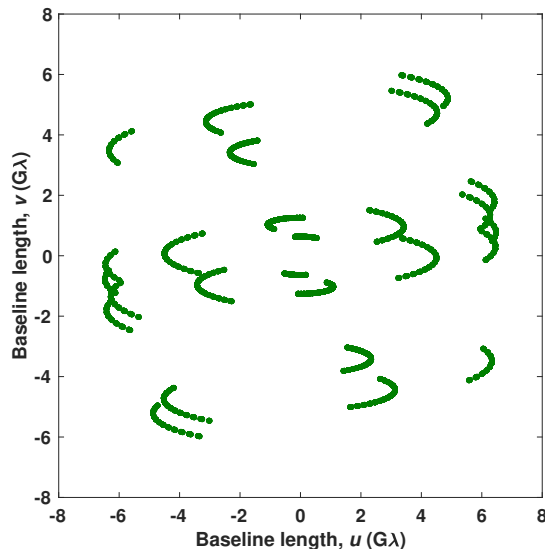


FIGURE 5.3: The EHT uv coverage used for simulations, taken from [133, 165]. It corresponds to the measurements made at 1.3 mm (230 GHz) using six stations of the VLBI array.

relativistic magnetohydrodynamic (GRMHD) simulation results [168] and polarimetric radiative transfer calculations [169]. We focus on imaging of Stokes I , Q and U parameters, as done in [165], by considering only three columns in the sought Stokes matrix. The two sets of images are displayed in Figure 6.6 in first and second row, respectively. In both the cases, the true Stokes I , Q and U images are presented along with the linear polarization image P , respectively in the columns one to four. For both these sets, we consider the image size $N = 100 \times 100$ with the field of view of $200 \mu\text{as}$. The resultant pixel size of $2 \mu\text{as}$ corresponds to a scale of $\sim 0.21 R_s$. For both the sets of model images, we simulate the noisy measurements as per equation (5.2) with the measurement operator given by (5.3), considering Mueller matrix to be identity. We further consider the measurements related to each column of the brightness matrix are corrupted by a Gaussian noise with the same variance σ^2 , where $\sigma = 5 \times 10^{-3}$ Jy. The scale of the chosen variance is broadly consistent with the EHT settings considered in [165]. Although we consider the same variance for all the visibilities, it is worth mentioning that the same approach can be applied for more realistic EHT settings having different variances. In particular, such a case can be dealt with by using suitable values in the matrix Θ .

Lastly, few things need to be pointed out. First, given a relatively small number of

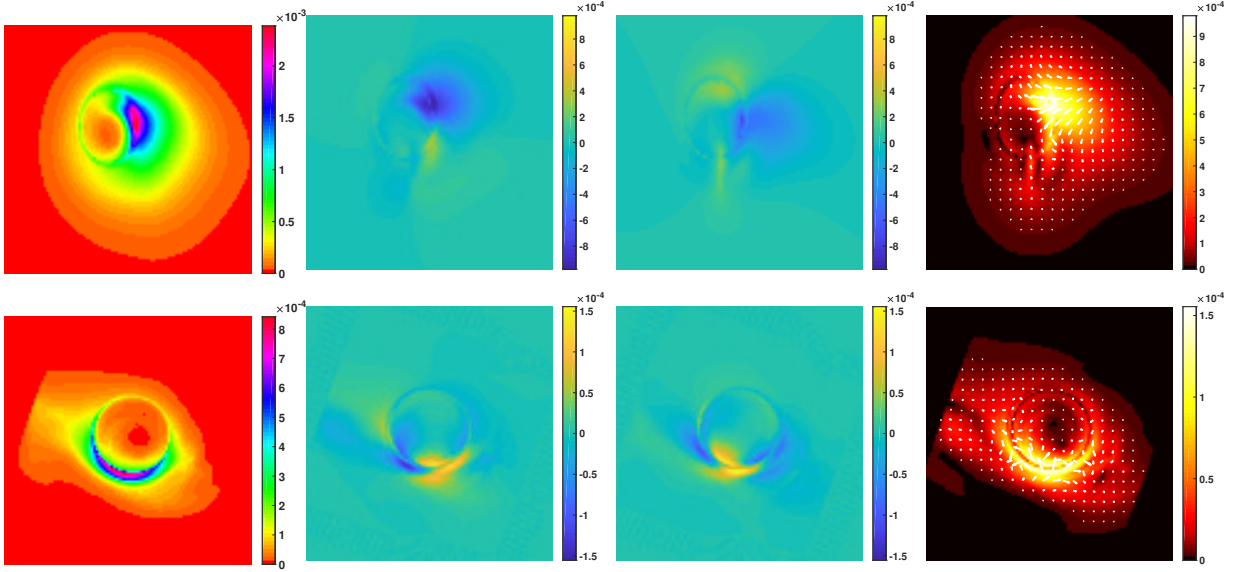


FIGURE 5.4: The ground truth images for forward-jet [166, 167] (first row) and counter-jet [168] (second row) models, used to perform simulations. In each row, left to right the following images are displayed: Stokes I , Stokes Q , Stokes U and the linear polarization image P . For the latter, the electric vector polarization angle (EVPA) distribution is shown in white bars, plotted over the linear polarization intensity ($|P|$). All the images are shown in linear scale.

measurements with M of the order of 10^3 , we do not exploit the block-data splitting and acceleration strategies, i.e. we consider $n_d = 1$ and the preconditioning matrix \mathbf{Q} to be identity in Algorithm 1. Doing so, the projection onto the ellipsoid in step 14 reduces to a projection onto the ℓ_2 ball (5.30). Second, we assume the ℓ_2 bound ϵ is known beforehand. To be more precise, in the considered settings, the residual norm resembles the χ^2 distribution with $8M$ degrees of freedom, and the bound ϵ for the ℓ_2 ball \mathbb{B} defined in (5.6) can be determined from the noise variance $\sigma^2/2$ of the real and imaginary parts of the noise. We thus set this bound as $\epsilon^2 = (8M + 2\sqrt{2(8M)})\sigma^2/2$, where the bound ϵ^2 is taken to be 2 standard deviations above the mean of the χ^2 distribution [45]. Following this, step 16 need not be performed in Algorithm 1.

5.4.1 Computational complexity

In each iteration $k \in \mathbb{N}$ of Algorithm 1, the major computational burdens come from the application of the measurement operator Φ' and of the Discrete Wavelet Transforms (DWT) Ψ , while enforcing data fidelity and sparsity, respectively. In particular, the usage of the measurement operator (and its adjoint) can be broadly

split into (a) computing the FFT of oversampled images contained in columns of the underlying matrix, each such image requiring a complexity of $\mathcal{O}(\kappa N \log \kappa N)$, and (b) applying the linear operator \mathbf{G} with complexity of $\mathcal{O}(n_s M \kappa N)$ for each Fourier transformed image. Here n_s is the sparsity percentage of each row of \mathbf{G} , due to the compact support convolution kernels used to reduce its computational burden. For large data sets having $M \gg N$, the term (b) dominates in the computational cost. Concerning the sparsity operation, the major computational load comes by the application of the DWT in step 10 (and its adjoint in step 9), where we use its fast implementation providing a complexity of $\mathcal{O}(N)$ considering compactly supported wavelets [70, 170]. Thus, for a dictionary Ψ consisting of n_b basis, it requires $\mathcal{O}(N)$ computations for each basis and each image stored in the underlying matrix. In the current code, we apply the sparsifying dictionary Ψ (and its adjoint) in parallel for each such image. Regarding the remaining steps in Algorithm 1 which involve performing projections onto the respective sets, each such projection scales linearly with the size of the argument matrix.

Investigation of the MATLAB code indicated that the epigraphical projections to impose the polarization constraint does not add much to the computational cost and thus, Polarized SARA takes about the same time to converge as taken by Polarized SARA without constraint. More specifically, in the current simulation settings, the MATLAB code takes few hours in total, consisting of 10 reweighting iterations, to provide the final estimates of the Stokes parameters. We also note that the larger datasets will incur a high computational cost and thus more time to converge to the solutions. Nonetheless, in this case, distribution and parallelization features can be used in Algorithm 1.

5.4.2 Effect of polarization constraint

As previously discussed in Section 5.3, the polarization constraint needs to be satisfied by the Stokes images to avoid unphysical reconstructions. To validate the importance of imposing this constraint explicitly in the reconstruction process, we perform tests with and without this constraint. The case of imposing this constraint, i.e. Polarized SARA, consists of solving the minimization problem (5.20) using Algorithm 2 with

each reweighting iteration consisting of implementing Algorithm 1. On the contrary, Polarized SARA without constraint implies solving the minimization problem (5.11). In this context, Algorithm 1 can still be used to solve the weighted ℓ_1 minimization problems within the reweighting scheme. However, Algorithm 1 is employed to solve only for the Stokes matrix \mathbf{S} (step 3), taking into account only the sparsity prior (steps 8 - 11) and the data fidelity term (steps 12 - 17). Additionally, recall that in the absence of the polarization constraint, the positivity of the Stokes I image is taken into account by the use of the modified set \mathcal{U}' (5.10). In step 3 of Algorithm 1, the projection needs to be performed on this set. This projection also consists in taking the real part of its arguments as described in (5.23), with an extra step of considering only the positive values for Stokes I , i.e. $\mathbf{X}_{:,1} = \max \left\{ \text{Re}(\mathbf{X}_{:,1}), \mathbf{0} \right\}$.

In order to compare between the tests performed with and without imposing polarization constraint, we keep track of the pixels not satisfying this constraint. It consists in analyzing the polarization error image, $\mathbf{p} \in \mathbb{R}_+^N$, where, for every $n \in \{1, \dots, N\}$,

$$p_n = \begin{cases} -S_{n,1} + \|\mathbf{S}_{n,2:3}\|_2, & \text{if } -S_{n,1} + \|\mathbf{S}_{n,2:3}\|_2 > \zeta, \\ 0, & \text{otherwise.} \end{cases}$$

Basically, this image is generated by taking the difference between the linear polarization intensity image and the total intensity image, where only the pixels with values larger than some threshold ζ are retained, while the others are put to zero. In essence, this image is a representation of the pixels not satisfying the polarization constraint, and having values greater than ζ . The value of ζ is taken to be 3 times the rms noise, which is estimated from the residual image. Thus, by considering this threshold, the pixels with values smaller than the noise level are discarded. Finally, we denote the percentage of the non-zero pixels in the image \mathbf{p} by N_p , where $N_p \in [0, 100]$.

5.4.3 Comparisons performed

Comparisons with the other methods

In the context of EHT imaging for full polarization, as mentioned earlier, the work in [165] represents the only existing method within the sparse modelling framework,

aiming to solve problem (5.36). In Section 5.3.3, we have proposed to generalize this problem by taking into account the polarization constraint and hence solving for problem (5.37). Keeping these in mind, we compare the results obtained by the following: Polarized SARA, Polarized SARA without constraint, TV problem with and without constraint, $\ell_1 + \text{TV}$ problem with and without constraint. It is important to emphasize that all these problems are solved using primal-dual approaches. More specifically, while the first two problems are solved by Algorithm 2 which incorporates Algorithm 1 in each iteration, Algorithm 3 is used to solve the last four problems. These comparisons correspond to analyzing not only the performance of different sparsifying regularizations for EHT imaging, but also the importance of polarization constraint for image recovery.

In order to be coherent with the previous studies [125, 133, 165] for EHT imaging, we also perform comparison with the widely used CS-CLEAN algorithm. To this purpose, for each considered dataset in this article, we implemented CS-CLEAN in the Common Astronomy Software Applications (CASA) package².

Comparison in the super-resolution regime

Another comparison which can be made between the results obtained by different sparsifying regularizations is regarding the optimal resolution achieved by the respective reconstructed images, especially in the super-resolution regime, i.e. when one goes beyond the nominal interferometric resolution (λ/B_{\max}), also referred to as the diffraction limit. In this context, we adopt the comparison scheme introduced in [125] and later on used in [124, 133, 165]. It consists in convolving the reconstructed images with circular Gaussian beams of varying full width half maximum (FWHM) sizes. We then compute the NRMSE between these convolved images and the corresponding ground truth images. It is to be mentioned that such a convolution varies the resolution of the underlying images. Therefore, not only the reconstruction errors, but also the errors due to loss of resolution will contribute to the computed NRMSEs. We compare the curves obtained from the TV problem with constraint, $\ell_1 + \text{TV}$ problem with constraint, Polarized SARA and CS-CLEAN. For the TV and $\ell_1 + \text{TV}$ problems with

²<https://casa.nrao.edu/>

constraint, we consider the implementation of Algorithm 3. This already provides a better scenario for these TV based regularizations, and hence accounts for a fair comparison of the performance of these methods with the Polarized SARA method.

5.4.4 Simulation settings

For each of the cases discussed earlier, we perform 5 simulations varying the noise realizations. In order to stop the computation of the algorithm at convergence, we consider a stopping criterion. First, we ensure that at convergence the residual norm is in the vicinity of the ℓ_2 upper bound ϵ defined earlier, i.e. $\|\Phi'(\tilde{\mathbf{S}}) - \mathbf{Y}\|_F \leq (1 + \vartheta)\epsilon$, where $\vartheta > 0$ is a tolerance parameter. We set it equal to 5×10^{-3} . In addition, as a second stopping criterion, we impose the relative variation between two consecutive iterates to be very small, i.e.:

$$\max_{i \in \{1,2,3\}} \left(\|\tilde{\mathbf{S}}_{:,i}^{(k+1)} - \tilde{\mathbf{S}}_{:,i}^{(k)}\|_2 / \|\tilde{\mathbf{S}}_{:,i}^{(k)}\|_2 \right) \leq \varepsilon, \quad (5.38)$$

where $\varepsilon > 0$. For the case with the polarization constraint, not only the above two mentioned criteria are taken into account, but we also verify that the constraint is satisfied, up to a small error, i.e., $N_p \leq \varrho$, where $\varrho > 0$.

As described previously, the proposed Polarized SARA method as well as the Polarized SARA without constraint method incorporate the reweighting scheme (Algorithm 2), wherein we perform 10 reweighting iterations. For each iteration and for both the methods, we choose $\varepsilon = 10^{-5}$ in (5.38). In addition to this, we choose $\varrho = 0.5$ to stop Algorithm 1 for Polarized SARA. This choice of ϱ stops the algorithm when only 0.5% of the pixels in the polarization error image, generated from the reconstructed Stokes images, are not satisfying the constraint.

Regarding the implementation of Algorithm 3 to solve for the TV and $\ell_1 + \text{TV}$ problems without constraint, we choose $\varepsilon = 10^{-5}$ for the forward-jet model, and 7×10^{-6} for the counter-jet model for the stopping criterion. While solving for the TV and $\ell_1 + \text{TV}$ problems with constraint, we also choose $\varrho = 0.5$. For the threshold parameters $\mathbf{\Lambda}$ in Algorithm 3, we tune these values to minimize the normalized root mean square error (NRMSE). For any true image $\bar{\mathbf{s}}$ and the corresponding reconstructed

Polarization constraint	TV	$\ell_1 + \text{TV}$	SARA
Stokes I image - SNR / NRMSE			
without constraint	27.53 / 0.2549	27.64 / 0.2542	33.09 / 0.1912
with constraint	28.19 / 0.2442	28.72 / 0.2378	33.15 / 0.1906
Linear polarization image - SNR / NRMSE			
without constraint	23.66 / 0.3063	24.46 / 0.2944	27.54 / 0.2527
with constraint	24.92 / 0.2876	24.91 / 0.2878	28.96 / 0.2350
(a)			
Polarization constraint	TV	$\ell_1 + \text{TV}$	SARA
Stokes I image - SNR / NRMSE			
without constraint	12.81 / 0.5269	12.82 / 0.5268	15.97 / 0.4502
with constraint	13.51 / 0.5089	13.51 / 0.5090	16.71 / 0.4337
Linear polarization image - SNR / NRMSE			
without constraint	5.03 / 0.7781	5.85 / 0.7469	9.01 / 0.6374
with constraint	8.62 / 0.6500	8.77 / 0.6449	9.51 / 0.6215
(b)			

TABLE 5.1: SNR and NRMSE values for the reconstructed images corresponding to the (a) forward-jet model, and (b) counter-jet model, obtained by different sparsifying regularizations. For each case, the mean values (computed over 5 simulations) are shown for the Stokes I image and the linear polarization image reconstructed with and without imposing the polarization constraint.

image \mathbf{s} , NRMSE is defined as

$$\text{NRMSE} = \sqrt{\frac{\sum_n |s_n - \bar{s}_n|^2}{\sum_n |\bar{s}_n|^2}}. \quad (5.39)$$

Therefore, with this definition, lower the NRMSE, better is the reconstruction.

5.4.5 Results and discussion

For a quantitative comparison between the reconstructed images from different cases, the reconstruction quality is assessed in terms of NRMSE as well as signal-to-noise ratio (SNR). It is defined as

$$\text{SNR} = 20 \log_{10} \left(\frac{\|\bar{\mathbf{s}}\|_2}{\|\mathbf{s} - \bar{\mathbf{s}}\|_2} \right), \quad (5.40)$$

Model	TV	$\ell_1 + \text{TV}$	SARA
Forward-jet	20.47	16.14	15.02
Counter-jet	62.97	59.96	41.97

TABLE 5.2: Percentage of pixels not satisfying the polarization constraint in the images reconstructed without the enforcement of the constraint. The percentage (mean value computed over 5 simulations) is listed for the reconstructed images corresponding to the forward-jet (first row) and counter-jet (second row) models, obtained by different sparsifying regularizations.

implying that higher SNR corresponds to better reconstruction quality. These NRMSE and SNR values for the reconstructed Stokes I image and the linear polarization image P , generated from the reconstructed Stokes Q and U images, are listed in Table 5.1 for both set of models: (a) forward-jet model, and (b) counter-jet model. In each case, the shown value corresponds to the mean value computed over the performed 5 simulations. It can be observed from Table 5.1 that, on the one hand, for a given regularization, imposing the polarization constraint yields lesser error (and thus higher SNR) in the reconstructions than that obtained by without imposing it. More precisely, irrespective of the chosen regularization, enforcement of this constraint leads to improvement in the reconstruction quality. On the other hand, comparison between different regularizations shows that the SARA regularization performs significantly better than the other two regularizations, having ~ 1 -5 dBs higher SNR. This holds true not only for Polarized SARA but also for Polarized SARA without constraint. This indicates the importance of choosing a suitable dictionary for better reconstruction. Concerning the importance of the polarization constraint, we quantify it by giving the percentage (N_p) of the pixels not fulfilling this constraint in Table 5.2. In particular, this table provides the values of N_p in the cases with absence of enforcement of the polarization constraint, whereas in its presence $N_p \leq 0.5\%$ as specified in the stopping criterion. Table 5.2 then demonstrates that without imposing this constraint, an appreciable percentage of pixels have non-physical values. Additionally, in terms of the sparsifying regularizations, it again indicates the better performance of the SARA regularization in comparison with the others.

For the comparison in the super-resolution regime and as mentioned in Section 5.4.3,

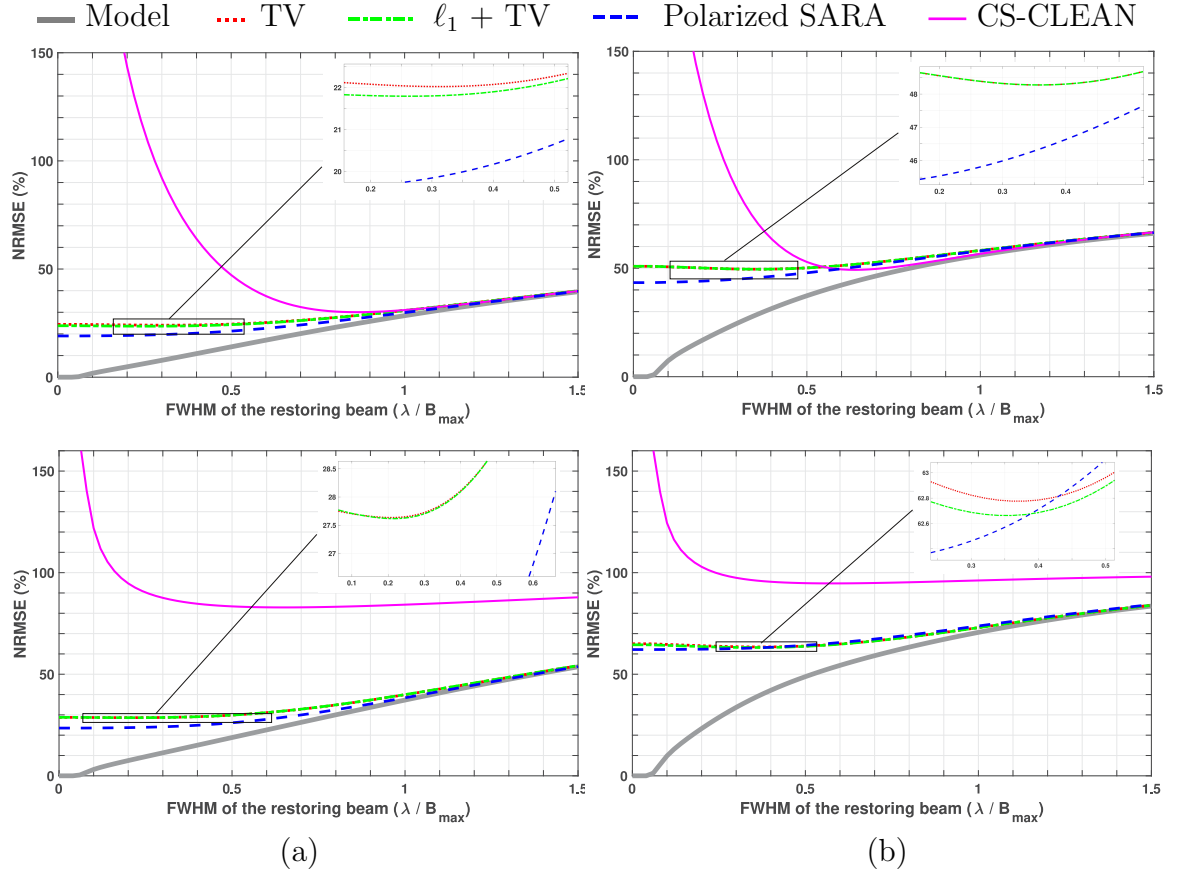


FIGURE 5.5: The NRMSE plots for the Stokes I image (first row) and the linear polarization image (second row) corresponding to (a) forward-jet model, and (b) counter-jet model, as a function of the FWHM size of the restoring beam. The NRMSE is evaluated between the original ground truth image and the beam-convolved reconstructed images. The shown curves correspond to the reconstructions obtained by: TV problem with constraint (dotted red curve), $\ell_1 + \text{TV}$ problem with constraint (dash-dotted green curve), Polarized SARA (dashed blue curve), CS-CLEAN (pink, continuous thin curve). The grey curve (continuous thick curve) shows the errors for the Model, i.e. error between the original ground truth image and the beam-convolved ground truth image. For each of the plots, a zoomed portion (of the curves inside the box) is shown to highlight the minimum error regions of the TV and $\ell_1 + \text{TV}$ problems.

the NRMSE plots for both the forward-jet (first column) and counter-jet (second column) model are shown in Figure 5.5. The first and second row respectively display the plots for the Stokes I and the linear polarization image P . In all these plots, the curve (continuous thick, grey curve) labelled Model, depicts the NRMSE values between the ground truth images convolved with circular Gaussian beams of varying FWHM sizes and the original ground truth images. Relating it to the previous discussion (Section 5.4.3), this curve basically represents the minimum attainable errors

at any given resolution, arising purely because of the loss of resolution. The other curves correspond to the following: TV problem with constraint (dotted red curve), $\ell_1 + \text{TV}$ problem with constraint (dash-dotted green curve), Polarized SARA (dashed blue curve). We also give the curve (continuous thin, pink curve) obtained by the reconstructions from the widely used CS-CLEAN algorithm using uniform weighting.

It can be seen that for the Stokes I images, CS-CLEAN NRMSE values start to increase rapidly in the super-resolution regime, where the diffraction limit is specified by the FWHM of size 1. This indicates the inability of CS-CLEAN to produce super-resolved images. Moreover, in this case, the minimum errors are obtained at a resolution of $\sim 50 - 80 \%$ of the diffraction limit. On the contrary, for the other considered sparsifying regularizations, the NRMSE values vary gradually even in the super-resolution regime. In fact the error tends to decrease. It can be noticed that the values for the TV and $\ell_1 + \text{TV}$ problems with constraint are quite close, whereas the errors from the Polarized SARA are lower than that obtained by the former two. Another interesting observation is related to the resolution at which the minimum error is achieved by these regularizations. While for the TV and $\ell_1 + \text{TV}$ problems, it is at $\sim 25 - 35 \%$ of the diffraction limit, the corresponding value for the Polarized SARA is 0% . This highlights that the reconstructions obtained by the latter do not need to be convolved with a restoring beam. This is in contrast to the results obtained by other curves, where convolution with a restoring beam is required to get the minimum error. The same features can be noticed from the plots of the linear polarization images. In this case, the errors obtained by CS-CLEAN are quite large, with the minimum being at around 60% of the interferometric resolution. These large errors indicate that CS-CLEAN is not particularly suitable for recovering the linearly polarized emission images.

For visual comparison of the results obtained from these tests, we show the reconstructed images and the respective error images. The latter are computed by taking the absolute difference between the true and the reconstructed images. Out of the 5 simulations, the displayed images correspond to the simulation results with the least NRMSE. The results for the forward-jet model images are shown in Figures 5.6 and

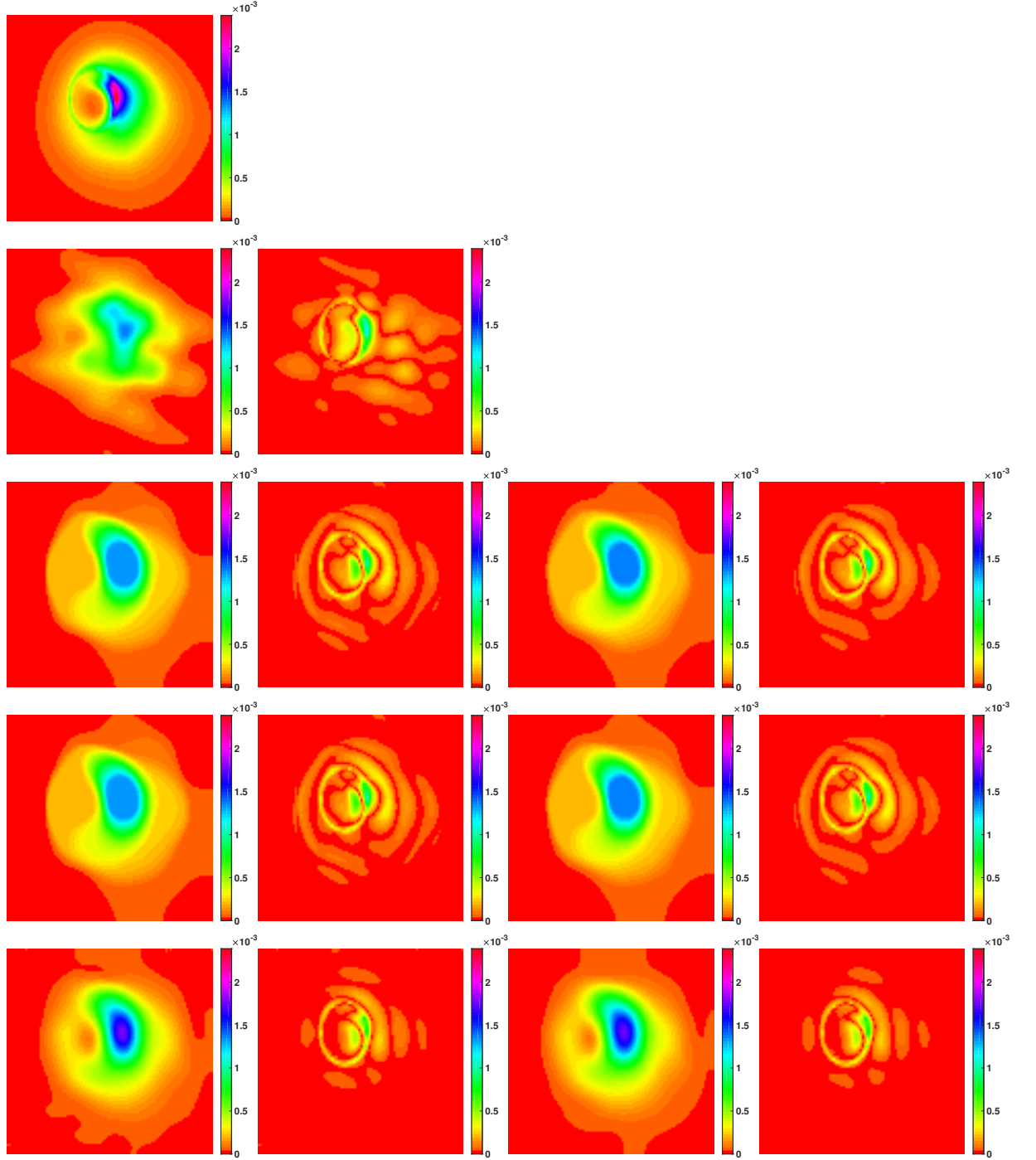


FIGURE 5.6: Results for the Stokes I forward-jet model image. First row shows the ground-truth image, whereas the second row shows the CS-CLEAN reconstructed image followed by its error image. Third, fourth and fifth rows show the results for the TV, ℓ_1 +TV problems and Polarized SARA, respectively. For these rows, the first two columns show the reconstructed and the error images obtained without imposing the polarization constraint in the reconstruction process, whereas the corresponding images in the case of imposing this constraint are shown in the last two columns. The shown images correspond to the best results obtained over 5 performed simulations for each case. All the images are shown in linear scale, normalized to the scale of the corresponding ground truth image.

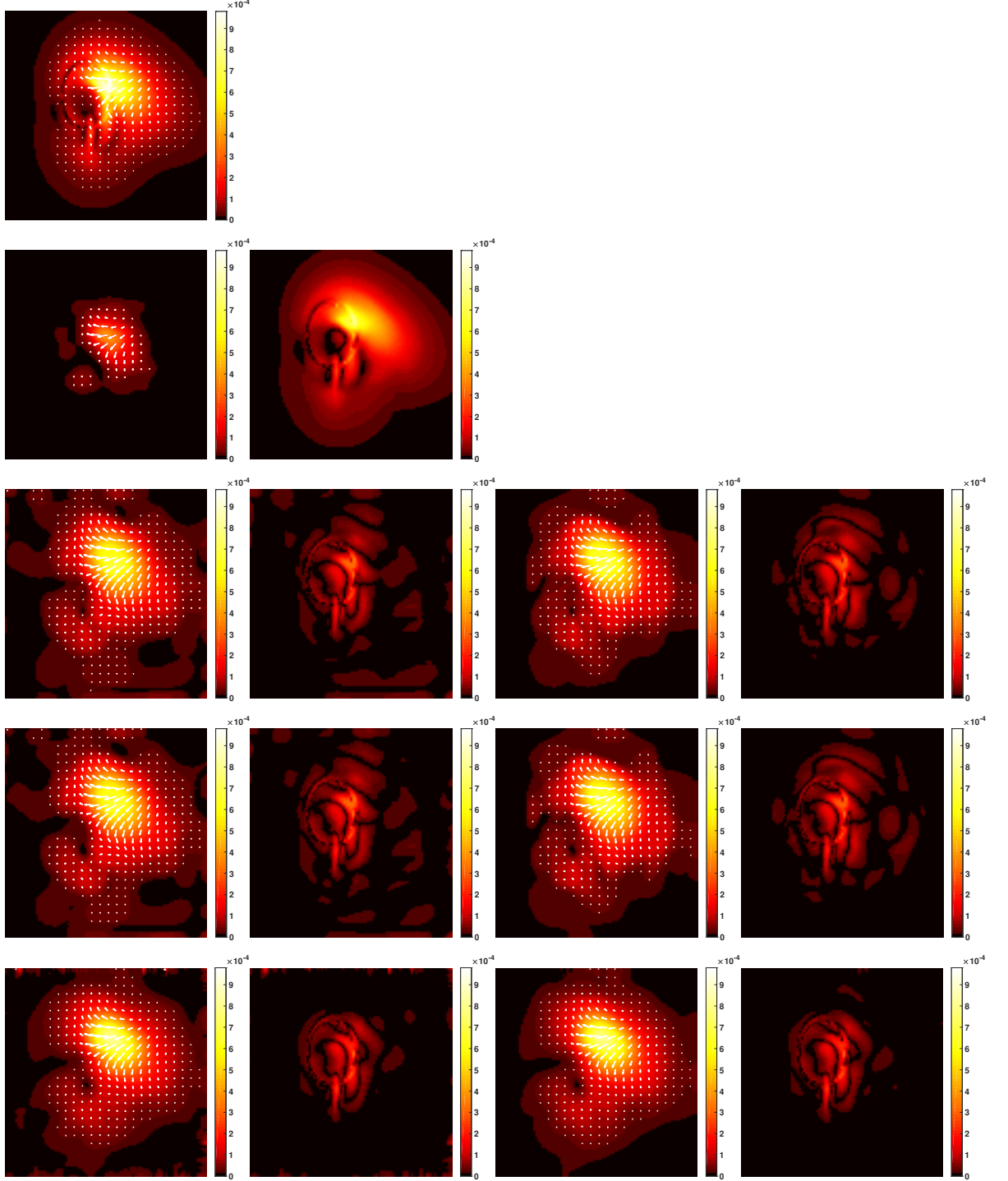


FIGURE 5.7: Results for the linear polarization forward-jet model image (linear polarization intensity images, overlaid by the white bars representing the EVPA). First row shows the ground-truth image, whereas the second row shows the CS-CLEAN reconstructed image followed by its error image. Third, fourth and fifth rows show the results for the TV, $\ell_1 + \text{TV}$ problems and Polarized SARA, respectively. For these rows, the first two columns show the reconstructed and the error images obtained without imposing the polarization constraint in the reconstruction process, whereas the corresponding images in the case of imposing this constraint are shown in the last two columns. The shown images correspond to the best results obtained over 5 performed simulations for each case. All the images are shown in linear scale, normalized to the scale of the corresponding ground-truth image.

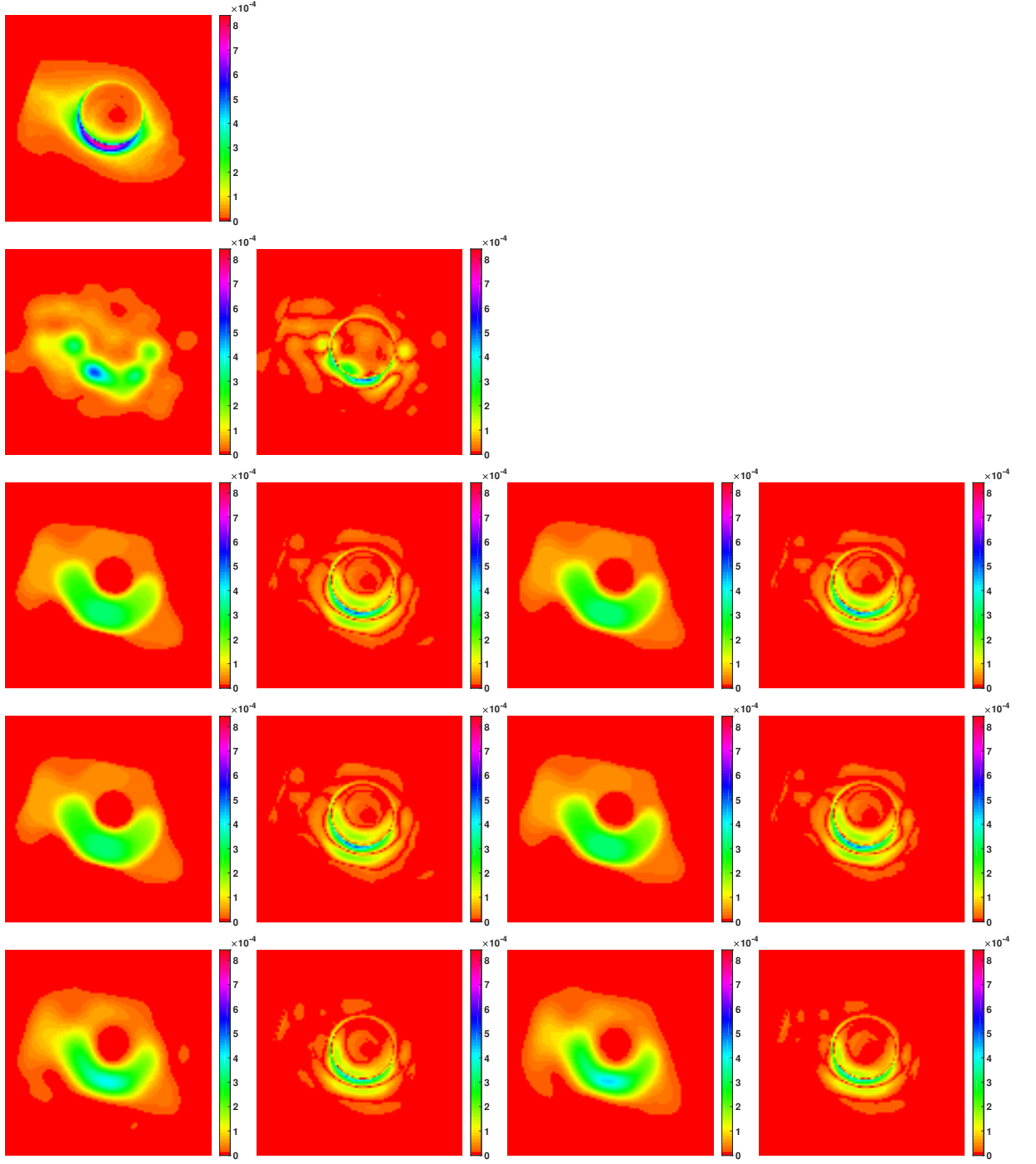


FIGURE 5.8: Results for the Stokes I counter-jet model image. First row shows the ground-truth image, whereas the second row shows the CS-CLEAN reconstructed image followed by its error image. Third, fourth and fifth rows show the results for the TV, ℓ_1 +TV problems and Polarized SARA, respectively. For these rows, the first two columns show the reconstructed and the error images obtained without imposing the polarization constraint in the reconstruction process, whereas the corresponding images in the case of imposing this constraint are shown in the last two columns. The shown images correspond to the best results obtained over 5 performed simulations for each case. All the images are shown in linear scale, normalized to the scale of the corresponding ground truth image.

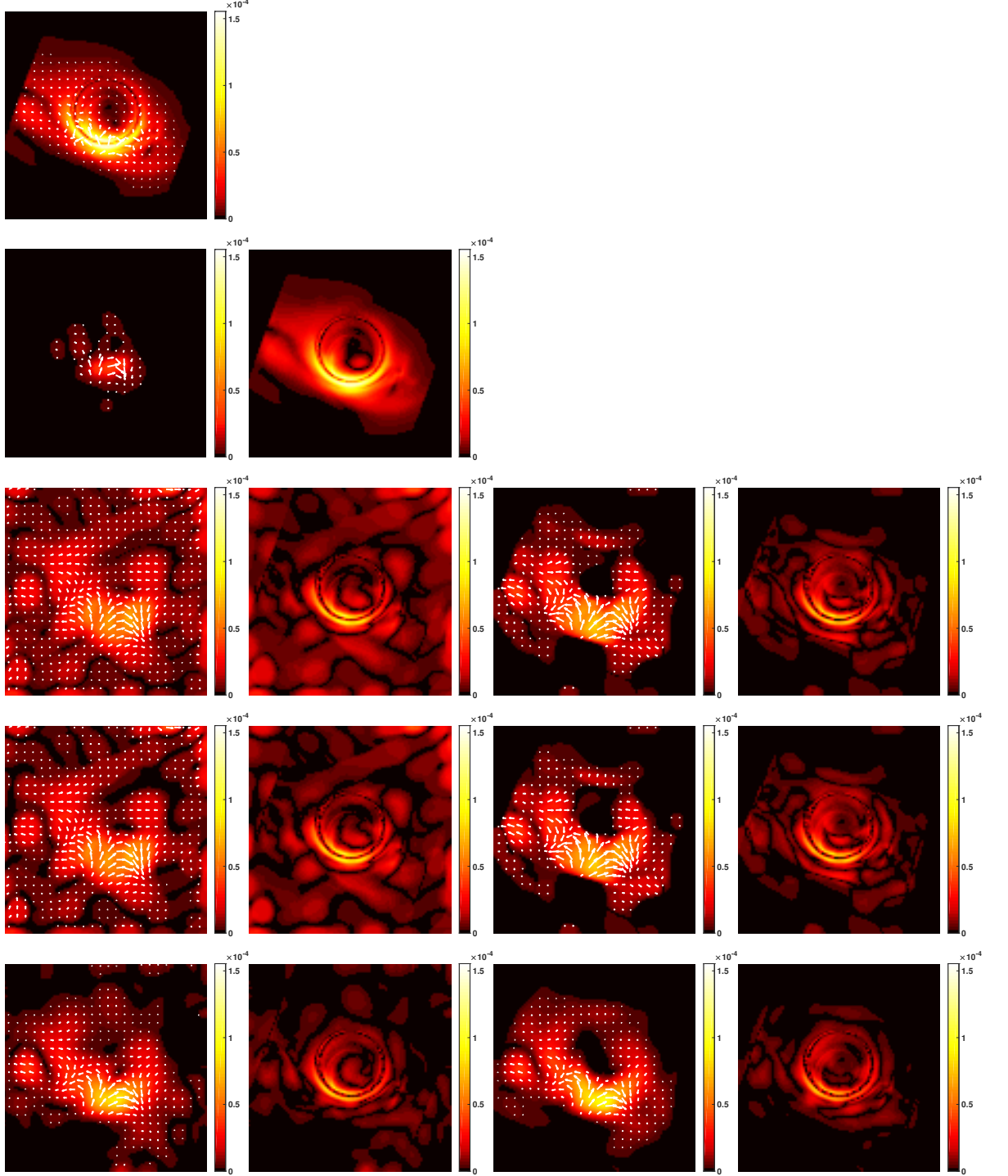


FIGURE 5.9: Results for the linear polarization counter-jet model image (linear polarization intensity images, overlaid by the white bars representing the EVPA). First row shows the ground-truth image, whereas the second row shows the CS-CLEAN reconstructed image followed by its error image. Third, fourth and fifth rows show the results for the TV, ℓ_1 +TV problems and Polarized SARA, respectively. For these rows, the first two columns show the reconstructed and the error images obtained without imposing the polarization constraint in the reconstruction process, whereas the corresponding images in the case of imposing this constraint are shown in the last two columns. The shown images correspond to the best results obtained over 5 performed simulations for each case. All the images are shown in linear scale, normalized to the scale of the corresponding ground-truth image.

5.7, respectively for the intensity image I and the linear polarization image P . In both the figures, the first row shows the ground truth image, whereas the second row shows the CS-CLEAN reconstruction followed by its error image. For the CS-CLEAN reconstruction, the shown image corresponds to the model image convolved with the restoring beam of FWHM size giving the minimum error for this method. The last three rows display the results for the TV, $\ell_1 + \text{TV}$ problem and Polarized SARA, respectively. In particular, the first two columns in these rows show the reconstructed and the error images obtained in the absence of enforcing the polarization constraint, whereas in its presence, the respective images are shown in the last two columns. In the same manner, the results for the intensity image and the linear polarization image for the counter-jet model are shown in Figures 5.8 and 5.9, respectively.

Comparing the different regularizations from these figures, we can observe that the reconstructions obtained using the TV and $\ell_1 + \text{TV}$ regularizations are similar, while employing the SARA regularization leads to a better reconstruction quality. First, in the case of the intensity image, for both forward and counter-jet models, the central region is much more resolved for the SARA regularization. It is in contrast with the reconstructions obtained by the TV and $\ell_1 + \text{TV}$ regularizations, where only the sharp edges are retained, leading to the staircase effect. One can recall that this effect arises due to the definition of the TV regularization, which tends to promote piece-wise constant images. Second, for the linear polarization images, while all the regularizations produce diffuse emission in the background, these artefacts in the background are lower in the case of SARA regularization. In particular for the counter-jet model, the SARA regularization performs significantly better than the other two. It is to be noted that with the same noise variance, the low intensity values of this model provides lesser signal-to-noise ratio than the forward-jet model images. Thus, the image reconstruction is much more challenging in this case. The superiority of the SARA regularization over other regularizations in reconstructing these images is also supported by the error images. All these images shown in the linear scale, one can notice that for the TV and $\ell_1 + \text{TV}$ regularizations, these images have more residual, especially in the background. Furthermore, for the CS-CLEAN reconstructions, it can be observed that the reconstruction quality is worse than that obtained by using any

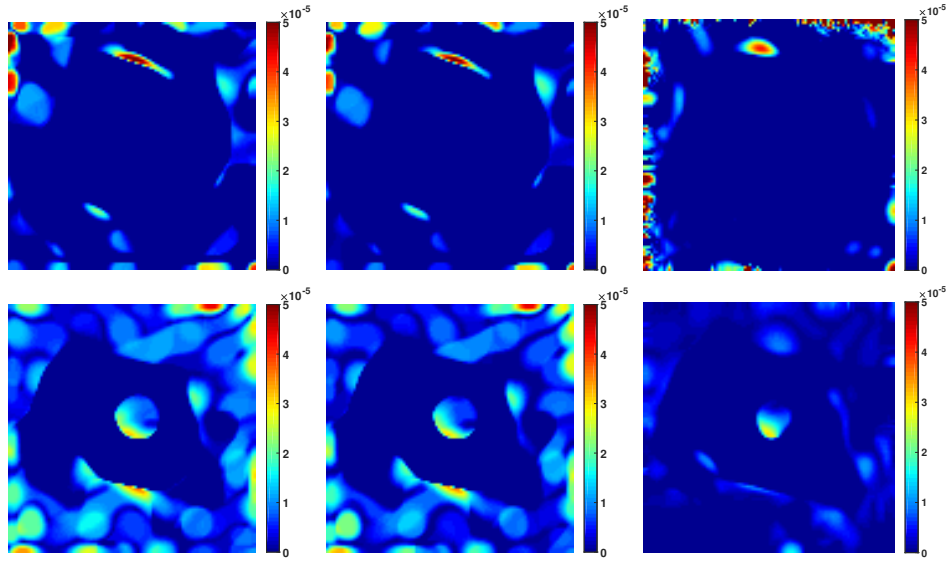


FIGURE 5.10: The polarization error images for the forward-jet model (first row) and the counter-jet model (second row) showing the pixels where the polarization constraint is not satisfied. These images are computed from the reconstructions obtained from the TV problem without constraint (first column), $\ell_1 + \text{TV}$ problem without constraint (second column) and Polarized SARA without constraint (third column). All the images are shown in linear scale. It is to be mentioned here that in the case of imposing this constraint, the corresponding polarization error images only have around 0.5 % non-zero pixels, as ensured by the stopping criterion.

other sparsifying regularization, especially for the linear polarization image, validating the high errors observed in Figure 5.5. These observations are consistent with those obtained in other studies [125, 133, 165].

Regarding the comparison between the cases with and without polarization constraint, reduction in the artificial diffuse background emission, especially for the linear polarization images, by enforcing the constraint can be noticed from the presented results. This is supported by the visual inspection of the results as well as by the lower residual in the error images. In particular for linear polarization images of counter-jet model, there is an appreciable improvement in the reconstruction quality for the TV and $\ell_1 + \text{TV}$ regularizations.

The results show the suitability of the SARA regularization for EHT imaging. Moreover, the use of the polarization constraint not only imposes the physical coherency between the reconstructed images, but it also tends to improve the reconstruction quality, independently of the choice of the sparsifying regularization. The latter is

even more evident in the reconstruction of the the images with low signal-to-noise ratio, as observed for the linear polarization images for the counter-jet model. Furthermore, it is to be noted that the non-physical reconstructions obtained in the absence of the constraint are more likely to appear in the background where the total intensity image has smaller values. To illustrate this assertion, the corresponding polarization error images are presented in Figure 5.10 for the forward and counter-jet models, respectively in first and second columns. As previously mentioned, these images basically show the pixels where the polarization constraint is not satisfied by the reconstructed Stokes images. Having only 0.5 % (corresponding to the chosen stopping criterion) of such undesirable pixels, we do not show the polarization error images obtained in the presence of the constraint. In Figure 5.10, the images are shown column-wise for the following: TV problem without constraint (first column), $\ell_1 + \text{TV}$ problem without constraint (second column) and Polarized SARA without constraint (third column). It can be clearly seen from these images that not imposing the constraint leads to the reconstruction of many pixels with physically unacceptable values. Another observation is regarding the SARA regularization, which performs better in suppressing these pixels than the other two regularizations, coherent with the values in Table 5.2.

5.5 Generalization to real data

While the numerical experiments in the previous section provided a proof of concept for the Polarized SARA method, we apply it to real data in the current section. In this context, we exploit the parallel data-block strategy and preconditioning scheme in Algorithm 1. Let us recall that the latter is used to accelerate the convergence of the algorithm by utilizing additional prior information about the data. In the considered settings, it takes into account the Fourier sampling density, mimicking the uniform weighting scheme in RI [14].

As discussed in Section 5.3.2, by the incorporation of this preconditioning matrix, the proximity operator of the data fidelity term reduces to a projection onto the ellipsoid \mathbb{L}_j that requires the knowledge of the bounds ϵ_j for each data block. However, when

dealing with real data sets, the measurement model and in particular, the noise model may not be perfectly known. In practice, these bounds not only incorporate the thermal noise, but also the calibration errors which are unknown. To address this

Algorithm 4 Adaptive scheme for ℓ_2 bound update

```

1: given  $\tilde{\mathbf{S}}^{(k+1)}, \tilde{\mathbf{S}}^{(k)}, \mathbf{Y}'_j, \Phi'_j, k, \epsilon_j^{(k)}, t_j^{(k)}, K' \in \mathbb{N}, (\varepsilon_1, \varepsilon_2) \in \mathbb{R}_+^2$ , and  $\varepsilon_3 \in ]0, 1[$ .
2:  $\Delta = \frac{\|\tilde{\mathbf{S}}^{(k+1)} - \tilde{\mathbf{S}}^{(k)}\|_F}{\|\tilde{\mathbf{S}}^{(k+1)}\|_F}$ 
3:  $\mu_j = \|\mathbf{Y}'_j - \Phi'_j(\tilde{\mathbf{S}}^{(k+1)})\|_F$ 
4: if  $\Delta < \varepsilon_1$  &  $(k - t_j^{(k)} \geq K')$  &  $\left(\frac{\|\mu_j - \epsilon_j^{(k)}\|_2}{\epsilon_j^{(k)}} > \varepsilon_2\right)$ 
5:    $\epsilon_j^{(k+1)} = \varepsilon_3 \mu_j + (1 - \varepsilon_3) \epsilon_j^{(k)}$ 
6:    $t_j^{(k+1)} = k$ 
7: else
8:    $\epsilon_j^{(k+1)} = \epsilon_j^{(k)}$ 
9:    $t_j^{(k+1)} = t_j^{(k)}$ 
10: end if
11: return  $\epsilon_j^{(k+1)}, t_j^{(k+1)}$ 

```

issue, we leverage the noise bound estimation adaptive scheme proposed in [11] while performing Stokes I imaging. Applying it to our case of full polarization imaging, we present it as Algorithm 4. More specifically, at each iteration k of Algorithm 1, step 16 performs this ℓ_2 bound update for each data block j by calling Algorithm 4. In this algorithm, ϵ_j is updated in step 5 as a weighted mean of the current value of this bound $\epsilon_j^{(k)}$ and the ℓ_2 norm of the corresponding residual data block μ_j . This update is only performed if (i) the relative variation between two consecutive estimates of the Stokes images (Δ in step 2) is below a fixed threshold ε_1 , (ii) a minimum number of iterations K' has been executed and, (iii) the relative difference between μ_j and $\epsilon_j^{(k)}$ is above a fixed threshold ε_2 . It is important to highlight that with every update of the ℓ_2 bound, the underlying minimization problem is redefined. Nonetheless, the stability of this adaptive scheme is ensured by avoiding unnecessary updates that are performed only if the aforementioned conditions are met.

For the initialization $\epsilon_j^{(0)}$ of the epsilon bounds, we solve a non-negative least squares (NNLS) problem for each of the data blocks. The initial values for the bounds ϵ_j

are then provided by the ℓ_2 norms of the obtained residuals. Conceptually, in the absence of any regularization term, the estimates obtained by the NNLS are likely to be overfitting the data, leading to under-estimated bounds. With the introduction of the priors (sparsity and polarization constraint) and the adaptive noise bound estimation scheme, these bounds tend to increase to the true values in an adaptive manner.

5.6 Results on real data

We apply our method on VLA observations of the radio galaxy Cygnus A, performed over the period 2015-2016. The data consists of measurements made in X band (8-12 GHz) with a spectral window of 128 MHz and a spectral resolution of 2 MHz. The data set used for the current study corresponds to the single-channel observations centred at the frequency 8.422 GHz, taken with the VLA in B-configuration. The total synthesis time of the observations is 3 hr, with integration time of 2 s. The phase centre of the observed sky is given by RA = 19^{hr} 59^m 28.356^s (*J*2000) and DEC = +40° 44' 2.07". The size of the processed data set is $M = 3.6 \times 10^5$. We implement Algorithm 1 in MATLAB to image the Stokes parameters I , Q and U (Stokes V being of negligible intensity), each of size 1024×1024 pixels with the corresponding pixel size $\delta l = 0.16''$. It corresponds to recovering the images at 1.5 times the nominal resolution, i.e. the interferometric resolution determined by the maximum baseline. We split the dataset into three blocks and perform 15 reweighting iterations in total, where each iteration is stopped when the relative variation between consecutive estimates of the Stokes images is less than 10^{-5} , and the percentage of pixels (in the estimated images) not satisfying the polarization constraint is less than 0.1.

We compare our method with the RI imaging algorithm MS-CLEAN with Briggs weighting, implemented in the WSCLEAN package [117]. For visual comparison, Figure 5.11 shows the reconstructed images for Stokes I (first column) and the linear polarization intensity image $|P|$ (second column), generated from the reconstructed Stokes Q and U images. We scale recovered images from our method with the flux of the CLEAN beam, and since the MS-CLEAN restored images are dominated by the

noise, we also show the beam convolved model images. The shown images are cropped to the size 512×1024 pixels. Furthermore, in Figure 5.12, we display the zoomed west jet hotspot (marked with a white box in the associated full images in Figure 5.11). The results indicate the super-resolution capability of our method, capturing the finer details in the source structure, in contrast with MS-CLEAN which provides images at the nominal resolution by convolving with the CLEAN beam. Moreover, the model images from MS-CLEAN have around 15% of the pixels with non-physical values, violating the polarization constraint. This holds true for the restored images as well, having around 28% of such pixels, as illustrated in Figure 5.13. It is interesting to note that such pixels are mostly observed in the background region where we do not expect emission and can be attributed primarily to the added residual. Nevertheless, these observations are in contrast with our method which explicitly enforces the polarization constraint and thus, is bound to produce images with physical values.

Additionally, comparing our method's reconstruction with the MS-CLEAN model image, both smoothed at the nominal resolution, gives a similarity of 29.4 dB for Stokes I and 19.3 dB for linear polarization image. It implies that the reconstructions from the two methods, especially for Stokes I , are in agreement in terms of their low spatial frequency content.

5.7 Conclusion

We have presented a new method, named Polarized SARA, for joint estimation of sparse Stokes images in the context of RI, considering explicitly the polarization constraint. The latter is used to exploit the physical link between the Stokes images, imposing the polarization intensity as a lower bound on the total intensity. We have proposed to deal with this constraint using the techniques of epigraphical projection, solving for a convex optimization problem. In addition, our method leverages the sparsity of the underlying images using SARA regularization which consists in promoting the average sparsity of each Stokes parameter using the weighted ℓ_1 norm encompassed in a reweighted scheme. Thanks to this weighting, the proposed method does not require the tuning of any regularization parameter and only the noise bound

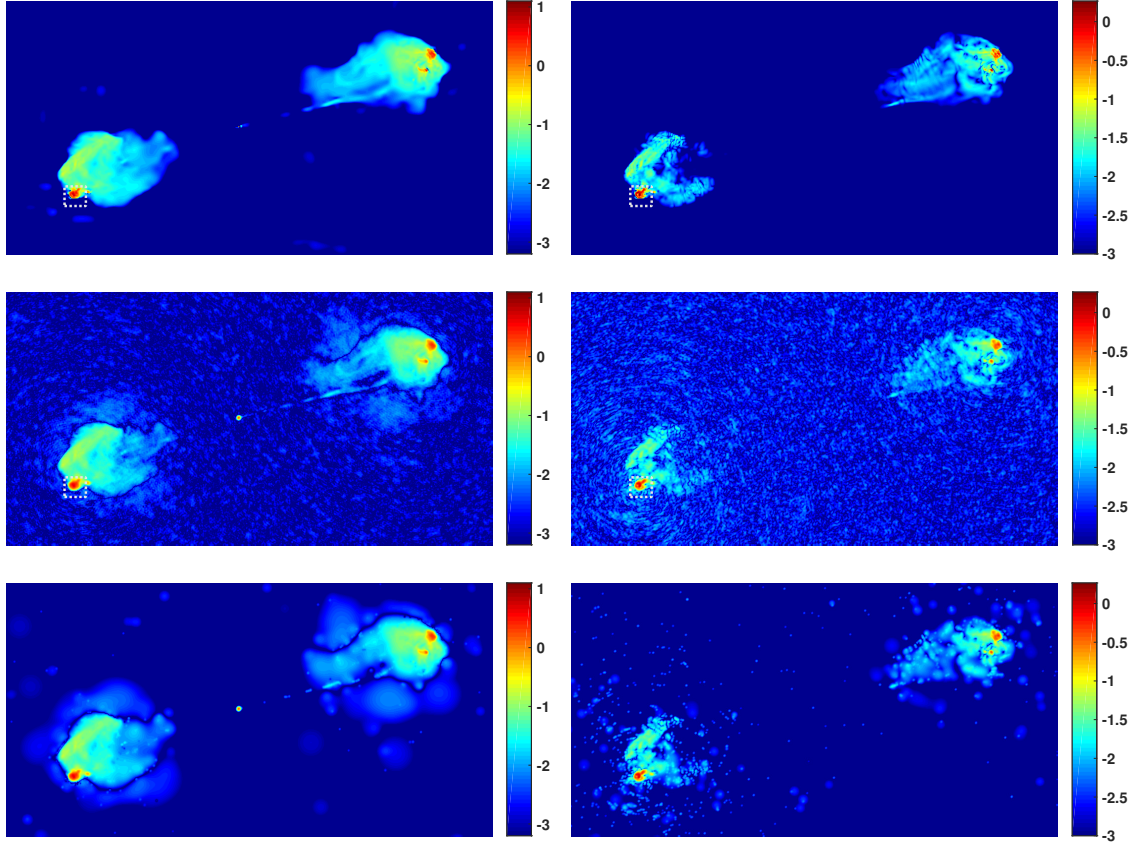


FIGURE 5.11: Results obtained for Stokes I (first column) and linear polarization intensity ($|P|$) (second column) images, displayed in log scale. Row-wise, from top to bottom: Polarized SARA reconstructed images, MS-CLEAN restored images using Briggs weighting, and CLEAN beam convolved model images of MS-CLEAN using Briggs weighting.

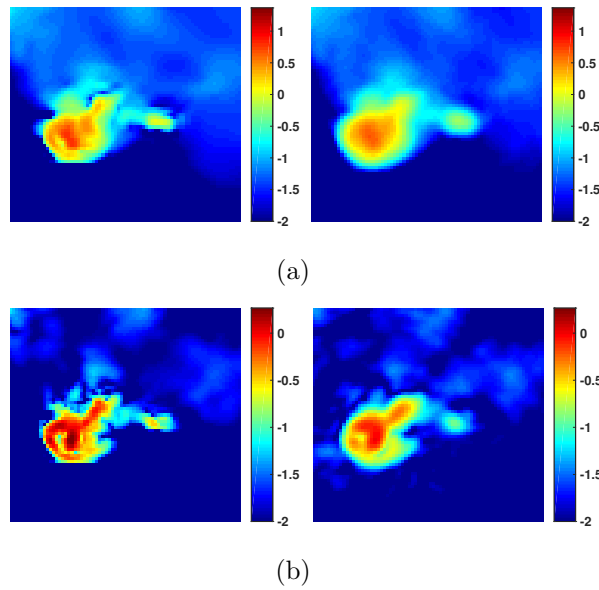


FIGURE 5.12: Zoomed west jet hotspot in (a) Stokes I and (b) linear polarization intensity images from our method's reconstructions (first column) and MS-CLEAN restored images (second column). All the images are shown in log scale.

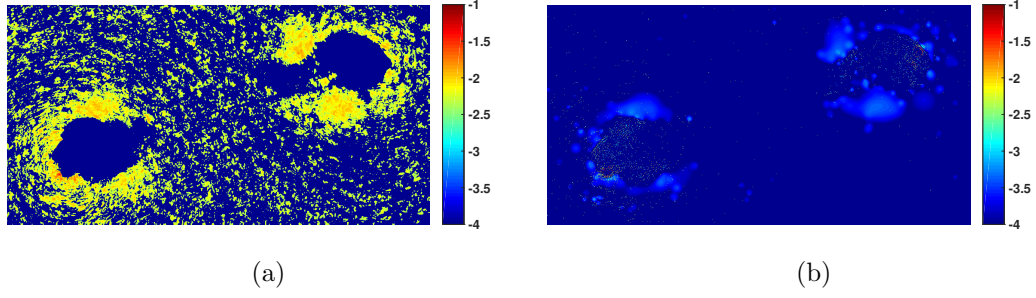


FIGURE 5.13: Polarization error images showing the pixels in the image ($|P| - I$) violating the polarization constraint, corresponding to MS-CLEAN (a) restored and (b) model images. All the images are shown in log scale.

needs to be specified. To solve the resultant image reconstruction problem, we have designed an iterative proximal primal-dual algorithm. In this respect, the proposed approach presents the first application of sparsity based optimization techniques for the reconstruction of Stokes images, taking into account the polarization constraint within a convex formulation. Moreover, our algorithm presents a highly versatile structure. On the one hand, this allows the incorporation of different sparsifying regularizations in the algorithm. On the other hand, this renders scalability of the method by employing distributed and parallel processing coupled with a preconditioning strategy. The MATLAB code of the proposed method is available on GitHub (<https://basp-group.github.io/Polarised-SARA/>).

To investigate the performance of the proposed Polarized SARA method, we have applied it on the simulated EHT datasets. For the choice of sparsifying regularization, apart from the SARA regularization, we have also considered the TV and $\ell_1 + \text{TV}$ regularizations, the latter two being suggested in [165] for full-polarization EHT imaging. To judge the effect of the polarization constraint on the reconstruction quality, we have also generalized the problem considered in [165] to take into account this constraint. It is solved using a modified version of the proposed algorithm. It is to be noted that this generalization provides an improvement over the technique used in [165], because of its scalability, non-sub-iterative nature (especially for $\ell_1 + \text{TV}$ regularized problem) as well as the incorporation of the polarization constraint. Comparison between different cases considered, on the one hand, indicates the importance of imposing the polarization constraint in reconstructing physically acceptable images. Additionally, irrespective of the considered sparsifying regularization, the enforcement

of this constraint tends to enhance the reconstruction quality, particularly for the linear polarization images. This enhancement is significant for the results obtained by solving the TV and $\ell_1 + \text{TV}$ problems with constraint. Thus, we can conclude that the polarization constraint is highly effective in producing images not only with physical meaning, but also with fewer artefacts.

On the other hand, regarding the choice of sparsifying regularization, the results demonstrate the ability of the SARA regularization to produce images with better reconstruction quality and higher resolution, without requiring the convolution of the reconstructed images with any restoring beam. First, for Stokes I imaging, for which this regularization was initially proposed, its good performance is in agreement with the previous studies [14, 24, 45]. These reconstructions also prevail over those obtained by the standard CS-CLEAN algorithm. Second, the obtained results also highlight the suitability of SARA regularization for polarimetric imaging. Indeed, Polarized SARA yields better results for the considered datasets than solving the TV-based problems, both with and without the constraint. Thus, the proposed Polarized SARA method stands out as a promising candidate for polarimetric imaging in RI.

Finally, we have tested the developed method on a real data set. It shows the superiority of our method over MS-CLEAN, both in terms of encapsulating the source structure details going beyond the nominal resolution, and in producing physical images satisfying the polarization constraint.

Chapter 6

Self DDE calibration and imaging for radio interferometry

Contents

6.1	Motivation	112
6.2	Stokes I imaging and DDE calibration	113
6.2.1	Description of the proposed method	113
6.2.2	Simulations and results	117
6.2.3	Sparse images with point sources	119
6.2.4	Image with an extended source	123
6.3	Concluding remarks	125
6.4	Full polarization DDE calibration and imaging	126
6.4.1	Calibration problem	128
6.4.2	Polca SARA - Proposed calibration & imaging approach . .	131
6.4.3	Algorithm formulation	133
6.4.4	Convergence properties	138
6.4.5	Computational complexity	139
6.5	Simulations and results	140
6.5.1	Comparisons performed	141
6.5.2	Simulation settings	143
6.5.3	Results and analysis	144
6.6	Conclusion	157

This chapter has been adapted from the published works [27], [28], [29] and [30] (submitted).

6.1 Motivation

The RI measurements, in practice, rather than providing an accurate representation of the true sky distribution, are corrupted by various atmospheric and instrumental effects that are often unknown. To produce high fidelity, high dynamic range images from the given measurements, calibration of these unknown effects is of utmost importance. In fact in the wake of new generation radio interferometers, the direction-dependency of the calibration terms (the DDEs) needs to be accounted for. Conventionally, calibration and imaging have been considered as two separate processes implemented using their respective techniques, but linked together in an iterative approach like selfcal. In this respect, any of the existing calibration approaches is usually combined with a CLEAN based imaging strategy within a selfcal loop. However, by doing so, the global algorithm fails to have any convergence guarantees. We make the first step in the direction of addressing this issue and propose a joint DDE calibration and imaging algorithm that leverages recent non-convex optimization techniques and benefits from convergence guarantees. The basic idea behind the developed approach is to alternate between the estimation of the images of interest and the DDEs, relying on an iterative structure using the same optimization toolbox for both the images and the DDEs estimation. In addition to the convergence guarantees, unlike the approaches requiring sky partitioning that may not always be best achieved in an automatic manner, the key point of our algorithm is that it works globally on the whole image with minimal user intervention.

In the first part of this chapter, without delving into the mathematical details, I describe the developed approach considering only the model for Stokes I imaging and calibration. Grasping the main idea and inspired by the achieved promising performance of this approach, I provide a detailed presentation of the proposed generalization to the full polarization model in the next part.

6.2 Stokes I imaging and DDE calibration

6.2.1 Description of the proposed method

Before going onto the challenging case of full polarization model, we first consider the case when the sky is considered to be unpolarized and only Stokes I imaging needs to be performed. In this respect, the 2×2 Jones matrix is often replaced by a scalar value and instead of using the whole Stokes matrix, the Stokes I image is represented by $\bar{\mathbf{x}} \in \mathbb{R}^N$ for notational brevity. The observation model (2.19) can then be simplified. In particular, the visibility $y'_{t,\alpha,\beta} \in \mathbb{C}$ measured by the antenna pair (α, β) at time instant t at the discrete spatial frequency $k_{t,\alpha,\beta}$ can be modelled as

$$y'_{t,\alpha,\beta} = \sum_{n=-N/2}^{N/2-1} \bar{d}_{t,\alpha}(n) \bar{d}_{t,\beta}(n)^* \bar{x}(n) e^{-2i\pi k_{t,\alpha,\beta} \frac{n}{N}} + \omega'_{t,\alpha,\beta}, \quad (6.1)$$

where $\bar{\mathbf{d}}_{t,\alpha} = (\bar{d}_{t,\alpha}(n))_{-N/2 \leq n \leq N/2-1} \in \mathbb{C}^N$ is the sampled DDE related to antenna α , and $\boldsymbol{\omega}' = (\omega'_{t,\alpha,\beta})_{\substack{1 \leq t \leq T \\ 1 \leq \alpha < \beta \leq n_a}} \in \mathbb{C}^M$ is a realization of a complex i.i.d. Gaussian additive noise. In practical scenarios, the DDEs are unknown. Thus, in order to obtain the sought image using this data model, both the image and the DDEs need to be estimated. In this context, the underlying minimization problem is non-convex, and adapted techniques have to be designed. To this end, inspired by the imaging techniques using optimization and CS theories, and the alternating calibration method StEFCal (Section 4.3), we propose the first joint calibration and imaging method in RI, with proven convergence guarantees.

First, for the imaging step, we consider the matrix formulation of problem (6.1), given by $\mathbf{y}' = \bar{\mathbf{G}}\mathbf{F}\bar{\mathbf{x}} + \boldsymbol{\omega}'$, where \mathbf{F} is the Fourier matrix and $\bar{\mathbf{G}}$ is the matrix containing on each row the antenna-based gain related to each antenna pair acquiring the complex visibilities. In the case of a perfectly calibrated antenna array (i.e. $\bar{\mathbf{G}}$ is known), the imaging problem is linear and can be solved efficiently using convex optimization methods as previously discussed in Section 3.4. For instance, FB algorithm presents a simple technique to solve the underlying minimization problem consisting of data fidelity and regularization terms. Moreover, in the considered case of unknown DDEs

where joint calibration and imaging needs to be performed, the non-convexity of the underlying optimization problem demands for a critically chosen initialization as per the discussion in Section 3.5.1. With this in mind, we make use of the prior information on the bright sources of the original image. We note that this assumption is common in the context of DDE calibration methods [15, 16], and is useful to reduce the ambiguity problems appearing between the image and the DDEs [149]. More precisely, we assume that the original image $\bar{\mathbf{x}}$ can be split as a sum of two images \mathbf{x}_0 and $\bar{\epsilon}$, where \mathbf{x}_0 is assumed to be known exactly, while $\bar{\epsilon}$ has to be estimated.

Second, for the calibration step, we generalize the inverse problem used by StEF-Cal (4.2) in order to take into account the DDEs in \mathbf{C}_1 and \mathbf{C}_2 . To this aim, we assume that the DDEs are smooth functions across the field of view, i.e. they are spatially band-limited (see Figure 6.1). Therefore, we propose to reduce drastically the dimensionality of the problem by estimating only the non-zero Fourier coefficients of the DDEs, now represented by compact-support kernels $\check{\mathbf{U}}$. Furthermore, following [171] we adopt a bi-linear inverse calibration problem by introducing $\check{\mathbf{U}}_1 = \check{\mathbf{U}}_2 = \check{\mathbf{U}}$.

Finally, instead of using two different algorithms to estimate the DDEs and the image, respectively, we design a joint framework. In essence, this joint method involves alternating between the estimation of $\check{\mathbf{U}}_1, \check{\mathbf{U}}_2$ and the faint sources $\bar{\epsilon}$ contained in $\bar{\mathbf{x}}$, using the same algorithmic structure, based on the FB iterations. To do so, we propose to

$$\underset{\epsilon, \check{\mathbf{U}}_1, \check{\mathbf{U}}_2}{\text{minimize}} \ h_1(\epsilon, \check{\mathbf{U}}_1, \check{\mathbf{U}}_2) + r_1(\epsilon) + p_1(\check{\mathbf{U}}_1, \check{\mathbf{U}}_2), \quad (6.2)$$

where h_1 is the data-fidelity term corresponding to a least-squares criterion, r_1 and p_1 are the regularization functions for the image and the DDEs, respectively. In particular, r_1 is chosen to constrain the image to be positive and to promote sparsity either directly in the image domain or in a given dictionary. Concerning the DDEs, p_1 is chosen to incorporate constraints on the direction-dependent Fourier coefficients, and to control the similarities between $\check{\mathbf{U}}_1$ and $\check{\mathbf{U}}_2$.

Recalling the discussion in Section 3.5.1, it can be observed that problem (6.2) is non-convex with respect to the concatenation of the variables $(\epsilon, \check{\mathbf{U}}_1, \check{\mathbf{U}}_2)$, but is convex

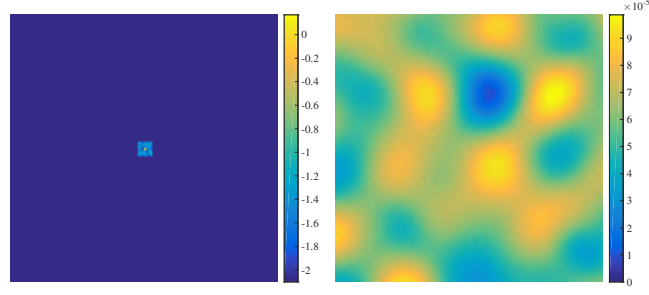


FIGURE 6.1: Example of considered DDEs, with $K = 7 \times 7$ non-zero Fourier coefficients. Modulus of (left) the Fourier transform of the DDE $\widehat{\bar{\mathbf{d}}}_{t,\alpha}$ in log scale, and (right) the DDE $\bar{\mathbf{d}}_{t,\alpha}$ in image space in linear scale.

with respect to each of them. In other words, keeping $(\check{\mathbf{U}}_1, \check{\mathbf{U}}_2)$ [resp. $(\epsilon, \check{\mathbf{U}}_2)$ and $(\epsilon, \check{\mathbf{U}}_1)$] fixed, problem (6.2) is convex with respect to the variable ϵ (resp. $\check{\mathbf{U}}_1$ and $\check{\mathbf{U}}_2$). Exploiting this block-structure of the underlying problem, we propose to solve it using an iterative method based on a block-coordinate FB approach that benefits from the convergence guarantees [107]. More precisely, at each iteration, we first estimate approximately the DDEs computing a fixed number of FB iterations, and then estimate approximately the image again using FB iterations. It is important to emphasize that, as a particular case, the proposed approach can be applied to solve the joint DIE calibration and imaging problem.

It is interesting to note that the global structure of the proposed algorithm is very similar to the traditional selfcal method, since they both aim to alternate between the estimation of the gains and the estimation of the image. To illustrate the similarities and differences between the two methods, diagrams depicting the relevant steps of the proposed method and the traditional selfcal method are given in Figure 6.2 (left) and (right), respectively¹. One can observe that the global structure of the two diagrams are very similar, but they differ in the structure of the inner-loops. In particular, in our method, $J_{\text{cyc}} - 1$ inner-loops are performed to estimate *approximately* the DDEs $(\check{\mathbf{U}}_1, \check{\mathbf{U}}_2)$. Within each of these inner-loops, $J_{\check{\mathbf{U}}_1}$ FB steps are performed to estimate $\check{\mathbf{U}}_1$, followed by $J_{\check{\mathbf{U}}_2}$ FB steps to estimate $\check{\mathbf{U}}_2$. Importantly, $J_{\check{\mathbf{U}}_1}$ and $J_{\check{\mathbf{U}}_2}$ are finite so as to have *approximate* estimations of $\check{\mathbf{U}}_1$ and $\check{\mathbf{U}}_2$, respectively. Then, to complete one global iteration (i.e. a *cycle*), J_ϵ FB steps are performed to estimate *approximately* the

¹The selfcal method presented in this diagram consists in alternating between the StEFCal algorithm and CLEAN. However, StEFCal can be coupled with other imaging methods as well.

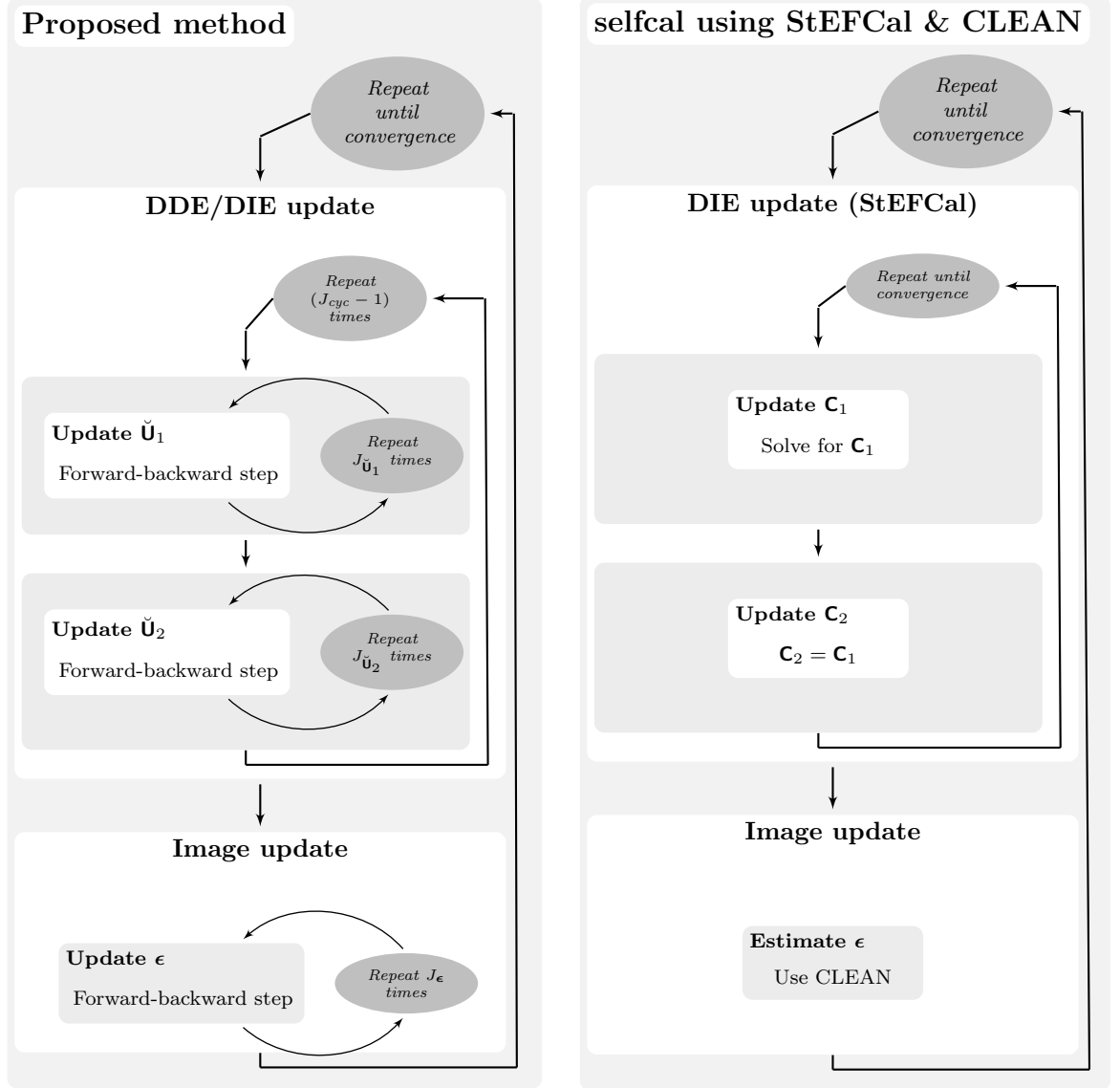


FIGURE 6.2: The diagrams of the proposed method (left) and the traditional selfcal method using StEFCal and CLEAN (right). In the proposed method, only a finite number of iterations are performed to estimate $\check{\mathbf{U}}_1$, $\check{\mathbf{U}}_2$, and ϵ , given by $J_{\check{\mathbf{U}}_1} \in \mathbb{N}$, $J_{\check{\mathbf{U}}_2} \in \mathbb{N}$, and $J_\epsilon \in \mathbb{N}$ respectively. The parameter $J_{cyc} \in \mathbb{N}$ gives the number of sub-iterations performed on the DDEs before estimating the image. The structure of the two methods is very similar consisting in alternating between the estimation of the DIEs (and possibly the DDEs for the proposed method) and the estimation of the image. The main differences are: (i) our method uses the same FB based steps to estimate both the DDEs and the image, while the selfcal method uses two independent techniques to estimate them, and (ii) unlike the selfcal method, our method computes only a finite number of sub-iterations in each inner-loop. These two differences are crucial to ensure the convergence of the global proposed method.

image ϵ . It is worth highlighting that computing only *approximated* estimates is very important in practice to ensure the convergence of the overall algorithm. Intuitively, one can understand this point as follows: when the algorithm is initialized with a very poor estimation of the image, it is obvious that estimating *completely* the DDEs from this incorrect image can be inefficient. Therefore, it is important to control the accuracy of the estimates at each iteration in order to make the overall algorithm converge step by step for the image and the DDEs together. This adopted methodology for approximate estimates is different from the traditional selfcal method, where the problem of estimating the gains (restricted to DDEs) is solved *completely* before solving the imaging problem, and *vice versa*. As explained above, this strategy can lead to poor reconstruction results. Furthermore, the calibration part is different from the StEFCal approach where we instead adopt a FB approach. Using a FB-based algorithm allows us to introduce constraints on the DDEs. Moreover, StEFCal is an *implicit* method, stating directly that the update of \mathbf{C}_2 is equal to \mathbf{C}_1 , whereas our method updates independently the variables $\check{\mathbf{U}}_1$ and $\check{\mathbf{U}}_2$. Thus, in order to constrain them to be equal at convergence, the distance between $\check{\mathbf{U}}_1$ and $\check{\mathbf{U}}_2$ is *explicitly* controlled in the minimization problem. Finally, StEFCal is only designed for DIE calibration, while our method jointly corrects for the DDEs and estimates the image. It can be noted that traditional selfcal method does not benefit from the convergence guarantees of the proposed method since both rely on different algorithmic structures. Therefore, our method can be seen as generalizing the framework of selfcal, with theoretical convergence guarantees.

6.2.2 Simulations and results

To investigate the performance of our method, we conducted an extensive study by considering a wide variety of cases, varying parameters for both the calibration and the imaging part. Concerning the uv coverage, we consider n_a randomly distributed antennas, where each antenna pair acquires T measurements. The Earth rotation is incorporated to track the (u, v) positions of each resulting baseline by considering a time interval of 10 hours². Moreover, in order to simplify the experiments, we

²The uv tracks are simulated using the code available at <http://www.astro.umd.edu/~cychen/MATLAB/ASTR410/uvAndBeams.html>

use discrete versions of the associated uv coverages, done by considering the nearest discrete (u, v) position of each antenna. This approximation is adopted in order to avoid introduction of gridding and degridding operations to model the non-uniform FFT in this first presentation of the proposed DDE selfcal algorithm. Regarding the DDE kernels for each antenna and at each time instant, we simulate them randomly in the Fourier domain, with their real and imaginary parts lying around ± 1 for DIEs and in the neighbourhood of 0 for DDEs (in both cases with standard deviation v). It can be noticed that it is reasonable to consider small values for the higher order spatial frequencies since they represent direction-dependent variations in the gain across the field of view with respect to the mean gain. Furthermore, the size K of the support of the direction-dependent Fourier coefficients is assumed to be known exactly. Lastly, keeping in mind the sensitivity of the final solution to the initialization for the underlying non-convex optimization algorithm, we first perform joint DIE calibration and imaging, where the former implies estimation of only the central zero coefficients of the DDE Fourier kernels themselves initialized randomly. The obtained solutions are then used to initialize the algorithm jointly solving for the full support of the DDEs and the image.

To validate the performance of our approach, I present here two main classes of results obtained, considering images with point sources and the image with sophisticated extended sources. In both cases, I display the results obtained using our method to reconstruct the DDEs and the image ϵ , the results obtained with the StEFCal algorithm solving only for the DIEs, and combined with an imaging method based on the FB iterations, referred to as StEFCal-FB.

To assess the reconstruction quality, we use SNR of the reconstructed image ϵ^* with respect to the original image $\bar{\epsilon}$ and the ℓ_2 norm of the residual images, obtained either considering the estimated DDEs or the true DDEs. More precisely, we will consider the weighted ℓ_2 norm of the residual images $\|\mathbf{F}^\dagger \mathbf{G}^{\star\dagger} (\mathbf{G}^* \mathbf{F} \mathbf{x}^* - \mathbf{y}')\|_2 / \sqrt{N}$, where $\mathbf{x}^* = \mathbf{x}_o + \epsilon^*$ corresponds to the global estimated image and \mathbf{G}^* corresponds to the estimated DDEs. Similarly, we will consider the weighted ℓ_2 norm of the residual images $\|\mathbf{F}^\dagger \bar{\mathbf{G}}^\dagger (\bar{\mathbf{G}} \mathbf{F} \mathbf{x}^* - \mathbf{y}')\|_2 / \sqrt{N}$, where the matrix $\bar{\mathbf{G}}$ corresponds to the original

DDEs. The latter metric is used in order to point out the ambiguity problems which can appear between \mathbf{x}^* and \mathbf{G}^* , i.e. due to the imaging inverse problem formulation, parts of \mathbf{x}^* can be absorbed in \mathbf{G}^* , and *vice versa*.

6.2.3 Sparse images with point sources

In this first part, we consider simulated sky images, $\bar{\mathbf{x}} (= \mathbf{x}_o + \bar{\boldsymbol{\epsilon}})$ of size 128×128 , consisting of point sources, where each source corresponds to a small 2D Gaussian kernel of size 3×3 . We assume that \mathbf{x}_o corresponds to 10 bright sources generated randomly such that their total flux, computed as $E(\mathbf{x}_o) = (\sum_{n=1}^N |x_o(n)|^2)^{1/2}$, is $E(\mathbf{x}_o) = 10$. Moreover, the sources in $\bar{\boldsymbol{\epsilon}}$ are generated randomly with two intensity levels, i.e. $\bar{\boldsymbol{\epsilon}} = \bar{\boldsymbol{\epsilon}}_1 + \bar{\boldsymbol{\epsilon}}_2$, where we consider $E(\bar{\boldsymbol{\epsilon}}_2) = 10^{-5}$ and to be composed of 200 sources. The latter has sources with intensity $\sim 10^7$ weaker than the sources belonging to \mathbf{x}_o and is thus considered in our simulations as astrophysical noise, and we do not focus on its estimation. Therefore, our main objective is to find an estimate of $\bar{\boldsymbol{\epsilon}}_1$, reconstructing its faint sources. Furthermore, regarding the sparsity of the sought image that contains only point sources, it is promoted in its domain itself. Finally, we adopt an additional metric in this case in the form of a success rate counting the number of successfully recovered positions of the sources in $\boldsymbol{\epsilon}_1$, when compared with the true image $\bar{\boldsymbol{\epsilon}}_1$.

With the aim to illustrate the assertion that accounting for the DDEs is crucial for more accurate reconstruction of the images with high dynamic range [6, 149], we perform tests by varying the total flux ($E(\bar{\boldsymbol{\epsilon}}_1) \in \{10, 1, 10^{-1}, 10^{-2}, 10^{-3}\}$) and the number of sources (10, 50 and 90) belonging to $\bar{\boldsymbol{\epsilon}}_1$. Considering $n_a = 200$ antennas for a single time interval $T = 1$, and DDE Fourier kernels with support size $K = 7 \times 7$ and standard deviation set to be $v = 0.05$, the obtained results are shown in Figures 6.3 and 6.4 for quantitative and qualitative comparison, respectively,

Figure 6.3 gives the results, as a function of $E(\bar{\boldsymbol{\epsilon}}_1)$ using different metrics. In particular, the first two graphs correspond to SNR and sources' positions recovery success rate, respectively and show that, irrespective of the number of considered sources in $\bar{\boldsymbol{\epsilon}}_1$ and the value of $E(\bar{\boldsymbol{\epsilon}}_1)$, our method outperforms the StEFCal-FB method, showing

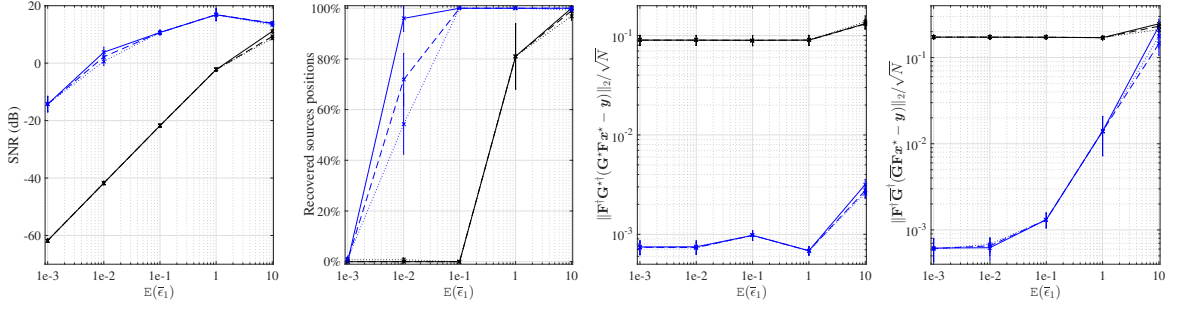


FIGURE 6.3: Results obtained for simulations using the proposed method (blue lines) and estimating only the DDEs with StEFCal-FB (black lines), considering 10, 50, and 90 sources in $\bar{\epsilon}_1$ (resp. solid lines, dashed lines, and dotted lines), varying $E(\bar{\epsilon}_1) \in \{10^{-3}, 10^{-2}, 10^{-1}, 1, 10\}$, while $E(\mathbf{x}_o) = 10$. From left to right: SNR of the reconstructed ϵ^* with respect to $\bar{\epsilon}$; Success rate determining the percentage of recovered sources positions from $\bar{\epsilon}_1$; ℓ_2 norm of the residual image $\|\mathbf{F}^\dagger \mathbf{G}^{\star\dagger}(\mathbf{G}^* \mathbf{F} \mathbf{x}^* - \mathbf{y}')\|_2 / \sqrt{N}$ considering \mathbf{G}^* obtained with the estimated DDEs; ℓ_2 norm of the residual image $\|\mathbf{F}^\dagger \bar{\mathbf{G}}^\dagger(\bar{\mathbf{G}} \mathbf{F} \mathbf{x}^* - \mathbf{y}')\|_2 / \sqrt{N}$ considering $\bar{\mathbf{G}}$ obtained with the true DDEs. Results are given for an average over 10 realizations varying the antenna distribution, the random images, and the DDEs.

the importance of reconstructing the DDEs. More precisely, on the one hand, our method is able to recover 100% of sources' positions for $E(\bar{\epsilon}_1) \in \{0.1, 1, 10\}$, with respective SNR values of 10.7, 16.9 and 13.4 dBs, independently of the number of sources belonging to $\bar{\epsilon}_1$. It is important to emphasize that, in these three cases, the reconstruction quality depends mainly on the total flux of the image and not on the intensity level of the constituting sources. Indeed, if $\bar{\epsilon}_1$ contains 90 sources with $E(\bar{\epsilon}_1) = 10$, the intensity of sources belonging to $\bar{\epsilon}_1$ is almost two times lower than the intensity of the sources in \mathbf{x}_o . On the other hand, the StEFCal-FB obtains approximately 100% success rate only in the case $E(\bar{\epsilon}_1) = 10$ with SNR value of 11 dB (resp. 9.1 dB and 8.6 dB) when 10 (resp. 50 and 90) sources belong to $\bar{\epsilon}_1$. It can be observed that the latter corresponds to the case when the sources in $\bar{\epsilon}_1$ are almost of same intensity as the sources in \mathbf{x}_o . Concerning our method, the only case when the number of sources considered in $\bar{\epsilon}_1$ gives different reconstruction results is when $E(\bar{\epsilon}_1) = 10^{-2}$. Therefore, this case can be seen as a limit case, since for $E(\bar{\epsilon}_1) = 10^{-3}$ our method has a success rate for position recovery of 0%. It suggests that the proposed method is able to improve the dynamic range by at least three orders of magnitude compared to accounting for DDEs only. The last two graphs for weighted ℓ_2 norms of the residual images show again the advantage of reconstructing

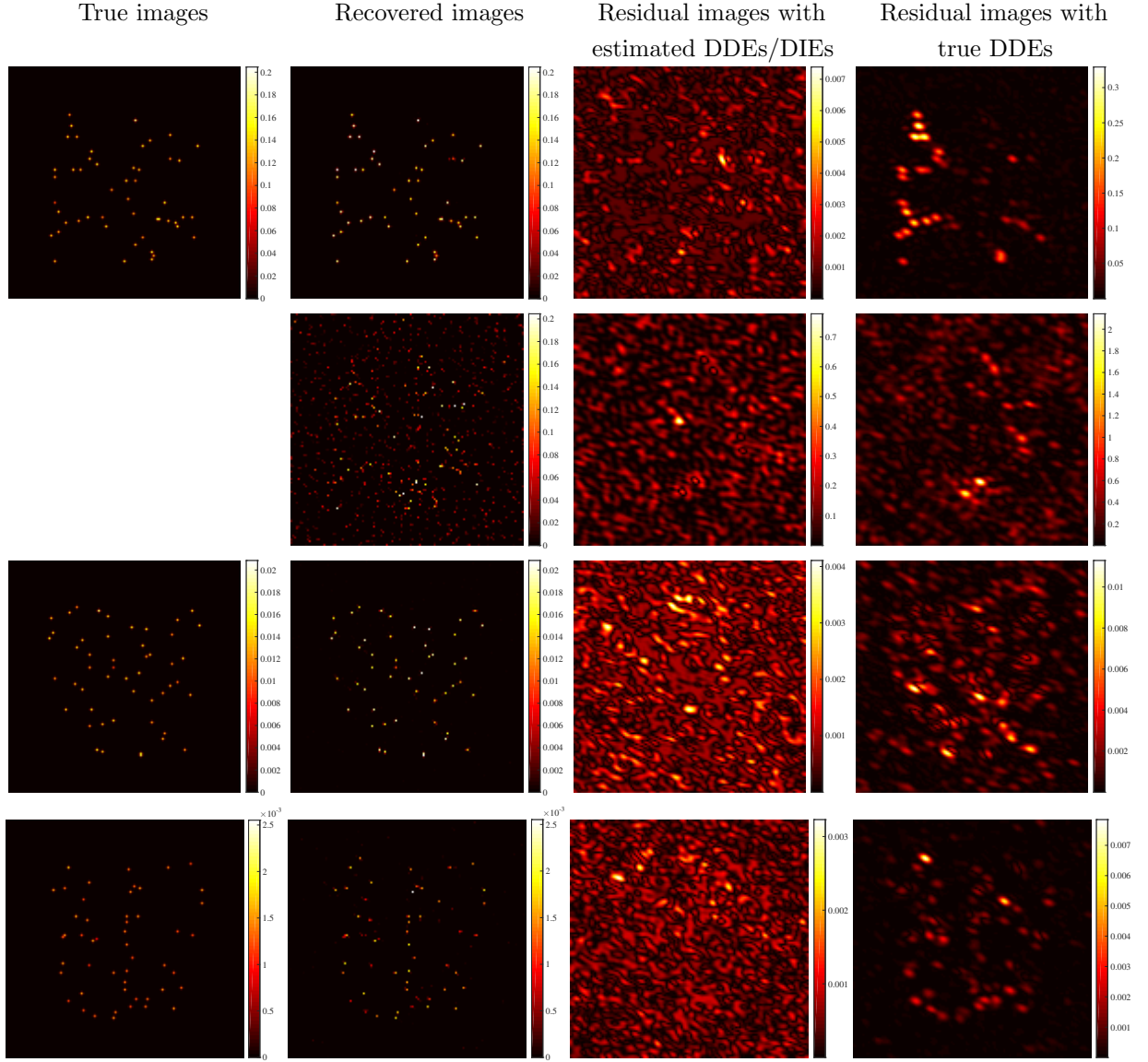


FIGURE 6.4: Images corresponding to the simulations performed considering 50 sources in $\bar{\epsilon}_1$. The first column shows the original unknown images $\bar{\epsilon}$; the second column gives the associated reconstructions; the third column shows the residual images considering \mathbf{G}^* and ϵ^* obtained either with the proposed method or with StEFCal-FB; and the fourth column corresponds to the residual images considering the true DDEs and ϵ^* obtained either with the proposed method or with StEFCal-FB. The first and second rows correspond to the case when $E(\bar{\epsilon}_1) = 1$. In the first row the results are obtained using our method, and in the second row using StEFCal-FB. The third and fourth rows correspond to the cases when $E(\bar{\epsilon}_1) = 0.1$ and $E(\bar{\epsilon}_1) = 0.01$, respectively, and the results are obtained using our method.

the full DDEs instead of considering only DIES. In particular, the third graph shows that our method gives a smaller norm of the residual images (of order 10^{-3} vs. 10^{-1} with StEFCal-FB), taking into account both the estimated image and the estimated DDEs. However, the fourth graph suggests that there is an ambiguity error between \mathbf{G}^* and \mathbf{x}^* , mainly when $E(\bar{\epsilon}_1) \in \{1, 10\}$ (i.e. corresponding to the cases when the sources in $\bar{\epsilon}$ are of similar range as the sources in \mathbf{x}_o) leading to important errors in the residual images when the true DDEs are considered. In particular, as can be observed in Figure 6.4, the most significant ambiguities are associated with the brightest sources positions. This behaviour has already been observed in previous works, even in the DIE calibration case, and is known as “ghost sources” (see e.g. [172]).

The above global observations are supported by Figure 6.4 showing images obtained considering 50 sources in $\bar{\epsilon}_1$, with total flux $E(\bar{\epsilon}_1) \in \{0.01, 0.1, 1\}$. The first two rows correspond to $E(\bar{\epsilon}_1) = 1$ with second column showing the reconstructed images obtained using the proposed method (first row) and the StEFCal-FB method (second row). For this realization, our method finds 100% of the positions of the sources in $\bar{\epsilon}_1$ and the estimate has an SNR equal to 18.9 dB, while the StEFCal-FB method finds 90% of the sources with a reconstructed image of $\text{SNR} = -3.22$ dB. This difference of SNR in the reconstruction can be understood by noticing that the background of the estimated image with StEFCal-FB is very noisy due to the non-estimation of the DDEs, which is not the case using our method. Similarly, the third and the fourth columns correspond to the different computed residual images. In both cases, one can notice that the errors of the residual images obtained using our method and considering \mathbf{G}^* (resp. $\bar{\mathbf{G}}$) are 100 (resp. 10) times smaller than using the StEFCal-FB method. However, as already observed in Figure 6.3, there is obviously an ambiguity error between \mathbf{G}^* and \mathbf{x}^* leading to larger errors when the true observation matrix $\bar{\mathbf{G}}$ is considered. The third and fourth rows show similar results, in the cases when $E(\bar{\epsilon}_1) = 0.1$ and $E(\bar{\epsilon}_1) = 0.01$, respectively. However, since in these cases the StEFCal-FB method has a success rate of 0% for finding the positions of faint sources, only the results obtained using our method are shown. Particularly, for the case $E(\bar{\epsilon}_1) = 0.1$, the proposed method recovers all the positions of the faint sources, and the

reconstructed image has an SNR of 12.32 dB. Similarly, for the case $E(\bar{\epsilon}_1) = 0.01$, our method recovers 90% of the faint sources positions, and the SNR of the estimate is equal to 6.5 dB. Thus, when the SNR is low, one can still observe visually that our method leads to good reconstruction results. Furthermore, as observed in Figure 6.3, the ℓ_2 norm of the residual images decreases with the total flux of $\bar{\epsilon}_1$.

6.2.4 Image with an extended source

In this second part, to show the behaviour of the proposed algorithm in the context of images involving extended sources, we consider an image ($\bar{\mathbf{x}} = \mathbf{x}_0 + \bar{\epsilon}$) of M31 of size 128×128 , with $n_a = 100$ antennas, $T = 10$, $K = 9 \times 9$, and associated standard deviation $v = 0.05$. In this case, we generate \mathbf{x}_o and $\bar{\epsilon}$ such that $E(\bar{\epsilon}) = \kappa E(\mathbf{x}_o)$, where $\kappa > 0$. In the performed simulations, we investigate the reconstruction of the image $\bar{\epsilon}$ for the cases when $\kappa \in \{0.1, 0.5, 1\}$. The original image is not sparse in its domain and thus, we propose to promote its sparsity choosing Ψ to be the SARA collection of wavelets.

The results obtained considering the two extreme cases of $\kappa \in \{0.1, 1\}$ are displayed in Figure 6.5 in first two and last two columns, respectively. For each set of columns, the following are shown. The first row displays (left) the known approximation \mathbf{x}_o , and (right) the unknown background $\bar{\epsilon}$ to be estimated. The second row shows the estimated image ϵ^* of $\bar{\epsilon}$, obtained (left) using the StEFCal-FB method solving only for DDEs, and (right) after the complete estimation of $\bar{\epsilon}$ and the DDEs using the proposed method. As a matter of fact, the StEFCal-FB method gives similar reconstruction results as those obtained after the initialization of our method considering only the zero spatial frequency coefficients of the DDEs. The SNR between the true $\bar{\epsilon}$ and its estimate ϵ^* obtained using StEFCal-FB is equal to 0.65 dB (resp. 5.52 dB and 3.64 dB) for $\kappa = 0.1$ (resp. $\kappa = 0.5$ and $\kappa = 1$). Similarly, the estimate ϵ^* obtained after the complete estimation of the DDEs using our method has an SNR equal to 16.83 dB (resp. 17.47 dB and 13.54 dB) for $\kappa = 0.1$ (resp. $\kappa = 0.5$ and $\kappa = 1$). These results suggest that our method is efficient not only for the reconstruction of point sources, but also to estimate the background of extended sources. Similar to the simulations presented earlier, the accuracy of the reconstruction for extended sources

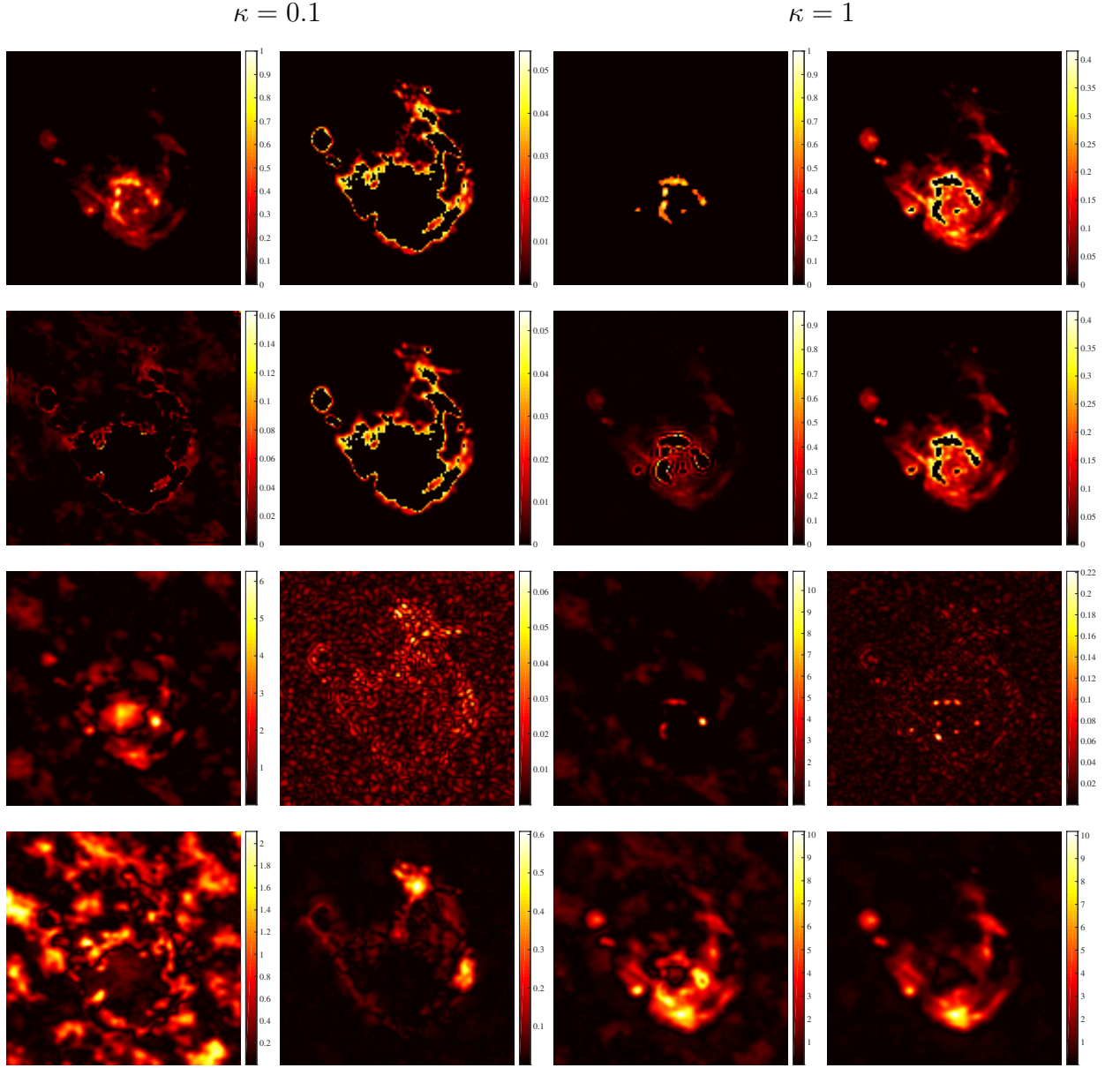


FIGURE 6.5: Images corresponding to the simulations performed with $\kappa = 0.1$ (first two columns) and $\kappa = 1$ (last two columns). For each set of columns, the first row corresponds to (left) the known bright sources \mathbf{x}_o of the original image $\bar{\mathbf{x}}$ and (right) the unknown image $\bar{\mathbf{e}}$. The second row corresponds to the estimates ϵ^* of $\bar{\mathbf{e}}$ obtained using (left) StEFCal-FB solving for DDEs, and (right) the proposed algorithm estimating the full DDEs. The third row shows the residual images considering the estimated \mathbf{G}^* and ϵ^* obtained using (left) StEFCal-FB solving for DDEs, and (right) the proposed algorithm estimating the full DDEs. The fourth row corresponds to the residual images considering the true DDEs and the estimated image ϵ^* obtained using (left) StEFCal-FB solving for DDEs, and (right) the proposed algorithm estimating the full DDEs.

depends on the total flux of the known approximation \mathbf{x}_o with respect to the total flux of the unknown image $\bar{\epsilon}$. As observed previously, if $E(\bar{\epsilon}) \ll E(\mathbf{x}_o)$, our method reconstructs accurately the unknown sources. However, in the case when $E(\bar{\epsilon})$ is of the same order as $E(\mathbf{x}_o)$, the reconstruction is more difficult. Nonetheless, in the worst case considered when $E(\bar{\epsilon}) = E(\mathbf{x}_o)$ (i.e. $\kappa = 1$), visually it can be observed that our method gives a good estimate ϵ^* of $\bar{\epsilon}$. The two last rows of Figure 6.5 are dedicated to the residual images obtained considering $\kappa \in \{0.1, 1\}$. More precisely, the third row shows the residual images $|\mathbf{F}^\dagger \mathbf{G}^{*\dagger}(\mathbf{G}^* \mathbf{F} \mathbf{x}^* - \mathbf{y}')|$ considering the estimated \mathbf{G}^* and \mathbf{x}^* obtained (left) using the StEFCal-FB method solving only for DDEs, and (right) after the complete estimation of the image and the DDEs using our method. Similarly, the last row shows the residual images $|\mathbf{F}^\dagger \bar{\mathbf{G}}^\dagger(\bar{\mathbf{G}} \mathbf{x}^* - \mathbf{y}')|$. As expected, it can be observed that estimating the full DDEs with respect to estimating only the DDEs leads to residual images with smaller amplitudes for all the cases presented. Moreover, for the final results with DDEs estimation, the residual images have smaller amplitude considering the estimated DDEs (third row) than the original DDEs (fourth row). This observation again sheds light onto the ambiguity errors between the image and the direction-dependent Fourier kernels that need to be corrected.

6.3 Concluding remarks

We have proposed a non-convex optimization algorithm to jointly calibrate DDEs and estimate the sky intensity, making use of suitable priors on both the image and the DDEs. Our method presents several advantages. First, it benefits from the convergence guarantees for both the image and the DDEs. Second, in contrast with DDE calibration methods developed recently, our method does not require a selection of calibrator directions since it constructs a smooth DDE screen applied to all the sources across the image. Finally, the proposed method is very general and can be easily adapted to the nature of the considered image. The MATLAB code of the proposed method is available on GitHub (<https://basp-group.github.io/SARA-CALIB/>).

We have studied the performance of the proposed method considering a variety of

simulations and in all the presented simulations, we have shown that our method leads to better reconstruction quality than obtained by only estimating the DDEs. Moreover, our simulations suggest that using our method to jointly estimate the DDEs and the image result in significant improvement of the dynamic range, which is orders of magnitude higher when compared to accounting for DDEs only.

Even though the proposed method is very promising, there are some points to work on. Particularly, although the presented simulations assume the exact knowledge of the bright sources in the images, a more suitable initialization strategy needs to be adopted for practical cases. In addition, to model more realistic data simulations, the gridding (and degriding) steps need to be incorporated in the algorithm using non-uniform FFT. More importantly, this approach has been developed only for Stokes I imaging and calibration, without dealing with the full polarization model. As a matter of fact, in the case of full Stokes imaging and calibration, even the global algorithm consisting of combination of CLEAN based imaging and any of the standard RI calibration techniques, do not adopt any polarimetric imaging specific approach. These factors raise the scope for the development of a globally convergent algorithm which not only incorporates full polarization model, but also uses advanced approaches specific for full Stokes imaging to produce high quality images. We thus work on generalizing this approach to the full polarization model, that is the focus of study for the next sections.

6.4 Full polarization DDE calibration and imaging

Although the approach developed above aims to estimate the sky model while having imperfect knowledge of the calibration terms, it cannot deal with the full polarization model. The rest of this chapter is devoted to this case where we propose a joint calibration and imaging algorithm for full polarization model with proven convergence guarantees. In particular, we build our method on the approach developed earlier for Stokes I imaging and calibration model only, that has been later on extended in [173] and [174], assuming spatial and temporal smoothness of the DDEs. On the one hand, we generalize this approach to the full polarization model, developing an

algorithm alternating between the estimation of the DDEs and the Stokes images. On the other hand, thanks to the underlying non-convex optimization technique, the proposed approach can deal with sophisticated priors suited to the images under consideration as well as to the DDEs. Leveraging this flexibility, we adapt Polarized SARA method, specifically designed for Stokes imaging, to be used for the imaging step in the considered case.

While the overall structure of the proposed joint calibration and imaging algorithm remains the same as before, the main difference arises from the adopted data observation model. More specifically, it relies on the full polarization model introduced in equation (2.19). Using this model, let us briefly recall the imaging problem to be solved in the case when either pre-calibrated data or knowledge of DDEs/DDEs beforehand is available. For this purpose, we adapt the previously developed Polarized SARA approach. In particular, due to the technical assumptions related to the proposed joint imaging and calibration algorithm [107], we propose to solve an unconstrained version of the imaging problem, given by

$$\underset{\mathbf{S}}{\text{minimize}} \quad \bar{h}(\mathbf{S}) + r(\mathbf{S}). \quad (6.3)$$

Using this formulation and assuming that the additive noise is i.i.d. Gaussian, the data fidelity term is given by a least squares criterion

$$(\forall \mathbf{S} \in \mathbb{R}^{2 \times 2N}) \quad \bar{h}(\mathbf{S}) = \frac{1}{2} \|\check{\Phi}(\mathbf{S}) - \mathbf{y}\|_2^2. \quad (6.4)$$

In order to incorporate various prior informations in the regularization function r , we again consider the SARA regularization as well as the polarization constraint.

I now introduce the calibration problem in detail. A blend of the imaging and calibration problems to give the resultant joint calibration and imaging problem and the proposed algorithm to solve it are detailed afterwards.

6.4.1 Calibration problem

In practice, the DDEs are often unknown and need to be estimated. In this section, the corresponding calibration problem to be solved is formulated. We assume that the DDEs exhibit a smooth variation both across the field of view and in time. It implies that DDEs are band-limited spatially as well as temporally. This is enforced by considering compact-support kernels of the DDEs in both spatial [27, 173] and temporal Fourier domains [174]. More specifically, for each antenna $\alpha \in \{1, \dots, n_a\}$, the DDEs $(\bar{\mathbf{D}}_{t,\alpha})_{1 \leq t \leq T}$ are represented by the Fourier kernels $\bar{\mathbf{U}}_\alpha \in \mathbb{C}^{2 \times 2K \times P}$, where K and P are the support sizes in spatial and temporal Fourier domain, respectively, with $K \ll N, P \ll T$. Then, the task is to estimate only non-zero Fourier coefficients of the DDEs, thereby reducing the dimension of the underlying problem significantly. Analogous to the calibration inverse problem in [27], problem (2.19) can be reformulated as

$$\mathbf{Y}_{t,\alpha,\beta} = \mathcal{D}_t(\bar{\mathbf{U}}_\alpha) \mathcal{X}_{t,\alpha,\beta}(\mathbf{F} \tilde{\mathbf{Z}} \tilde{\mathcal{L}}(\bar{\mathbf{S}})) \mathcal{D}'_t(\bar{\mathbf{U}}_\beta) + \boldsymbol{\Omega}_{t,\alpha,\beta}, \quad (6.5)$$

where $\mathcal{D}_t: \mathbb{C}^{2 \times 2K \times P} \rightarrow \mathbb{C}^{2 \times 2N}$ is the operator acting on $\bar{\mathbf{U}}_\alpha$ to give a sparse matrix $\mathcal{D}_t(\bar{\mathbf{U}}_\alpha)$ containing the compact support kernels in $\widehat{\bar{\mathbf{D}}}_{t,\alpha}$, flipped and centred at the zero spatial frequency. Similarly, the operator $\mathcal{D}'_t: \mathbb{C}^{2 \times 2K \times P} \rightarrow \mathbb{C}^{2N \times 2}$ is defined such that $\mathcal{D}'_t(\bar{\mathbf{U}}_\beta)$ is a sparse matrix consisting of the compact support kernels in $\widehat{\bar{\mathbf{D}}}_{t,\beta}^\dagger$ centred at the zero spatial frequency. Finally, $\mathcal{X}_{t,\alpha,\beta}(\mathbf{F} \tilde{\mathbf{Z}} \tilde{\mathcal{L}}(\bar{\mathbf{S}})) \in \mathbb{C}^{2N \times 2N}$ is a 2×2 block matrix, with each block of size $N \times N$. Each row/column of such a block consists of a shifted version of the Fourier transform of the corresponding image in reshaped brightness vector $\tilde{\mathcal{L}}(\bar{\mathbf{S}})$, mimicking the convolution operation. Moreover, to account for the continuous sampled frequencies, these Fourier transforms are convolved with the degriding kernels centred at the associated frequency $k_{t,\alpha,\beta}$.

It can be observed that problem (6.5) is non-linear with respect to the compact-support kernels $(\bar{\mathbf{U}}_\alpha)_{1 \leq \alpha \leq n_a}$. Following the approach proposed in [171] and [27], we linearize it by introducing the matrices $\bar{\mathbf{U}}_{\alpha,1}$ and $\bar{\mathbf{U}}_{\alpha,2}$ such that $\bar{\mathbf{U}}_{\alpha,1} = \bar{\mathbf{U}}_{\alpha,2} = \bar{\mathbf{U}}_\alpha$ for every $\alpha \in \{1, \dots, n_a\}$. Using this strategy, the problem becomes bi-linear and then the objective is to estimate both the matrices $\bar{\mathbf{U}}_1 = (\bar{\mathbf{U}}_{\alpha,1})_{1 \leq \alpha \leq n_a} \in \mathbb{C}^{2 \times 2K \times P \times n_a}$

and $\bar{\mathbf{U}}_2 = (\bar{\mathbf{U}}_{\alpha,2})_{1 \leq \alpha \leq n_a} \in \mathbb{C}^{2 \times 2K \times P \times n_a}$, where $\bar{\mathbf{U}}_1$ (resp. $\bar{\mathbf{U}}_2$) concatenates the non-zero Fourier coefficients $\bar{\mathbf{U}}_{\alpha,1}$ (resp. $\bar{\mathbf{U}}_{\alpha,2}$) for all the antennas. These matrices are estimated by solving the following minimization problem for DDE calibration:

$$\underset{\mathbf{U}_1, \mathbf{U}_2}{\text{minimize}} \quad \tilde{h}(\mathbf{U}_1, \mathbf{U}_2) + p(\mathbf{U}_1, \mathbf{U}_2), \quad (6.6)$$

where \tilde{h} is the least-squares data fidelity term and p is the regularization function for \mathbf{U}_1 and \mathbf{U}_2 . The data fidelity term for DDE calibration reads as

$$\tilde{h}(\mathbf{U}_1, \mathbf{U}_2) = \sum_{1 \leq \alpha \leq n_a} \frac{1}{2} \|\mathcal{G}_{\alpha,1}(\mathbf{U}_{\alpha,1}) - \mathbf{Y}_\alpha\|_F^2, \quad (6.7)$$

$$= \sum_{1 \leq \alpha \leq n_a} \frac{1}{2} \|\mathcal{G}_{\alpha,2}(\mathbf{U}_{\alpha,2}) - \mathbf{Y}_\alpha\|_F^2, \quad (6.8)$$

where $\mathbf{Y}_\alpha = (\mathbf{Y}_{t,\alpha,\beta})_{t,\beta \neq \alpha}$ with t and β taking all the values respectively in the ranges $\{1, \dots, T\}$ and $\{1, \dots, n_a\}$. Considering inverse problem (6.5) for all possible values of (t, β) , the operators $\mathcal{G}_{\alpha,1}(\cdot)$ and $\mathcal{G}_{\alpha,2}(\cdot)$ are defined as a function of $\mathbf{U}_{\alpha,1}$ and $\mathbf{U}_{\alpha,2}$ to model the measurements respectively in equations (6.7) and (6.8). To be more precise, for all values of (t, β) , $\mathcal{G}_{\alpha,1}(\mathbf{U}_{\alpha,1})$ generates a concatenation of the terms of the form $\mathcal{D}_t(\mathbf{U}_{\alpha,1}) \mathcal{X}_{t,\alpha,\beta}(\mathbf{F} \tilde{\mathbf{Z}} \tilde{\mathcal{L}}(\mathbf{S})) \mathcal{D}'_t(\mathbf{U}_{\beta,2})$, whereas $\mathcal{G}_{\alpha,2}(\mathbf{U}_{\alpha,2})$ consists of concatenating the terms $\mathcal{D}_t(\mathbf{U}_{\beta,1}) \mathcal{X}_{t,\beta,\alpha}(\mathbf{F} \tilde{\mathbf{Z}} \tilde{\mathcal{L}}(\mathbf{S})) \mathcal{D}'_t(\mathbf{U}_{\alpha,2})$.

The regularization term p in problem (6.6) is given by

$$p(\mathbf{U}_1, \mathbf{U}_2) = \bar{\gamma} \|\mathbf{U}_1 - \mathbf{U}_2\|_F^2 + \iota_{\mathbb{D}}(\mathbf{U}_1) + \iota_{\mathbb{D}}(\mathbf{U}_2), \quad (6.9)$$

where $\bar{\gamma} > 0$ is the regularization parameter and the first term in equation (6.9) controls the distance between the matrices \mathbf{U}_1 and \mathbf{U}_2 , thereby imposing the constraint that these two matrices should be equal. The set \mathbb{D} is defined to constrain the values of the Fourier coefficients of the DDEs to lie within the specified bounds. In particular, \mathbb{D} is defined such that for each $t \in \{1, \dots, T\}$, the Fourier kernels stored in diagonal terms of $\hat{\mathbf{D}}_{t,\alpha}$ have the central coefficients ($[\hat{\mathbf{D}}_{t,\alpha}(0)]_{11}$ and $[\hat{\mathbf{D}}_{t,\alpha}(0)]_{22}$) belonging to an ℓ_∞ complex ball centred at 1 with radius $\theta_1 > 0$, whereas the rest of the coefficients

belong to an ℓ_∞ complex ball centred at 0 with radius θ_1 . For the Fourier kernels at the off-diagonal terms, the central and the other coefficients are assumed to be contained in ℓ_∞ balls centred at 0 with radius θ_2 and θ_3 , respectively. Intuitively, this can be understood as follows.

The calibration terms to be dealt with mainly consist of the standard gain terms and the polarimetric calibration terms that include the polarization leakage and the cross-hand phase terms [175]. In the current study, we focus primarily on the calibration of the leakage terms. This relies on the assumption that the gain terms and the cross-hand phase terms have been pre-calibrated and transferred. Typically, this process carries out DIE calibration on a nearby calibrator source using the technique of external calibration (Section 4.3.1) and transfers the interpolated DIEs to the field of interest. Each measurement is then divided by these approximated DIE solutions, thereby producing normalized DIEs. Under this assumption, the Jones matrices can be considered as identity as a first instance. We will refer to this case as ‘calibrator transfer’ in the rest of the chapter. We further note that a complete framework would be provided by calibrating for the cross-hand phase terms as well. Formally speaking, it would require the incorporation of these terms within the measurement operator that can then be calibrated for using the same algorithmic structure.

In the considered settings of the calibrator transfer, the zero spatial frequency coefficient of the DDEs (i.e. the Fourier coefficient for the DIEs) encoded in the diagonal terms of the Jones matrices are normalized to 1, thus lying in a complex neighbourhood of $1 + i0$. Moreover, while the central coefficient in the spatial Fourier domain represents the mean gain, the higher order spatial frequencies characterize the gain variations across the field of view with respect to this mean gain. Therefore, these coefficients have smaller values in comparison with the central coefficient. Lastly, concerning the off-diagonal terms which encompass the polarization leakage, their values are usually much smaller than the diagonal terms.

6.4.2 Polca SARA - Proposed calibration & imaging approach

The current work deals with a practical case when neither the Stokes images nor the DDEs are known. Motivated by the good performance obtained by the previously proposed Stokes I imaging and calibration method, we extend this approach for full polarization model and propose a joint calibration and imaging algorithm to solve a global minimization problem estimating the Stokes parameters \mathbf{S} and the calibration matrices \mathbf{U}_1 and \mathbf{U}_2 . This non-convex problem can be cast by combining the minimization problems (6.3) and (6.6) that were proposed in the earlier sections solely for Stokes imaging and DDE calibration, respectively.

Given the non-convexity of the underlying minimization problem, choice of initialization is crucial. In this context, we exploit the fact that the calibrator transfer has been performed to (i) initialize the DDEs, and (ii) obtain an initial estimate of the Stokes images for the joint calibration and imaging algorithm. To be more precise, this first imaging step consists in solving the associated minimization problem for imaging while considering Jones matrices as identity (analogous to work in [173] for Stokes I imaging only). Let \mathbf{S}' be the Stokes parameters estimated by solving problem (6.3). Since these are obtained ignoring the DDEs, in general, these may contain artefacts. Therefore, we instead use a thresholded version of \mathbf{S}' , denoted by \mathbf{S}_0 , which contains only the high amplitude coefficients of \mathbf{S}' . With this first approximation of the images at hand, the original unknown images can be seen as a sum of \mathbf{S}_0 and $\mathbf{E} \in \mathbb{R}^{2 \times 2N}$, where the latter is unknown and need to be estimated.

Finally, we propose to define the estimates $(\mathbf{E}, \mathbf{U}_1, \mathbf{U}_2)$ as solutions to the following global, non-convex minimization problem:

$$\underset{\mathbf{E}, \mathbf{U}_1, \mathbf{U}_2}{\text{minimize}} \quad h(\mathbf{E}, \mathbf{U}_1, \mathbf{U}_2) + r(\mathbf{E}) + p(\mathbf{U}_1, \mathbf{U}_2), \quad (6.10)$$

where h is the least squares data fidelity term associated with the data model. With $\mathbf{S} = \mathbf{S}_0 + \mathbf{E}$, the data fidelity term is given by the least squares criterion as proposed

in equations (6.4), (6.7) and (6.8), i.e.

$$h(\mathbf{E}, \mathbf{U}_1, \mathbf{U}_2) = \|\check{\Phi}(\mathbf{S}_0 + \mathbf{E}) - \mathbf{y}\|_2^2 \quad (6.11)$$

$$= \sum_{1 \leq \alpha \leq n_a} \frac{1}{2} \|\mathcal{G}_{\alpha,1}(\mathbf{U}_{\alpha,1}) - \mathbf{Y}_\alpha\|_F^2, \quad (6.12)$$

$$= \sum_{1 \leq \alpha \leq n_a} \frac{1}{2} \|\mathcal{G}_{\alpha,2}(\mathbf{U}_{\alpha,2}) - \mathbf{Y}_\alpha\|_F^2, \quad (6.13)$$

where operator $\check{\Phi}$ in equation (6.11) is formed using fixed values of $(\mathbf{U}_1, \mathbf{U}_2)$. Similarly, $\mathcal{G}_{\alpha,1}(\mathbf{U}_{\alpha,1})$ in equation (6.12) (and $\mathcal{G}_{\alpha,2}(\mathbf{U}_{\alpha,2})$ in equation (6.13), resp.) is determined by fixed $(\mathbf{U}_{\beta,2}, \mathbf{E})$ ($(\mathbf{U}_{\beta,1}, \mathbf{E})$, resp.) with $\beta \in \{1, \dots, n_a\}$ and $\beta \neq \alpha$. While estimating the Stokes parameters, equation (6.11) is employed as the data fidelity term. Keeping $(\mathbf{U}_1, \mathbf{U}_2)$ fixed, the convexity of this term with respect to \mathbf{E} can be noticed. Similarly, equation (6.12) ((6.13), resp.) is chosen while updating \mathbf{U}_1 (\mathbf{U}_2 , resp.), which is convex with respect to \mathbf{U}_1 (\mathbf{U}_2 , resp.) keeping the other two variables fixed. It is then straightforward to see that the non-convex function h is in fact convex for each of the variables while fixing the others.

Concerning the regularization terms, the function $p(\mathbf{U}_1, \mathbf{U}_2)$ is given from equation (6.9), whereas the function $r(\mathbf{E})$ for the images is associated with the priors introduced in the previous chapter. In particular, one can choose whether to take the polarization constraint into account or not. In the former case, the regularization term boils down to

$$r(\mathbf{E}) = g(\mathbf{E}) + \iota_{\mathbb{P}}(\mathbf{S}_0 + \mathbf{E}) + \iota_{\mathbb{K}}(\mathbf{E}), \quad (6.14)$$

where $g(\mathbf{E}) = \sum_{i=1}^4 \mu_i \|(\Psi^\dagger \mathcal{R}(\mathbf{S}_0 + \mathbf{E}))_{:,i}\|_1$ denotes the SARA prior and for every $i \in \{1, 2, 3, 4\}$, $\mu_i > 0$ is the regularization parameter. Here we have taken the weighting matrix to be equal to identity, i.e. without adapting the reweighting scheme. The set \mathbb{K} is chosen to take into account the errors that might appear on the estimated non-zero coefficients of \mathbf{S}_0 . Formally, it is defined as

$$\mathbb{K} = \{\mathbf{E} \in \mathbb{R}^{2 \times 2N} | (\forall n \in \mathbb{S}_0) \mathbf{E}(n) \in [-\vartheta \mathbf{S}_0(n), \vartheta \mathbf{S}_0(n)]\}, \quad (6.15)$$

where \mathbb{S}_0 is the support of \mathbf{S}_0 . The parameter $\vartheta \in [0, 1]$ is chosen according to the error percentage assumed for \mathbf{S}_0 .

In the absence of the polarization constraint, the positivity of Stokes I image needs to be imposed explicitly, that can be accounted for by replacing the set \mathbb{K} in equation (6.14) by a set \mathbb{K}' , defined as

$$\mathbb{K}' = \{\mathbf{E} \in \mathbb{R}^{2 \times 2N} | (\forall n \in \mathbb{S}_0) \mathbf{E}(n) \in [-\vartheta \mathbf{S}_0(n), \vartheta \mathbf{S}_0(n)], (\forall n \notin \mathbb{S}_0) [\mathbf{E}(n)]_{1,1} \geq 0\}. \quad (6.16)$$

In such a case, the function r reads as

$$r(\mathbf{E}) = g(\mathbf{E}) + \iota_{\mathbb{K}'}(\mathbf{E}). \quad (6.17)$$

6.4.3 Algorithm formulation

In order to solve problem (6.10), we observe that it has a block-variable structure with $\mathbf{U}_1, \mathbf{U}_2$ and \mathbf{E} being the three blocks constituting the problem. On top of it, although the global problem is non-convex, it is convex with respect to each of these blocks. Leveraging this block-variable structure, we propose to use an iterative algorithm based on a block-coordinate forward-backward approach [107] to solve problem (6.10). It consists in alternating between the estimation of the DDEs and the Stokes images. In turn, for each of these estimations, FB iterations are employed. In light of the discussion above, we present the proposed algorithm as Algorithm 5. It consists of a global loop and inner iteration loops. At each iteration of the global loop, indexed by $i \in \mathbb{N}$ (step 2), we choose either to update the DDEs or the image following an essentially cyclic rule, that is each of the variables must be updated at least once within a given finite number of iterations. For every i^{th} iteration, this is taken care by the choice of number of inner loop iterations $L^{(i)} \in \mathbb{N}$ and $J^{(i)} \in \mathbb{N}$ to update the DDEs and the images, respectively. To be more precise, in the former case, each of the calibration matrices $\mathbf{U}_1^{(i)}$ (step 5) and $\mathbf{U}_2^{(i)}$ (step 9) are updated by performing $L^{(i)}$ number of FB iterations in the inner loop, using the images estimated at the

previous global iterate. When the images are chosen to be updated in the global loop, the updated DDEs from the previous iterate are used to estimate the image in step 15, executing $J^{(i)}$ FB iterations. The overall algorithm can then be understood by splitting it into two parts: Calibration and Imaging. These two parts are explained in what follows.

Algorithm 5 Joint DDE calibration and Stokes imaging algorithm

```

1: Initialization:  $\mathbf{E}^{(0)} \in \mathbb{R}^{2 \times 2N}$ ,  $(\mathbf{U}_1^{(0)}, \mathbf{U}_2^{(0)}) \in (\mathbb{C}^{2 \times 2K \times P \times n_a})^2$ . Let, for every  $i \in \mathbb{N}$ ,  $(L^{(i)}, J^{(i)}) \in \mathbb{N}^2$ .
2: for  $i = 0, 1, \dots$  do
    Choose to update either the DDEs or the images.
    If the DDEs are updated:
3:    $(\mathbf{U}_1^{(i,0)}, \mathbf{U}_2^{(i,0)}) = (\mathbf{U}_1^{(i)}, \mathbf{U}_2^{(i)})$ 
4:   for  $\ell = 0, \dots, L^{(i)} - 1$  do
5:      $\mathbf{U}_1^{(i,\ell+1)} = \mathcal{P}_{\mathbb{D}} \left( \mathbf{U}_1^{(i,\ell)} - \Gamma_1^{(i)} \cdot \nabla_{\mathbf{U}_1} h(\mathbf{E}^{(i)}, \mathbf{U}_1^{(i,\ell)}, \mathbf{U}_2^{(i)}) - \Gamma_1^{(i)} \cdot \bar{\gamma}(\mathbf{U}_1^{(i,\ell)} - \mathbf{U}_2^{(i)}) \right)$ 
6:   end for
7:    $\mathbf{U}_1^{(i+1)} = \mathbf{U}_1^{(i,L^{(i)})}$ 
8:   for  $\ell = 0, \dots, L^{(i)} - 1$  do
9:      $\mathbf{U}_2^{(i,\ell+1)} = \mathcal{P}_{\mathbb{D}} \left( \mathbf{U}_2^{(i,\ell)} - \Gamma_2^{(i)} \cdot \nabla_{\mathbf{U}_2} h(\mathbf{E}^{(i)}, \mathbf{U}_1^{(i+1)}, \mathbf{U}_2^{(i,\ell)}) - \Gamma_2^{(i)} \cdot \bar{\gamma}(\mathbf{U}_2^{(i,\ell)} - \mathbf{U}_1^{(i+1)}) \right)$ 
10:  end for
11:   $\mathbf{U}_2^{(i+1)} = \mathbf{U}_2^{(i,L^{(i)})}$ 
12:   $\mathbf{E}^{(i+1)} = \mathbf{E}^{(i)}$ 
    If the Stokes images are updated:
13:    $\mathbf{E}^{(i,0)} = \mathbf{E}^{(i)}$ 
14:   for  $j = 0, \dots, J^{(i)} - 1$  do
15:      $\mathbf{E}^{(i,j+1)} = \text{prox}_{\sigma^{(i)}r} \left( \mathbf{E}^{(i,j)} - \sigma^{(i)} \nabla_{\mathbf{E}} h(\mathbf{E}^{(i,j)}, \mathbf{U}_1^{(i+1)}, \mathbf{U}_2^{(i+1)}) \right)$ 
16:   end for
17:    $\mathbf{E}^{(i+1)} = \mathbf{E}^{(i,J^{(i)})}$ 
18:    $(\mathbf{U}_1^{(i+1)}, \mathbf{U}_2^{(i+1)}) = (\mathbf{U}_1^{(i)}, \mathbf{U}_2^{(i)})$ .
19: end for
    
```

Calibration: It comprises of the estimation of the matrices \mathbf{U}_1 and \mathbf{U}_2 . In this case, while the data fidelity term h is differentiable, the regularization term p consists of both smooth and non-smooth terms. Thus, in each ℓ^{th} FB iteration to estimate either of these matrices, the gradient step for the differentiable terms is coupled with the

projection step for the non-smooth term, as shown in steps 5 and 9. In particular, for the gradient step, for every $q \in \{1, 2\}$, the step size $\Gamma_q^{(i)} \in \mathbb{R}^{2 \times 2K \times P \times n_a}$ is chosen as

$$\Gamma_q^{(i)} = (\zeta_{q,\alpha}^{(i)} \mathbf{1}_{2 \times 2K \times P})_{1 \leq \alpha \leq n_a}, \quad (6.18)$$

where $\mathbf{1}_R$ is a matrix of ones of dimension R , and $\zeta_{q,\alpha}^{(i)}$ is given by $0 < \zeta_{q,\alpha}^{(i)} < 1/(\bar{\gamma} + v_{q,\alpha}^{(i)})$, with $v_{q,\alpha}^{(i)}$ denoting the Lipschitz constant of the partial derivative of h with respect to $\mathbf{U}_{q,\alpha}^{(i)}$.

Furthermore, since in this case the non-smooth term is the indicator function of the set \mathbb{D} , as explained previously, this reduces to performing projection $\mathcal{P}_{\mathbb{D}}$ on this set, which basically ensures that the values of the estimated DDE Fourier coefficients lie within the earlier specified bounds.

Imaging: This step updates the Stokes images while using the DDEs estimates from the previous iterate. As shown in step 15, it involves computing the gradient of the data fidelity term, followed by the proximity operator of the regularization function r . In this case, the step size $\sigma^{(i)}$ for the gradient step is chosen such that it satisfies

$$0 < \sigma^{(i)} < 1/\|\check{\Phi}\|_2, \quad (6.19)$$

where $\|\check{\Phi}\|_2$ computes the spectral norm of $\check{\Phi}$ that is generated using the updated values $(\mathbf{U}_1^{(i+1)}, \mathbf{U}_2^{(i+1)})$.

For the proximity step, the regularization term $r(\mathbf{E})$ is a hybrid term incorporating a mixture of prior information. Particularly, based on the choice of inclusion or exclusion of the polarization constraint, the computation of the proximity operator differs. For comparison purposes, here we consider both the cases.

Regularization without polarization constraint: When we work in the absence of the polarization constraint, the regularization term $r(\mathbf{E})$ is given by equation (6.17).

Then, the proximity operator of r evaluated at any point $\mathbf{R} \in \mathbb{R}^{2 \times 2N}$ amounts to

$$\text{prox}_{\sigma^{(i)}r}(\mathbf{R}) = \underset{\tilde{\mathbf{E}}}{\operatorname{argmin}} \sigma^{(i)}g(\tilde{\mathbf{E}}) + \iota_{\mathbb{K}'}(\tilde{\mathbf{E}}) + \frac{1}{2}\|\tilde{\mathbf{E}} - \mathbf{R}\|_F^2, \quad (6.20)$$

which does not have an explicit formulation and thus requires sub-iterations for its computation. One such possibility is to employ dual forward-backward algorithm [90, 176], as presented in Algorithm 6. In particular, step 3 of Algorithm 6 performs the projection onto the set \mathbb{K}' . It is followed by the computation of the proximity operator of function g in step 5, which in the current case of g being the ℓ_1 norm, corresponds to the soft-thresholding operator.

Algorithm 6 Dual Forward-Backward algorithm to compute (6.20)

- 1: **Initialization:** Let $\tilde{\mathbf{P}}^{(0)} \in \mathbb{R}^{J \times 4}$, $\bar{\epsilon} \in]0, \min\{1, 1/\|\Psi^\dagger\|_2^2\}[$, $\bar{\mu} \in [\bar{\epsilon}, 2/\|\Psi^\dagger\|_2^2 - \bar{\epsilon}]$
 - 2: **for** $k = 0, 1, \dots$
 - 3: $\mathbf{V}^{(k)} = \mathcal{P}_{\mathbb{K}'}\left(\mathbf{R} - \mathcal{R}^\dagger(\Psi\tilde{\mathbf{P}}^{(k)})\right)$
 - 4: $\mathbf{H}^{(k)} = \tilde{\mathbf{P}}^{(k)} + \bar{\mu}\Psi^\dagger\mathcal{R}(\mathbf{V}^{(k)})$
 - 5: $\tilde{\mathbf{P}}^{(k+1)} = \mathbf{H}^{(k)} - \bar{\mu}\mathcal{T}_{\sigma^{(i)}/\mu}(\bar{\mu}^{-1}\mathbf{H}^{(k)})$
 - 6: **end for**
 - 7: **Return:** $\tilde{\mathbf{E}} = \lim_k \mathbf{V}^{(k)}$
-

Regularization with polarization constraint: In the case when the polarization constraint is to be enforced, the regularization term is given by equation (6.14) and the associated proximity operator at a point \mathbf{R} is given by

$$\text{prox}_{\sigma^{(i)}r}(\mathbf{R}) = \underset{\tilde{\mathbf{E}}}{\operatorname{argmin}} \sigma^{(i)}g(\tilde{\mathbf{E}}) + \iota_{\mathbb{K}}(\tilde{\mathbf{E}}) + \iota_{\mathbb{P}}(\tilde{\mathbf{E}} + \mathbf{S}_0) + \frac{1}{2}\|\tilde{\mathbf{E}} - \mathbf{R}\|_F^2. \quad (6.21)$$

The evaluation of this operator requires projection onto the set \mathbb{P} , that does not have a closed form solution. To circumvent this difficulty, we adapt the previously proposed Polarized SARA method, that enforces this constraint leveraging the epigraphical projection technique. In this context, with the introduction of an auxiliary variable $\mathbf{Z} \in \mathbb{R}^{N \times 2}$, the polarization constraint set is split into simpler, easily manageable constraint sets, thereby performing the projection onto these sets. Formally,

it corresponds to the following reformulation of problem (6.21):

$$\text{prox}_{\sigma^{(i)}r}(\mathbf{R}) = \underset{\tilde{\mathbf{E}}, \mathbf{Z}}{\text{argmin}} \sigma^{(i)}g(\tilde{\mathbf{E}}) + \iota_{\mathbb{K}}(\tilde{\mathbf{E}}) + \frac{1}{2}\|\tilde{\mathbf{E}} - \mathbf{R}\|_F^2 \quad (6.22a)$$

subject to $(\forall n \in \{1, \dots, N\})$

$$\begin{cases} h_1(\mathcal{R}(\tilde{\mathbf{E}} + \mathbf{S}_0)_{n,1}) = -\mathcal{R}(\tilde{\mathbf{E}} + \mathbf{S}_0)_{n,1} \leq Z_{n,1}, & (6.22b) \end{cases}$$

$$\begin{cases} h_2(\mathcal{R}(\tilde{\mathbf{E}} + \mathbf{S}_0)_{n,2:4}) = \|\mathcal{R}(\tilde{\mathbf{E}} + \mathbf{S}_0)_{n,2:4}\|_2 \leq Z_{n,2}, & (6.22c) \end{cases}$$

$$\begin{cases} Z_{n,1} + Z_{n,2} \leq 0. & (6.22d) \end{cases}$$

In order to impose the constraints (6.22b)- (6.22d), we make use of the indicator functions of the corresponding sets, as explained in the previous chapter. Doing so, this proximity operator results in

$$\begin{aligned} \text{prox}_{\sigma^{(i)}r}(\mathbf{R}) = \underset{\tilde{\mathbf{E}}, \mathbf{Z}}{\text{argmin}} & \sigma^{(i)}g(\tilde{\mathbf{E}}) + \iota_{\mathbb{K}}(\tilde{\mathbf{E}}) + \frac{1}{2}\|\tilde{\mathbf{E}} - \mathbf{R}\|_F^2 + \iota_{\mathbb{V}}(\mathbf{Z}) \\ & + \iota_{\mathbb{E}_1}(\mathcal{R}(\tilde{\mathbf{E}} + \mathbf{S}_0)_{:,1}, \mathbf{Z}_{:,1}) + \iota_{\mathbb{E}_2}(\mathcal{R}(\tilde{\mathbf{E}} + \mathbf{S}_0)_{:,2:4}, \mathbf{Z}_{:,2}), \end{aligned} \quad (6.23)$$

that is computed employing Polarized SARA method which is based on primal-dual forward-backward algorithm. Particularly, leveraging the flexibility and parallelizability offered by the primal-dual algorithms, we can easily adapt Polarized SARA method to solve our underlying problem (6.23). For the sake of completeness, we also present this adapted version in Algorithm 7. To recall, it comprises of solving for the variables of interest, the primal variables, along with the associated auxiliary variables, the dual variables. In this context, the update of the primal variables is similar to the FB strategy. For the current case, it implies projection onto the set \mathbb{K} (step 3) and \mathbb{V} (step 5) for the update of the variables $\tilde{\mathbf{E}}$ and \mathbf{Z} , respectively. It is to be noted that these updates incorporate an additive term based on the corresponding dual variables. More precisely, the update of $\tilde{\mathbf{E}}$ involves the variables $\mathbf{A}_l \in \mathbb{R}^{J \times 4} (\forall l \in \{1, \dots, n_b\})$ and $\mathbf{C} \in \mathbb{R}^{N \times 4}$ related to the sparsity prior and the epigraphical constraints, respectively. Similarly, step 5 comprises of the variable $\mathbf{H} \in \mathbb{R}^{N \times 2}$ associated with the epigraphical constraints. These dual variables are in turn updated by the computation of their

associated proximity operators, that is the soft-thresholding operation (step 8) and the projections onto the sets \mathbb{E}_1 and \mathbb{E}_2 .

Algorithm 7 Primal-dual algorithm to solve problem (6.23)

1: **given** $\tilde{\mathbf{E}}^{(0)} \in \mathbb{R}^{2 \times 2N}$, $\mathbf{Z}^{(0)} \in \mathbb{R}^{N \times 2}$, $(\forall l \in \{1, \dots, n_b\}) \mathbf{A}_l^{(0)} \in \mathbb{R}^{J \times 4}$, $\tilde{\mathbf{A}}_l^{(0)} = \Psi_l \mathbf{A}_l^{(0)}$, $\Lambda_l \in \mathbb{R}_+^{J \times 4}$, $\mathbf{C}^{(0)} \in \mathbb{R}^{N \times 4}$, $\mathbf{H}^{(0)} \in \mathbb{R}^{N \times 2}$.

2: **For** $k = 0, 1, \dots$

Primal updates

$$3: \quad \tilde{\mathbf{E}}^{(k+1)} = \mathcal{P}_{\mathbb{K}} \left(\tilde{\mathbf{E}}^{(k)} - \tau \left((\tilde{\mathbf{E}}^{(k)} - \mathbf{R}) + \mathcal{R}^\dagger \left(\rho_1 \sum_{l=1}^{n_b} \tilde{\mathbf{A}}_l^{(k)} + \rho_3 \mathbf{C}^{(k)} \right) \right) \right)$$

$$4: \quad \check{\mathbf{E}}^{(k+1)} = \mathcal{R} \left(2 \tilde{\mathbf{E}}^{(k+1)} + \mathbf{S}_0 - \tilde{\mathbf{E}}^{(k)} \right)$$

$$5: \quad \mathbf{Z}^{(k+1)} = \mathcal{P}_{\mathbb{V}} \left(\mathbf{Z}^{(k)} - \tau \rho_3 \mathbf{H}^{(k)} \right)$$

$$6: \quad \check{\mathbf{Z}}^{(k+1)} = 2 \mathbf{Z}^{(k+1)} - \mathbf{Z}^{(k)}$$

Dual updates

Promoting sparsity:

7: **for** $l \in \{1, \dots, n_b\}$ and $\forall i \in \{1, 2, 3, 4\}$ **do in parallel**

$$8: \quad [\mathbf{A}_l^{(k+1)}]_{:,i} = \left(\mathbf{1}_J - \mathcal{T}_{[\Lambda_l]_{:,i}} \right) \left([\mathbf{A}_l^{(k)}]_{:,i} + \Psi_l^\dagger \check{\mathbf{E}}_{:,i}^{(k+1)} \right)$$

$$9: \quad [\tilde{\mathbf{A}}_l^{(k+1)}]_{:,i} = \Psi_l [\mathbf{A}_l^{(k+1)}]_{:,i}$$

10: **end for**

Enforcing polarization constraint:

$$11: \quad \begin{bmatrix} \mathbf{C}_{:,1}^{(k+1)} \\ \mathbf{H}_{:,1}^{(k+1)} \end{bmatrix} = \begin{bmatrix} \mathbf{C}_{:,1}^{(k)} + \check{\mathbf{E}}_{:,1}^{(k+1)} \\ \mathbf{H}_{:,1}^{(k)} + \check{\mathbf{Z}}_{:,1}^{(k+1)} \end{bmatrix} - \mathcal{P}_{\mathbb{E}_1} \left(\begin{bmatrix} \mathbf{C}_{:,1}^{(k)} + \check{\mathbf{E}}_{:,1}^{(k+1)} \\ \mathbf{H}_{:,1}^{(k)} + \check{\mathbf{Z}}_{:,1}^{(k+1)} \end{bmatrix} \right)$$

$$12: \quad \begin{bmatrix} \mathbf{C}_{:,2:4}^{(k+1)} \\ \mathbf{H}_{:,2}^{(k+1)} \end{bmatrix} = \begin{bmatrix} \mathbf{C}_{:,2:4}^{(k)} + \check{\mathbf{E}}_{:,2:4}^{(k+1)} \\ \mathbf{H}_{:,2}^{(k)} + \check{\mathbf{Z}}_{:,2}^{(k+1)} \end{bmatrix} - \mathcal{P}_{\mathbb{E}_2} \left(\begin{bmatrix} \mathbf{C}_{:,2:4}^{(k)} + \check{\mathbf{E}}_{:,2:4}^{(k+1)} \\ \mathbf{H}_{:,2}^{(k)} + \check{\mathbf{Z}}_{:,2}^{(k+1)} \end{bmatrix} \right)$$

13: **end For**

6.4.4 Convergence properties

The convergence properties of the proposed joint calibration and imaging algorithm for full polarization model (Algorithm 5) can be deduced from [107]. Particularly, if a finite number of iterations are performed to update each of the variables, that is for every i^{th} iteration, choosing $L^{(i)}$ and $J^{(i)}$ to be finite in Algorithm 5, and if the

- blocks $(\mathbf{E}^{(i)}, \mathbf{U}_1^{(i)}, \mathbf{U}_2^{(i)})$ in Algorithm 5 are estimated at least once in every finite number of given iterations,
- step sizes $\Gamma_1^{(i)}$ and $\Gamma_2^{(i)}$ for the gradient steps while updating \mathbf{U}_1 and \mathbf{U}_2 , respectively are chosen as per equation (6.18), and
- step size $\sigma^{(i)}$ for the update of \mathbf{E} is chosen as per equation (6.19),

then Algorithm 5 is guaranteed to converge to a critical point $(\mathbf{E}', \mathbf{U}_1', \mathbf{U}_2')$ of the underlying objective function given in equation (6.10). Additionally, iteration-by-iteration, the value of this objective function decreases.

6.4.5 Computational complexity

The computational complexity of Algorithm 5 can be analyzed from its two sub-parts: Calibration and Imaging. In the former case, the update of matrix \mathbf{U}_1 in steps 4 - 6 (and \mathbf{U}_2 in steps 8 - 10) is performed in parallel for n_a antennas, using FB iterations. In this case, the gradient evaluation of the data fidelity term in equation (6.12) (and in (6.13)) is required. It involves the degriding operation while generating the matrix $\mathcal{X}_{t,\alpha,\beta}(\mathbf{F} \tilde{\mathbf{Z}} \tilde{\mathcal{L}}(\mathbf{S}_0 + \mathbf{E}))$ for all $t \in \{1, \dots, T\}$ and $\beta \in \{1, \dots, n_a\}$, with $\beta \neq \alpha$. This turns out to be the most expensive step. However, it is to be noted that for each global calibration iteration, this matrix needs to be computed only once before the inner FB iterations (both for \mathbf{U}_1 and \mathbf{U}_2 updates).

For the imaging step, the FB strategy presents the computationally most demanding part of the algorithm. In particular, in step 15, the gradient computation (forward step) of the data fidelity term (equation (6.11)) consists in performing the application of the operator $\check{\Phi}$, followed by its adjoint operator. Furthermore, the evaluation of the proximity operator (backward step) involves sub-iterations, performed either by Algorithm 6 or Algorithm 7. While this iterative process adds to the computational cost, the heaviest steps within either of the algorithms is the application of the wavelet transform operator Ψ consisting of eight wavelet bases and the Dirac basis (having $n_b = 9$) to impose sparsity. This can in turn be implemented in a parallel fashion, for each sparsity basis as well as for each of the underlying images.

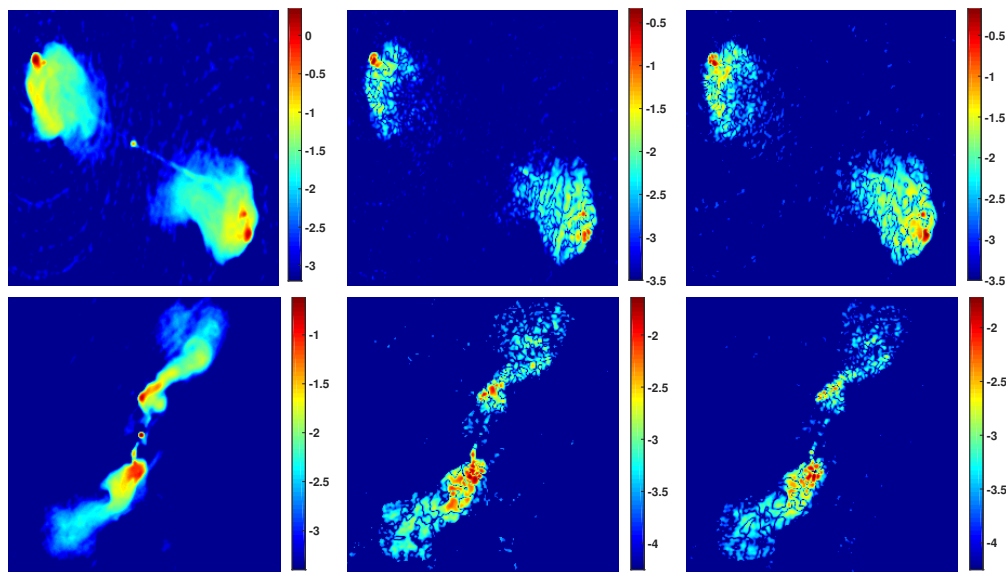


FIGURE 6.6: Cygnus A (first row) and Hydra A (second row) ground truth images used for performing simulations. In each row, from left to right the following images are shown (all in log scale): Stokes I , Stokes Q and Stokes U .

6.5 Simulations and results

In this section, we describe the various numerical experiments performed to assess the performance of the proposed algorithm, using its MATLAB implementation.

We simulate the observations with the VLA in A-configuration, at a frequency of 1 GHz. It consists of $n_a = 27$ antennas and the measurements are acquired over a total synthesis time of 12 hr for $T = 200$ time integrations³. In the current simulation settings, we have considered linear feeds for the antennas. In practice, our approach presents a general framework and can thus be implemented for circular feeds as well. While performing the non-uniform Fourier transform at the sampled frequencies, we make use of the Kaiser-Bessel kernels of size 5×5 for interpolation [157]. We perform tests on two sets of model images of size $N = 256 \times 256$. The two sets correspond to the images of the radio galaxies Cygnus A and Hydra A, shown respectively in first and second rows of Figure 6.6. For each set, Stokes I , Q and U images ($V = 0$ due to negligible circular polarization) are displayed from left to right.

³The u - v tracks are simulated using the code available at <http://www.astro.umd.edu/~cychen/MATLAB/ASTR410/uvAndBeams.html>

Regarding the DDE Fourier kernels, for every antenna $\alpha \in \{1, \dots, n_a\}$ and at each time integration $t \in \{1, \dots, T\}$, these kernels are generated randomly in the Fourier domain, with a spatial Fourier support of $K = 5 \times 5$ and a temporal Fourier support of size $P = 3 \times 3$. The values of the Fourier coefficients are chosen as per the discussion in Section 6.4.1. More precisely, for the diagonal terms in the Jones matrix, the central coefficients that correspond to the Fourier coefficients of the DDEs have their real and imaginary parts lying in the interval $[1 - \theta_1, 1 + \theta_1]$ and $[-\theta_1, \theta_1]$, respectively, whereas the other frequency coefficients (related to the DDEs Fourier coefficients) belong to $[-\theta_1, \theta_1]$ with $\theta_1 = 5 \times 10^{-2}$. The central and all the other coefficients in the off-diagonal terms belong to $[-\theta_2, \theta_2]$ and $[-\theta_3, \theta_3]$, respectively. Here we choose $(\theta_2, \theta_3) = (5 \times 10^{-2}, 5 \times 10^{-4})$. The chosen values are in line with VLA characteristics, wherein the leakage terms (i.e. the off-diagonal terms) are $\sim 10^{-2}$ lower in peak amplitude compared to the diagonal terms, representing a leakage of around 5% of the diagonal terms [138].

6.5.1 Comparisons performed

For an assessment of the proposed algorithm, we perform an extensive study on a number of cases based on choices made both on calibration and imaging fronts. From the calibration viewpoint, we consider different generations of calibration schemes, i.e. 1GC, 2GC and 3GC, consisting in comparing the results obtained by DDE calibration with those of considering only DDEs. We also run tests with and without calibrating for the off-diagonal Jones terms to study their importance. From the imaging perspective, it is interesting to analyze the performance of different regularizations for the Stokes parameters. Thus, we consider the cases with and without enforcement of the polarization constraint. A blend of these approaches leads to following list of tests:

- (1) Imaging with calibrator transfer (1GC): Working under the assumption of calibrator transfer having been applied, the first step is to consider the Jones matrices as identity, without any directional dependency. It is important to mention that this is the usual case considered by RI imaging algorithms, either ignoring the calibration effects or relying on the pre-calibrated data. In such a

scenario, only imaging step is performed to obtain an estimation of the Stokes images **S**. Furthermore, in this imaging problem, we can consider two different regularizations and hence two sub-cases: Imaging with calibrator transfer (1.a) without and (1.b) with the enforcement of the polarization constraint.

- (2) Joint DIE calibration and imaging (2GC): This involves using the proposed algorithm for calibration and imaging. While calibrating, only the DIEs, i.e. considering support size $K = 1$ for Fourier kernels, are solved for. A thresholded version of the images estimated from (1.a) and (1.b) are used respectively to initialize the problems while working in the absence and presence of the polarization constraint. This corresponds to two sub-cases: DIE calibration and imaging (2.a) without and (2.b) with the polarization constraint.
- (3) Joint DDE calibration and imaging (3GC-polarized): This consists of using the proposed algorithm for calibrating the DDEs in conjunction with the imaging step. Similar to (2), the images are initialized from thresholded versions of (1.a) and (1.b), resulting into four cases:
 - (3.a) DDE calibration for the Jones matrices, excluding the off-diagonal terms & imaging without the polarization constraint: This corresponds to the case when the calibration steps are applied only to update the diagonal terms of the Jones matrices and without accounting for the polarization constraint in the imaging step.
 - (3.b) DDE calibration for the Jones matrices, excluding the off-diagonal terms & imaging with the polarization constraint: Here, the calibration strategy is the same as (3.a), whereas the polarization constraint is considered in the imaging step.
 - (3.c) DDE calibration for the whole Jones matrix, including the off-diagonal terms & imaging without the polarization constraint: This consists in calibrating for the full Jones matrix and without enforcing the polarization constraint in the imaging step.
 - (3.d) DDE calibration for the whole Jones matrix, including the off-diagonal terms & imaging with the polarization constraint: This approach comprises

of full Jones matrix calibration and imposing the polarization constraint in the imaging step.

6.5.2 Simulation settings

As previously mentioned, one of the key points for convergence of the proposed algorithm is to update the variables at least once in every finite number of given iterations. To ensure this, within the global loop of Algorithm 5, we perform $L_{\text{cyc}} = 2$ global iterations for the DDEs (i.e. steps 3 to 12 are iterated twice) followed by an update of the Stokes images (steps 13 to 18). After a certain number of global loops, it may happen that the DDE updates stabilize in fewer than L_{cyc} iterations. Thus, to avoid unnecessary computation, we define a stopping criterion for the DDE updates as the relative variation between the consecutive estimates of DDEs to be less than a threshold $\varepsilon_U > 0$, i.e.

$$\max_{q \in \{1,2\}} \left(\|\mathbf{U}_q^{(i+1)} - \mathbf{U}_q^{(i)}\|_F / \|\mathbf{U}_q^{(i)}\|_F \right) \leq \varepsilon_U, \quad (6.24)$$

where we set $\varepsilon_U = 10^{-5}$. In other words, if this criterion is met, no more DDE update iterations are performed, and the algorithm leaps to the imaging step using the estimated DDEs. The estimation of the Stokes images adopts a similar strategy where the iterations in the inner imaging loop are stopped and the algorithm resorts to the calibration step once, for the considered i^{th} global iteration, the following stopping criterion is satisfied:

$$\max_{q \in \{1,2,3\}} \left(\|\mathbf{E}_{:,q}^{(i,j+1)} - \mathbf{E}_{:,q}^{(i,j)}\|_2 / \|\mathbf{E}_{:,q}^{(i,j)}\|_2 \right) \leq \varepsilon_E, \quad (6.25)$$

with $\varepsilon_E = 10^{-5}$. In addition to it, to ensure stopping of the global algorithm at convergence, we define a stopping criterion as the relative variation between the values of the objective function at consecutive iterates to be less than a threshold $\varepsilon_0 > 0$, i.e.

$$\|\varphi^{(i+1)} - \varphi^{(i)}\|_2 / \|\varphi^{(i)}\|_2 \leq \varepsilon_0, \quad (6.26)$$

where $\varphi^{(i)}$ denotes the objective function value for the i^{th} iteration computed using the updated values $(\mathbf{E}^{(i+1)}, \mathbf{U}_1^{(i+1)}, \mathbf{U}_2^{(i+1)})$ and ε_0 is fixed to 2×10^{-2} . For the choice of

number of iterations $L^{(i)}$ and $J^{(i)}$ for calibration and imaging inner loops, respectively, we choose $L^{(i)} = 5$ when DDE updates need to be performed and $J^{(i)} = 100$ when imaging step is carried out. On a further note, for each of the above mentioned cases, we run 5 simulations varying the DDEs/DDEs and noise realizations.

For quantitative comparison of the results obtained by different tests, we use signal-to-noise ratio (SNR) as a metric. Given an original image $\bar{\mathbf{s}} \in \mathbb{R}^N$, the SNR of the reconstructed image \mathbf{s}' with respect to $\bar{\mathbf{s}}$ is defined as

$$\text{SNR} = 20 \log_{10} \left(\frac{\|\bar{\mathbf{s}}\|_2}{\|v' \mathbf{s}' - \bar{\mathbf{s}}\|_2} \right), \quad (6.27)$$

where $v' = \underset{v>0}{\operatorname{argmin}} \|v \mathbf{s}' - \bar{\mathbf{s}}\|_2^2$ accounts for the ambiguity problem in the underlying blind deconvolution problem. The values of the regularization parameters $\boldsymbol{\mu} = [\mu_1, \mu_2, \mu_3]$ and $\bar{\gamma}$ are chosen to maximize the SNR.

We also report the dynamic range (DR) obtained for the reconstructed images. For every image contained in the estimated Stokes matrix $\mathbf{S}' = \mathbf{S}_0 + \mathbf{E}'$, with $(i, j) \in \{1, 2\}^2$ it is defined as follows:

$$\text{DR}_{ij} = \frac{\sqrt{N} \|\check{\Phi}\|_2^2}{\|[\check{\Phi}^\dagger(\mathbf{y} - \check{\Phi}(\mathbf{S}'))]_{ij}\|_2} \max_n [\mathbf{S}'(n)]_{ij}, \quad (6.28)$$

where $\check{\Phi}$ is generated using the estimated calibration matrices.

6.5.3 Results and analysis

This section presents the results obtained by conducting tests on the various cases mentioned before. For quantitative comparison, Table 6.1 provides the obtained SNR and DR values for both the sets of images, for the different cases performed. In each case, the mean values evaluated over the 5 performed simulations are shown.

First, consider the cases of calibrator transfer and DIE calibration. They differ as the latter also accounts for the DIEs in the off-diagonal Jones terms, and thus further affected by the estimation of these terms. These terms are mainly responsible for the flux leakage from one Stokes parameter to others and if not perfectly calibrated,

can lead to error propagation. It particularly affects the low amplitude Stokes Q and U images. This can be seen from the smaller SNR values of Cygnus A's Stokes Q image with DIE calibration than that obtained by the case of calibrator transfer (Table 6.1(a)). On a further note, these cases appear to suffer strongly from the inherent ambiguity problem in the considered approach, especially when the polarization constraint is not imposed. To be more precise, any unitary matrix \mathbf{R} can be subsumed into the sought sky model and the recovered calibration matrices, without affecting the observed visibilities [6]. Considering a general RIME given in (2.16), this can be shown by the following equation:

$$\mathbf{Y}_{\alpha,\beta} = \mathcal{F}((\mathbf{D}_\alpha \mathbf{R}^\dagger)(\mathbf{R} \mathbf{B} \mathbf{R}^\dagger)(\mathbf{R} \mathbf{D}_\beta^\dagger)). \quad (6.29)$$

It is apparent then that this ambiguity, which manifests itself as a rotation and a phase term, can lead to recovering a source brightness model $\mathbf{B}' = \mathbf{R} \mathbf{B} \mathbf{R}^\dagger$ that is a misrepresentation of the original sky model \mathbf{B} . In fact, the observed visibilities provide information only about the quantities that are invariant under the unitary transformation. Such quantities include the total intensity and the polarized intensity (i.e. $\sqrt{Q^2 + U^2 + V^2}$) [120]. Nevertheless, the latter only preserves the net magnitude of the polarization state of the radio emission. The angles specifying the polarization vector's orientation (i.e. $[Q, U, V]$ in three-dimensional space) at each point of the polarization image is affected by the ambiguity [144]. To give some more intuition, consider the case of linear polarization ($V = 0$). The net polarized intensity can be distributed in the recovered Stokes Q and U in a way that the polarization angle that is deduced from it appears to be rotated, referred to as *polrotation*.

The effect of such an ambiguity can be seen particularly in the DR values of the reconstructed Stokes Q and U images for the cases of calibrator transfer and DIE calibration. More precisely, the residuals $\check{\Phi}^\dagger(\mathbf{y} - \check{\Phi}(\mathbf{S}'))$ obtained using the estimated calibration matrices and the estimated Stokes images have smaller ℓ_2 norms for Stokes Q and U than those of the residuals obtained using the true calibration matrices and the estimated images. While indicating the ambiguity problem, it causes Stokes Q and U images to have high DR values (having inverse relation with the residual norm

	without polarization constraint				with polarization constraint			
Stokes images	Calibrator transfer	DIE cal.	DDE cal. w/o off-diagonal terms	DDE cal. of full Jones matrix	Calibrator transfer	DIE cal.	DDE cal. w/o off-diagonal terms	DDE cal. of full Jones matrix
I	19.4	21.4	34	34.7	18.4	20.2	33.6	37.4
Q	18.6	16.9	20.8	21.2	16.3	15.2	23.4	24.9
U	16.9	18	19.9	22.5	15.6	16.7	21.3	25.2

(a) SNR (in dB) values for Cygnus A

	without polarization constraint				with polarization constraint			
Stokes images	Calibrator transfer	DIE cal.	DDE cal. w/o off-diagonal terms	DDE cal. of full Jones matrix	Calibrator transfer	DIE cal.	DDE cal. w/o off-diagonal terms	DDE cal. of full Jones matrix
I	1.04	1.73	10.8	12.8	1.07	1.82	9.64	41.4
Q	3.31	3.43	4.79	4.94	2.59	2.16	6.79	9.61
U	2	2.14	2.62	3.38	0.55	0.87	1.39	19.8

(b) Dynamic range (DR) values for Cygnus A in units of 10^4

	without polarization constraint				with polarization constraint			
Stokes images	Calibrator transfer	DIE cal.	DDE cal. w/o off-diagonal terms	DDE cal. of full Jones matrix	Calibrator transfer	DIE cal.	DDE cal. w/o off-diagonal terms	DDE cal. of full Jones matrix
I	18.3	20.6	24.9	25	18.3	20.7	31.2	33.2
Q	17.8	18.6	11.3	11.4	17.9	18.8	19.7	20.7
U	10.3	11.5	8.09	9.07	10.9	12.2	12.6	19.8

(c) SNR (in dB) values for Hydra A

	without polarization constraint				with polarization constraint			
Stokes images	Calibrator transfer	DIE cal.	DDE cal. w/o off-diagonal terms	DDE cal. of full Jones matrix	Calibrator transfer	DIE cal.	DDE cal. w/o off-diagonal terms	DDE cal. of full Jones matrix
I	0.82	1.54	2.35	2.45	0.82	1.49	6.43	15.9
Q	2.01	2.21	0.23	0.23	0.68	0.93	1.01	1.19
U	2.44	2.53	0.21	0.28	0.31	0.5	0.48	2.7

(d) Dynamic range (DR) values for Hydra A in units of 10^4

TABLE 6.1: Cygnus A (top two tables) and Hydra A (bottom two tables) results: SNR and Dynamic range values for different considered cases. For each of the reconstructed Stokes image, the shown values are the mean computed over 5 performed simulations for the cases with following considerations - for calibration step: calibrator transfer, DIE calibration, only diagonal Jones terms DDE calibration, and full Jones matrix DDE calibration; and for imaging step: without and with the enforcement of the polarization constraint.

(equation (6.28))), which for the considered cases turn out to be even higher than that of Stokes I in Table 6.1. Another thing to be noticed is that regularizing the underlying problem with the polarization constraint may not be very effective when DDEs are not accounted for (i.e. cases of calibrator transfer and DIE calibration). Indeed, not enforcing it can produce slightly better results than those obtained by its enforcement for these cases.

Second, consider the cases incorporating the DDE calibration scheme. In this context, an interesting observation is the degradation in the quality of Stokes Q and U images (Table 6.1(c) and 6.1(d)), when reconstructed in the absence of the polarization constraint. This could be attributed to the fact that with an increase in the number of degrees of freedom (i.e more variables to be estimated owing to DDEs incorporation), if the underlying non-convex joint DDE calibration and imaging problem is not well regularized, it may stuck in a local minimum, leading to poor reconstruction quality. This assertion is supported by the results analysis for the case when the DDEs are calibrated along with the enforcement of the constraint. These cases achieve superior performance when compared with not only the calibrator transfer and DIE calibration cases without the constraint, but also with the DDE calibration performed without the constraint. Further comparison between the DDE calibration cases with and without the constraint indicates an appreciable improvement of $\sim 9 - 10$ dBs in SNR of Stokes Q and U images (Table 6.1(c)) and around one order of magnitude in DR (Table 6.1(d)) especially for Hydra A, with the enforcement of the constraint. It should be noted that Hydra A images have lesser amplitude than the first set of images (Cygnus A). This is true specifically for Stokes Q and U images which are around one order of magnitude lower in amplitude than the corresponding Stokes I image and hence, difficult to be recovered. In this respect, the obtained results emphasize the crucial role played by suitably chosen regularization prior in enhancing the reconstruction quality. Thus, the good performance of the polarization constraint to recover these images shows suitability of this prior for full polarization imaging. This validates the findings of [25] and further extends these findings to the case of joint calibration and imaging. Lastly, comparing the results obtained with and without calibrating for the

off-diagonal Jones terms highlights higher SNR and DR values are achieved in the former case.

The above listed observations are further supported by the visual inspection of the recovered images and the associated absolute error images, shown in Figures 6.7-6.12. While Figures 6.7, 6.8 and 6.9 display the Cygnus A images for Stokes I , Q and U , respectively, the corresponding images for Hydra A are shown in Figures 6.10, 6.11 and 6.12. The error images are obtained by computing the absolute difference between the ground truth and the reconstructed images. In each of these figures, the recovered images (first and third columns) followed by their absolute error images (second and fourth columns) are shown. The shown images correspond to the reconstructions (and the associated error images) obtained when imaging is performed with: (second row) calibrator transfer (1.a) without and (1.b) with the polarization constraint, and (third row) DIE calibration (2.a) without and (2.b) with the enforcement of the polarization constraint. Similarly, the reconstructed images (and the associated error images) for the case of joint DDE calibration and imaging, excluding the off-diagonal terms and performing full Jones matrix calibration are presented respectively in third and fourth rows, both for (3.a) (and (3.c)) without the polarization constraint case and (3.b) (and (3.d)) with the polarization constraint case. It can be observed that joint DDE calibration and imaging offers remarkable advantage over considering only DIEs, mitigating the artefacts occurring because of the calibration errors. Moreover, in line with other studies [138], calibration of the off-diagonal Jones terms aids in producing high dynamic range images by diminishing the diffused calibration artefacts in the background. In addition to these remarks, the quality of reconstruction is promoted by considering the polarization constraint in the reconstruction process, specially in conjunction with DDE calibration. While the enforcement of this constraint yields lesser residual in the error images, a careful examination of the recovered images also indicates that this prior is able to produce highly resolved images with finer details as opposed to the case when the constraint is not taken into account.

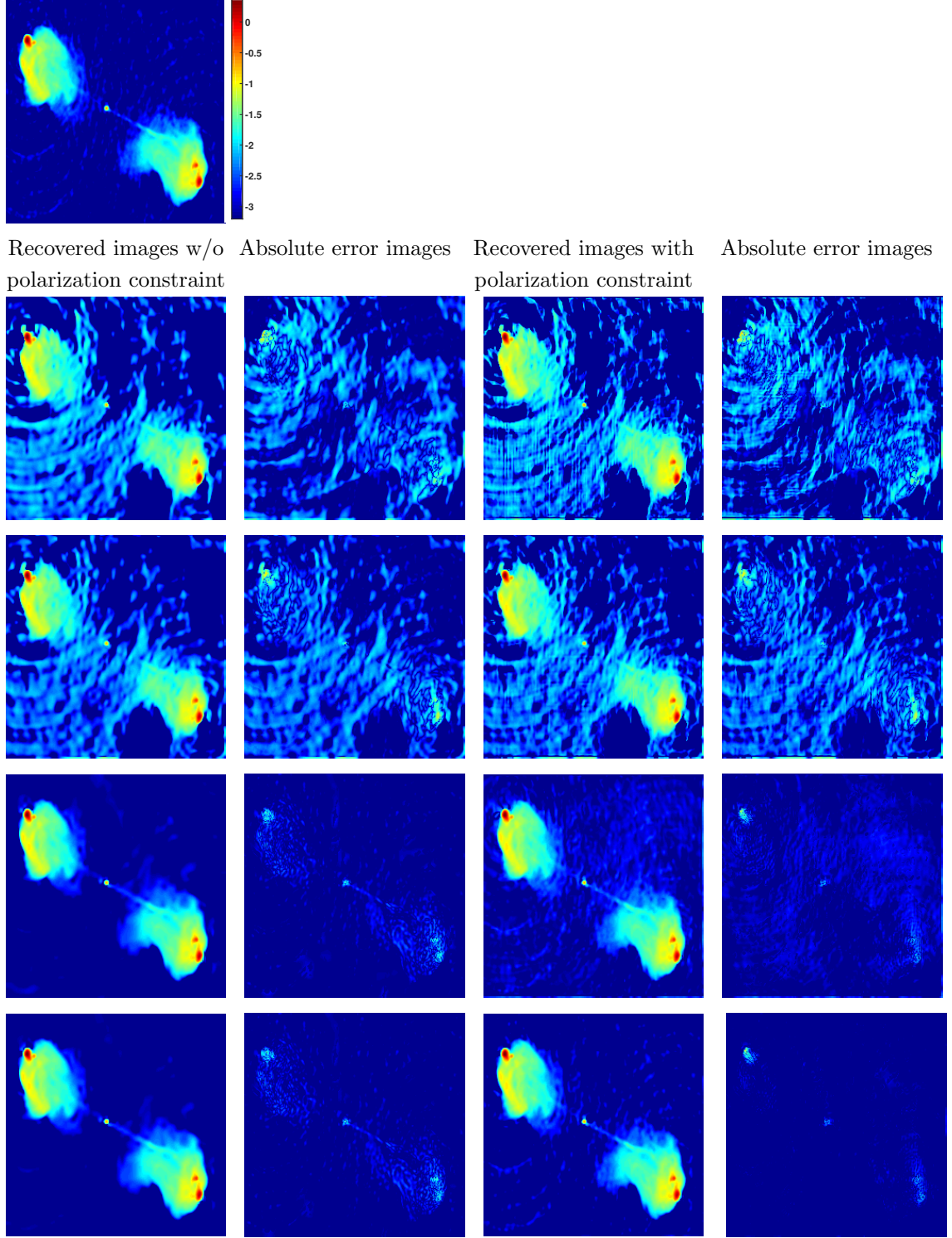


FIGURE 6.7: Cygnus A Stokes I true image in first row and reconstructed images (best ones over 5 performed simulations for each case) in other rows for the cases: Imaging with calibrator transfer (second row), Joint DIE calibration and imaging (third row), Joint DDE calibration and imaging excluding the off-diagonal terms (fourth row), and considering full Jones matrix (fifth row). In each case, column-wise recovered images followed by their corresponding error images are displayed when imaging is performed without the polarization constraint (first two columns) and with the polarization constraint (last two columns). All the images are shown in log scale, with the same color range corresponding to the colorbar in first row.

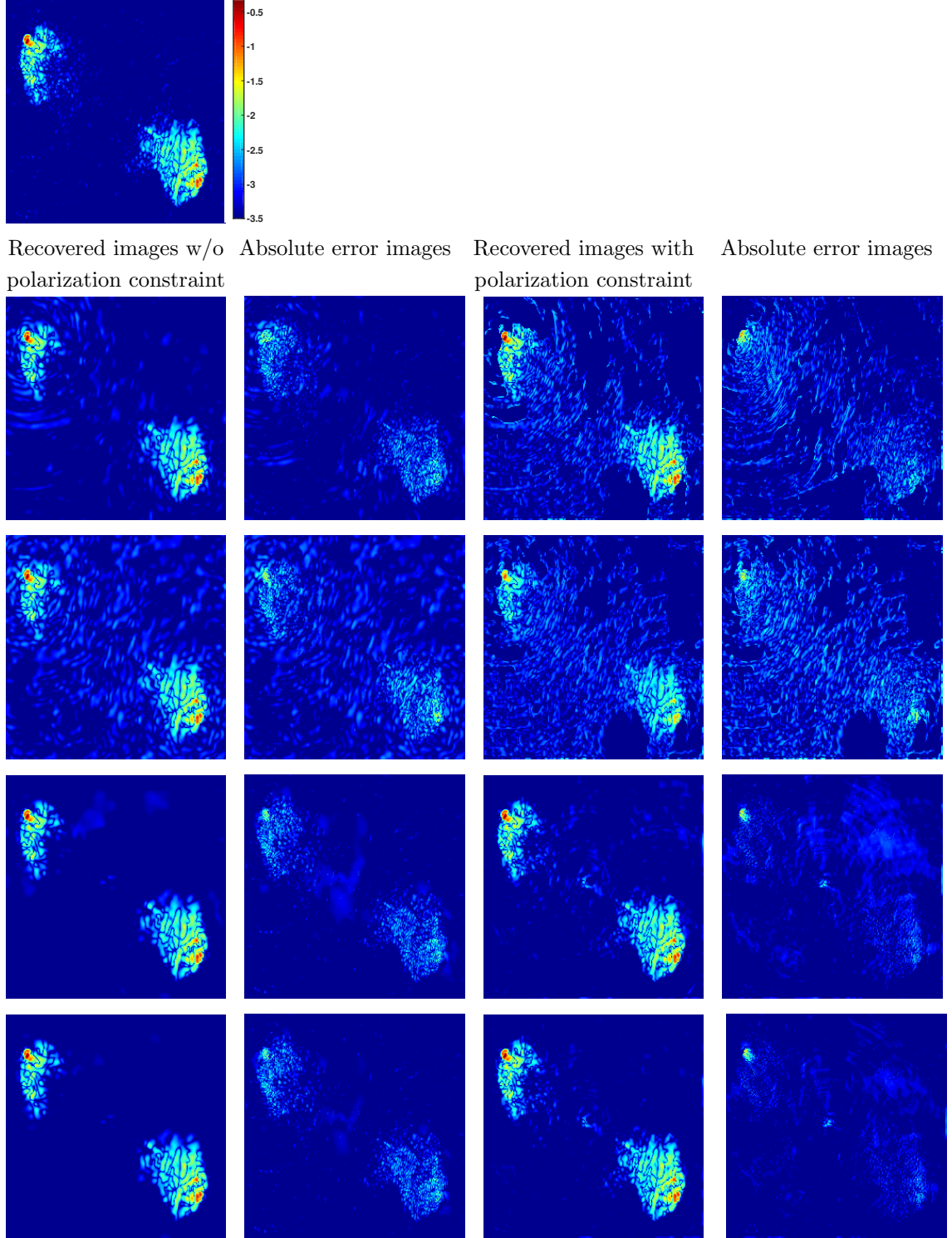


FIGURE 6.8: Cygnus A Stokes Q true image in first row and reconstructed images (best ones over 5 performed simulations for each case) in other rows for the cases: Imaging with calibrator transfer (second row), Joint DIE calibration and imaging (third row), Joint DDE calibration and imaging excluding the off-diagonal terms (fourth row), and considering full Jones matrix (fifth row). In each case, column-wise recovered images followed by their corresponding error images are displayed when imaging is performed without the polarization constraint (first two columns) and with the polarization constraint (last two columns). All the images are shown in log scale, with the same color range corresponding to the colorbar in first row.

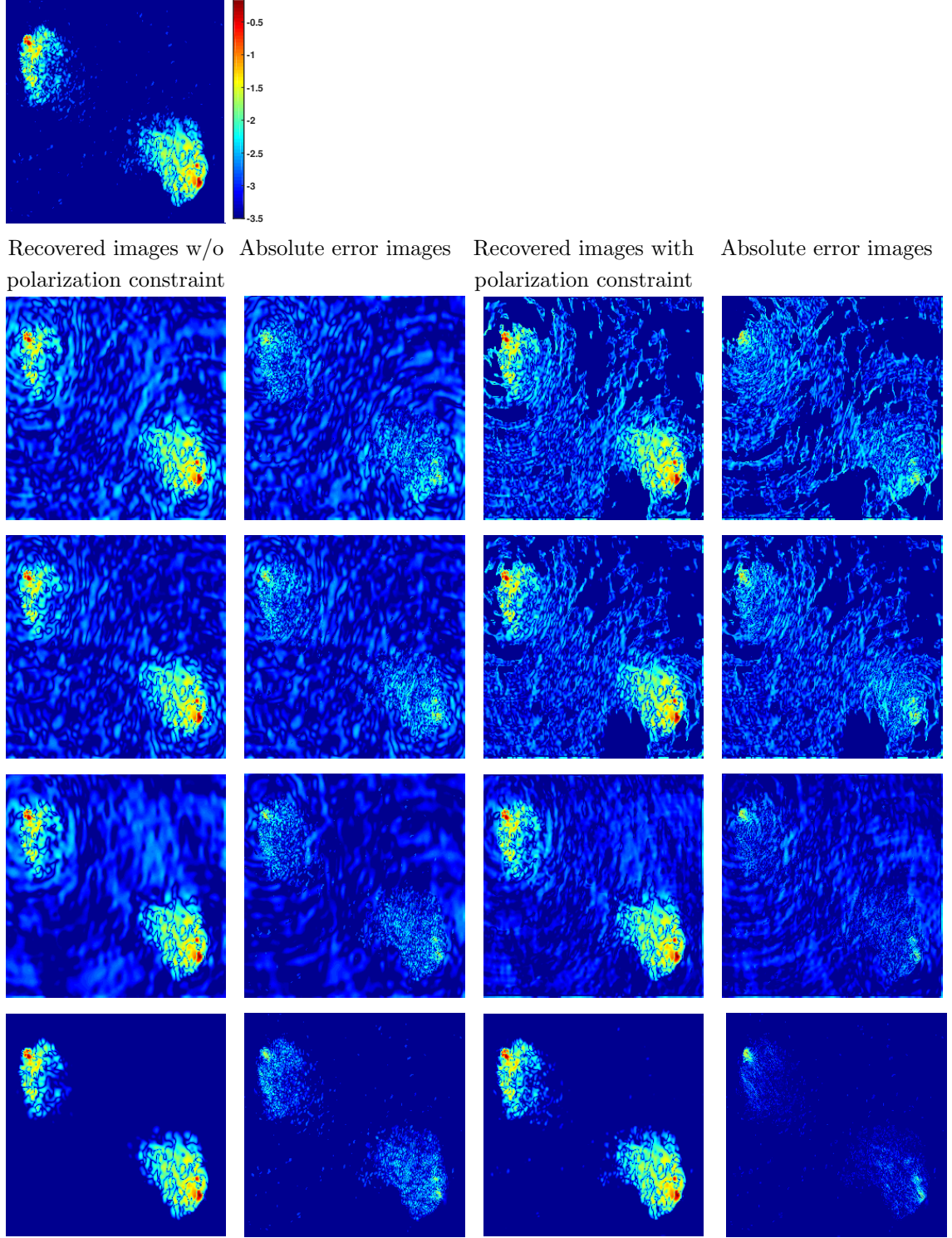


FIGURE 6.9: Cygnus A Stokes U true image in first row and reconstructed images (best ones over 5 performed simulations for each case) in other rows for the cases: Imaging with calibrator transfer (second row), Joint DIE calibration and imaging (third row), Joint DDE calibration and imaging excluding the off-diagonal terms (fourth row), and considering full Jones matrix (fifth row). In each case, column-wise recovered images followed by their corresponding error images are displayed when imaging is performed without the polarization constraint (first two columns) and with the polarization constraint (last two columns). All the images are shown in log scale, with the same color range corresponding to the colorbar in first row.

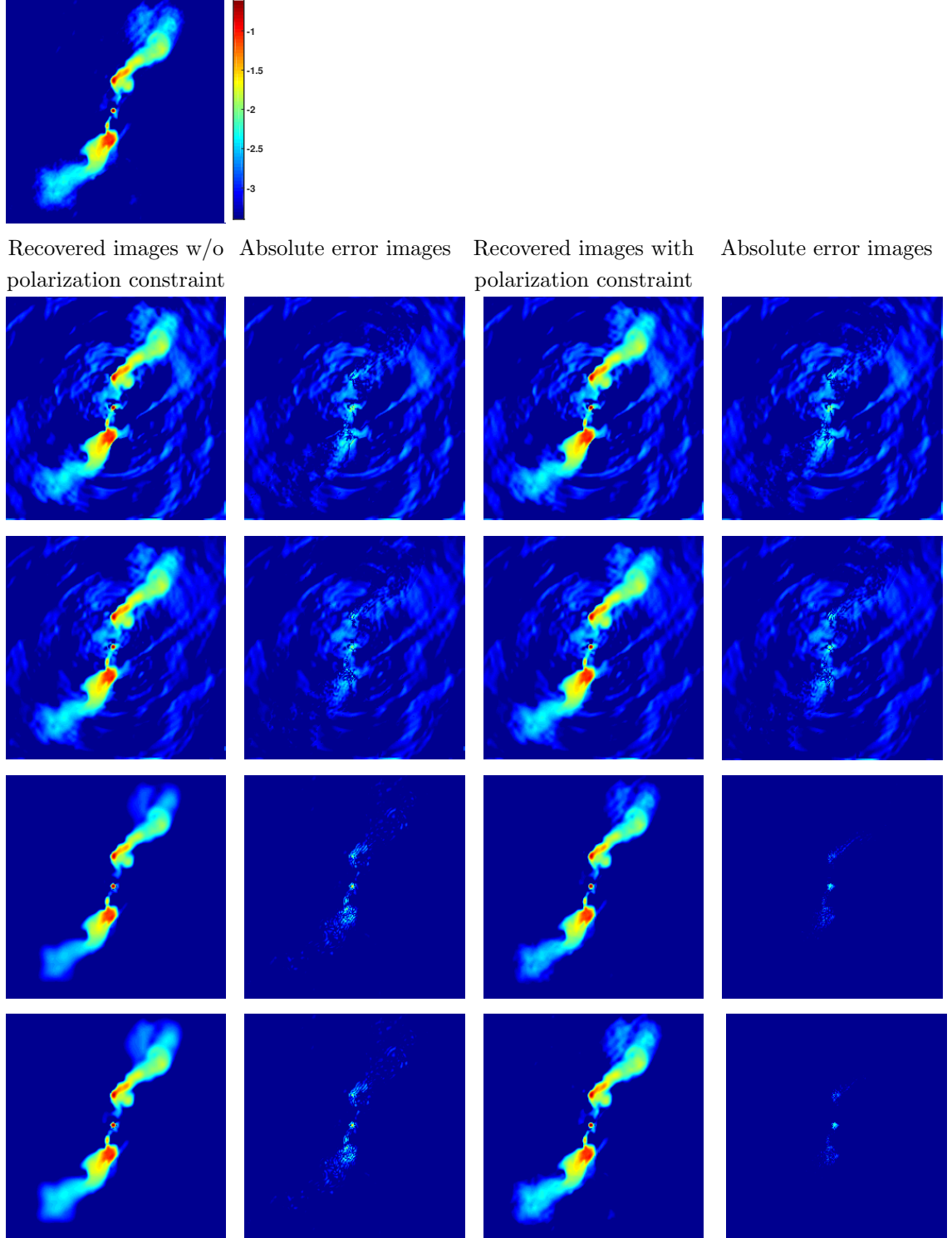


FIGURE 6.10: Hydra A Stokes I true image in first row and reconstructed images (best ones over 5 performed simulations for each case) in other rows for the cases: Imaging with calibrator transfer (second row), Joint DIE calibration and imaging (third row), Joint DDE calibration and imaging excluding the off-diagonal terms (fourth row), and considering full Jones matrix (fifth row). In each case, column-wise recovered images followed by their corresponding error images are displayed when imaging is performed without the polarization constraint (first two columns) and with the polarization constraint (last two columns). All the images are shown in log scale, with the same color range corresponding to the colorbar in first row.

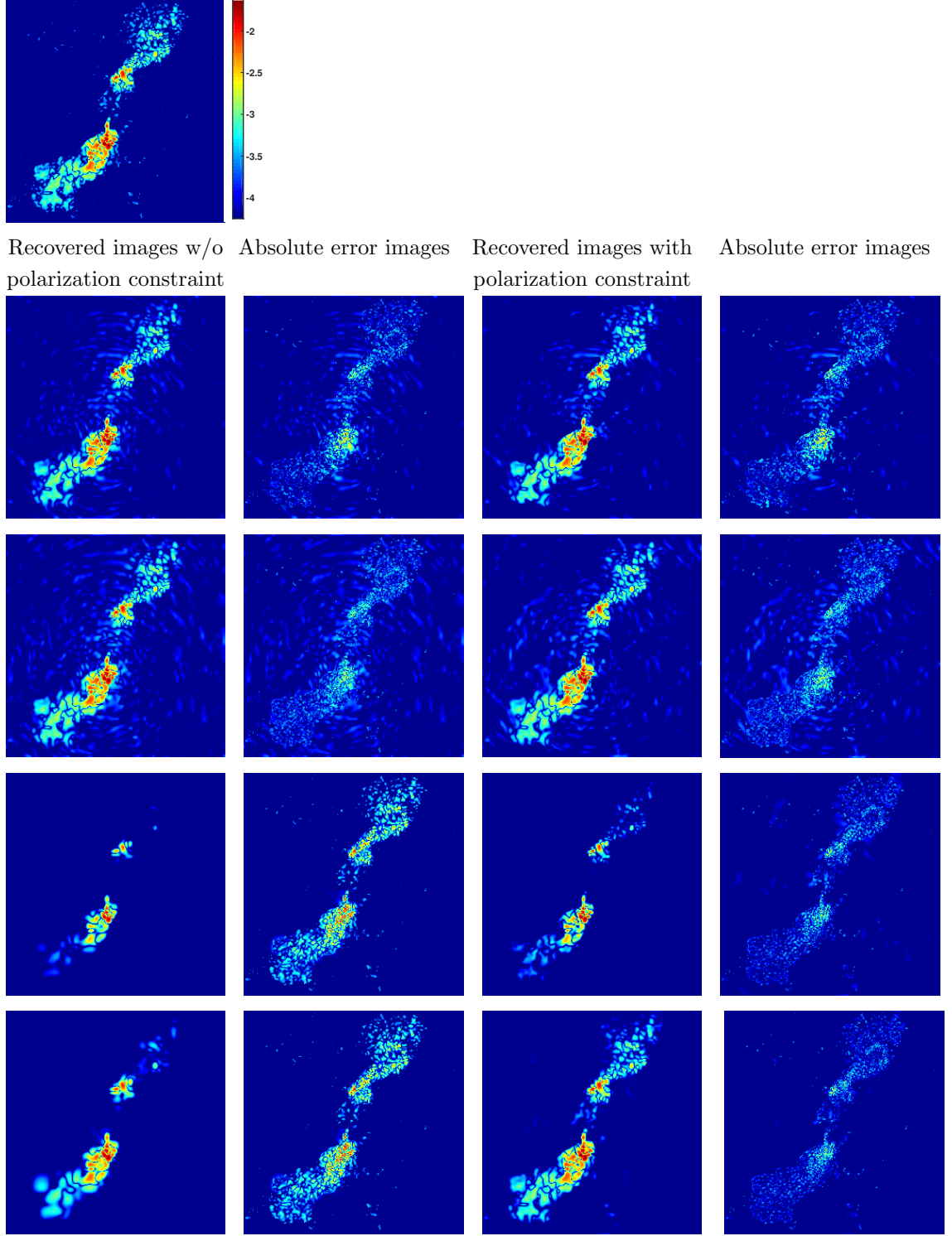


FIGURE 6.11: Hydra A Stokes Q true image in first row and reconstructed images (best ones over 5 performed simulations for each case) in other rows for the cases: Imaging with calibrator transfer (second row), Joint DIE calibration and imaging (third row), Joint DDE calibration and imaging excluding the off-diagonal terms (fourth row), and considering full Jones matrix (fifth row). In each case, column-wise recovered images followed by their corresponding error images are displayed when imaging is performed without the polarization constraint (first two columns) and with the polarization constraint (last two columns). All the images are shown in log scale, with the same color range corresponding to the colorbar in first row.

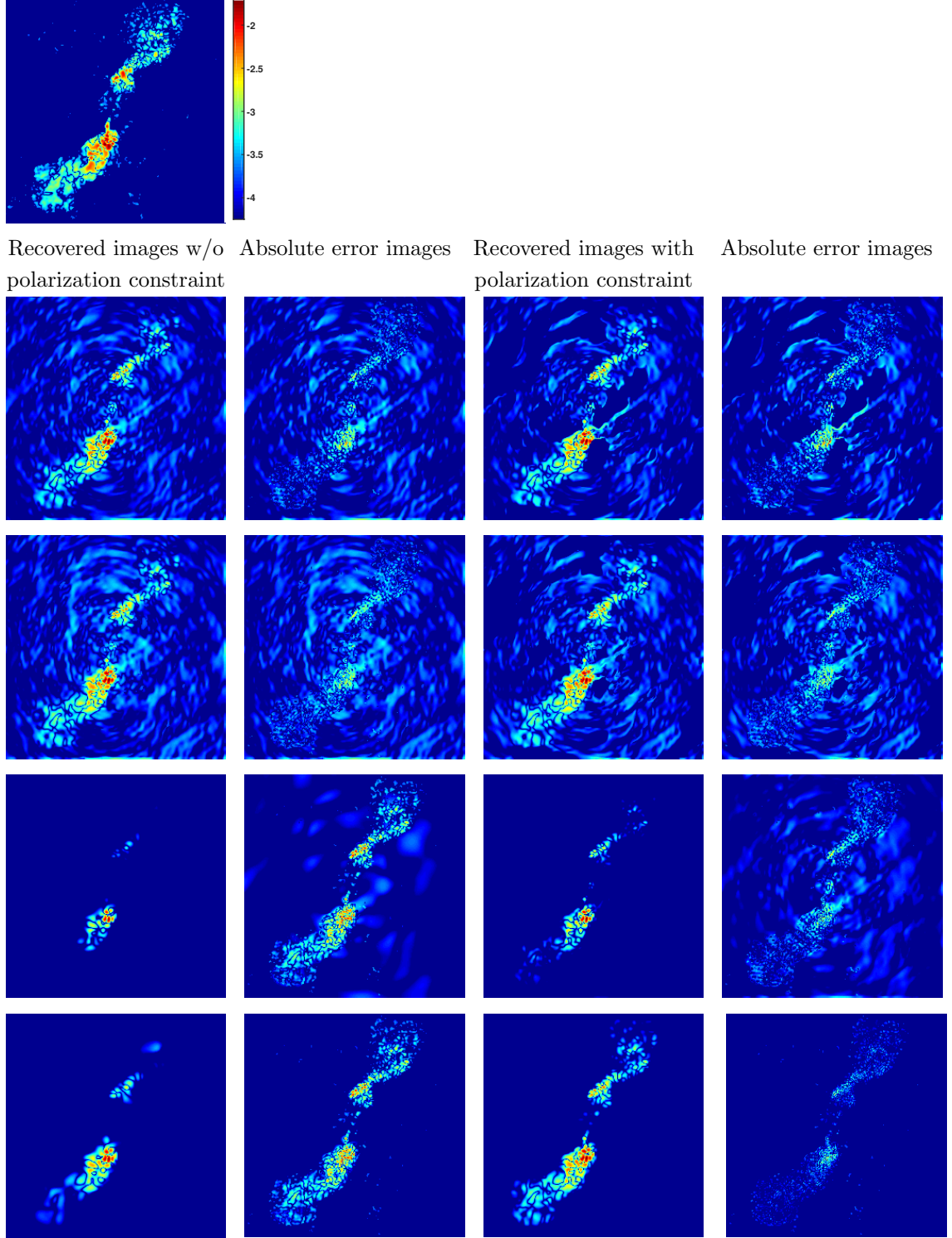
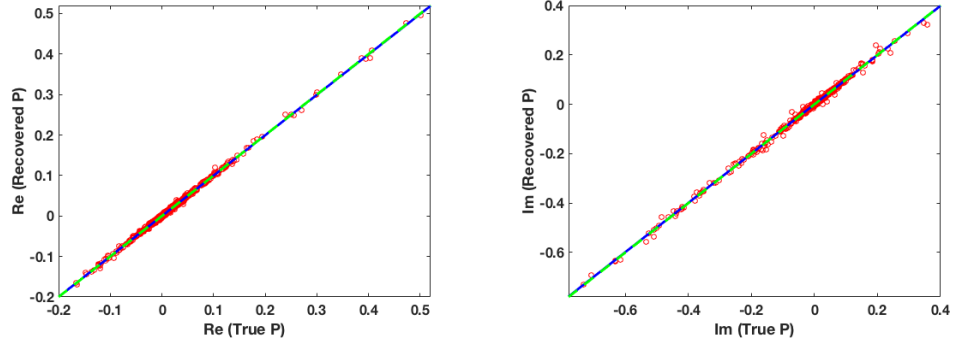


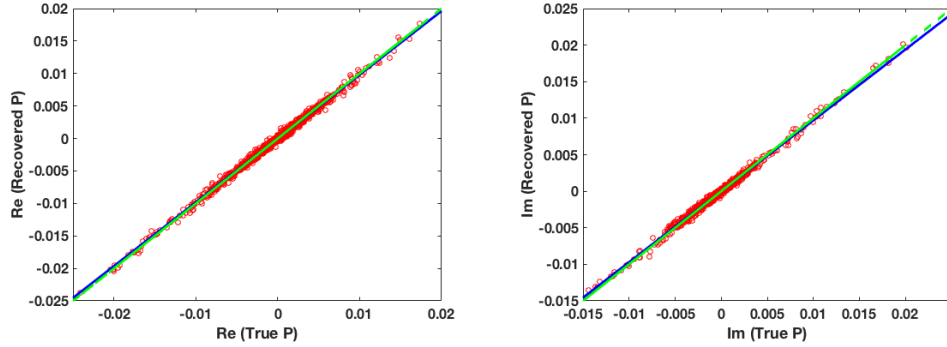
FIGURE 6.12: Hydra A Stokes U true image in first row and reconstructed images (best ones over 5 performed simulations for each case) in other rows for the cases: Imaging with calibrator transfer (second row), Joint DIE calibration and imaging (third row), Joint DDE calibration and imaging excluding the off-diagonal terms (fourth row), and considering full Jones matrix (fifth row). In each case, column-wise recovered images followed by their corresponding error images are displayed when imaging is performed without the polarization constraint (first two columns) and with the polarization constraint (last two columns). All the images are shown in log scale, with the same color range corresponding to the colorbar in first row.

Before concluding, we further investigate the ambiguity issue for the proposed approach, performing DDE calibration and Stokes imaging in the presence of the polarization constraint. For the same, the plots in Figure 6.13 compare the pixel values of (a) Cygnus A and (b) Hydra A for the real $\text{Re}(\cdot)$ component (Stokes Q) and imaginary $\text{Im}(\cdot)$ component (Stokes U) in their true and recovered linear polarization images P ($=Q + iU$). In the ideal case with perfect recovery and rotational invariance, the true and the recovered values (shown by red circles) will be equal in each plot, corresponding to a straight line passing through the origin and having slope 1 (dashed green line). However, in the current scenario, the blue line represents the least squares fit to the data. For each case, it can be observed that this line (having slope ~ 0.9) is deviated only slightly from the ideal fit, implying that the recovered images (and hence, the polarization angles) are in close agreement with the true values.

Thus, the results suggest that the ambiguity is implicitly dealt with (at least to some extent) due to the considered choice of the regularization terms. On the one hand, the enforcement of the sparsity priors separately for Stokes Q and U images causes the solution of the sky model to be driven towards certain polarization angles. To give an intuitive idea, let us consider the simplest case of a single point source with 1 Jy of linearly polarized flux. Because of the ambiguity, this flux can be rotated between Stokes Q and U (provided the total linearly polarized flux is 1 Jy), with the rotation being absorbed into the Jones matrices. Relating it to the imposed ℓ_1 sparsity prior, the algorithm will prefer a sky model with $Q = 1, U = 0$ that has lower ℓ_1 norm than say, $Q = U = 1/\sqrt{2}$, and thus implicitly implies certain polarization angles. On the other hand, the amplitude and the smoothness constraints considered for the DDEs diminish this bias and act tighter than the sparsity prior. To be more precise, the amplitude constraints dictate that the calibration matrices should lie in a neighbourhood of an identity matrix, and thus the calibration solutions cannot be deviated far away from unity. Moreover, if a unitary matrix also exhibit direction dependence, then it should comply with the smoothness prior that is enforced on the calibration matrices by the algorithm. As such, the absorption of any unitary matrix that does not vary as smoothly as the DDEs will be restricted, causing the model to be resilient to introduction of any such matrix. To shed more light onto the



(a) Cygnus A plots



(b) Hydra A plots

FIGURE 6.13: Plots comparing the pixel values of (a) Cygnus A and (b) Hydra A true and recovered linear polarization images P , for its real $\text{Re}(\cdot)$ component (Stokes Q) on left and imaginary $\text{Im}(\cdot)$ component (Stokes U) on right. The red circles show the values, the dashed green line is for the ideal fit when the true and recovered values are equal, whereas the blue line represents the least-squares straight line fit ($y = mx + c$) to the data. For Cygnus A, $m = 0.9981$ (resp. 0.9974), $c = -1.0199 \times 10^{-5}$ (resp. -2.3432×10^{-5}) for real (resp. imaginary) component of P . For Hydra A, $m = 0.9818$ (resp. 0.9704), $c = -4.7429 \times 10^{-6}$ (resp. -2.2115×10^{-7}) for real (resp. imaginary) component of P .

last assertion, let us recall that while the net polarized intensity is unaffected by the ambiguity issue, the polarization angles (i.e. the phases) might be absorbed into the calibration matrices. A careful examination of the images under scrutiny highlighted that the DDEs exhibit far more smoothness than the phases computed from the true Stokes Q and U images. This justifies the inability of the phases to be completely lost in the calibration matrices, and thus recovered accurately to a large extent by our approach.

In view of the discussion above, we further point out that although the proposed approach offers implicit handling of the unitary ambiguity issue, the extent to which

it is handled is governed by the specifications of the priors for the DDEs. For instance, an ambiguity matrix having values within the amplitude range permitted by the approach can still be observed. As a result, some uncertainties on the recovered non-invariant quantities will remain. To handle this problem explicitly, a future line of investigation should be to solve directly for the invariant quantities only such as the linear polarization image, as suggested in [120]. Relating it to the proposed approach, this would involve imposing the sparsity prior directly on the linear polarization image, rather than on Stokes Q and U . In addition, as a next step, the obtained solutions can be used as an initialization to solve the problem explicitly for the estimation of the non-invariant polarization angles. A way to deal with it could be to add exterior constraints on the ambiguity by incorporating prior information based on the average feed characteristics and external calibration [144]. In terms of the minimization problem to be solved, it resorts to adding this prior either strongly in the form of an indicator function or as a loose bound with a least-squares criterion, constraining the calibration matrices to follow these characteristics. These modifications can still be dealt with by the proposed approach using gradient or proximity/projection steps depending on the property of the underlying terms.

6.6 Conclusion

In this chapter, we have proposed a joint calibration and imaging technique for RI. Starting from Stokes I model, the technique is generalized to full polarization model. The proposed approach, dubbed Polca SARA, unifies the estimation of the DDEs for the full Jones matrix and the Stokes images of interest within a global algorithmic structure, exploiting the same optimization framework for both calibration and imaging. In particular, it solves the underlying non-convex minimization problem employing a block-coordinate forward-backward algorithm, thereby following a FB scheme for estimation of each of the variables. The MATLAB code of the proposed method is available on GitHub (<https://basp-group.github.io/Polca-SARA/>).

Our approach, shipped with convergence guarantees, can also be adapted to incorporate suitable regularization priors for the variables under consideration. Thanks to

this flexibility, for the imaging step in the global algorithm, we have employed the Polarized SARA approach specifically developed for full Stokes imaging enforcing the physical polarization constraint. These features offered by our method are in contrast with the existing calibration and imaging algorithms in RI which (i) do not benefit from global convergence guarantees and (ii) use in fact Stokes I imaging based techniques even for polarimetric imaging. Finally, the results have shown that when DDEs are calibrated along with imaging in the presence of the polarization constraint, superior performance is obtained. While mitigating the artefacts appearing otherwise in the reconstructed images, this case produces high dynamic range images without being strongly affected by the ambiguity errors.

Chapter 7

From radio to optical interferometric imaging

Contents

7.1	Motivation	160
7.2	Background	160
7.2.1	Basics of Optical Interferometry	160
7.2.2	Phase retrieval algorithms	163
7.2.3	Standard approaches for OI imaging	165
7.3	Monochromatic OI imaging	168
7.3.1	Observation model	168
7.3.2	Proposed regularized minimization problem	169
7.3.3	Proposed algorithm	173
7.4	Simulations and results	178
7.4.1	Simulation settings	178
7.4.2	Synthetic uv coverage	180
7.4.3	Realistic uv coverage	186
7.5	Hyperspectral OI imaging	188
7.5.1	Problem statement	188
7.5.2	Algorithmic details	191
7.6	Simulations and results	191
7.7	Conclusion	195

This chapter has been adapted from the published works [32] and [33].

7.1 Motivation

While the previous chapters have dealt with the algorithmic developments to solve imaging and calibration problems in RI, an analogy can be drawn between the RI and optical interferometry (OI) problems. In particular, owing to a sparser uv coverage and loss of partial phase information in the acquired data, a highly under-determined, non-linear imaging inverse problem is encountered in OI. Compared to the RI imaging literature that is brimming with a variety of techniques both for monochromatic and hyperspectral imaging, reconstruction methodology aiming to solve the extremely challenging OI imaging problem is still in its infancy. To perform this task of image recovery, we bridge the gap between the RI and OI world. On the one hand, from the perspective of inverse problems, we observe that posing a tri-linear model for OI imaging exhibits a direct correspondence with the tri-linear problem formulated earlier for RI calibration. In this respect, a similar approach exploiting the block-structure characteristic of the problem can be designed for OI imaging. On the other hand, inspired by the promising performance of sparsity priors for RI imaging, it can further be extended to recover astronomical images in the optical wavelength regimes. Working in this direction and leveraging the RI techniques proposed in this thesis, we furthermore propose a sparsity regularized tri-linear approach for OI imaging.

In this chapter, I first present the background required to understand the image recovery problem in OI. It is followed by an overview of the standard approaches to solve the corresponding problem. I then move onto the description of the proposed approach, detailing the adopted measurement model and the developed algorithm. This is done for both monochromatic and hyperspectral imaging. In both the cases, simulation results are presented to validate the approach.

7.2 Background

7.2.1 Basics of Optical Interferometry

The basic principle behind the data acquisition strategy for OI is the same as that for RI. However, the two differ in the manner the signals are finally correlated and

time averaged to produce the final output. For a better understanding, let us recall from Chapter 2 that for each antenna pair, the measurement (so-called complex visibility) is obtained by averaging the correlated signals from the two antennas over a finite, small observation time interval. Exploiting the long wavelength characteristic of the radio waves, it relies on the assumption that the random phase fluctuations induced by atmospheric turbulence are small and can be neglected during the averaging time interval. On the contrary, at optical wavelengths that are shorter than the radio wavelengths, fast and random variation in the phase over the exposure interval implies that the complex visibility values cannot be measured directly. This drives the measurement of phase-insensitive observables in OI, namely power spectrum and bispectrum [20]. In particular, power spectrum corresponds to the squared modulus of the complex visibilities. It does not contain any phase part, and thus not affected by the phase variations due to atmospheric turbulence, rendering its measurement possible. Formally, considering pre-calibrated data and the total intensity image I , the sampled power spectrum $y_{p,\alpha,\beta,t}$ at the spatial frequency $\boldsymbol{\nu}_{\alpha,\beta,t}$ is given by

$$y_{p,\alpha,\beta,t} = |\hat{I}_{\alpha,\beta,t}|^2 + \eta_{p,\alpha,\beta,t} , \quad (7.1)$$

where $\hat{I}_{\alpha,\beta,t}$ is the Fourier coefficient of the image of interest at the sampled frequency $\boldsymbol{\nu}_{\alpha,\beta,t}$ and $\eta_{p,\alpha,\beta,t}$ is the associated random additive Gaussian noise.

However, power spectrum does not provide any information about the Fourier phases, making the reconstruction even tougher. This Fourier phase information can be retrieved by measuring what is called bispectrum, represented as a triple product of the complex visibilities measured by the interferences from three optical telescopes:

$$y_{b,\alpha,\beta,\gamma,t} = \hat{I}_{\alpha,\beta,t} \hat{I}_{\beta,\gamma,t} \hat{I}_{\gamma,\alpha,t} + \eta_{b,\alpha,\beta,\gamma,t} , \quad (7.2)$$

where α, β and γ are the indices of the involved telescopes, with the corresponding bispectrum measurement $y_{b,\alpha,\beta,\gamma,t}$ being corrupted by a Gaussian noise $\eta_{b,\alpha,\beta,\gamma,t}$. We especially focus on the phase of the bispectrum, commonly referred to as the phase

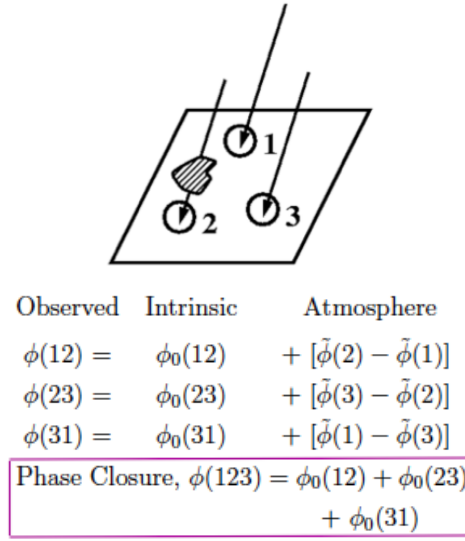


FIGURE 7.1: Illustration of the principle behind phase closure analysis. Phase errors introduced at any telescope causes equal but opposite phase shifts, cancelling out in the closure phase (figure after [177]). This figure is reproduced through the courtesy of the NASA/Jet Propulsion Laboratory, California Institute of Technology, Pasadena, California.

closure and is given by

$$\phi(\alpha\beta\gamma, t) = \arg(y_{b,\alpha,\beta,\gamma,t}) = \phi_0(\alpha\beta, t) + \phi_0(\beta\gamma, t) + \phi_0(\gamma\alpha, t) \mod 2\pi, \quad (7.3)$$

where for every $(\alpha, \beta) \in \{1, \dots, n_a\}^2$ (with $\alpha \neq \beta$), $\phi_0(\alpha\beta, t) = \arg(\hat{I}_{\alpha,\beta,t})$ is the intrinsic phase of the complex visibility $\hat{I}_{\alpha,\beta,t}$. A point worth highlighting is that since the phase closure encompasses the sum of three phases probed with the baselines forming a closed triangle, it is unaffected by the external phase errors. This principle behind phase closure analysis is further illustrated in Figure 7.1. Phase errors due to atmospheric turbulence cause shifts in the phases of the complex visibilities measured by the three considered telescopes. However, these phase shifts are equal and opposite such that they cancel out in phase closure. This insensitivity towards random phase fluctuations makes bispectrum/phase closure a good interferometric observable, especially for OI.

Exploiting this property, the phase of the underlying Fourier transformed image can thus be retrieved from the bispectrum measurements. However, each phase closure is a sum of three phases and provides only a single phase out of three spatial sampled

frequencies. To add to the difficulty, not all of it are independent. More precisely, for a n_a number of telescopes in an interferometer, the independent spatial frequencies sampled, each probed by a pair of telescopes, are equal to $\binom{n_a}{2} = n_a(n_a - 1)/2$, and the number of possible closing triangles (i.e. phase closures) is $\binom{n_a}{3} = n_a(n_a - 1)(n_a - 2)/(3 \times 2)$. Out of these, only those phase closures that contain a unique frequency/baseline are independent giving a total of $\binom{n_a-1}{2} = \frac{(n_a-1)(n_a-2)}{2}$ independent phase estimates [21, 178]. Coupled with the small number of telescopes involved in an optical interferometer, only partial phase information is obtained. It is then clear that additional difficulties arise in OI due to much sparser sampling of the spatial frequencies in the uv plane and the loss of most of the Fourier phase information.

In terms of image reconstruction, since the uv plane is highly under-sampled, many solutions are possible satisfying the measured data leading to an ill-posed imaging inverse problem. Moreover, owing to the non-linearity of the power spectrum and bispectrum measurements, this partial phase retrieval problem results into a non-convex minimization problem to be solved, further worsening the situation. In the next sections, we discuss the phase retrieval algorithms existing in the signal processing literature and then describe such standard approaches adapted for OI imaging.

7.2.2 Phase retrieval algorithms

Consider the measurements of the form $\mathbf{y} = |\mathbf{A}\bar{\mathbf{x}}|^2 + \boldsymbol{\eta}$, where $\bar{\mathbf{x}} = (\bar{x}_n)_{1 \leq n \leq N} \in \mathbb{R}_+^N$ is a discretized representation of the intensity image of interest, $\mathbf{A} \in \mathbb{C}^{M \times N}$ denotes the measurement matrix and $\boldsymbol{\eta} \in \mathbb{C}^M$ is the additive Gaussian noise. The phase retrieval problem seeks to recover the signal $\bar{\mathbf{x}}$ from the measurements \mathbf{y} by solving a non-convex minimization problem of the form

$$\underset{\mathbf{x} \in \mathbb{R}^N}{\text{minimize}} \quad \|\mathbf{y} - |\mathbf{A}\mathbf{x}|^2\|_2^2. \quad (7.4)$$

In the context of OI, we have $\mathbf{A} = \mathbf{L}_s \mathbf{F}$, where \mathbf{F} denotes the 2D Fourier transform operator and \mathbf{L}_s is an under-sampling selection operator such that $|\mathbf{A}\mathbf{x}|^2$ are the squared moduli of the under-sampled Fourier coefficients of $\bar{\mathbf{x}}$, i.e. power spectrum. Since it

is measured along with partial phase information from the phase closure data, the recovery of the sought signal can be seen as solving a partial phase retrieval problem.

Alternating projections

For the well studied phase retrieval problem, early methods were based on alternated projections. In this context, the pioneering work of Gerchberg and Saxton (GS) [179] exploits two intensity measurements: one at the real (imaging) plane and other at the Fourier (diffraction) plane. In essence, the algorithm involves alternating between the real-space and the Fourier-space imposing the measured magnitudes at the respective planes. An extension of this idea has been proposed as the Fienup algorithm [180], which in addition to ensuring consistency with the measured Fourier magnitude in the Fourier space, enforces constraints like positivity in the image space.

In practice, these algorithms are very sensitive to additive noise and they do not benefit from any convergence guarantees due to the non-convexity of the underlying problem.

Semi-definite programming algorithms

An alternative approach is provided by the techniques relying on relaxing this problem as a semi-definite program (SDP). PhaseLift [181] presents one such prominent method where the key idea is to *lift* the problem to a higher dimensional space. To be more precise, instead of the vector $\bar{\mathbf{x}}$, it aims to solve for a positive semi-definite matrix $\mathbf{X} = \bar{\mathbf{x}}\bar{\mathbf{x}}^\dagger$ resulting into solving a linear inverse problem. Another method called PhaseCut [182] incorporates separating the sought vector into its amplitude and phase components, and then optimizing only for the phase variable. On the one hand, SDP relaxations come with convergence guarantees and in many instances, as described in [183], SDP methods are seen to outperform GS and Fienup algorithms. On the other hand, the major drawback of these methods lies in the fact that they become computationally very demanding as the dimension of the problem increases.

Regularized methods

In general, the aforementioned methods tend to be less efficient when solving for under-determined problems. For such cases, several other methods based on alternating projections [184], SDP relaxations [185, 186] and greedy pursuit [187] have been proposed that leverage sparsity of the sought signal to regularize the phase retrieval problem. Furthermore, a regularized non-convex technique has been proposed in [188] aiming to minimize a penalized criterion in accordance with MAP approach. While ensuring data consistency of the estimated solution, the algorithm can also take into account priors (such as sparsity) to regularize the problem. Accompanied with the convergence guarantees, this algorithm also benefits from low computational cost, making it suitable for large dimensional problems.

Apart from being a partial phase retrieval problem, the OI image recovery problem suffers from incomplete sampling of the Fourier domain of the sought image. To counteract this additional difficulty, the imaging techniques draw upon the ideas from any of the existing phase retrieval algorithms in the signal processing literature, as discussed previously, and adapt it for the OI settings. A brief description of several such OI imaging techniques is provided in the next section.

7.2.3 Standard approaches for OI imaging

While RI flourishes with well established imaging algorithms, the same is not true for OI. Nevertheless, the latter has witnessed emergence of few algorithms in the past decade or so demonstrating success on realistic OI data [20]. In [22], the MIRA method has been developed, using a MAP approach to recover the image, where different types of quadratic regularization can be considered. The resultant minimization problem is solved using a limited variable metric algorithm (the VMLMB algorithm [189]) accounting for parameter bounds to enforce positivity of the sought image. Another technique, namely WISARD, proposed by [23] makes use of a self-calibration approach to solve for missing phase information, using smooth regularizations. In particular, it recovers Fourier phase information from the current image estimate and the phase closure data. These phases are then used to produce pseudo-complex visibilities from which the image is reconstructed following any RI imaging methodology. The so-called

BSMEM method, proposed in [190], consists of using MEM to impose smoothness on the estimated image. More recently, [191] proposed the IRBis method (image reconstruction software using the bispectrum), which solves the minimization problem from a MAP approach, considering smooth regularization terms, and employing a non-linear optimization algorithm based on conjugate gradients [192, 193].

Due to non-linearity of the underlying OI imaging inverse problem, the minimization problems solved by the aforementioned methods perform only local optimization. For global minimum search, different approaches have been proposed these last years. In particular, techniques based on a *Markov Chain Monte Carlo* (MCMC) method [194] have been adopted in MACIM [195] and SQUEEZE [196], while in [31], a tensor approach has been proposed. In the latter, following the idea of phase-lift methods for phase retrieval problems [181, 182], the data model is lifted from a vector to a super-symmetric rank-1 order-3 tensor formed by the tensor product of the vector representing the sought image with itself. This yields a linear inverse problem, and a convex minimization problem can be deduced from a MAP approach. In [197], the tensor approach has been extended to account for the signal sparsity, thereby improving the reconstruction quality. However, solving for order-3 tensor instead of an image (represented by a vector) increases the dimensionality of the problem drastically and makes this approach computationally very expensive. Thus, [31] proposed another method wherein the data model is reformulated as a tri-linear model: $\mathbf{y} = \mathbf{T}_1 \bar{\mathbf{u}}_1 \cdot \mathbf{T}_2 \bar{\mathbf{u}}_2 \cdot \mathbf{T}_3 \bar{\mathbf{u}}_3 + \boldsymbol{\eta}$, where for every $i \in \{1, 2, 3\}$, \mathbf{T}_i is the operator computing the Fourier transform followed by a suitable selection operator to generate measurements, and $\bar{\mathbf{u}}_1 = \bar{\mathbf{u}}_2 = \bar{\mathbf{u}}_3 = \bar{\mathbf{x}}$. Linear and convex sub-problems are then obtained for each of these images, which are solved alternately and iteratively. Although the global minimization problem remains non-convex and dependent on the initial guess, in practice, it has been shown that it provides much better reconstruction quality and accelerates the convergence speed as compared to the tensor approach. Moreover, contrary to the state-of-the-art-methods, it brings convexity to the sub-problems. However, [31] proposed to solve this tri-linear problem using a Gauss-Seidel method ([198], [199, Chapter 7], [200, Chapter 2]), which does not have any convergence guarantees in this context. Additionally, only positivity constraints have been considered,

without imposing any other *a priori* information on the underlying image.

All of the above mentioned methods are designed to reconstruct monochromatic images. However, electromagnetic radiations at different wavelengths can be emitted from an astrophysical source, corresponding to its spectrum. In order to exploit the spectrum of the source, modern optical interferometers are paving the way for multi-wavelength imaging. Instruments such as AMBER [18], GRAVITY [19] and MATISSE [201], can take measurements at multiple wavelength channels. This necessitates the progression of imaging techniques from monochromatic to hyperspectral case. Lately, initial works have been done in the direction of OI hyperspectral imaging. In particular, the method proposed by [202], namely SPARCO, is a semi-parametric approach for image reconstruction of chromatic objects, whereas the method proposed by [203] deals with a sparsity regularized approach considering the observed scene to be a collection of point-like sources. Recently, the use of differential phases for hyperspectral imaging has been proposed in PAINTER [204]. In particular, the methods proposed by [203] and [204] use the ADMM algorithm [132] to solve the considered minimization problem.

In view of the discussion above, we aim to develop an image reconstruction algorithm that can be applied both for monochromatic and hyperspectral cases in OI. More precisely, in the monochromatic case, we propose to improve the method based on the tri-linear data model proposed by [31]. First, we propose to regularize the problem using sparsity priors [5, 45]. Second, the adopted tri-linear model bears similarity with the RI calibration and imaging model, and thus we develop an algorithm based on the block-coordinate forward-backward algorithm [107, 108, 205], which has previously been adapted for joint calibration and imaging in RI. Finally, we generalize the proposed method to the hyperspectral case. It translates to a new approach for hyperspectral imaging in OI. In this context, we exploit the joint sparsity of the image cube through an $\ell_{2,1}$ norm [203].

The rest of the chapter deals with a detailed presentation and performance evaluation of the proposed OI imaging approach.

7.3 Monochromatic OI imaging

7.3.1 Observation model

Let the discrete Fourier transform of the image of interest $\bar{\mathbf{x}}$ be denoted by $\hat{\mathbf{x}} = (\hat{x}_n)_{1 \leq n \leq N} \in \mathbb{C}^N$. We furthermore note that the total flux is assumed to be measured independently and the zero frequency Fourier coefficient, denoted by \hat{x}_c , is normalized to be equal to 1. In particular, each OI measurement can be represented by a triple product of Fourier coefficients of the image of interest, i.e. $\hat{x}_i \hat{x}_j \hat{x}_k$, where i, j and k belong to $\{1, \dots, N\}$. Considering the Hermitian symmetry, we denote by \hat{x}_{i^*} the Fourier coefficient at the opposite spatial frequency to that related with \hat{x}_i . Following this notation, the power spectrum measurements are obtained by choosing indices $j = i^*$ and $k = c$, thus giving triple product of the form $\hat{x}_i \hat{x}_{i^*} \hat{x}_c = |\hat{x}_i|^2$. Similarly, for the bispectrum measurements, phase closure should be satisfied so that the spatial frequencies corresponding to \hat{x}_i, \hat{x}_j and \hat{x}_k sum to zero [21]. As a result, the bispectrum measurements are given by $\hat{x}_i \hat{x}_j \hat{x}_{(i+j)^*}$.

In view of the description provided above, the OI imaging inverse problem can be written as

$$\mathbf{y} = [(\mathbf{T}_1 \bar{\mathbf{x}}) \cdot (\mathbf{T}_2 \bar{\mathbf{x}}) \cdot (\mathbf{T}_3 \bar{\mathbf{x}})] + \boldsymbol{\eta}, \quad (7.5)$$

where \cdot denotes the Hadamard product, $\mathbf{y} = (y_m)_{1 \leq m \leq M} \in \mathbb{C}^M$, with $M = M_{\mathcal{P}} + M_{\mathcal{B}}$, i.e. sum of $M_{\mathcal{P}}$ power spectrum measurements and $M_{\mathcal{B}}$ bispectrum measurements. $\boldsymbol{\eta} \in \mathbb{C}^M$ is a realization of an additive i.i.d. Gaussian noise, and $\mathbf{T}_1, \mathbf{T}_2, \mathbf{T}_3$ are linear operators from \mathbb{R}^N to \mathbb{C}^M . More precisely, for every $p \in \{1, 2, 3\}$, \mathbf{T}_p performs a discrete 2D Fourier transform $\mathbf{F} \in \mathbb{C}^{N \times N}$, followed by selection operators, denoted by $\mathbf{K} \in \mathbb{R}^{M_{\mathcal{P}} \times N}$ and $\mathbf{L}_p \in \mathbb{R}^{M \times M_{\mathcal{P}}}$, i.e.

$$\mathbf{T}_p = \mathbf{L}_p \mathbf{K} \mathbf{F}. \quad (7.6)$$

First, the operator \mathbf{K} selects $M_{\mathcal{P}}$ Fourier coefficients corresponding to the spatial frequencies given by the telescopes' position. It is to be noted that due to Hermitian symmetry, only half of the Fourier plane is sampled. Then, the operators $\mathbf{L}_1, \mathbf{L}_2$ and

\mathbf{L}_3 select the different coefficients from $\mathbf{KF}\bar{\mathbf{x}}$, in order to construct the triple products corresponding to the power spectrum and bispectrum measurements. This makes these three operators different from each other.

7.3.2 Proposed regularized minimization problem

Problem formulation

The data model in equation (7.5) being non-linear, applying directly a MAP approach would lead to a non-convex minimization problem. To bring linearity in (7.5), following the model proposed by [31], we introduce $(\bar{\mathbf{u}}_1, \bar{\mathbf{u}}_2, \bar{\mathbf{u}}_3) \in (\mathbb{R}_+^N)^3$ such that

$$\bar{\mathbf{u}}_1 = \bar{\mathbf{u}}_2 = \bar{\mathbf{u}}_3 = \bar{\mathbf{x}}. \quad (7.7)$$

Then, the data model (7.5) is equivalent to

$$\mathbf{y} = [(\mathbf{T}_1 \bar{\mathbf{u}}_1) \cdot (\mathbf{T}_2 \bar{\mathbf{u}}_2) \cdot (\mathbf{T}_3 \bar{\mathbf{u}}_3)] + \boldsymbol{\eta}, \quad (7.8)$$

where $\bar{\mathbf{u}}_1$, $\bar{\mathbf{u}}_2$ and $\bar{\mathbf{u}}_3$ correspond to the unknown image to be estimated. The new model described in (7.8) is tri-linear, i.e., it is linear in each of the variables $\bar{\mathbf{u}}_1$, $\bar{\mathbf{u}}_2$ and $\bar{\mathbf{u}}_3$. Thus, the problem can be solved separately for each of these variables, keeping other two fixed.

We propose to use a MAP approach to find an estimation of the original image $\bar{\mathbf{x}}$. More precisely, we propose to define the estimation of $(\bar{\mathbf{u}}_1, \bar{\mathbf{u}}_2, \bar{\mathbf{u}}_3)$ as a solution to

$$\underset{(\mathbf{u}_1, \mathbf{u}_2, \mathbf{u}_3) \in (\mathbb{R}^N)^3}{\text{minimize}} \quad f(\mathbf{u}_1, \mathbf{u}_2, \mathbf{u}_3) + \sum_{p=1}^3 r(\mathbf{u}_p), \quad (7.9)$$

where $f: \mathbb{R}^N \rightarrow]-\infty, +\infty[$ is the data fidelity term and $r: \mathbb{R}^N \rightarrow]-\infty, +\infty[$ is a regularization term incorporating *a priori* information on the target image $\bar{\mathbf{x}}$. Here, due to equality (7.7), we propose to choose the same regularization for \mathbf{u}_1 , \mathbf{u}_2 and \mathbf{u}_3 .

Since $\boldsymbol{\eta}$ in (7.8) is assumed to be a realization of an i.i.d. Gaussian noise, the usual least-squares criterion can be used for the data fidelity term:

$$f(\mathbf{u}_1, \mathbf{u}_2, \mathbf{u}_3) = \frac{1}{2} \left\| \mathbf{y} - (\mathbf{T}_1 \mathbf{u}_1) \cdot (\mathbf{T}_2 \mathbf{u}_2) \cdot (\mathbf{T}_3 \mathbf{u}_3) \right\|_2^2. \quad (7.10)$$

This formulation is under the assumption that the noise variance is same for both the power spectrum and bispectrum measurements. However, in practice, the bispectrum measurements are degraded by a noise with greater variance than that of the noise associated to the power spectrum [206]. In such scenario, the above formulation can be easily extended to incorporate information from the noise covariance matrix by using a weighted least-squares data fidelity term [191].

In order to ensure a good reconstruction quality, we propose to use a hybrid regularization term:

$$(\forall \mathbf{x} \in \mathbb{R}^N) \quad r(\mathbf{x}) = \iota_{\mathbb{R}_+^N}(\mathbf{x}) + \mu g(\mathbf{x}), \quad (7.11)$$

where the first term $\iota_{\mathbb{R}_+^N}(\mathbf{x})$ enforces reality and positivity of the sought image, $\mu > 0$ is the regularization parameter and $g: \mathbb{R}^N \rightarrow]-\infty, +\infty]$ is a convex non-necessarily smooth function. Thus, the proposed formulation can be seen as a generalization of the model proposed in [31]. Indeed, [31] proposed to solve (7.9) using f defined in (7.10), and r given by (7.11) when $\mu \equiv 0$.

Symmetrized data fidelity term

Problem (7.9) can be solved by alternating sequentially between the estimation of each variable \mathbf{u}_1 , \mathbf{u}_2 and \mathbf{u}_3 while keeping the other two fixed. Since the vectors are solved separately in each sub-problem, the 3 estimated vectors can converge to different estimations. One method to avoid this issue is to add the information (7.7) in the regularization term, e.g. to consider quadratic terms controlling the distance between the variables \mathbf{u}_1 , \mathbf{u}_2 and \mathbf{u}_3 . However, introducing such regularization terms involve additional regularization parameters to be tuned. Thus, to ensure convergence of the three vectors to similar estimations, while avoiding to complicate the minimization problem with additional regularization parameters, we consider a symmetric data fidelity term for \mathbf{u}_1 , \mathbf{u}_2 and \mathbf{u}_3 , instead of considering the usual least-squares criterion

(7.10). More precisely, in order to take into account the symmetry between $\bar{\mathbf{u}}_1$, $\bar{\mathbf{u}}_2$ and $\bar{\mathbf{u}}_3$, we propose to consider the following data fidelity term:

$$\begin{aligned} \tilde{f}(\mathbf{u}_1, \mathbf{u}_2, \mathbf{u}_3) = \frac{1}{6} & \left(f(\mathbf{u}_1, \mathbf{u}_2, \mathbf{u}_3) + f(\mathbf{u}_1, \mathbf{u}_3, \mathbf{u}_2) + f(\mathbf{u}_2, \mathbf{u}_1, \mathbf{u}_3) + f(\mathbf{u}_2, \mathbf{u}_3, \mathbf{u}_1) \right. \\ & \left. + f(\mathbf{u}_3, \mathbf{u}_1, \mathbf{u}_2) + f(\mathbf{u}_3, \mathbf{u}_2, \mathbf{u}_1) \right), \end{aligned} \quad (7.12)$$

where f is given by (7.10). In this case, it can be noticed that $\bar{\mathbf{u}}_1$, $\bar{\mathbf{u}}_2$ and $\bar{\mathbf{u}}_3$ are commutative in (7.12), i.e. we have

$$\begin{aligned} \tilde{f}(\mathbf{u}_1, \mathbf{u}_2, \mathbf{u}_3) &= \tilde{f}(\mathbf{u}_1, \mathbf{u}_3, \mathbf{u}_2) = \tilde{f}(\mathbf{u}_2, \mathbf{u}_1, \mathbf{u}_3) = \tilde{f}(\mathbf{u}_2, \mathbf{u}_3, \mathbf{u}_1) \\ &= \tilde{f}(\mathbf{u}_3, \mathbf{u}_1, \mathbf{u}_2) = \tilde{f}(\mathbf{u}_3, \mathbf{u}_2, \mathbf{u}_1). \end{aligned} \quad (7.13)$$

The symmetrization of the data fidelity term can be explained as follows. Due to equality (7.7), images $\bar{\mathbf{u}}_1$, $\bar{\mathbf{u}}_2$ and $\bar{\mathbf{u}}_3$ correspond to the sought image $\bar{\mathbf{x}}$. Let $\hat{\mathbf{u}}_p = (\hat{u}_{p,i})_{1 \leq i \leq N}$ denote the Fourier transform of $\bar{\mathbf{u}}_p$, for $p \in \{1, 2, 3\}$. Then, for a given frequency index i , we have $\hat{u}_{1,i} = \hat{u}_{2,i} = \hat{u}_{3,i}$. This implies that each measurement y_{ijk} , where (i, j, k) is a triplet of frequency indices, can be given by $\hat{u}_{p,i} \hat{u}_{q,j} \hat{u}_{s,k}$, for all the possible permutations of $(p, q, s) \in (\{1, 2, 3\})^3$, with $p \neq q \neq s$.

Thus, following this symmetrized approach, we propose to

$$\underset{(\mathbf{u}_1, \mathbf{u}_2, \mathbf{u}_3) \in (\mathbb{R}^N)^3}{\text{minimize}} \left\{ h(\mathbf{u}_1, \mathbf{u}_2, \mathbf{u}_3) = \tilde{f}(\mathbf{u}_1, \mathbf{u}_2, \mathbf{u}_3) + \sum_{p=1}^3 r(\mathbf{u}_p) \right\}, \quad (7.14)$$

where \tilde{f} is defined by (7.12), and r is given by (7.11). It can be observed that since the data fidelity term is symmetrized and the same regularization term is used for $\mathbf{u}_1, \mathbf{u}_2, \mathbf{u}_3$, the global cost function h is symmetric as well with respect to $\mathbf{u}_1, \mathbf{u}_2, \mathbf{u}_3$. Furthermore, the minimization problem is solved using identical initialization for the unknown vectors \mathbf{u}_1 , \mathbf{u}_2 , and \mathbf{u}_3 , and the final estimation \mathbf{x}^* of $\bar{\mathbf{x}}$ is taken to be the mean of the three estimated vectors. We will demonstrate in Section 7.4, through simulation results, that the recovered estimations of $\bar{\mathbf{u}}_1$, $\bar{\mathbf{u}}_2$ and $\bar{\mathbf{u}}_3$ are indeed very close.

Alternated minimization

As discussed earlier, problem (7.14) can be solved sequentially, alternating between the estimations of $\bar{\mathbf{u}}_1$, $\bar{\mathbf{u}}_2$, and $\bar{\mathbf{u}}_3$. To describe the three corresponding sub-problems, additional notations are introduced. In particular, let us rewrite the considered symmetrized data fidelity term (7.12) as follows

$$\tilde{f}(\mathbf{u}_1, \mathbf{u}_2, \mathbf{u}_3) = \frac{1}{2} \|\tilde{\mathbf{y}} - (\tilde{\mathbf{T}}_1 \mathbf{u}_1) \cdot (\tilde{\mathbf{T}}_2 \mathbf{u}_2) \cdot (\tilde{\mathbf{T}}_3 \mathbf{u}_3)\|_2^2, \quad (7.15)$$

where $\tilde{\mathbf{T}}_1$, $\tilde{\mathbf{T}}_2$, and $\tilde{\mathbf{T}}_3$ are linear operators defined to be the concatenations of the permutations of the operators $(\mathbf{T}_p)_{1 \leq p \leq 3}$:

$$\tilde{\mathbf{T}}_1 = \frac{1}{6^{1/6}} \begin{bmatrix} \mathbf{T}_1 \\ \mathbf{T}_1 \\ \mathbf{T}_2 \\ \mathbf{T}_2 \\ \mathbf{T}_3 \\ \mathbf{T}_3 \end{bmatrix}, \quad \tilde{\mathbf{T}}_2 = \frac{1}{6^{1/6}} \begin{bmatrix} \mathbf{T}_2 \\ \mathbf{T}_3 \\ \mathbf{T}_1 \\ \mathbf{T}_3 \\ \mathbf{T}_1 \\ \mathbf{T}_2 \end{bmatrix}, \quad \text{and} \quad \tilde{\mathbf{T}}_3 = \frac{1}{6^{1/6}} \begin{bmatrix} \mathbf{T}_3 \\ \mathbf{T}_2 \\ \mathbf{T}_3 \\ \mathbf{T}_1 \\ \mathbf{T}_2 \\ \mathbf{T}_1 \end{bmatrix}, \quad (7.16)$$

and $\tilde{\mathbf{y}} \in \mathbb{C}^{(6M)}$ is the concatenation of the corresponding 6 permutations of the observation vector \mathbf{y} , divided by $6^{1/2}$. Let $(p, q, s) \in \{1, 2, 3\}$. Fix $\mathbf{u}_q \in \mathbb{R}^N$ and $\mathbf{u}_s \in \mathbb{R}^N$ such that $p \neq q \neq s$, and consider the operator $\tilde{\mathbf{T}}_{(\mathbf{u}_q, \mathbf{u}_s)}: \mathbb{R}^N \rightarrow \mathbb{C}^M$ defined by

$$\tilde{\mathbf{T}}_{(\mathbf{u}_q, \mathbf{u}_s)} \mathbf{u}_p = [(\tilde{\mathbf{T}}_1 \mathbf{u}_q) \cdot (\tilde{\mathbf{T}}_2 \mathbf{u}_s) \cdot (\tilde{\mathbf{T}}_3 \mathbf{u}_p)]. \quad (7.17)$$

Then, the minimization of h with respect to \mathbf{u}_p (while \mathbf{u}_q and \mathbf{u}_s are fixed) can be rewritten as follows

$$\underset{\mathbf{u}_p \in \mathbb{R}^N}{\text{minimize}} \quad \tilde{f}_p(\mathbf{u}_p | \mathbf{u}_q, \mathbf{u}_s) + r(\mathbf{u}_p), \quad (7.18)$$

where r is given by (7.11) and

$$\tilde{f}_p(\mathbf{u}_p | \mathbf{u}_q, \mathbf{u}_s) = \frac{1}{2} \|\tilde{\mathbf{y}} - \tilde{\mathbf{T}}_{(\mathbf{u}_q, \mathbf{u}_s)} \mathbf{u}_p\|_2^2. \quad (7.19)$$

We further highlight that the data fidelity term $\tilde{f}_p(\cdot | \mathbf{u}_q, \mathbf{u}_s)$ defined by (7.19) is a convex differentiable function, with its gradient given by

$$\nabla \tilde{f}_p(\mathbf{u}_p | \mathbf{u}_q, \mathbf{u}_s) = \tilde{\mathbf{T}}_{(\mathbf{u}_q, \mathbf{u}_s)}^\dagger (\tilde{\mathbf{T}}_{(\mathbf{u}_q, \mathbf{u}_s)} \mathbf{u}_p - \tilde{\mathbf{y}}). \quad (7.20)$$

Moreover, $\nabla \tilde{f}_p$ is $\kappa(\mathbf{u}_q, \mathbf{u}_s)$ -Lipschitzian [103, Def. 1.46] with

$$\kappa(\mathbf{u}_q, \mathbf{u}_s) = \|\tilde{\mathbf{T}}_{(\mathbf{u}_q, \mathbf{u}_s)}\|_2, \quad (7.21)$$

$\|\cdot\|_2$ denoting the spectral norm of its argument.

Concerning the choice of g in (7.11), inspired by the performance of sparsity regularization for RI imaging, we consider both ℓ_1 and reweighted- ℓ_1 terms to promote sparsity. Particularly, in the latter case, a sequence of weighted- ℓ_1 minimization problems is considered, i.e. problem (7.14) with

$$g(\mathbf{x}) = \|\mathbf{W}\Psi^\dagger \mathbf{x}\|_1, \quad (7.22)$$

where the weights $\mathbf{W} = \text{Diag}(w_1, \dots, w_J)$, with $(w_j)_{1 \leq j \leq J} \in]0, +\infty[^J$, are computed from the current estimation of \mathbf{x} . Let us recall that when \mathbf{W} is taken to be identity, equation (7.22) reduces to usual ℓ_1 minimization.

7.3.3 Proposed algorithm

Algorithm formulation

In this section, we will describe more in detail the proposed alternating minimization algorithm to solve problem (7.14). In particular, exploiting its analogy with the variable block-structure experienced for RI calibration as well, we adopt the block-coordinate forward-backward algorithm for the current case.

In this method, \mathbf{u}_1 , \mathbf{u}_2 and \mathbf{u}_3 are updated sequentially, by solving (7.18), as described in Algorithm 8. More precisely, this algorithm consists in computing, at each iteration $k \in \mathbb{N}$,

1. $\mathbf{u}_1^{(k+1)}$ while $(\mathbf{u}_2^{(k)}, \mathbf{u}_3^{(k)})$ are fixed,
2. $\mathbf{u}_2^{(k+1)}$ while $(\mathbf{u}_1^{(k+1)}, \mathbf{u}_3^{(k)})$ are fixed,
3. $\mathbf{u}_3^{(k+1)}$ while $(\mathbf{u}_1^{(k+1)}, \mathbf{u}_2^{(k+1)})$ are fixed.

The update of each variable $(\mathbf{u}_p^{(k+1)})_{1 \leq p \leq 3}$ is computed with the FB iterations described in steps 7-12 of Algorithm 8. Each iteration involves alternating between

- Step 9: gradient step (or forward step) on the corresponding differentiable function, i.e., $\tilde{f}_1(\cdot | \mathbf{u}_2^{(k)}, \mathbf{u}_3^{(k)})$ for \mathbf{u}_1 , $\tilde{f}_2(\cdot | \mathbf{u}_1^{(k+1)}, \mathbf{u}_3^{(k)})$ for \mathbf{u}_2 and $\tilde{f}_3(\cdot | \mathbf{u}_1^{(k+1)}, \mathbf{u}_2^{(k+1)})$ for \mathbf{u}_3 ,
- Step 10: proximity step (or backward step) on the non-necessarily smooth function r .

It can be observed that in Algorithm 8, for every $k \in \mathbb{N}$, the gradient of $\tilde{f}_1(\cdot | \mathbf{u}_2^{(k)}, \mathbf{u}_3^{(k)})$ (resp. $\tilde{f}_2(\cdot | \mathbf{u}_1^{(k+1)}, \mathbf{u}_3^{(k)})$ and $\tilde{f}_3(\cdot | \mathbf{u}_1^{(k+1)}, \mathbf{u}_2^{(k+1)})$) depends on the current iterates $(\mathbf{u}_2^{(k)}, \mathbf{u}_3^{(k)})$ (resp. $(\mathbf{u}_1^{(k+1)}, \mathbf{u}_3^{(k)})$ and $(\mathbf{u}_1^{(k+1)}, \mathbf{u}_2^{(k+1)})$). Thus, the linear operator $\tilde{\mathbf{T}}_{(\mathbf{u}_2^{(k)}, \mathbf{u}_3^{(k)})}$ (resp. $\tilde{\mathbf{T}}_{(\mathbf{u}_1^{(k+1)}, \mathbf{u}_3^{(k)})}$ and $\tilde{\mathbf{T}}_{(\mathbf{u}_1^{(k+1)}, \mathbf{u}_2^{(k+1)})}$) needs to be updated at each iteration $k \in \mathbb{N}$.

Convergence results

The key point of the proposed Algorithm 8 is that its convergence can be derived from [107, 108]. Let $(\mathbf{u}_1^{(k)})_{k \in \mathbb{N}}$, $(\mathbf{u}_2^{(k)})_{k \in \mathbb{N}}$ and $(\mathbf{u}_3^{(k)})_{k \in \mathbb{N}}$ be sequences generated by Algorithm 8. Assume that, for every $k \in \mathbb{N}$ and $t \in \{0, \dots, t_{\max}\}$,

$$\begin{cases} \delta_1^{(k,t)} \in]0, 2/\kappa(\mathbf{u}_2^{(k)}, \mathbf{u}_3^{(k)})[, \\ \delta_2^{(k,t)} \in]0, 2/\kappa(\mathbf{u}_1^{(k+1)}, \mathbf{u}_3^{(k)})[, \\ \delta_3^{(k,t)} \in]0, 2/\kappa(\mathbf{u}_1^{(k+1)}, \mathbf{u}_2^{(k+1)})[, \end{cases} \quad (7.23)$$

Algorithm 8 Block coordinate Forward-Backward algorithm

```

1: Initialization: Let  $\mathbf{u}_1^{(0)} = \mathbf{u}_2^{(0)} = \mathbf{u}_3^{(0)} \in \mathbb{R}_+^N$ ,  $t_{\max} \in \mathbb{N}^*$ , and, for every  $k \in \mathbb{N}$ , let
    $(\delta_1^{(k,t)})_{0 \leq t \leq t_{\max}-1}$ ,  $(\delta_2^{(k,t)})_{0 \leq t \leq t_{\max}-1}$  and  $(\delta_3^{(k,t)})_{0 \leq t \leq t_{\max}-1}$  be positive sequences.

2: for  $k = 0, 1, \dots$ 
3:   for  $p = 1, 2, 3$ 
4:     if  $p = 1$  ;  $\mathbf{T} = \tilde{\mathbf{T}}_{(\mathbf{u}_2^{(k)}, \mathbf{u}_3^{(k)})}$  ; end if
5:     if  $p = 2$  ;  $\mathbf{T} = \tilde{\mathbf{T}}_{(\mathbf{u}_1^{(k+1)}, \mathbf{u}_3^{(k)})}$  ; end if
6:     if  $p = 3$  ;  $\mathbf{T} = \tilde{\mathbf{T}}_{(\mathbf{u}_1^{(k+1)}, \mathbf{u}_2^{(k+1)})}$  ; end if
7:      $\tilde{\mathbf{u}}^{(0)} = \mathbf{u}_p^{(k)}$ 
8:     for  $t = 0, \dots, t_{\max} - 1$ 
9:        $\mathbf{z}^{(t)} = \tilde{\mathbf{u}}^{(t)} - \delta_p^{(k,t)} \mathbf{T}^\dagger (\mathbf{T} \tilde{\mathbf{u}}^{(t)} - \mathbf{y})$ 
10:       $\tilde{\mathbf{u}}^{(t+1)} = \text{prox}_{\delta_p^{(k,t)} r} (\mathbf{z}^{(t)})$ 
11:    end for
12:     $\mathbf{u}_p^{(k+1)} = \tilde{\mathbf{u}}^{(t_{\max})}$ 
13:  end for
14: end for

15: Return:  $\mathbf{x}^* = (\mathbf{u}_1^* + \mathbf{u}_2^* + \mathbf{u}_3^*)/3$ , where  $\mathbf{u}_1^* = \lim_k \mathbf{u}_1^{(k)}$ ,  $\mathbf{u}_2^* = \lim_k \mathbf{u}_2^{(k)}$ ,  $\mathbf{u}_3^* = \lim_k \mathbf{u}_3^{(k)}$ .

```

where $\kappa(\cdot, \cdot)$ is defined by (7.21). If g is a semi-algebraic function¹, then $(\mathbf{u}_1^{(k)}, \mathbf{u}_2^{(k)}, \mathbf{u}_3^{(k)})_{k \in \mathbb{N}}$ converges to a critical point $(\mathbf{u}_1^*, \mathbf{u}_2^*, \mathbf{u}_3^*)$ of h , and $(h(\mathbf{u}_1^{(k)}, \mathbf{u}_2^{(k)}, \mathbf{u}_3^{(k)}))_{k \in \mathbb{N}}$ is a non-increasing function converging to $h(\mathbf{u}_1^*, \mathbf{u}_2^*, \mathbf{u}_3^*)$.

Moreover, according to [107], to ensure the convergence of Algorithm 8, t_{\max} needs to be finite (and equal to 1 in [108]). In the limit case that $t_{\max} \rightarrow +\infty$, Algorithm 8 can be viewed as an approximated Gauss-Seidel algorithm ([198], [199, Chapter 7], [200, Chapter 2]). However, up to the best of our knowledge, the most general convergence results for the Gauss-Seidel method are presented in [106], and require technical assumptions on $\tilde{f}_p + r$ that are not necessarily satisfied in our minimization problem, due to the selection operators involved in (7.8)². Thus, it is important to note that our

¹A function is semi-algebraic if its graph is a finite union of sets defined by a finite number of polynomial inequalities. Semi-algebraicity property is satisfied by a wide class of functions. In particular, it is satisfied by the function g used in the current settings.

²In particular, convexity of sub-problems $\tilde{f}_p + r$, $p \in \{1, 2, 3\}$ is not enough to ensure the convergence of the Gauss-Seidel algorithm [207].

method is in contrast with the algorithm proposed by [31], where an approximated Gauss-Seidel method is adopted.

Implementation details

As mentioned earlier, each sub-problem (7.18) is solved using the FB iterations. At each sub-iteration $t \in \{0, \dots, t_{\max} - 1\}$, for every $p \in \{1, 2, 3\}$, step 10 performs the proximity operator of r , computed as follows:

$$\begin{aligned}\tilde{\mathbf{u}}^{(t+1)} &= \text{prox}_{\delta_p^{(k,t)} r}(\mathbf{z}^{(t)}) \\ &= \underset{\mathbf{u} \in \mathbb{R}^N}{\text{argmin}} \ \iota_{\mathbb{R}_+^N}(\mathbf{u}) + \zeta_p^{(k,t)} g(\mathbf{u}) + \frac{1}{2} \|\mathbf{u} - \mathbf{z}^{(t)}\|_2^2,\end{aligned}\tag{7.24}$$

where $\zeta_p^{(k,t)} = \delta_p^{(k,t)} \mu$. The computation of the proximity operator in (7.24) depends on the choice of g . It can have either an explicit formulation or need to be computed using sub-iterations. In the following, we describe briefly the proximity steps obtained for the different regularization terms g .

Positivity and reality. In [31], only positivity and reality constraints have been considered. Thus, the regularization term (7.11) corresponds to the case when $\mu = 0$. In this case, the proximity step 10 boils down to the projection of the current iterate onto the real positive set \mathbb{R}_+^N , i.e. $\mathcal{P}_{\mathbb{R}_+^N}(\mathbf{z}^{(t)}) = \left(\max \{ \text{Re}(z_n^{(t)}), 0 \} \right)_{1 \leq n \leq N}$.

Positivity, reality and sparsity in the image space. In the case when the original image is known to be sparse, function g can be used to promote sparsity directly in the image space. This corresponds to regularization (7.22) with Ψ (and the weighting matrix) chosen equal to the identity matrix. The proximity step 10 then boils down to the positive soft-thresholding operator [208, Table 10.2(ix)].

Positivity, reality and sparsity in a given dictionary. In the particular yet common case of the sought astronomical image not being sparse, its sparse representation in a given dictionary Ψ is rather exploited by using equation (7.22). However,

the proximity operator (7.24) does not have a closed form solution. Its computation in step 10 involves sub-iterations, which we propose to perform using the dual forward-backward algorithm [90, 208], described in Algorithm 9.

Algorithm 9 Dual Forward-Backward algorithm to compute (7.24)

- 1: **Initialization:** Let $\tilde{\mathbf{p}}^{(0)} \in \mathbb{R}^N$, $\bar{\epsilon} \in]0, \min\{1, 1/\|\mathbf{W}\Psi^\dagger\|^2\}[$, $\bar{\mu} \in [\bar{\epsilon}, 2/\|\mathbf{W}\Psi^\dagger\|^2 - \bar{\epsilon}]$.
 - 2: **for** $\ell = 0, 1, \dots$
 - 3: $\mathbf{v}^{(\ell)} = \mathcal{P}_{\mathbb{R}_+^N}(\mathbf{z}^{(t)} - \Psi\mathbf{W}^\dagger\tilde{\mathbf{p}}^{(\ell)})$
 - 4: $\mathbf{s}^{(\ell)} = \tilde{\mathbf{p}}^{(\ell)} + \bar{\mu}\mathbf{W}\Psi^\dagger\mathbf{v}^{(\ell)}$
 - 5: $\tilde{\mathbf{p}}^{(\ell+1)} = \mathbf{s}^{(\ell)} - \bar{\mu} \operatorname{prox}_{\bar{\mu}^{-1}\zeta_p^{(k,t)}g}(\bar{\mu}^{-1}\mathbf{s}^{(\ell)})$
 - 6: **end for**
 - 7: **Return:** $\tilde{\mathbf{u}}^{(t+1)} = \lim_{\ell} \mathbf{v}^{(\ell)}$.
-

In Algorithm 9, \mathbf{W} is the identity matrix if the ℓ_1 regularization is used, or \mathbf{W} corresponds to a diagonal matrix with positive weights (w_1, \dots, w_J) if weighted- ℓ_1 regularization is chosen. The proximity operator in step 5 corresponds to the soft-thresholding operator [93] computed in the dictionary space. Unlike the positive soft-thresholding, it does not impose positivity.

Reweighting approach

In the current work, we propose to use a reweighted- ℓ_1 regularization term to promote sparsity. As described in Chapter 3, initial step consists in solving the minimization problem either without the sparsity term or by including ℓ_1 regularization term. The solution obtained is then used to compute the weights for the first weighting procedure. Using these computed weights, Algorithm 8 is executed again to solve the new minimization problem, taking into account the weighted- ℓ_1 regularization (7.22). In the same manner, the new obtained solution is used to compute the weights for the next reweighting iteration. The resultant reweighted- ℓ_1 minimization problem can be solved in turn using Algorithm 8. This reweighting procedure can be repeated until a stable solution is obtained.

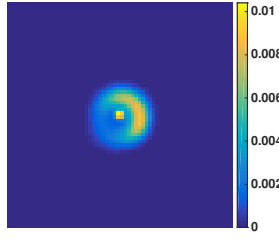


FIGURE 7.2: Original image LkH α , of size 64×64 , used for simulations, taken from the 2004 Imaging Beauty Contest [210].

7.4 Simulations and results

In this section, we investigate the performance of the proposed method and present simulation results, obtained by implementing the proposed algorithm in MATLAB.

7.4.1 Simulation settings

All the simulations are performed on the image of LkH α , a star with a powerful H α emission line, which is a famous subject of study for various astrophysical interests [209]. The image is shown in Figure 7.2, taken from the 2004 Optical Interferometric Imaging Beauty Contest [210], with $N = 64^2$ corresponding to a resolution of the order of milli-arcseconds. Two types of uv coverages are considered:

- Figure 7.3(a): Synthetic uv coverage, which consists of random variable-density sampling scheme in 2D discrete Fourier space. In this case, the uv coverage is generated by random Gaussian sampling such that low frequencies are more likely to be sampled than high frequencies.
- Figure 7.3(b): Realistic uv coverage, corresponding to discretized version of the 2016 Optical Interferometric Imaging Beauty Contest coverage plan [211]. It corresponds to the measurements made by the GRAVITY instrument at the VLTI. The observation wavelength is $1.95 \mu\text{m}$. It samples 72 points in the uv plane resulting in 72 power spectrum measurements.

For simplification, the bispectrum points are chosen at random (mainly the low frequency region) from the sampled spatial frequencies, i.e. the phase closure constraint

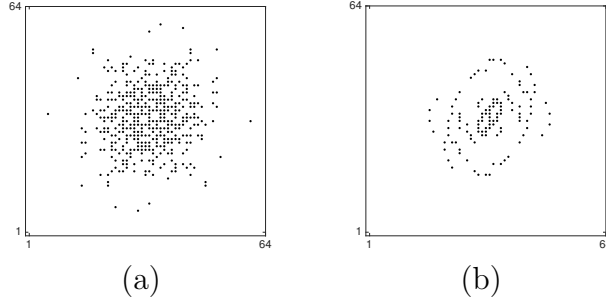


FIGURE 7.3: Discretized spatial frequencies coverage plans for the image of size 64×64 . (a) Synthetic uv coverage for $M_P/N = 0.05$: consists of random variable-density sampling scheme. (b) Realistic uv coverage: taken from the 2016 Imaging Beauty Contest for Optical Interferometry [211].

is relaxed. It is taken care that no two bispectrum measurements correspond to the same triple product. Furthermore, for both coverages, the simulated measurements in (7.8) are obtained by taking the input signal-to-noise ratio (iSNR) equal to 30 dB, where

$$\text{iSNR} = 20 \log_{10} \left(\frac{\|\mathbf{y}\|_2}{\sqrt{M}\sigma_\eta} \right), \quad (7.25)$$

σ_η^2 being the variance of the noise. For quantitative comparison of the reconstructed images, SNR is considered. In our simulations, results are presented considering a stopping criterion for Algorithm 8, given by $\max_{p \in \{1,2,3\}} (\|\mathbf{u}_p^{(k)} - \mathbf{u}_p^{(k-1)}\|_2 / \|\mathbf{u}_p^{(k)}\|_2) \leq 10^{-2}$.

Finally, let us define the power spectrum under-sampling ratio as $u_P = M_P/N$, and the bispectrum under-sampling ratio as $u_B = M_B/N$. It is worth emphasizing here that due to the Hermitian symmetry, M_P power spectrum measurements in fact correspond to $2M_P$ sampled spatial frequencies in the Fourier plane. This implies that in the particular case when $u_P = 0.5$, all the spatial frequencies in the Fourier plane are sampled.

As discussed in Section 7.3, the number of spatial frequencies probed M_P depends on the number of telescopes n_a . Thus, u_P will change, depending on n_a . Also, for a given u_P , there can be at most $\binom{n_a}{3}$ possible bispectrum measurements (that are not all independent), i.e. $M_B \leq \binom{n_a}{3}$. Keeping this in mind, for a fixed u_P , we have performed simulations by varying the number of bispectrum measurements considered, which results in varying u_B . Furthermore, for each pair (u_P, u_B) , 10 simulations

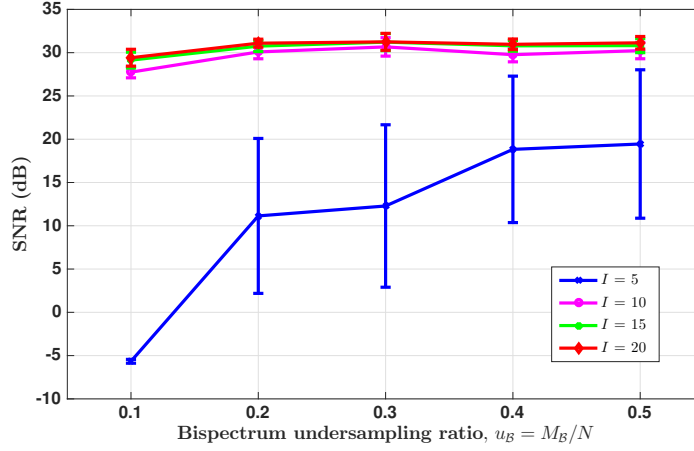


FIGURE 7.4: SNR graph obtained for positivity and reality constrained case with LkH α image and synthetic uv coverage for $u_P = 0.2$, considering iSNR = 30 dB and varying u_B . The graph shows the comparison of average SNR values (over 10 simulations), and corresponding 1-standard-deviation error bars, for different number of initializations I : $I = 5$ (blue), $I = 10$ (pink), $I = 15$ (green), and $I = 20$ (red).

are performed, varying the noise realization, and for the synthetic uv coverage, the sampling pattern as well.

7.4.2 Synthetic uv coverage

This section presents the simulations performed on the image LkH α considering the synthetic uv coverage given in Figure 7.3(a). Simulations corresponding to the different regularization terms are described below.

Positivity and reality constraints. We consider the simplest case, described by [31], corresponding to the minimization problem (7.14) with only positivity and reality constraints taken into account. Details of the implementation of the Algorithm 8 in this case are described in Section 7.3.3.

As mentioned in Section 7.3.3, given the non-convexity of the minimization problem (7.14), Algorithm 8 can only converge to a critical point of h . Thus, the reconstructed image depends on the initialization. To avoid local minima, we propose to run Algorithm 8 several times, for I random initializations $\mathbf{x}_i^{(0)} = \mathbf{u}_1^{(0)} = \mathbf{u}_2^{(0)} = \mathbf{u}_3^{(0)}$, with $i \in \{1, \dots, I\}$. Let \mathbf{x}_i^* be the estimation found with initialization $\mathbf{x}_i^{(0)}$. Then the best

estimation \mathbf{x}^* is selected by taking $\mathbf{x}^* = \mathbf{x}_{i^*}^*$, where i^* corresponds to the initialization index with minimum value of the objective function, i.e. for every $i \in \{1, \dots, I\}$, $f(\mathbf{x}_{i^*}^*) + r(\mathbf{x}_{i^*}^*) \leq f(\mathbf{x}_i^*) + r(\mathbf{x}_i^*)$.

To choose the number I of random initializations, first tests for different I are performed and presented in Figure 7.4. Four curves are depicted, corresponding to the different number of initializations considered, $I \in \{5, 10, 15, 20\}$. Each curve represents the average SNR values over 10 simulations, along with 1-standard-deviation error bars, as a function of the under-sampling ratio u_B , for a fixed $u_P = 0.2$. It can be seen from the graph that the SNR changes a lot as the number of random initializations increases from 5 to 20. It reflects the sensitivity of the minimization problem to the number of initializations. However, between 15 and 20 initializations, the SNR not only saturates, in fact it exhibits very small standard deviation error bars. Thus, in all the subsequent simulations, when only positivity and reality constraints are taken into account, we consider $I = 15$ random initializations for each pair (u_P, u_B) .

ℓ_1 and weighted- ℓ_1 regularizations. In order to solve the minimization problem (7.14) promoting sparsity, we consider the regularization function given by (7.11), and we examine both ℓ_1 and weighted- ℓ_1 regularizations, using Ψ to be Daubechies 8 wavelet basis [70]. In this case, we use Algorithm 8 with the implementation details and the reweighting process described in Section 7.3.3.

Concerning the initialization, both for ℓ_1 and weighted- ℓ_1 minimization problems, two different cases have been tested. On the one hand, we considered the same initialization strategy as described earlier, with $I = 15$. On the other hand, we used the final estimation obtained from the positivity constrained problem, itself initialized with $I = 15$. Preliminary simulations indicated that the results obtained in the two cases have similar reconstruction quality. However, the computation time was much longer considering several random initializations than using the solution obtained from the positivity constrained problem. Thus, for computational efficiency, all further simulations for ℓ_1 and weighted- ℓ_1 regularization are performed using the

final solution obtained when only positivity constraint is considered, as described earlier.

To inspect the quality of reconstruction, we consider two sub-cases for ℓ_1 minimization with different number of FB sub-iterations (corresponding to steps 9-10 in Algorithm 8): $t_{\max} = 200$ and $t_{\max} = 400$. In addition, for the weighting scheme, two sub-cases are considered for different number of weighting iterations: a weighted- ℓ_1 regularization (with only one weighting computation), and a second weighting iteration (i.e. reweighted- ℓ_1)³. As discussed in Section 7.3.3, the weights are computed using (3.13), where, for the weighted- ℓ_1 regularization, we take \mathbf{x}^* to be the solution obtained from the positivity constrained minimization problem, whereas for the reweighted- ℓ_1 regularization, \mathbf{x}^* is the solution obtained from the weighted- ℓ_1 minimization problem.

Note that during weighted and reweighted- ℓ_1 , t_{\max} is taken to be 200. In the simulations performed, the regularization parameter μ in (7.11) is tuned to maximize the SNR: $\mu = 10^{-5}$ (resp. $\mu = 1.5 \times 10^{-5}$) for ℓ_1 (resp. weighted and reweighted- ℓ_1) minimization problem.

Simulation results

We have implemented several tests to analyze the performance of the proposed method with respect to the number of measurements made by the interferometer. More precisely, to take into account different under-sampling ratios of the u - v plane, we have performed simulations by varying $u_{\mathcal{P}}$ and $u_{\mathcal{B}}$. First, concerning the choice of $u_{\mathcal{P}}$, we have considered two cases: $u_{\mathcal{P}} = 0.05$ corresponding to highly under-sampled u - v plane, and $u_{\mathcal{P}} = 0.2$ to simulate a less under-sampled data set. Second, for each of the considered values of $u_{\mathcal{P}}$, we have varied number of bispectrum measurements, i.e. $u_{\mathcal{B}}$. Taking these different values of $u_{\mathcal{P}}$ and $u_{\mathcal{B}}$ into account, Figure 7.5 shows the SNR graphs corresponding to the reconstructed images, as a function of $u_{\mathcal{B}}$ for $u_{\mathcal{P}} = 0.05$

³Note that the simulations were performed with more than 2 weighting iterations. However, preliminary results indicated that after the second weighting iteration, a stable solution was achieved both in terms of the SNR and visual quality.

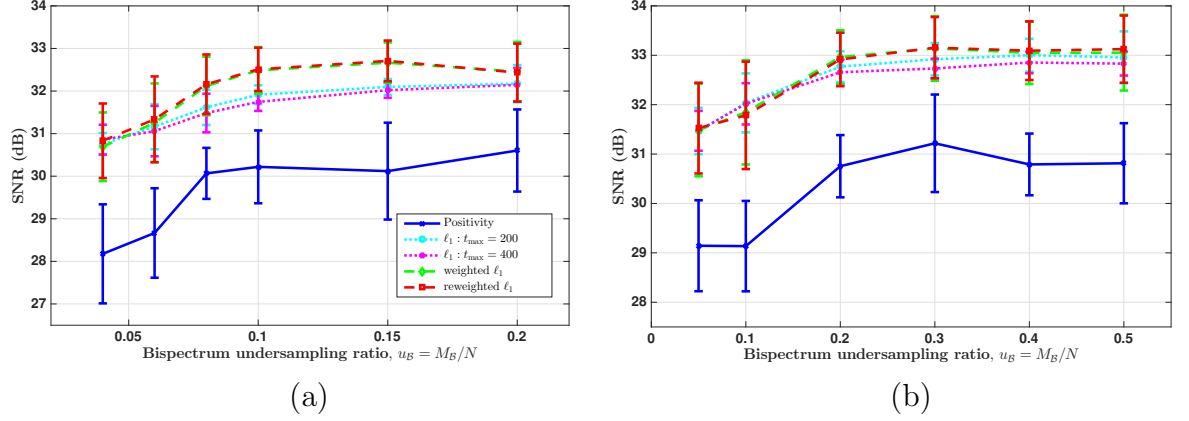


FIGURE 7.5: SNR graphs obtained with LkH α image and synthetic uv coverage, considering iSNR = 30 dB, varying u_B for two different power spectrum undersampling ratios: (a) $u_P = 0.05$ and (b) $u_P = 0.2$. In each graph, comparison of average SNR values (over 10 simulations), and corresponding 1-standard-deviation error bars, for different regularization terms is shown: positivity constraints (solid blue), ℓ_1 regularization with $t_{\max} = 200$ (dotted cyan) and $t_{\max} = 400$ (dotted pink), weighted- ℓ_1 regularization (dashed green) and reweighted- ℓ_1 regularization (dashed red).

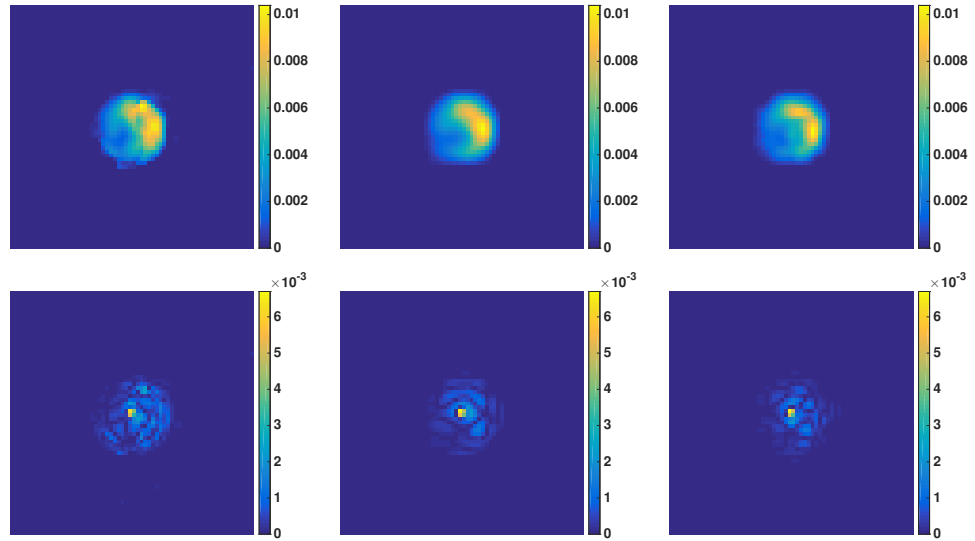


FIGURE 7.6: Reconstructed (first row) and error (second row) images corresponding to median SNR (over 10 simulations), obtained by considering the true image LkH α with synthetic uv coverage for $(u_P, u_B) = (0.05, 0.1)$. In each row, images corresponding to different regularization terms are shown column-wise: positivity constraint (first column), ℓ_1 regularization with $t_{\max} = 200$ (second column), and reweighted- ℓ_1 regularization (third column).

(left) and 0.2 (right), respectively. Typically, the range over which u_B is varied is chosen depending on the value of u_P . As such, we have taken the values of u_B comparable to and greater than u_P . Consequently, for the smaller value of $u_P = 0.05$, we have considered a smaller number of bispectrum measurements with $u_B \in \{0.04, 0.2\}$, whereas for the larger value of $u_P = 0.2$, the number of bispectrum measurements considered are also increased, $u_B \in \{0.05, 0.5\}$.

In each graph of Figure 7.5, comparisons are given for the results obtained using the aforementioned different regularizations. For visual assessment, reconstructed images having SNR corresponding to the median of the SNRs obtained for 10 performed simulations are shown in Figures 7.6 and 7.7. The reconstructed images for ℓ_1 regularization with different t_{\max} are visually very similar. Same is the case for reconstructed images with weighted ℓ_1 and reweighted ℓ_1 regularization. Hence, in Figure 7.6 and Figure 7.7, we show the images corresponding to positivity constrained case, ℓ_1 regularization with $t_{\max} = 200$ and reweighted ℓ_1 regularization. The respective error images are also displayed to show the absolute error $|\mathbf{x}^* - \bar{\mathbf{x}}|$ between the reconstructed image \mathbf{x}^* and the true image $\bar{\mathbf{x}}$. From Figures 7.5, 7.6 and 7.7, we can observe that promoting sparsity, either by ℓ_1 , weighted- ℓ_1 , or reweighted- ℓ_1 regularization term, gives better reconstruction quality, and hence lesser residual in the error images, than the positivity and reality constrained case (SNR improves between 2 and 3 dB depending on the considered (u_P, u_B)).

Another observation that can be made is regarding the non-recovery of the central compact source in the estimated images. This could be because of the chosen value of the regularization parameter μ that is set to maximize the SNR. However, it might not be the optimal one and as demonstrated in [20] through various examples, if the problem is over-regularized, the obtained image could be over simplified. On a further note, from the results given in Figure 7.5, it can be seen that when $u_P = 0.2$ (Figure 7.5(b)), the quality of reconstruction obtained with the ℓ_1 regularization and the (re)weighted- ℓ_1 regularization is almost the same. On the contrary, when $u_P = 0.05$ (Figure 7.5(a)), as u_B is increased, the SNR values obtained with either of the weighted- ℓ_1 or reweighted- ℓ_1 regularization terms are greater than the SNR

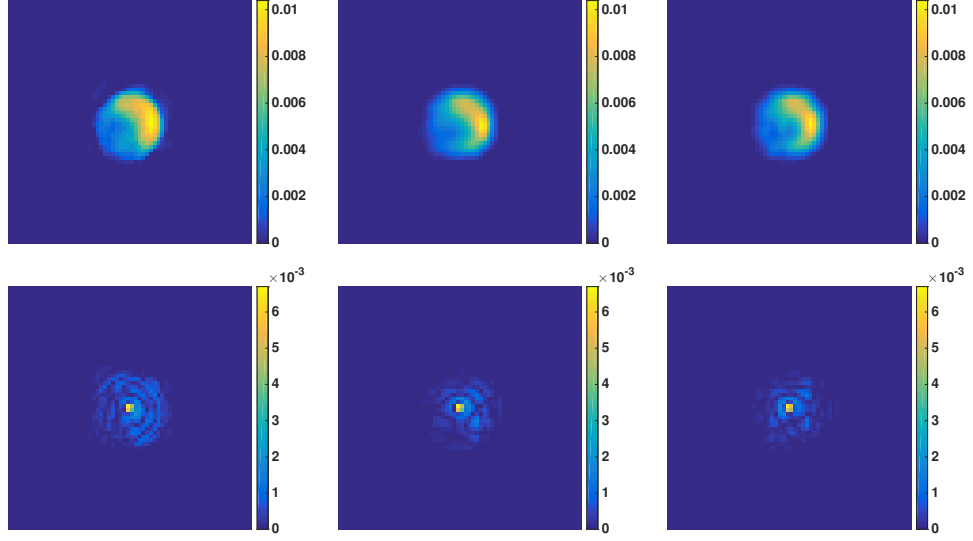


FIGURE 7.7: Reconstructed (first row) and error (second row) images corresponding to median SNR (over 10 simulations), obtained by considering the true image LkH α with synthetic uv coverage for $(u_P, u_B) = (0.2, 0.3)$. In each row, images corresponding to different regularization terms are shown column-wise: positivity constraint (first column), ℓ_1 regularization with $t_{\max} = 200$ (second column), and reweighted- ℓ_1 regularization (third column).

obtained using an ℓ_1 regularization. This implies that weighting scheme tends to be more beneficial for the case of highly undersampled uv plane.

Considering the importance of symmetrization, it is worth mentioning here that the reconstructed images for the final solution $\mathbf{x}^* = (1/3)(\mathbf{u}_1^* + \mathbf{u}_2^* + \mathbf{u}_3^*)$ as well as for the solutions of \mathbf{u}_1^* , \mathbf{u}_2^* , \mathbf{u}_3^* are visually indistinguishable. This observation is supported by the small values of the variations between the solutions : $\|\mathbf{u}_1^* - \mathbf{u}_2^*\|_2$, $\|\mathbf{u}_2^* - \mathbf{u}_3^*\|_2$ and $\|\mathbf{u}_3^* - \mathbf{u}_1^*\|_2$, which are of the order of 10^{-2} , 10^{-4} and 10^{-2} , respectively.

Image reconstruction without the bispectrum measurements

In order to emphasize the benefit of using phase information from bispectrum measurements, simulations have been performed considering only the power spectrum measurements, i.e. with $u_B = M_B = 0$. In this case, Algorithm 8 has been implemented by considering only positivity and reality constraints. Moreover, as explained earlier, owing to the non-convexity of the minimization problem (7.14), several simulations are performed with different random initializations. Particularly, considering

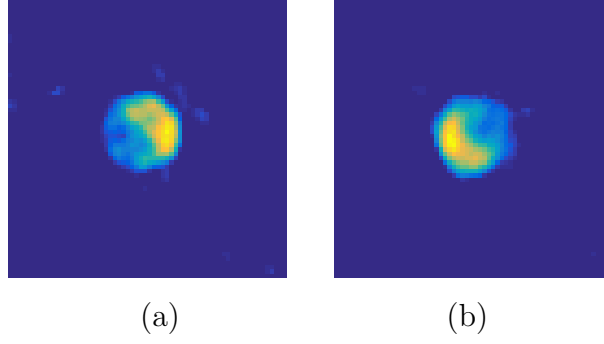


FIGURE 7.8: The figure illustrating the orientation uncertainty when no phase information is taken into account. Reconstructed images with (a) the correct orientation of the true image $\text{LkH}\alpha$ and (b) the opposite orientation, respectively obtained by considering two different initializations for positivity and reality constrained case, with synthetic uv coverage for $(u_{\mathcal{P}}, u_{\mathcal{B}}) = (0.05, 0)$ (considering only power spectrum measurements) and having median SNR over 10 simulations.

a synthetic uv coverage with $u_{\mathcal{P}} = 0.05$ and $u_{\mathcal{B}} = 0$ (no bispectrum measurements), the reconstructed images obtained from two different random initializations for positivity and reality constrained case are shown in Figure 7.8. Since the power spectrum measurements do not contain any phase information, it can be observed that the reconstructed images suffer from phase ambiguity. This arises from the space-reversal property of the Fourier transform, i.e. if a signal is inverted in the spatial domain, then in the Fourier domain, this inversion only reverses the sign of the phase of the Fourier coefficients. It implies that with no phase information, the uncertainty related to signal inversion remains. While the image in Figure 7.8(a) is recovered with correct orientation, i.e. the same orientation as that of the original image $\text{LkH}\alpha$ given in Figure 7.2, the image in Figure 7.8(b) is recovered with the opposite orientation.

On the one hand, this indicates that the proposed Algorithm 8 is still able to restore images with only power spectrum measurements, i.e. without any phase information, though with the uncertainty in the orientation. On the other hand, the results obtained from the case when $u_{\mathcal{B}} > 0$ highlight that the incorporation of phase information is essential to recover properly oriented images.

7.4.3 Realistic uv coverage

The performance of the proposed algorithm has been assessed for the realistic uv coverage given in Figure 7.3(b). We have performed several simulations by varying

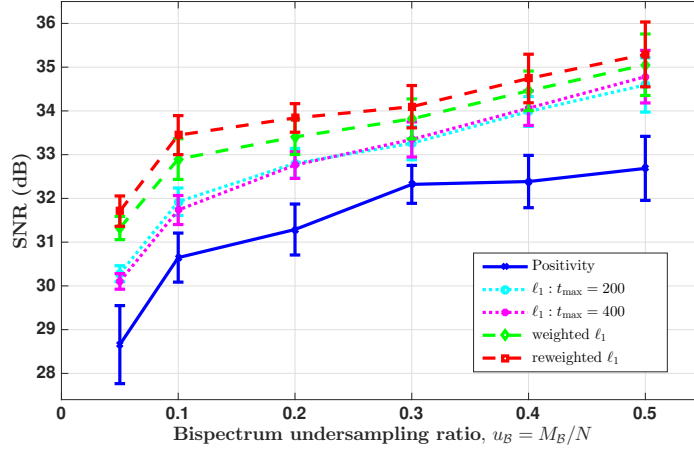


FIGURE 7.9: SNR graph obtained with LkH α image and realistic uv coverage, considering iSNR = 30 dB, varying u_B . In the graph, comparison of average SNR values (over 10 simulations), and corresponding 1-standard-deviation error bars, for different regularization terms is shown: positivity constraints (solid blue), ℓ_1 regularization with $t_{\max} = 200$ (dotted cyan) and $t_{\max} = 400$ (dotted pink), weighted- ℓ_1 regularization (dashed green) and reweighted- ℓ_1 regularization (dashed red).

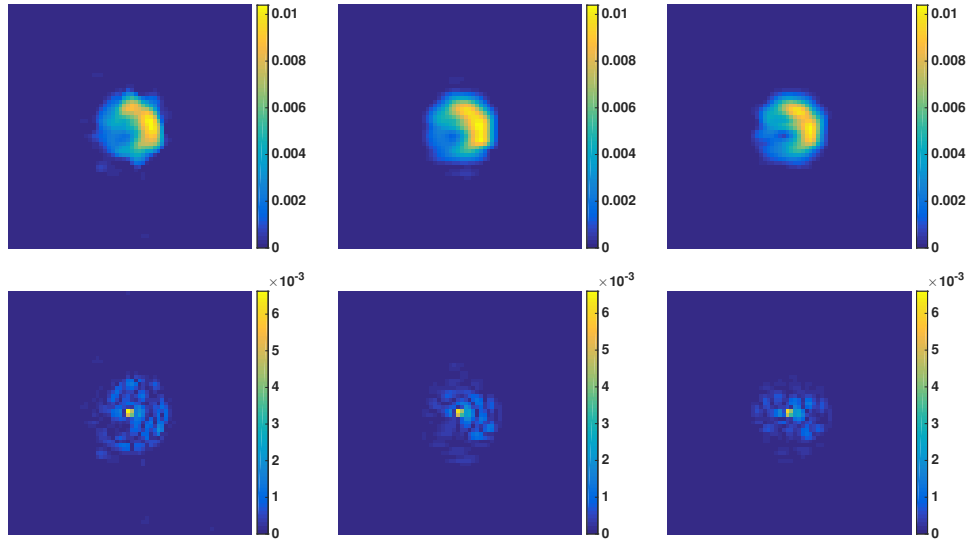


FIGURE 7.10: Reconstructed (first row) and error (second row) images corresponding to median SNR (over 10 simulations), obtained by considering the true image LkH α with realistic uv coverage for $u_B = 0.2$. In each row, images corresponding to different regularization terms are shown column-wise: positivity constraint (first column), ℓ_1 regularization with $t_{\max} = 200$ (second column), and reweighted- ℓ_1 regularization (third column).

the number of bispectrum measurements and thus in turn the bispectrum under-sampling ratio $u_{\mathcal{B}}$. Recalling that for the considered realistic uv coverage, $M_{\mathcal{P}} = 72$, and with $N = 64^2$, this implies that $u_{\mathcal{P}} \simeq 0.018$. Figures 7.9 and 7.10 illustrate the results obtained for the different considered regularization terms. While Figure 7.9 depicts the SNR graph for the reconstructed images as a function of $u_{\mathcal{B}} \in \{0.05, 0.5\}$, the corresponding recovered images and the error images for $u_{\mathcal{B}} = 0.2$, with median SNR, are shown in Figure 7.10. Here again considering the visual similarity between the reconstructed images for ℓ_1 regularization with different t_{\max} , and that between images for weighted and reweighted ℓ_1 regularization, we only show the images for positivity constraint, ℓ_1 with $t_{\max} = 200$ and reweighted ℓ_1 .

It is to be remarked here that the results obtained are in coherence with the observations made for the synthetic uv coverage. More precisely, the results indicate the superiority of promoting sparsity relative to just positivity and reality over the full under-sampling range, leading to an improvement of the SNR between 3 and 4 dB, depending on the considered value of $u_{\mathcal{B}}$. Moreover, given the small value of $u_{\mathcal{P}}$, the SNR gets better not only with increasing $u_{\mathcal{B}}$, but also by considering the (re)weighted- ℓ_1 regularization term.

7.5 Hyperspectral OI imaging

7.5.1 Problem statement

The spatial frequencies sampled by an interferometer depend on the observation wavelength. It means that the interferometric measurements made at different wavelengths correspond to probing different spatial frequencies in the uv plane of the image of interest. Considering L spectral channels, in accordance with the data model proposed for the monochromatic case (7.5), the measurement equation at each spectral channel $l \in \{1, \dots, L\}$, can be written as:

$$\mathbf{y}_l = [(\mathbf{T}_{1,l} \bar{\mathbf{x}}_l) \cdot (\mathbf{T}_{2,l} \bar{\mathbf{x}}_l) \cdot (\mathbf{T}_{3,l} \bar{\mathbf{x}}_l)] + \boldsymbol{\eta}_l, \quad (7.26)$$

where $\mathbf{y}_l \in \mathbb{C}^M$ denotes the measurement vector, $\bar{\mathbf{x}}_l \in \mathbb{R}_+^N$ is the intensity image, $\boldsymbol{\eta}_l \in \mathbb{C}^M$ is a realization of an additive Gaussian noise, and, in analogy with (7.6), the l -th measurement operators are given by $\mathbf{T}_{p,l} = \mathbf{L}_{p,l} \mathbf{K}_l \mathbf{F}$, for every $p \in \{1, 2, 3\}$. Following the approach adopted in the monochromatic case and considering $\bar{\mathbf{u}}_{1,l} = \bar{\mathbf{u}}_{2,l} = \bar{\mathbf{u}}_{3,l} = \bar{\mathbf{x}}_l$ for $1 \leq l \leq L$, the tri-linear counter-part of the inverse problem (7.26) becomes

$$\mathbf{y}_l = [(\mathbf{T}_{1,l} \bar{\mathbf{u}}_{1,l}) \cdot (\mathbf{T}_{2,l} \bar{\mathbf{u}}_{2,l}) \cdot (\mathbf{T}_{3,l} \bar{\mathbf{u}}_{3,l})] + \boldsymbol{\eta}_l. \quad (7.27)$$

Then, concatenating all the spectral channels, we define the ill-posed hyperspectral inverse problem as

$$\mathbf{Y} = [\mathbf{T}_1(\bar{\mathbf{X}}_1) \cdot \mathbf{T}_2(\bar{\mathbf{X}}_2) \cdot \mathbf{T}_3(\bar{\mathbf{X}}_3)] + \mathbf{H}, \quad (7.28)$$

where $\mathbf{Y} = [\mathbf{y}_1, \dots, \mathbf{y}_L] \in \mathbb{C}^{M \times L}$ is the measurement matrix, for every $p \in \{1, 2, 3\}$, $\bar{\mathbf{X}}_p = [\bar{\mathbf{u}}_{p,1}, \dots, \bar{\mathbf{u}}_{p,L}] \in \mathbb{R}_+^{N \times L}$ is the image matrix. More precisely, column $l \in \{1, \dots, L\}$ of $\bar{\mathbf{X}}_p$ represents the intensity image at wavelength λ_l , whereas row $n \in \{1, \dots, N\}$ represents the variation of pixel values along the spectral channels. In equation (7.28), $\mathbf{H} = [\boldsymbol{\eta}_1, \dots, \boldsymbol{\eta}_L] \in \mathbb{C}^{M \times L}$ is the noise matrix, and $\mathbf{T}_1, \mathbf{T}_2, \mathbf{T}_3$ are the concatenated measurement operators such that, for $p \in \{1, 2, 3\}$, $\mathbf{T}_p(\bar{\mathbf{X}}_p) = (\mathbf{T}_{p,l} \bar{\mathbf{u}}_{p,l})_{1 \leq l \leq L}$.

In analogy with the monochromatic case and the minimization problem described in (7.14) by symmetrizing the data fidelity term, we propose to define the estimate of $(\bar{\mathbf{X}}_1, \bar{\mathbf{X}}_2, \bar{\mathbf{X}}_3)$ as a solution to

$$\underset{(\mathbf{X}_1, \mathbf{X}_2, \mathbf{X}_3) \in (\mathbb{R}^{N \times L})^3}{\text{minimize}} \left\{ h(\mathbf{X}_1, \mathbf{X}_2, \mathbf{X}_3) = \tilde{f}(\mathbf{X}_1, \mathbf{X}_2, \mathbf{X}_3) + \sum_{p=1}^3 r(\mathbf{X}_p) \right\}, \quad (7.29)$$

where the same regularization term

$$(\forall \mathbf{X} \in \mathbb{R}^{N \times L}) \quad r(\mathbf{X}) = \iota_{\mathbb{R}_+^{N \times L}}(\mathbf{X}) + \mu g(\mathbf{X}), \quad (7.30)$$

is chosen for $\mathbf{X}_1, \mathbf{X}_2$, and \mathbf{X}_3 , and \tilde{f} is the symmetrized data fidelity term given by

$$\tilde{f}(\mathbf{X}_1, \mathbf{X}_2, \mathbf{X}_3) = \frac{1}{2} \|\tilde{\mathbf{Y}} - \tilde{\mathbf{T}}_1(\mathbf{X}_1) \cdot \tilde{\mathbf{T}}_2(\mathbf{X}_2) \cdot \tilde{\mathbf{T}}_3(\mathbf{X}_3)\|_2^2 = \sum_{l=1}^L \check{f}_l(\mathbf{u}_{1,l}, \mathbf{u}_{2,l}, \mathbf{u}_{3,l}), \quad (7.31)$$

with

$$\check{f}_l(\mathbf{u}_{1,l}, \mathbf{u}_{2,l}, \mathbf{u}_{3,l}) = \frac{1}{2} \|\tilde{\mathbf{y}}_l - (\tilde{\mathbf{T}}_{1,l} \mathbf{u}_{1,l}) \cdot (\tilde{\mathbf{T}}_{2,l} \mathbf{u}_{2,l}) \cdot (\tilde{\mathbf{T}}_{3,l} \mathbf{u}_{3,l})\|_2^2. \quad (7.32)$$

$\tilde{\mathbf{Y}} = [\tilde{\mathbf{y}}_1, \dots, \tilde{\mathbf{y}}_L] \in \mathbb{C}^{6M \times L}$ and $\tilde{\mathbf{T}}_p(\mathbf{X}_p) = (\tilde{\mathbf{T}}_{p,l} \mathbf{u}_{p,l})_{1 \leq l \leq L}$ are the symmetrized versions of the measurements matrix and the linear operators for $p \in \{1, 2, 3\}$, respectively in accordance with Section 7.3.2.

As discussed in the earlier sections, given the voids in the uv coverage, ensuring data consistency is not sufficient to obtain a good estimation from the measurements, and imposing *a priori* information is essential. In the monochromatic case, we have considered promoting sparsity prior with a, possibly weighted, ℓ_1 regularization term. In the context of hyperspectral imaging, joint sparsity gives an additional degree of possible regularization, in the spectral dimension, that should be leveraged to improve the overall image reconstruction quality compared to reconstructing each channel separately [203, 212, 213]. Mathematically, joint sparsity is defined for a set of sparse signals such that the non-zero entries of each signal are located at the same spatial position. From physical point of view, if a source is absent, i.e., the corresponding pixel has a zero value in a spectral channel, then the pixels at the same spatial positions along all the spectral channels will be zero. Thus, the joint sparsity prior enforces spatial sparsity while imposing spectral continuity. We propose to promote the joint sparsity prior using an $\ell_{2,1}$ norm [203, 214] for the regularization term, defined as follows:

$$(\forall \mathbf{X} = [\mathbf{x}_1, \dots, \mathbf{x}_L]) \quad g(\mathbf{X}) = \sum_{j=1}^J \left(\sum_{l=1}^L |[\Psi^\dagger \mathbf{x}_l]_j|^2 \right)^{1/2}, \quad (7.33)$$

where Ψ can either be identity matrix, or a given dictionary belonging to $\mathbb{R}^{J \times N}$. The $\ell_{2,1}$ norm is characterized by taking ℓ_2 norm along the columns and then ℓ_1 norm of the resultant vector.

In order to solve the minimization problem (7.29), we propose to adopt the same methodology as developed for monochromatic case.

7.5.2 Algorithmic details

The implementation of Algorithm 8 to solve (7.29) requires replacing the variables and the operators with the corresponding variables and operators for hyper-spectral case, as defined in Section 7.5.1.

First, according to (7.31)-(7.32), for every $l \in \{1, \dots, L\}$, partial gradients of \check{f}_l are independent. Thus, the gradient descent step 9 of Algorithm 8 can be computed in parallel for each spectral channel. Second, the proximity operator of the non-smooth function r defined by (7.30), with g given by (7.33), does not have a closed form solution. In order to compute this, we propose to resort once more to Algorithm 9. In this case, step 3 in Algorithm 9 requires performing the proximity operator of (7.33), defined, for every $\mathbf{B} \in \mathbb{R}^{J \times L}$ and $\nu > 0$, as

$$\text{prox}_{\nu \|\cdot\|_{2,1}}(\mathbf{B}) = \begin{bmatrix} \mathbf{p}_1 \\ \vdots \\ \mathbf{p}_J \end{bmatrix}, \quad (7.34)$$

where, for every $j \in \{1, \dots, J\}$, \mathbf{p}_j is a line vector given by

$$\mathbf{p}_j = \begin{cases} \mathbf{b}_j \frac{\|\mathbf{b}_j\|_2 - \nu}{\|\mathbf{b}_j\|_2} & \text{if } \|\mathbf{b}_j\|_2 \geq \nu, \\ \mathbf{0} & \text{otherwise,} \end{cases} \quad (7.35)$$

\mathbf{b}_j denoting the n -th row of \mathbf{B} . Thus, the proximity operator of the $\ell_{2,1}$ norm corresponds to a soft-thresholding operation row-wise.

7.6 Simulations and results

In this section, we show the performance of Algorithm 8 for hyperspectral imaging by solving (7.29). Simulations are performed on two sets of images, with $N = 64^2$ for each image. More precisely, two original images are considered: $\text{LkH}\alpha$, given in the top left of Figure 7.12, and an image consisting of two simulated uniform discs,

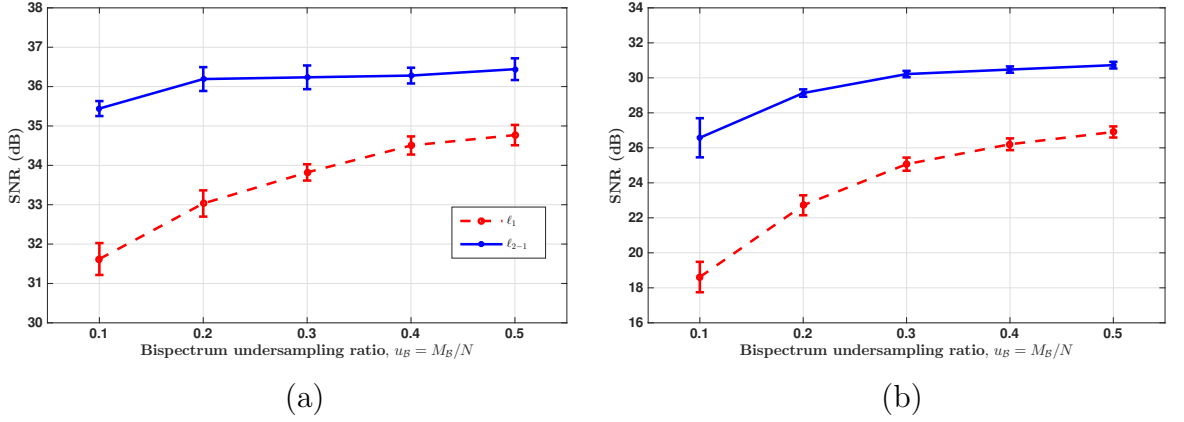


FIGURE 7.11: SNR graphs obtained for the reconstruction of two different hyper-spectral image cubes with the realistic uv coverage, considering iSNR = 30 dB for each spectral channel, varying u_B . For the two graphs, the ground truth images at first spectral channel are given by: (a) LkH α (top left image in Figure 7.12), and (b) **synthetic image** (top left image in Figure 7.13). Each graph depicts the comparison of the average SNR values (over 10 simulations) and corresponding 1-standard-deviation error bars, between single-channel reconstruction with ℓ_1 regularization (7.37) (red dashed) and reconstruction by considering joint sparsity with $\ell_{2,1}$ regularization (7.33) (blue solid).

which we refer to as **synthetic image**, shown as the top left image in Figure 7.13. These images correspond to the observed image at the first spectral channel $\bar{\mathbf{x}}_1$. Then, the images corresponding to other spectral channels $l \in \{2, \dots, L\}$ are obtained by following power-law model. In this context, we have, for $\bar{\mathbf{x}}_l = (\bar{x}_{l,n})_{1 \leq n \leq N}$,

$$\bar{x}_{l,n} = \bar{x}_{1,n} \left(\frac{\lambda_1}{\lambda_l} \right)^{\alpha_n}, \quad (7.36)$$

where λ_l denotes the wavelength at spectral channel l , and $\boldsymbol{\alpha} = (\alpha_n)_{1 \leq n \leq N}$ is the spectral indices' vector [215]. Spatial correlation is ensured by taking $\boldsymbol{\alpha}$ to be a linear combination of a random Gaussian field and the reference image convolved with a Gaussian kernel of size 3×3 at FWHM [216]. For both the images, $L = 8$ spectral channels in the wavelength range 1.95-1.97 μm are considered. The corresponding uv coverage plan is given in Figure 7.3(b) for observation wavelength 1.95 μm . The generated ground-truth images for $l = 8$ are shown as top right images in Figures 7.12 and 7.13, respectively for LkH α and **synthetic image**.

We compare the results obtained considering the $\ell_{2,1}$ norm with the case when each

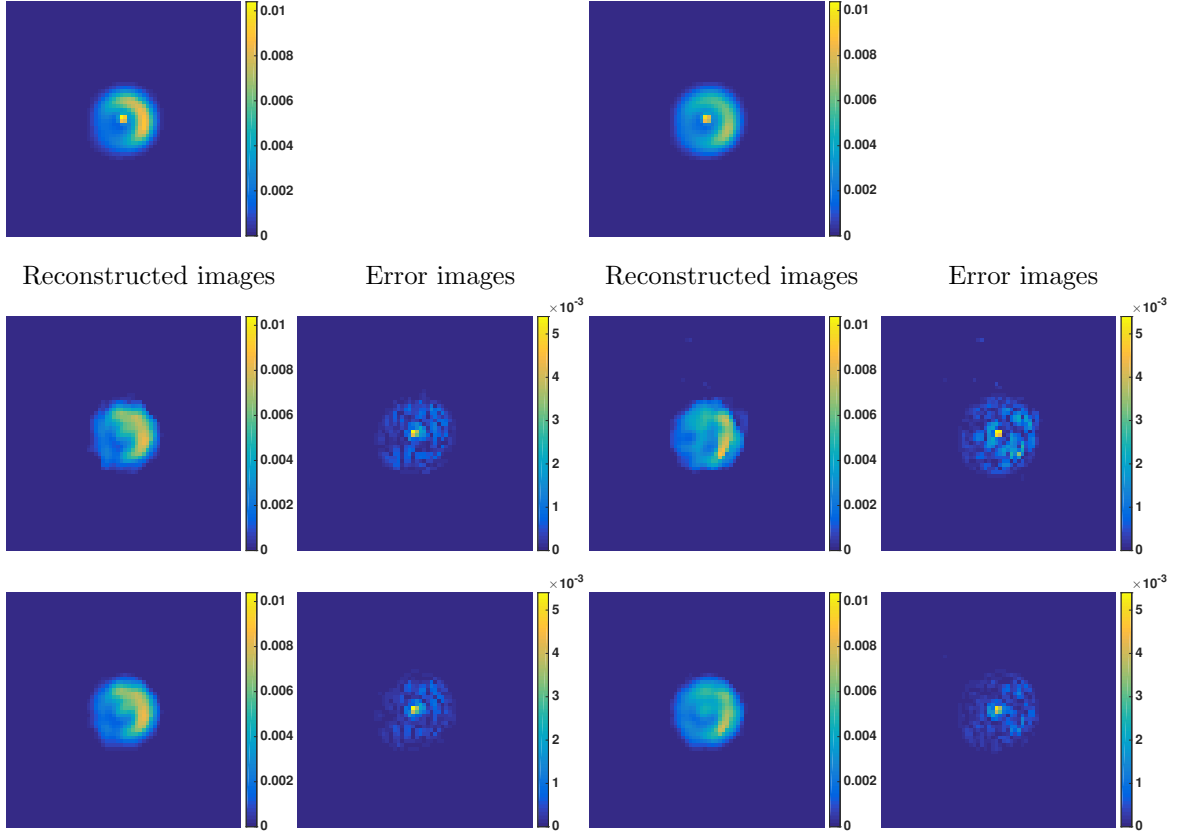


FIGURE 7.12: Results for hyperspectral imaging with realistic uv coverage for $L = 8$, $u_B = 0.1$ and $\text{LkH}\alpha$ as the original image. Images corresponding to first ($l = 1$) and last ($l = 8$) spectral channels are shown respectively in first two and last two columns. For each pair of columns, the following are shown row-wise from top to bottom: true image, reconstructed image with ℓ_1 regularization (7.37), reconstructed image with $\ell_{2,1}$ regularization (7.33). Each such reconstructed image is followed by its respective error image in the next column.

channel is treated separately, considering an ℓ_1 norm on each image produced by each spectral channel:

$$(\forall \mathbf{X} \in \mathbb{R}^{N \times L}) \quad g(\mathbf{X}) = \sum_{l=1}^L \|\Psi^\dagger \mathbf{x}_l\|_1. \quad (7.37)$$

While the case considering ℓ_1 norm is initialized with the solution of problem (7.29) obtained with only positivity and reality constraints (i.e. $\mu = 0$ in (7.30)), the solution obtained for each channel by ℓ_1 regularized case is in turn used to initialize $\ell_{2,1}$ regularized case. For both cases, the FB iterations (steps 8-11 in Algorithm 8) are performed with $t_{\max} = 200$. In the hyperspectral case, we observed that considering Ψ as the identity matrix gives better reconstruction results than using Daubechies wavelets. Moreover, the SNR of the reconstructed image matrix \mathbf{X}^* is computed as

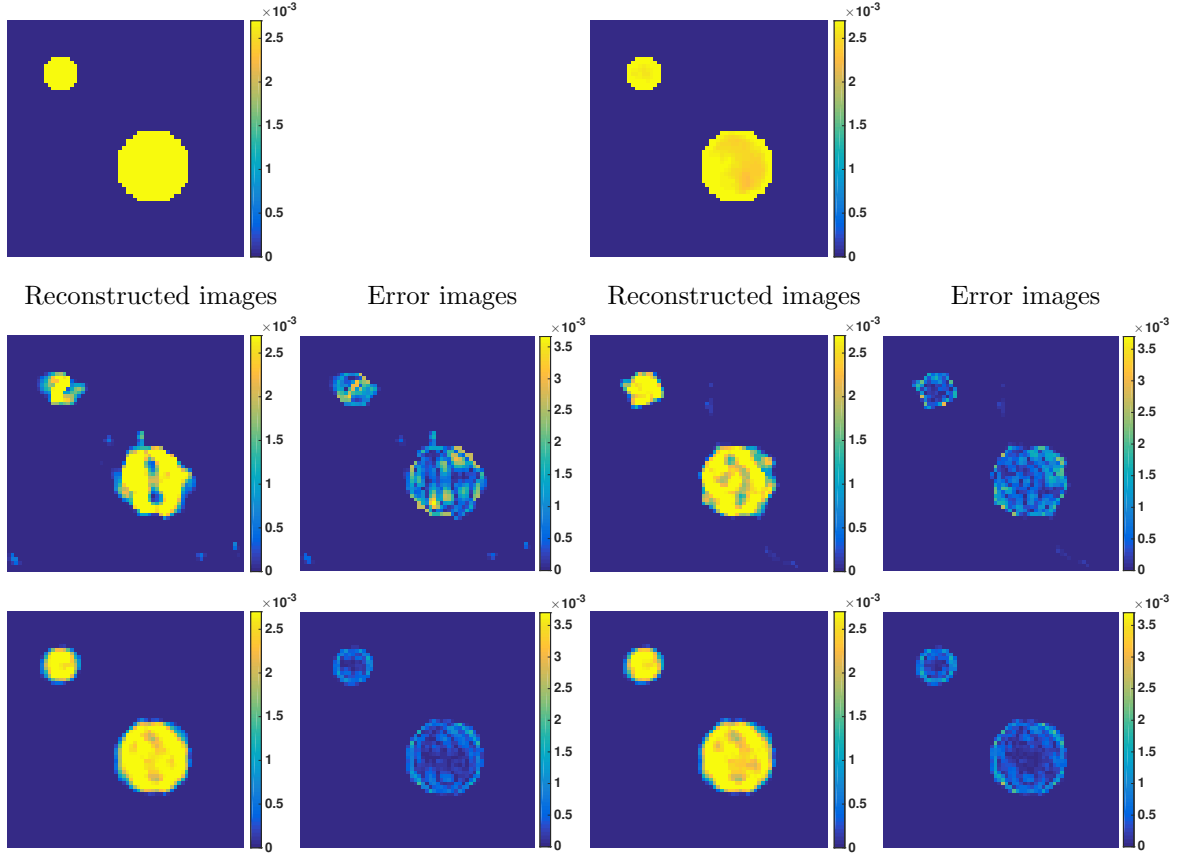


FIGURE 7.13: Results for hyperspectral imaging with realistic uv coverage for $L = 8$, $u_B = 0.1$ and **synthetic image** as the original image. Images corresponding to first ($l = 1$) and last ($l = 8$) spectral channels are shown respectively in first two and last two columns. For each pair of columns, the following are shown row-wise from top to bottom: true image, reconstructed image with ℓ_1 regularization (7.37), reconstructed image with $\ell_{2,1}$ regularization (7.33). Each such reconstructed image is followed by its respective error image in the next column.

the mean of the SNRs from the reconstructed images of each channel $(\mathbf{x}_l^*)_{1 \leq l \leq L}$. The SNR comparisons between the regularizations (7.33) and (7.37) are provided in Figure 7.11. For both cases, average SNR curves with 1-standard-deviation error bars are presented (performed over 10 simulations, varying both the noise realization and the measured bispectrum). From these plots, we can observe that using $\ell_{2,1}$ norm as a regularization term leads to better reconstruction than considering only ℓ_1 independently in each channel. The reconstructed and the corresponding error images for the first and the last spectral channels, considering Ψ to be the identity matrix, are shown in Figures 7.12 and 7.13. For the two image examples, the figures demonstrate the superiority of solving globally for the hyperspectral channels over single-channel

reconstruction, where no advantage of inter-channel information is taken.

7.7 Conclusion

We have presented a new method for image reconstruction in OI, based on the trilinear data model proposed in [31]. While only monochromatic imaging has been considered in the previous work, we extended this model to hyperspectral imaging. Furthermore, to improve the reconstruction quality, since in [31] only positivity constraints have been considered, we proposed additionally to promote sparsity using either an ℓ_1 or a weighted- ℓ_1 regularization term in the monochromatic case, and an $\ell_{2,1}$ regularization term in the hyperspectral case. Moreover, the sparsity of the sought image can be promoted not necessarily in its domain, but in fact in any suitable sparsifying domain based on the underlying image. In order to solve the resultant minimization problem, we have developed an alternated minimization algorithm, based on a block-coordinate forward backward algorithm. This algorithm presents convergence guarantees, and benefits from the fact that it can be designed to work with smooth functions, using gradient steps, and with non-necessarily smooth functions thanks to proximity steps. The MATLAB code of the proposed method is available on GitHub (<https://basp-group.github.io/Optical-Interferometry-Trilinear/>).

We have assessed the performance of the proposed method on several simulations both for synthetic and realistic uv coverages, in monochromatic and hyperspectral cases. On the one hand, for monochromatic imaging, adding a sparsity prior gives promising results. On the other hand, for hyperspectral imaging, we have shown numerically that exploiting joint sparsity, using an $\ell_{2,1}$ norm, improves drastically the quality of reconstruction as compared to single-channel reconstruction. To summarize, we have proposed a method which presents a general framework, where the regularization term can be non-smooth and adapted either for the monochromatic case or for the hyperspectral case.

Chapter 8

Conclusions and Perspectives

The research reported in this thesis proposes novel optimization techniques to solve imaging inverse problems encountered in astronomical interferometry spanning the radio and optical wavelength regimes. In particular, to recover the images from the given set of measurements, the developed methods leverage the notion of sparsity popularised recently by the compressive sensing framework, providing superior reconstruction quality in comparison with state-of-the-art methods. From an optimization perspective, the methods described in this manuscript are based on convex and non-convex optimization framework, benefiting from convergence guarantees and flexible features to adapt to the structure of the problem of interest.

In the context of radio interferometry, we have considered a complete treatment of the monochromatic radio interferometric measurement equation, accounting for full polarization model and calibration issues. In the absence of calibration errors, the proposed Polarized SARA method [25] adopts a primal-dual scheme for image recovery. Sparsity priors and the physical polarization constraint are incorporated into the reconstruction process. When compared with standard radio interferometric imaging approaches, Polarized SARA has been shown to produce higher quality, super-resolved images with physical meaning and reduced artefacts. Furthermore, the underpinning convex optimization technique not only guarantees convergence to a solution of the problem, but is also equipped with various desirable features. Particularly, while offering flexibility to incorporate sophisticated regularization priors in the problem, it

also benefits from the parallelizability features leveraging which the involved functions and the associated variables can be dealt with in a parallel fashion. The latter feature is exploited to render scalability to the Polarized SARA method [26] to deal with the large data volumes provided by the new generation radio interferometers. Moreover, for the more challenging case of unknown DDEs that need to be calibrated, we have taken the first step towards designing a global joint calibration and imaging technique with proven convergence guarantees. In this context, the proposed self DDE calibration and imaging method for Stokes I model [27–29] and further extended to full polarization model, named Polca SARA [30], showcase a unifying framework, merging the calibration and imaging methodologies into a global algorithmic structure. In particular, the non-linearity of the underlying inverse problem is tackled by introducing a tri-linear model, thereby solving convex sub-problems for each of the variables of interest, in an alternating and iterative manner. The proposed approach is able to deal with sophisticated priors to regularize the sought images and/or DDEs. Leveraging the latter characteristic, we have adapted Polarized SARA method for the imaging step when dealing with the full polarization model. This feature coupled with the DDE calibration of the full Jones matrices has been shown to be instrumental in producing high dynamic range Stokes images.

Finally, we have extended the aforementioned developments to optical interferometry, where we have exploited a tri-linear data model to propose an image recovery method [32, 33]. In particular, it is inspired by the performance of sparsity priors in radio interferometric imaging and the non-convex optimization technique developed for radio interferometric self-calibration and imaging. The developed approach benefits from convergence guarantees and is applicable for both monochromatic and hyperspectral imaging in optical interferometry, exhibiting good performance in the various numerical studies performed.

Perspectives

Performance assessment on real data

Although the work presented in this thesis has been intensively analysed, mainly over

simulated data sets using realistic models, the achieved promising performance of the developed methods calls for testing them on real data sets for their wider acceptability in the research community.

Particularly for the Polarized SARA method, an interesting next step would be to apply on such data sets where the radio emissions are *apparently* polarized more than 100%. Such instances can arise (for eg. while observing diffuse galactic emission) when the total intensity of the target sky is very smooth and broad, while the polarization maps consist of high resolution, small scale structures [217, 218]. In such cases, owing to the lack of short baselines, it is highly likely for the acquired data to not capture the information in Stokes I maps, thereby presenting more than 100% polarization. Enforcing polarization constraint to jointly reconstruct the Stokes parameters maps would tend to produce physical images, ensuring consistency of the total intensity with the polarized emissions. And thus, it could be useful to recover the ‘unseen’ large-scale total intensity structure.

Concerning optical interferometry, the novelty and convergence guarantees of the proposed method makes it a potential candidate for imaging. Thus, its application on more realistic data sets is worth exploring. The validation of our method for image recovery and explicit comparison with other imaging modalities in optical interferometry would be a step closer to reality, promoting our contribution.

Evolution of the model: a fully integrated approach (wide-band full polarization joint calibration and imaging)

An important line of future work involves the merger of polarization imaging with the hyperspectral imaging modalities. Such developments are of critical interest particularly for Faraday synthesis [219, 220]. In this respect, noting that the polarization constraint acts independently at each wavelength, our work can be directly adapted. Moreover, exploiting the flexibility of the underlying convex optimization framework, more complex priors can be incorporated to regularize the images in the spectral domain [221]. In fact, to further solve for the calibration errors, the adaptability offered by our developed self-calibration and imaging algorithm can be leveraged. This would

involve blending the wide-band polarimetric imaging technique with the calibration scheme incorporating DIEs/DDEs variation with the observation frequency . We believe that such an extension of our work to spectral dimension would result into an invaluable, complete formalism for radio interferometry.

Bibliography

- [1] M. Born and E. Wolf, *Principles of optics: electromagnetic theory of propagation, interference and diffraction of light*. Elsevier, 2013.
- [2] D. Li, R. Nan, and Z. Pan, “The Five-hundred-meter Aperture Spherical radio Telescope project and its early science opportunities,” *Proceedings of the International Astronomical Union*, vol. 291, pp. 325–330, 2013.
- [3] K. Akiyama, A. Alberdi, W. Alef, K. Asada, R. Azulay, A.-K. Baczko, D. Ball, M. Baloković, J. Barrett, D. Bintley, *et al.*, “First M87 Event Horizon Telescope Results. I. The shadow of the supermassive black hole,” *The Astrophysical Journal Letters*, vol. 875, p. L1, 2019.
- [4] A. Thompson, J. Moran, and G. Swenson, *Interferometry and Synthesis in Radio Astronomy*. Wiley-Interscience, New York, 2001.
- [5] Y. Wiaux, L. Jacques, G. Puy, A. Scaife, and P. Vandergheynst, “Compressed sensing imaging techniques for radio interferometry,” *Monthly Notices of the Royal Astronomical Society*, vol. 395, pp. 1733–1742, 2009.
- [6] O. Smirnov, “Revisiting the radio interferometer measurement equation-II. Calibration and direction-dependent effects,” *Astronomy & Astrophysics*, vol. 527, p. A107, 2011.
- [7] P. C. Broekema, R. V. van Nieuwpoort, and H. E. Bal, “The square kilometre array science data processor. preliminary compute platform design,” *Journal of Instrumentation*, vol. 10, no. 07, p. C07004, 2015.

- [8] J. A. Högbom, “Aperture synthesis with a non-regular distribution of interferometer baselines,” *Astronomy & Astrophysics*, vol. 15, pp. 417–426, 1974.
- [9] A. Onose, R. Carrillo, A. Repetti, J. McEwen, J. Thiran, J.-C. Pesquet, and Y. Wiaux, “Scalable splitting algorithms for big-data interferometric imaging in the SKA era,” *Monthly Notices of the Royal Astronomical Society*, vol. 462, pp. 4314–4335, 2016.
- [10] L. Pratley, J. D. McEwen, M. d’Avezac, R. E. Carrillo, A. Onose, and Y. Wiaux, “Robust sparse image reconstruction of radio interferometric observations with purify,” *Monthly Notices of the Royal Astronomical Society*, vol. 473, no. 1, pp. 1038–1058, 2017.
- [11] A. Dabbech, A. Onose, A. Abdulaziz, R. A. Perley, O. M. Smirnov, and Y. Wiaux, “Cygnus A super-resolved via convex optimization from VLA data,” *Monthly Notices of the Royal Astronomical Society*, vol. 476, no. 3, pp. 2853–2866, 2018.
- [12] F. Li, T. Cornwell, and F. De hoog, “The application of compressive sampling to radio astronomy. i. deconvolution,” *Astronomy & Astrophysics*, vol. 528, p. A31, 2011.
- [13] A. Ferrari, D. Mary, R. Flamary, and C. Richard, “Distributed image reconstruction for very large arrays in radio astronomy,” in *2014 IEEE 8th Sensor Array and Multichannel Signal Processing Workshop (SAM)*, pp. 389–392, IEEE, 2014.
- [14] A. Onose, A. Dabbech, and Y. Wiaux, “An accelerated splitting algorithm for radio-interferometric imaging: when natural and uniform weighting meet,” *Monthly Notices of the Royal Astronomical Society*, vol. 469, p. 938, 2017.
- [15] R. Van Weeren, W. Williams, M. Hardcastle, T. Shimwell, D. Rafferty, J. Sabater, G. Heald, S. Sridhar, T. Dijkema, G. Brunetti, *et al.*, “Lofar facet calibration,” *The Astrophysical Journal Supplement Series*, vol. 223, no. 1, p. 2, 2016.

- [16] S. Yatawatta, S. Zaroubi, A. De Bruyn, L. Koopmans, and J. Noordam, “Radio interferometric calibration using the SAGE algorithm,” in *2009 IEEE 13th Digital Signal Processing Workshop and 5th IEEE Signal Processing Education Workshop*, pp. 150–155, IEEE, 2009.
- [17] R. Oudmaijer, C. Haniff, D. Buscher, and J. Young, “Optical interferometry - the sharpest tool in the box,” *Astronomy & Geophysics*, vol. 53, no. 2, pp. 2–14, 2012.
- [18] R. G. Petrov, F. Malbet, A. Richichi, K.-H. Hofmann, D. Mourard, K. Agabi, P. Antonelli, E. Aristidi, C. Baffa, U. Beckmann, *et al.*, “AMBER: a near infrared focal instrument for the VLTI,” *Comptes Rendus de l’Académie des Sciences-Series IV-Physics*, vol. 2, no. 1, pp. 67–77, 2001.
- [19] F. Eisenhauer, G. Perrin, C. Straubmeier, W. Brandner, A. Boehm, F. Cassaing, Y. Clenet, K. Dodds-Eden, A. Eckart, P. Fedou, *et al.*, “GRAVITY: microarcsecond astrometry and deep interferometric imaging with the VLTI,” *Proceedings of the International Astronomical Union*, vol. 3, no. S248, pp. 100–101, 2007.
- [20] E. Thiébaud and J. Giovannelli, “Image reconstruction in optical interferometry,” *IEEE Signal Processing Magazine*, vol. 27, no. 1, pp. 97–109, 2010.
- [21] J. D. Monnier, “Phases in interferometry,” *New Astronomy Reviews*, vol. 51, no. 8-9, pp. 604–616, 2007.
- [22] E. Thiébaud, “MIRA: an effective imaging algorithm for optical interferometry,” in *Optical and Infrared Interferometry*, vol. 7013, p. 70131I, International Society for Optics and Photonics, 2008.
- [23] S. Meimon, L. Mugnier, and G. Le Besnerais, “Reconstruction method for weak-phase optical interferometry,” *Optics Letters*, vol. 30, no. 14, p. 1809, 2005.
- [24] R. Carrillo, J. McEwen, and Y. Wiaux, “PURIFY: a new approach to radio-interferometric imaging,” *Monthly Notices of the Royal Astronomical Society*, vol. 439, no. 4, pp. 3591–3604, 2014.

- [25] J. Birdi, A. Repetti, and Y. Wiaux, “Sparse interferometric Stokes imaging under the polarization constraint (Polarized SARA),” *Monthly Notices of the Royal Astronomical Society*, vol. 478, pp. 4442–4463, 2018.
- [26] J. Birdi, A. Repetti, and Y. Wiaux, “Scalable algorithm for polarization constrained sparse interferometric Stokes imaging,” in *2018 IEEE 10th Sensor Array and Multichannel Signal Processing Workshop (SAM)*, pp. 465–469, IEEE, 2018.
- [27] A. Repetti, J. Birdi, A. Dabbech, and Y. Wiaux, “Non-convex optimization for self-calibration of direction-dependent effects in radio interferometric imaging,” *Monthly Notices of the Royal Astronomical Society*, vol. 470, no. 4, pp. 3981–4006, 2017.
- [28] A. Repetti, J. Birdi, and Y. Wiaux, “Joint imaging and DDEs calibration for radio interferometry,” in *Villars-sur-Ollon, Switzerland: Biomedical and Astronomical Signal Processing (BASP) Frontiers workshop*, vol. 29, p. 25, 2017.
- [29] A. Repetti, J. Birdi, and Y. Wiaux, “Non-convex blind deconvolution approach for sparse radio interferometric imaging,” *Lisbon, Portugal: Signal Processing with Adaptive Sparse Structured Representations (SPARS) workshop*, p. 130, 2017.
- [30] J. Birdi, A. Repetti, and Y. Wiaux, “Polca SARA - Full polarization, direction-dependent calibration and sparse imaging for radio interferometry,” *arXiv preprint, arXiv:1904.00663*, 2019.
- [31] A. Auria, R. Carrillo, J.-P. Thiran, and Y. Wiaux, “Tensor optimisation for optical-interferometric imaging,” *Monthly Notices of the Royal Astronomical Society*, vol. 437, pp. 2083 – 2091, 2014.
- [32] J. Birdi, A. Repetti, and Y. Wiaux, “A regularized tri-linear approach for optical interferometric imaging,” *Monthly Notices of the Royal Astronomical Society*, vol. 468, no. 1, pp. 1142–1155, 2017.

- [33] J. Birdi, A. Repetti, and Y. Wiaux, “Sparsity regularized optical interferometric imaging,” *Lisbon, Portugal: Signal Processing with Adaptive Sparse Structured Representations (SPARS) workshop*, p. 44, 2017.
- [34] T. Young, “On the theory of light and colours, bakerian lecture 1801,” *Philosophical transactions of the Royal Society of London*, vol. 92, pp. 12–48, 1802.
- [35] O. M. Smirnov, “Revisiting the radio interferometer measurement equation-I. A full-sky Jones formalism,” *Astronomy & Astrophysics*, vol. 527, p. A106, 2011.
- [36] J. Hamaker, J. Bregman, and R. Sault, “Understanding radio polarimetry. I. mathematical foundations,” *Astronomy and Astrophysics Supplement Series*, vol. 117, pp. 137–147, 1996.
- [37] F. Zernike, “The concept of degree of coherence and its application to optical problems,” *Physica*, vol. 5, no. 8, pp. 785–795, 1938.
- [38] M. Ryle and A. Hewish, “The synthesis of large radio telescopes,” *Monthly Notices of the Royal Astronomical Society*, vol. 120, no. 3, pp. 220–230, 1960.
- [39] E. O. Brigham, *The fast Fourier transform and its applications*, vol. 448. Prentice Hall Englewood Cliffs, NJ, 1988.
- [40] D. S. Briggs, *High fidelity deconvolution of moderately resolved sources*. PhD thesis, New Mexico Institute of Mining and Technology, 1995.
- [41] F. Boone, “Weighting interferometric data for direct imaging,” *Experimental Astronomy*, vol. 36, no. 1-2, pp. 77–104, 2013.
- [42] S. Myers, J. Ott, and N. Elias *CASA Synthesis & Single Dish Reduction Cookbook.*, 2010. Release 3.0.1.
- [43] A. Bjorck, *Numerical methods for least squares problems*, vol. 51. Siam, 1996.
- [44] H. W. Engl, M. Hanke, and A. Neubauer, *Regularization of inverse problems*, vol. 375. Springer Science & Business Media, 1996.

- [45] R. Carrillo, J. McEwen, and Y. Wiaux, “Sparsity Averaging Reweighted Analysis (SARA): A novel algorithm for radio-interferometric imaging,” *Monthly Notices of the Royal Astronomical Society*, vol. 426, no. 2, pp. 1223–1234, 2012.
- [46] I. Daubechies, M. Defrise, and C. De Mol, “An iterative thresholding algorithm for linear inverse problems with a sparsity constraint,” *Communications on Pure and Applied Mathematics: A Journal Issued by the Courant Institute of Mathematical Sciences*, vol. 57, no. 11, pp. 1413–1457, 2004.
- [47] M. A. Figueiredo, R. D. Nowak, and S. J. Wright, “Gradient projection for sparse reconstruction: Application to compressed sensing and other inverse problems,” *IEEE Journal of Selected Topics in Signal Processing*, vol. 1, no. 4, pp. 586–597, 2007.
- [48] E. J. Candès and M. B. Wakin, “An introduction to compressive sampling [a sensing/sampling paradigm that goes against the common knowledge in data acquisition],” *IEEE Signal Processing Magazine*, vol. 25, no. 2, pp. 21–30, 2008.
- [49] J.-L. Starck, F. Murtagh, and J. Fadili, *Sparse Image and Signal Processing: Wavelets, Curvelets, Morphological Diversity*. Cambridge University Press, 2010.
- [50] R. Rubinstein, A. Bruckstein, and M. Elad, “Dictionaries for sparse representation modeling,” in *Proceedings of the IEEE*, vol. 98, pp. 1045–1057, IEEE, 2010.
- [51] L. I. Rudin, S. Osher, and E. Fatemi, “Nonlinear total variation based noise removal algorithms,” *Physica D: nonlinear phenomena*, vol. 60, no. 1-4, pp. 259–268, 1992.
- [52] S. G. Mallat, *A wavelet tour of signal processing : the Sparse way*. Academic Press, Burlington, MA, 2nd ed., 2009.
- [53] J.-L. Starck and F. Murtagh, “Image restoration with noise suppression using the wavelet transform,” *Astronomy & Astrophysics*, vol. 288, pp. 342–348, 1994.

- [54] J.-L. Starck, D. L. Donoho, and E. J. Candès, “Astronomical image representation by the curvelet transform,” *Astronomy & Astrophysics*, vol. 398, no. 2, pp. 785–800, 2003.
- [55] H. L. Taylor, S. C. Banks, and J. F. McCoy, “Deconvolution with the l1 norm,” *Geophysics*, vol. 44, no. 1, pp. 39–52, 1979.
- [56] S. Levy and P. K. Fullagar, “Reconstruction of a sparse spike train from a portion of its spectrum and application to high-resolution deconvolution,” *Geophysics*, vol. 46, no. 9, pp. 1235–1243, 1981.
- [57] E. Candès, J. Romberg, and T. Tao, “Robust uncertainty principles: Exact signal reconstruction from highly incomplete frequency information,” *IEEE Transactions on Information Theory*, vol. 52, no. 2, pp. 489–509, 2006.
- [58] D. L. Donoho, “Compressed sensing,” *IEEE Transactions on Information Theory*, vol. 52, no. 4, pp. 1289–1306, 2006.
- [59] R. G. Baraniuk, “Compressive sensing [lecture notes],” *IEEE Signal Processing Magazine*, vol. 24, no. 4, pp. 118–121, 2007.
- [60] S. Mallat and Z. Zhang, “Matching pursuits with time-frequency dictionaries,” *IEEE Transactions on Signal Processing*, vol. 41, no. 12, pp. 3397–3415, 1993.
- [61] S. S. Chen, D. L. Donoho, and M. A. Saunders, “Atomic Decomposition by Basis Pursuit,” *SIAM Review*, vol. 43, no. 1, pp. 129–159, 2001.
- [62] M. A. Davenport, M. F. Duarte, Y. C. Eldar, and G. Kutyniok, “Introduction to compressed sensing,” *preprint*, vol. 93, no. 1, p. 2, 2011.
- [63] M. Fornasier and H. Rauhut, “Compressive sensing,” in *Handbook of mathematical methods in imaging*, pp. 187–228, Springer, 2011.
- [64] E. J. Candès, J. K. Romberg, and T. Tao, “Stable signal recovery from incomplete and inaccurate measurements,” *Communications on Pure and Applied Mathematics: A Journal Issued by the Courant Institute of Mathematical Sciences*, vol. 59, no. 8, pp. 1207–1223, 2006.

- [65] M. Elad, P. Milanfar, and R. Rubinstein, “Analysis versus synthesis in signal priors,” *Inverse problems*, vol. 23, no. 3, p. 947, 2007.
- [66] M. Elad, M. A. Figueiredo, and Y. Ma, “On the role of sparse and redundant representations in image processing,” *Proceedings of the IEEE*, vol. 98, no. 6, pp. 972–982, 2010.
- [67] E. Candès, M. Wakin, and S. Boyd, “Enhancing Sparsity by Reweighted l_1 Minimization,” *Journal of Fourier Analysis and Applications*, vol. 14, no. 5-6, pp. 877–905, 2008.
- [68] E. Chouzenoux, A. Jezierska, J.-C. Pesquet, and H. Talbot, “A majorize-minimize subspace approach for $l_2 - l_0$ image regularization,” *SIAM Journal on Imaging Sciences*, vol. 6, pp. 563–591, 2013.
- [69] A. Repetti, M. Q. Pham, L. Duval, E. Chouzenoux, and J.-C. Pesquet, “Euclid in a Taxicab: Sparse blind deconvolution with smoothed l_1/l_2 regularization,” *IEEE Signal Processing Letters*, vol. 22, no. 5, pp. 539–543, 2015.
- [70] S. Mallat, *A wavelet tour of signal processing*. Elsevier, 1999.
- [71] Y. C. Pati, R. Rezaiifar, and P. S. Krishnaprasad, “Orthogonal matching pursuit: Recursive function approximation with applications to wavelet decomposition,” in *Proceedings of 27th Asilomar Conference on Signals, Systems and Computers*, pp. 40–44, IEEE, 1993.
- [72] J. A. Tropp and A. C. Gilbert, “Signal recovery from random measurements via orthogonal matching pursuit,” *IEEE Transactions on Information Theory*, vol. 53, no. 12, pp. 4655–4666, 2007.
- [73] D. L. Donoho, Y. Tsaig, I. Drori, and J.-L. Starck, “Sparse solution of underdetermined systems of linear equations by stagewise orthogonal matching pursuit,” *IEEE Transactions on Information Theory*, vol. 58, no. 2, pp. 1094–1121, 2012.
- [74] D. Needell and J. A. Tropp, “Cosamp: Iterative signal recovery from incomplete and inaccurate samples,” *Applied and computational harmonic analysis*, vol. 26, no. 3, pp. 301–321, 2009.

- [75] D. Needell and R. Vershynin, “Uniform uncertainty principle and signal recovery via regularized orthogonal matching pursuit,” *Foundations of computational mathematics*, vol. 9, no. 3, pp. 317–334, 2009.
- [76] D. Needell and R. Vershynin, “Signal recovery from incomplete and inaccurate measurements via regularized orthogonal matching pursuit,” *IEEE Journal of Selected topics in Signal Processing*, vol. 4, no. 2, pp. 310–316, 2010.
- [77] R. Baraniuk, M. A. Davenport, M. F. Duarte, C. Hegde, *et al.*, “An introduction to compressive sensing,” *Connexions e-textbook*, 2011.
- [78] T. Blumensath and M. E. Davies, “Iterative thresholding for sparse approximations,” *Journal of Fourier Analysis and Applications*, vol. 14, no. 5-6, pp. 629–654, 2008.
- [79] T. Blumensath and M. E. Davies, “Iterative hard thresholding for compressed sensing,” *Applied and computational harmonic analysis*, vol. 27, no. 3, pp. 265–274, 2009.
- [80] S. Boyd and L. Vandenberghe, *Convex Optimization*. New York, NY, USA: Cambridge University Press, 2004.
- [81] M. A. Figueiredo and R. D. Nowak, “An EM algorithm for wavelet-based image restoration,” *IEEE Transactions on Image Processing*, vol. 12, no. 8, pp. 906–916, 2003.
- [82] M. Elad, B. Matalon, J. Shtok, and M. Zibulevsky, “A wide-angle view at iterated shrinkage algorithms,” in *Wavelets XII*, vol. 6701, p. 670102, International Society for Optics and Photonics, 2007.
- [83] S. J. Wright, R. D. Nowak, and M. A. Figueiredo, “Sparse reconstruction by separable approximation,” *IEEE Transactions on Signal Processing*, vol. 57, no. 7, pp. 2479–2493, 2009.
- [84] A. Beck and M. Teboulle, “Fast gradient-based algorithms for constrained total variation image denoising and deblurring problems,” *IEEE Transactions on Image Processing*, vol. 18, no. 11, pp. 2419–2434, 2009.

- [85] P. L. Combettes and J.-C. Pesquet, “Proximal thresholding algorithm for minimization over orthonormal bases,” *SIAM Journal on Optimization*, vol. 18, no. 4, pp. 1351–1376, 2007.
- [86] M. E. Tipping, “Sparse bayesian learning and the relevance vector machine,” *Journal of Machine Learning Research*, vol. 1, no. Jun, pp. 211–244, 2001.
- [87] D. P. Wipf and B. D. Rao, “Sparse bayesian learning for basis selection,” *IEEE Transactions on Signal Processing*, vol. 52, no. 8, pp. 2153–2164, 2004.
- [88] S. Ji, Y. Xue, L. Carin, *et al.*, “Bayesian compressive sensing,” *IEEE Transactions on Signal Processing*, vol. 56, no. 6, p. 2346, 2008.
- [89] P. J. Green, K. Łatuszyński, M. Pereyra, and C. P. Robert, “Bayesian computation: a summary of the current state, and samples backwards and forwards,” *Statistics and Computing*, vol. 25, no. 4, pp. 835–862, 2015.
- [90] P. L. Combettes and J.-C. Pesquet, *Fixed-Point Algorithms for Inverse Problems in Science and Engineering*. Springer, New York, 2011.
- [91] N. Komodakis and J.-C. Pesquet, “Playing with duality: An overview of recent primal-dual approaches for solving large-scale optimization problems,” *IEEE Signal Processing Magazine*, vol. 32, no. 6, pp. 31–54, 2015.
- [92] J.-J. Moreau, “Proximité et dualité dans un espace hilbertien,” *Bulletin de la Société mathématique de France*, vol. 93, pp. 273–299, 1965.
- [93] C. Chaux, P. L. Combettes, J.-C. Pesquet, and V. R. Wajs, “A variational formulation for frame-based inverse problems,” *Inverse Problems*, vol. 23, no. 4, pp. 1495–1518, 2007.
- [94] G. Chen and R. Rockafellar, “Convergence rates in forward-backward splitting,” *SIAM Journal on Optimization*, vol. 7, no. 2, pp. 421–444, 1997.
- [95] P. Tseng, “A modified forward-backward splitting method for maximal monotone mappings,” *SIAM Journal on Control and Optimization*, vol. 38, pp. 431–446, 2000.

- [96] J. Eckstein and D. Bertsekas, “On the Douglas — Rachford splitting method and the proximal point algorithm for maximal monotone operators,” *Mathematical Programming*, vol. 55, no. 1, pp. 293–318, 1992.
- [97] P. L. Combettes and V. Wajs, “Signal recovery by proximal forward-backward splitting,” *Multiscale Modeling & Simulation*, vol. 4, no. 4, pp. 1168–1200, 2005.
- [98] P. L. Combettes and J.-C. Pesquet, “Proximal Thresholding Algorithm for Minimization over Orthonormal Bases,” *SIAM Journal on Optimization*, vol. 18, no. 4, pp. 1351–1376, 2008.
- [99] A. Chambolle and T. Pock, “A first-order primal-dual algorithm for convex problems with applications to imaging,” *Journal of Mathematical Imaging and Vision*, vol. 40, no. 1, pp. 120–145, 2010.
- [100] L. Condat, “A primal–dual splitting method for convex optimization involving Lipschitzian, proximable and linear composite terms,” *Journal of Optimization Theory and Applications*, vol. 158, no. 2, pp. 460–479, 2013.
- [101] B. Vũ, “A splitting algorithm for dual monotone inclusions involving cocoercive operators,” *Advances in Computational Mathematics*, vol. 38, no. 3, pp. 667–681, 2013.
- [102] P. L. Combettes, L. Condat, J.-C. Pesquet, and B. Vũ, “A forward-backward view of some primal-dual optimization methods in image recovery,” in *2014 IEEE International Conference on Image Processing (ICIP)*, pp. 4141–4145, IEEE, 2014.
- [103] H. H. Bauschke and P. L. Combettes, *Convex Analysis and Monotone Operator Theory in Hilbert Spaces*. Springer-Verlag New York, 2011.
- [104] P. L. Combettes and J.-C. Pesquet, “Primal-dual splitting algorithm for solving inclusions with mixtures of composite, Lipschitzian, and parallel-sum type monotone operators,” *Set-Valued and variational analysis*, vol. 20, no. 2, pp. 307–330, 2012.

- [105] S. J. Wright, “Coordinate descent algorithms,” *Mathematical Programming*, vol. 151, no. 1, pp. 3–34, 2015.
- [106] P. Tseng, “Convergence of a block coordinate descent method for nondifferentiable minimization,” *Journal of Optimization Theory and Applications*, vol. 109, no. 3, pp. 475–494, 2001.
- [107] E. Chouzenoux, J.-C. Pesquet, and A. Repetti, “A block coordinate variable metric forward backward algorithm,” *Journal of Global Optimization*, pp. 1–29, 2016.
- [108] J. Bolte, S. Sabach, and M. Teboulle, “Proximal alternating linearized minimization for nonconvex and nonsmooth problems,” *Mathematical Programming*, vol. 146, no. 1-2, pp. 459–494, 2014.
- [109] R. Chartrand, “Exact reconstruction of sparse signals via nonconvex minimization,” *IEEE Signal Processing Letters*, vol. 14, no. 10, pp. 707–710, 2007.
- [110] B. D. Rao and K. Kreutz-Delgado, “An affine scaling methodology for best basis selection,” *IEEE Transactions on Signal Processing*, vol. 47, no. 1, pp. 187–200, 1999.
- [111] C. L. Lawson, “Contribution to the theory of linear least maximum approximation,” *Ph. D. dissertation, Univ. Calif.*, 1961.
- [112] D. Needell, “Noisy signal recovery via iterative reweighted l1-minimization,” *2009 Conference Record of the Forty-Third Asilomar Conference on Signals, Systems and Computers*, pp. 113–117, 2009.
- [113] B. Clark, “An efficient implementation of the algorithm ‘clean’,” *Astronomy & Astrophysics*, vol. 89, p. 377, 1980.
- [114] F. Schwab, “Relaxing the isoplanatism assumption in self-calibration; applications to low-frequency radio interferometry,” *The Astronomical Journal*, vol. 89, pp. 1076–1081, 1984.

- [115] D. Steer, P. Dewdney, and M. Ito, “Enhancements to the deconvolution algorithm clean,” *Astronomy & Astrophysics*, vol. 137, pp. 159–165, 1984.
- [116] T. J. Cornwell, “Multiscale clean deconvolution of radio synthesis images,” *IEEE Journal of Selected Topics in Signal Processing*, vol. 2, no. 5, pp. 793–801, 2008.
- [117] A. Offringa, B. McKinley, N. Hurley-Walker, F. Briggs, R. Wayth, D. Kaplan, M. Bell, L. Feng, A. Neben, J. Hughes, *et al.*, “WSCLEAN: an implementation of a fast, generic wide-field imager for radio astronomy,” *Monthly Notices of the Royal Astronomical Society*, vol. 444, no. 1, pp. 606–619, 2014.
- [118] A. Kepley, “Auto-multithresh: A General Purpose Automated Masking Algorithm for Clean,” tech. rep., 2018. Astronomical Data Analysis Software and Systems (ADASS) conference, XXVIII, <http://adass2018.astro.umd.edu/abstracts/O12.1.html>.
- [119] U. Rau, S. Bhatnagar, M. Voronkov, and T. Cornwell, “Advances in calibration and imaging techniques in radio interferometry,” in *Proceedings of the IEEE*, vol. 97, pp. 1472–1481, IEEE, 2009.
- [120] L. Pratley and M. Johnston-Hollitt, “An improved method for polarimetric image restoration in interferometry,” *Monthly Notices of the Royal Astronomical Society*, vol. 462, pp. 3483–3501, 2016.
- [121] T. J. Cornwell and K. F. Evans, “A simple maximum entropy deconvolution algorithm,” *Astronomy & Astrophysics*, vol. 143, pp. 77–83, 1985.
- [122] R. Narayan and R. Nityananda, “Maximum entropy image restoration in astronomy,” *Annual review of astronomy and astrophysics*, vol. 24, pp. 127–170, 1986.
- [123] M. Holdaway and J. Wardle, “Maximum entropy imaging of polarization in very long baseline interferometry,” *Digital Image Synthesis and Inverse Optics*, vol. 1351, pp. 714–724, 1990.

- [124] C. Coughlan and D. Gabuzda, “High resolution VLBI polarization imaging of AGN with the maximum entropy method,” *Monthly Notices of the Royal Astronomical Society*, vol. 463, pp. 1980–2001, 2016.
- [125] A. Chael, M. Johnson, R. Narayan, S. Doeleman, J. Wardle, and K. Bouman, “High-resolution Linear Polarimetric Imaging for the Event Horizon Telescope,” *The Astrophysical Journal*, vol. 829, no. 1, p. 11, 2016.
- [126] C. L. Lawson and R. J. Hanson, *Solving least squares problems*, vol. 15. SIAM, 1995.
- [127] J. Nocedal and S. Wright, *Numerical optimization*. Springer Science & Business Media, 2006.
- [128] D. S. Briggs, *High fidelity deconvolution of moderately resolved sources*. PhD thesis, New Mexico Institute of Mining and Technology, 1995.
- [129] A. M. Sardarabadi, A. Leshem, and A.-J. van der Veen, “Radio astronomical image formation using constrained least squares and krylov subspaces,” *Astronomy & Astrophysics*, vol. 588, p. A95, 2016.
- [130] H. Garsden, J. Girard, J. Starck, S. Corbel, C. Tasse, A. Woiselle, J. McKean, A. Van Amesfoort, J. Anderson, I. Avruch, and R. Beck, “Lofar sparse image reconstruction,” *Astronomy & Astrophysics*, vol. 575, p. A90, 2015.
- [131] A. Dabbech, C. Ferrari, D. Mary, E. Slezak, O. Smirnov, and J. S. Kenyon, “Moresane: Model reconstruction by synthesis-analysis estimators-a sparse deconvolution algorithm for radio interferometric imaging,” *Astronomy & Astrophysics*, vol. 576, p. A7, 2015.
- [132] S. Boyd, N. Parikh, E. Chu, B. Peleato, and J. Eckstein, “Distributed Optimization and Statistical Learning via the Alternating Direction Method of Multipliers,” *Foundations and Trends® in Machine learning*, vol. 3, no. 1, pp. 1–122, 2010.
- [133] K. Akiyama, K. Kuramochi, S. Ikeda, V. Fish, F. Tazaki, M. Honma, S. Doeleman, A. Broderick, J. Dexter, M. Mościbrodzka, and K. Bouman, “Imaging the

- Schwarzschild-radius-scale Structure of M87 with the Event Horizon Telescope Using Sparse Modeling,” *The Astrophysical Journal*, vol. 838, no. 1, p. 1, 2017.
- [134] A. Chambolle and P. Lions, “Image recovery via total variation minimization and related problems,” *Numerische Mathematik*, vol. 76, no. 2, pp. 167–188, 1997.
- [135] A. Beck and M. Teboulle, “A fast iterative shrinkage-thresholding algorithm for linear inverse problems,” *SIAM Journal on Imaging Sciences*, vol. 2, pp. 183–202, 2009.
- [136] M. Lochner, I. Natarajan, J. Zwart, O. Smirnov, B. Bassett, N. Oozeer, and M. Kunz, “Bayesian inference for radio observations,” *Monthly Notices of the Royal Astronomical Society*, vol. 450, no. 2, pp. 1308–1319, 2015.
- [137] H. Intema, S. Van der Tol, W. Cotton, A. Cohen, I. Van Bemmelen, and H. Röttgering, “Ionospheric calibration of low frequency radio interferometric observations using the peeling scheme-I. Method description and first results,” *Astronomy & Astrophysics*, vol. 501, no. 3, pp. 1185–1205, 2009.
- [138] S. Bhatnagar, T. Cornwell, K. Golap, and J. M. Uson, “Correcting direction-dependent gains in the deconvolution of radio interferometric images,” *Astronomy & Astrophysics*, vol. 487, no. 1, pp. 419–429, 2008.
- [139] S. Kazemi, S. Yatawatta, S. Zaroubi, P. Lampropoulos, A. De Bruyn, L. Koopmans, and J. Noordam, “Radio interferometric calibration using the SAGE algorithm,” *Monthly Notices of the Royal Astronomical Society*, vol. 414, no. 2, pp. 1656–1666, 2011.
- [140] S. Yatawatta, “On the interpolation of calibration solutions obtained in radio interferometry,” *Monthly Notices of the Royal Astronomical Society*, vol. 428, no. 1, pp. 828–833, 2012.
- [141] T. Cornwell and P. Wilkinson, “A new method for making maps with unstable radio interferometers,” *Monthly Notices of the Royal Astronomical Society*, vol. 196, no. 4, pp. 1067–1086, 1981.

- [142] T. Pearson and A. Readhead, “Image formation by self-calibration in radio astronomy,” *Annual review of astronomy and astrophysics*, vol. 22, no. 1, pp. 97–130, 1984.
- [143] J. Moré, *The Levenberg-Marquardt algorithm: implementation and theory*. Springer, Berlin, Heidelberg, 1978.
- [144] J. Hamaker, “Understanding radio polarimetry-IV. The full-coherency analogue of scalar self-calibration: Self-alignment, dynamic range and polarimetric fidelity,” *Astronomy and Astrophysics supplement series*, vol. 143, no. 3, pp. 515–534, 2000.
- [145] S. Salvini and S. Wijnholds, “Fast gain calibration in radio astronomy using alternating direction implicit methods: Analysis and applications,” *Astronomy & Astrophysics*, vol. 571, p. A97, 2014.
- [146] S. Salvini and S. J. Wijnholds, “Stefcal—an alternating direction implicit method for fast full polarization array calibration,” in *General Assembly and Scientific Symposium (URSI GASS), 2014 XXXIth URSI*, pp. 1–4, IEEE, 2014.
- [147] J. E. Noordam, “Lofar calibration challenges,” in *Ground-Based Telescopes*, vol. 5489, pp. 817–826, International Society for Optics and Photonics, 2004.
- [148] H. Intema, “SPAM: A data reduction recipe for high-resolution, low-frequency radio-interferometric observations.” 2014.
- [149] O. Smirnov and C. Tasse, “Radio interferometric gain calibration as a complex optimization problem,” *Monthly Notices of the Royal Astronomical Society*, vol. 449, pp. 2668–2684, 2015.
- [150] C. Tasse, B. Hugo, M. Mirmont, O. Smirnov, M. Atemkeng, L. Bester, M. Hardcastle, R. Lakhoo, S. Perkins, and T. Shimwell, “Faceting for direction-dependent spectral deconvolution,” *Astronomy & Astrophysics*, vol. 611, p. A87, 2018.

- [151] J. A. Fessler and A. O. Hero, “Space-alternating generalized expectation-maximization algorithm,” *IEEE Transactions on Signal Processing*, vol. 42, no. 10, pp. 2664–2677, 1994.
- [152] M. Feder and E. Weinstein, “Parameter estimation of superimposed signals using the em algorithm,” *IEEE Transactions on Acoustics, Speech, and Signal Processing*, vol. 36, no. 4, pp. 477–489, 1988.
- [153] S. Bhatnagar and T. Cornwell, “The pointing self-calibration algorithm for aperture synthesis radio telescopes,” *The Astronomical Journal*, vol. 154, no. 5, p. 197, 2017.
- [154] R. Carrillo, J. McEwen, D. Van De Ville, J.-P. Thiran, and Y. Wiaux, “Sparsity averaging for compressive imaging,” *IEEE Signal Processing Letters*, vol. 20, no. 6, pp. 591–594, 2013.
- [155] J.-C. Pesquet and A. Repetti, “A class of randomized primal-dual algorithms for distributed optimization,” *Journal of Nonlinear Convex Analysis*, vol. 16, no. 12, pp. 2453–2490, 2015.
- [156] S. Bhatnagar, U. Rau, and K. Golap, “Wide-field wide-band interferometric imaging: The WB A-Projection and hybrid algorithms,” *The Astrophysical Journal*, vol. 770, p. 91, 2013.
- [157] J. A. Fessler and B. P. Sutton, “Nonuniform fast Fourier transforms using min-max interpolation,” *IEEE Transactions on Signal Processing*, vol. 51, no. 2, pp. 560–574, 2003.
- [158] G. Chierchia, N. Pustelnik, J.-C. Pesquet, and B. Pesquet-Popescu, “Epigraphical projection and proximal tools for solving constrained convex optimization problems,” *Signal, Image and Video Processing*, vol. 9, no. 8, pp. 1737–1749, 2015.
- [159] S. Harizanov, J.-C. Pesquet, and G. Steidl, “Epigraphical projection for solving least squares Anscombe transformed constrained optimization problems,” in

- International Conference on Scale Space and Variational Methods in Computer Vision*, pp. 125–136, Springer, Berlin, Heidelberg, 2013.
- [160] G. Chierchia, N. Pustelnik, J.-C. Pesquet, and B. Pesquet-Popescu, “Epigraphical proximal projection for sparse multiclass SVM,” in *2014 IEEE International Conference on Acoustics, Speech and Signal Processing (ICASSP)*, pp. 8312–8316, IEEE, 2014.
 - [161] G. Moerkotte, M. Montag, A. Repetti, and G. Steidl, “Proximal operator of quotient functions with application to a feasibility problem in query optimization,” *Journal of Computational and Applied Mathematics*, vol. 285, pp. 243–255, 2015.
 - [162] M. El Gheche, G. Chierchia, and J.-C. Pesquet, “Proximity operators of discrete information divergences,” *IEEE Transactions on Information Theory*, vol. 64, no. 2, pp. 1092–1104, 2018.
 - [163] R. T. Rockafellar and R. J.-B. Wets, *Variational Analysis*, vol. 317. Springer-Verlag New York, first ed., 1997.
 - [164] J.-B. Hiriart-Urruty and C. Lemaréchal, *Convex analysis and minimization algorithms I: Fundamentals*, vol. 305. Springer science & business media, 2013.
 - [165] K. Akiyama, S. Ikeda, M. Pleau, V. Fish, F. Tazaki, K. Kuramochi, A. Broderick, J. Dexter, M. Mościbrodzka, M. Gowanlock, and M. Honma, “Superresolution Full-polarimetric Imaging for Radio Interferometry with Sparse Modeling,” *The Astrophysical Journal*, vol. 153, no. 4, p. 159, 2017.
 - [166] A. Broderick and A. Loeb, “Imaging the black hole silhouette of M87: implications for jet formation and black hole spin,” *The Astrophysical Journal*, vol. 697, p. 1164, 2009.
 - [167] R. Lu, A. Broderick, F. Baron, J. Monnier, V. Fish, S. Doeleman, and V. Pankratius, “Imaging the supermassive black hole shadow and jet base of M87 with the event horizon telescope,” *The Astrophysical Journal*, vol. 788, p. 120, 2014.

- [168] J. Dexter, J. McKinney, and E. Agol, “The size of the jet launching region in M87,” *Monthly Notices of the Royal Astronomical Society*, vol. 421, pp. 1517–1528, 2012.
- [169] J. Dexter, “A public code for general relativistic, polarised radiative transfer around spinning black holes,” *Monthly Notices of the Royal Astronomical Society*, vol. 462, pp. 115–136, 2016.
- [170] I. Daubechies and W. Sweldens, “Factoring wavelet transforms into lifting steps,” *Journal of Fourier Analysis and Applications*, vol. 4, pp. 247–269, 1998.
- [171] S. Salvini and S. Wijnholds, “Fast gain calibration in radio astronomy using alternating direction implicit methods: Analysis and applications,” *Astronomy & Astrophysics*, vol. 571, p. A97, 2014.
- [172] T. L. Grobler, C. Nunhokee, O. Smirnov, A. Van Zyl, and A. De Bruyn, “Calibration artefacts in radio interferometry–i. ghost sources in westerbork synthesis radio telescope data,” *Monthly Notices of the Royal Astronomical Society*, vol. 439, no. 4, pp. 4030–4047, 2014.
- [173] A. Repetti and Y. Wiaux, “A non-convex perspective on calibration and imaging in radio interferometry,” in *Wavelets and Sparsity XVII 2017*, vol. 10394, p. 103941W, International Society for Optics and Photonics, 2017.
- [174] P.-A. Thouvenin, A. Repetti, A. Dabbech, and Y. Wiaux, “Time-Regularized Blind Deconvolution Approach for Radio Interferometry,” in *2018 IEEE 10th Sensor Array and Multichannel Signal Processing Workshop (SAM)*, pp. 475–479, IEEE, 2018.
- [175] C. A. Hales, “Calibration errors in interferometric radio polarimetry,” *The Astronomical Journal*, vol. 154, no. 2, p. 54, 2017.
- [176] P. L. Combettes, D. Duňg, and B. C. Vũ, “Proximity for sums of composite functions,” *Journal of Mathematical Analysis and applications*, vol. 380, no. 2, pp. 680–688, 2011.

- [177] A. Readhead, T. Nakajima, T. Pearson, G. Neugebauer, J. Oke, and W. Sargent, “Diffraction-limited imaging with ground-based optical telescopes,” *Astronomical Journal*, vol. 95, no. 4, pp. 1278–1296, 1988.
- [178] J. D. Monnier, “Optical interferometry in astronomy,” *Reports on Progress in Physics*, vol. 66, no. 5, p. 789, 2003.
- [179] R. W. Gerchberg, “A practical algorithm for the determination of phase from image and diffraction plane pictures,” *Optik*, vol. 35, pp. 237–246, 1972.
- [180] J. R. Fienup, “Phase retrieval algorithms: a comparison,” *Applied Optics*, vol. 21, no. 15, pp. 2758–2769, 1982.
- [181] E. Candès, T. Strohmer, and V. Voroninski, “PhaseLift: Exact and stable signal recovery from magnitude measurements via convex programming,” *Communications on Pure and Applied Mathematics*, vol. 66, no. 8, pp. 1241–1274, 2011.
- [182] I. Waldspurger, A. D’Aspremont, and S. Mallat, “Phase recovery, MaxCut and complex semidefinite programming,” *Mathematical Programming*, pp. 1–35, 2013.
- [183] F. Fogel, I. Waldspurger, and A. d’Aspremont, “Phase retrieval for imaging problems,” *Mathematical programming computation*, vol. 8, no. 3, pp. 311–335, 2016.
- [184] S. Mukherjee and C. S. Seelamantula, “An iterative algorithm for phase retrieval with sparsity constraints: application to frequency domain optical coherence tomography,” in *2012 IEEE International Conference on Acoustics, Speech and Signal Processing (ICASSP)*, pp. 553–556, IEEE, 2012.
- [185] K. Jaganathan, S. Oymak, and B. Hassibi, “Recovery of sparse 1-d signals from the magnitudes of their fourier transform,” in *2012 IEEE International Symposium on Information Theory Proceedings*, pp. 1473–1477, IEEE, 2012.
- [186] Y. Shechtman, Y. C. Eldar, A. Szameit, and M. Segev, “Sparsity based sub-wavelength imaging with partially incoherent light via quadratic compressed sensing,” *Optics Express*, vol. 19, no. 16, pp. 14807–14822, 2011.

- [187] Y. Shechtman, A. Beck, and Y. C. Eldar, “Gespar: Efficient phase retrieval of sparse signals,” *IEEE Transactions on Signal Processing*, vol. 62, no. 4, pp. 928–938, 2014.
- [188] A. Repetti, E. Chouzenoux, and J.-C. Pesquet, “A nonconvex regularized approach for phase retrieval,” in *2014 IEEE International Conference on Image Processing (ICIP)*, pp. 1753–1757, IEEE, 2014.
- [189] E. Thiébaud, “Optimization issues in blind deconvolution algorithms,” in *Astronomical Data Analysis II*, vol. 4847, pp. 174–184, International Society for Optics and Photonics, 2002.
- [190] D. Buscher, “Direct maximum-entropy image reconstruction from the bispectrum,” in *Very High Angular Resolution Imaging*, pp. 91–93, Springer, 1994.
- [191] K.-H. Hofmann, G. Weigelt, and D. Schertl, “An image reconstruction method (IRBis) for optical/infrared interferometry,” *Astronomy & Astrophysics*, vol. 565, p. A48, 2014.
- [192] W. W. Hager and H. Zhang, “A New Conjugate Gradient Method with Guaranteed Descent and an Efficient Line Search,” *SIAM Journal on Optimization*, vol. 16, no. 1, pp. 170–192, 2005.
- [193] W. W. Hager and H. Zhang, “A new active set algorithm for box constrained optimization,” *SIAM Journal on Optimization*, vol. 17, no. 2, pp. 526–557, 2006.
- [194] A. Gamerman and H. F. Lopes, *Markov Chain Monte Carlo: Stochastic Simulation for Bayesian Inference*. Chapman and Hall/CRC, 1997.
- [195] M. J. Ireland, J. D. Monnier, and N. Thureau, “Monte-carlo imaging for optical interferometry,” in *Advances in Stellar Interferometry*, vol. 6268, p. 62681T, International Society for Optics and Photonics, 2006.
- [196] F. Baron, B. Kloppenborg, and J. Monnier, “Toward 5D image reconstruction for optical interferometry,” in *Proceedings of SPIE*, vol. 8445, pp. 84451D–84451D–9, 2012.

- [197] A. Auria, R. Carrillo, J.-P. Thiran, and Y. Wiaux, “Sparsity in tensor optimisation for optical-interferometric imaging,” in *2014 IEEE International Conference on Image Processing (ICIP)*, pp. 6026 – 6030, IEEE, 2015.
- [198] W. I. Zangwill, *Nonlinear programming : a unified approach*. Englewood Cliffs, N.J.: Prentice-Hall, 1969.
- [199] J. M. Ortega and W. C. Rheinboldt, *Iterative Solution of Nonlinear Equations in Several Variables*. New York: Academic Press, 1970.
- [200] D. Bertsekas, *Nonlinear programming*. Athena Scientific, Belmont, MA, 2nd ed., 1999.
- [201] B. Lopez, P. Antonelli, S. Wolf, S. Lagarde, W. Jaffe, R. Navarro, U. Graser, R. Petrov, G. Weigelt, Y. Bresson, *et al.*, “MATISSE: perspective of imaging in the mid-infrared at the VLTI,” in *Optical and Infrared Interferometry*, vol. 7013, p. 70132B, International Society for Optics and Photonics, 2008.
- [202] J. Kluska, F. Malbet, J. Berger, F. Baron, B. Lazare, J. L. Bouquin, J. D. Monnier, F. Soulez, and E. Thiébaut, “SPARCO : a semi-parametric approach for image reconstruction of chromatic objects,” *Astronomy & Astrophysics*, vol. 80, pp. 1–11, 2014.
- [203] E. Thiébaut, F. Soulez, and L. Denis, “Exploiting spatial sparsity for multi-wavelength imaging in optical interferometry,” *Journal of Optical Society of America*, vol. 30, no. 2, pp. 160–170, 2013.
- [204] A. Schutz, A. Ferrari, D. Mary, F. Soulez, E. Thiébaut, and M. Vannier, “PAINTER: a spatio-spectral image reconstruction algorithm for optical interferometry,” *Journal of Optical Society of America*, vol. 31, no. 11, p. 2334, 2014.
- [205] P. Frankel, G. Garrigos, and J. Peypouquet, “Splitting methods with variable metric for KL functions,” *Journal of Optimization Theory and Applications*, vol. 165, no. November, pp. 874–900, 2015.

- [206] T. A. Pauls, J. S. Young, W. D. Cotton, and J. D. Monnier, “A Data Exchange Standard for Optical (Visible / IR) Interferometry,” *Publications of the Astronomical Society of the Pacific*, vol. 117, pp. 1255–1262, 2005.
- [207] M. J. D. Powell, “On search directions for minimization algorithms,” *Mathematical Programming*, vol. 4, no. 1, pp. 193–201, 1973.
- [208] P. L. Combettes and J.-C. Pesquet, *Fixed-Point Algorithms for Inverse Problems in Science and Engineering*. Springer, New York, 2010.
- [209] P. Tuthill, J. Monnier, W. Danchi, D. Hale, and C. Townes, “Imaging the disk around the luminous young star LkH α 101 with infrared interferometry,” *The Astrophysical Journal*, vol. 577, no. 2, p. 826, 2002.
- [210] P. R. Lawson, W. D. Cotton, C. A. Hummel, J. D. Monnier, M. Zhao, J. S. Young, H. Thorsteinsson, S. C. Meimon, L. M. Mugnier, G. Le Besnerais, E. M. Thiebaut, and P. G. Tuthill, “An interferometry imaging beauty contest,” *Proceedings of SPIE*, vol. 5491, pp. 886–899, 2004.
- [211] J. Sanchez-Bermudez, E. Thiébaut, K.-H. Hofmann, M. Heininger, D. Schertl, G. Weigelt, F. Millour, A. Schutz, A. Ferrari, M. Vannier, *et al.*, “The 2016 interferometric imaging beauty contest,” in *Optical and Infrared Interferometry and Imaging V*, vol. 9907, p. 99071D, International Society for Optics and Photonics, 2016.
- [212] F. Soulez, S. Bongard, E. Thiébaut, and R. Bacon, “Restoration of hyperspectral astronomical data from integral field spectrograph,” in *Workshop on Hyperspectral Image and Signal Processing, Evolution in Remote Sensing*, 2011.
- [213] A. Abdulaziz, A. Dabbech, A. Onose, and Y. Wiaux, “A Low-rank and Joint-Sparsity Model for Hyper-Spectral Radio-Interferometric Imaging,” in *Proceedings of EUSIPCO*, pp. 388–392, IEEE, 2016.
- [214] M. Fornasier and H. Rauhut, “Recovery Algorithms for Vector-Valued Data with Joint Sparsity Constraints,” *SIAM Journal on Numerical Analysis*, vol. 46, no. 2, pp. 577–613, 2008.

- [215] U. Rau and T. J. Cornwell, “A multi-scale multi-frequency deconvolution algorithm for synthesis imaging in radio interferometry,” *Astronomy & Astrophysics*, vol. 532, p. A71, 2011.
- [216] H. Junklewitz, M. R. Bell, and T. Enslin, “A new approach to multifrequency synthesis in radio interferometry,” *Astronomy & Astrophysics*, vol. 581, p. A59, 2015.
- [217] M. Wieringa, A. De Bruyn, D. Jansen, W. Brouw, P. Katgert, *et al.*, “Small scale polarization structure in the diffuse galactic emission at 325 mhz,” *Astronomy & Astrophysics*, vol. 268, p. 215, 1993.
- [218] R. Sault and A. Duncan, “Polarimetric imaging of large fields in radio astronomy,” *Astronomy and Astrophysics Supplement Series*, vol. 139, no. 2, pp. 387–392, 1999.
- [219] M. Brentjens and A. De Bruyn, “Faraday rotation measure synthesis,” *Astronomy & Astrophysics*, vol. 441, pp. 1217–1228, 2005.
- [220] M. R. Bell and T. Enslin, “Faraday synthesis-The synergy of aperture and rotation measure synthesis,” *Astronomy & Astrophysics*, vol. 540, p. A80, 2012.
- [221] A. Abdulaziz, A. Dabbech, and Y. Wiaux, “Wideband super-resolution imaging in radio interferometry via low rankness and joint average sparsity models (HyperSARA),” *arXiv preprint arXiv:1806.04596*, 2018.